frontiers | Research Topics

Bioinspired superwettable materials from design, fabrication to application, volume II

Edited by
Jingxin Meng, Tailin Xu, Hongliang Liu, Feilong Zhang, Pengchao Zhang and Jun-Bing Fan

Published in
Frontiers in Bioengineering and Biotechnology

ISSN 1664-8714
ISBN 978-2-8325-3134-1
DOI 10.3389/978-2-8325-3134-1

About Frontiers

Frontiers is more than just an open access publisher of scholarly articles: it is a pioneering approach to the world of academia, radically improving the way scholarly research is managed. The grand vision of Frontiers is a world where all people have an equal opportunity to seek, share and generate knowledge. Frontiers provides immediate and permanent online open access to all its publications, but this alone is not enough to realize our grand goals.

Frontiers journal series

The Frontiers journal series is a multi-tier and interdisciplinary set of open-access, online journals, promising a paradigm shift from the current review, selection and dissemination processes in academic publishing. All Frontiers journals are driven by researchers for researchers; therefore, they constitute a service to the scholarly community. At the same time, the *Frontiers journal series* operates on a revolutionary invention, the tiered publishing system, initially addressing specific communities of scholars, and gradually climbing up to broader public understanding, thus serving the interests of the lay society, too.

Dedication to quality

Each Frontiers article is a landmark of the highest quality, thanks to genuinely collaborative interactions between authors and review editors, who include some of the world's best academicians. Research must be certified by peers before entering a stream of knowledge that may eventually reach the public - and shape society; therefore, Frontiers only applies the most rigorous and unbiased reviews. Frontiers revolutionizes research publishing by freely delivering the most outstanding research, evaluated with no bias from both the academic and social point of view. By applying the most advanced information technologies, Frontiers is catapulting scholarly publishing into a new generation.

What are Frontiers Research Topics?

Frontiers Research Topics are very popular trademarks of the *Frontiers journals series*: they are collections of at least ten articles, all centered on a particular subject. With their unique mix of varied contributions from Original Research to Review Articles, Frontiers Research Topics unify the most influential researchers, the latest key findings and historical advances in a hot research area.

Find out more on how to host your own Frontiers Research Topic or contribute to one as an author by contacting the Frontiers editorial office: frontiersin.org/about/contact

Bioinspired superwettable materials from design, fabrication to application, volume II

Topic editors

Jingxin Meng — Technical Institute of Physics and Chemistry, Chinese Academy of Sciences (CAS), China

Tailin Xu — Shenzhen University, China

Hongliang Liu — Yantai University, China

Feilong Zhang — Nanyang Technological University, Singapore

Pengchao Zhang — Wuhan University of Technology, China

Jun-Bing Fan — Southern Medical University, China

Citation

Meng, J., Xu, T., Liu, H., Zhang, F., Zhang, P., Fan, J.-B., eds. (2023). *Bioinspired Superwettable Materials from Design, Fabrication to Application, volume II*. Lausanne: Frontiers Media SA. doi: 10.3389/978-2-8325-3134-1

Table of contents

frontiers | Frontiers in Bioengineering and Biotechnology

TYPE Editorial
PUBLISHED 18 July 2023
DOI 10.3389/fbioe.2023.1249653

OPEN ACCESS

EDITED AND REVIEWED BY
Hasan Uludag,
University of Alberta, Canada

*CORRESPONDENCE
Feilong Zhang,
zhangfl@mail.ipc.ac.cn
Jingxin Meng,
mengjx628@mail.ipc.ac.cn

RECEIVED 29 June 2023
ACCEPTED 03 July 2023
PUBLISHED 18 July 2023

CITATION
Shang Z, Zhao R, Zhang F and Meng J (2023), Editorial: Bioinspired superwettable materials from design, fabrication to application, volume II. *Front. Bioeng. Biotechnol.* 11:1249653. doi: 10.3389/fbioe.2023.1249653

Editorial: Bioinspired superwettable materials from design, fabrication to application, volume II

Zhihao Shang[1,2], Ran Zhao[2,3], Feilong Zhang[2,3,4]* and Jingxin Meng[2,3,5]*

[1]Yanshan University, Qinhuangdao, China, [2]Technical Institute of Physics and Chemistry, Chinese Academy of Sciences (CAS), Beijing, China, [3]University of Chinese Academy of Sciences, Beijing, China, [4]Nanyang Technological University, Singapore, Singapore, [5]Binzhou Institute of Technology, Weiqiao-UCAS Science and Technology Park, Binzhou, China

KEYWORDS

bioinspired, anti-adhesion, adhesion, bone tissue recovery, wound healing, sensing detection

Editorial on the Research Topic
Bioinspired superwettable materials from design, fabrication to application, volume II

Superwettable materials, which combine the surface micro/nano structure and chemical composition, have already emitted light and heat in many fields, such as anti-fouling, signal monitoring, rehabilitation treatment, etc. Special biological phenomena in nature constantly provide inspiration for the design of superwettable materials, for example, self-cleaning materials inspired by lotus leaves, adhesive materials with superwettability inspired by barnacles, and signal recognition systems inspired by mammalian olfactory recognition. We believe that more biological phenomena can be explored and more applicable superwettable materials can be provided.

The primary task of this Research Topic is to compile high-quality researches on bioinspired superwettable materials for conquering real-life scientific problems. This Research Topic contains nine articles including six research articles and three review articles from world-leading scientists in various fields, aiming to emphasize practical evolution of bioinspired materials with superwetting properties in the fields such as fouling prevention, bone tissue recovery, wound healing and sensing detection.

Regulating the adhesion properties of various superwetting materials is a key foundation for their applications. Barnacles, one of the most common living organisms in the ocean, exhibit high underwater adhesion strength with the substrate due to their hydrogen bonding and electrostatic interaction. Inspired by this, Hao et al. reported a hydrogel adhesive composed of polyethylene imine and polymethacrylic acid, achieving high adhesion strength under water via overcoming the adverse effects of water layer. The adhesion strength under water or other solvents remains at high levels of 1.99 and 2.70 MPa, respectively. As a widely used liquid organic salt, ionic liquid has irreplaceable advantages such as negligible vapor pressure, adjustability and lubricity, etc. To develop bioinspired superwettable materials, Zhang et al. summarized the design of bioinspired ionic-liquid based interfacial materials

and then, exemplified their latest applications in the field of adhesion (e.g., wound dressing) and anti-adhesion (e.g., anti-scaling).

Repairing bone injuries has attracted much attention in the medical fields. To accelerate the healing of injured bone tissue, it is urgent to find powerful biocompatibility bone grafting materials. For example, Liu et al. proposed a bioinspired strontium doped magnesium phosphate cement (S-MPC) to solve sufficient biocompatibility which is the biggest shortcoming of MPC. A certain amount of strontium was introduced into the MPC, endowing the S-MPC with the advantages of high crystallinity, excellent biocompatibility and stable mechanical strength. S-MPC is not only beneficial to accelerate bone tissue repair, but also can meet different needs of patients with bone injury by changing its shape. In addition, the absorption of alveolar bone caused by dental surgical procedure is an irreversible bad phenomenon. To solve this problem, Guo et al. prepared the cell microspheres for bone repair by introducing mesenchymal stem cells and vascular endothelial cells into the polyether F127 diacrylate hydrogel. The autonomous diffusion ability of the fabricated cell microspheres can fully contact bone tissue defects in a three-dimensional manner, showing great biocompatibility and excellent mechanical properties.

As well known, skin is the largest protective organ of the human body, but skin replacement would be an inevitable solution if the damage area of the skin is too large. Skin transplantation means immune rejection and other problems, so bioinspired skin has attracted extensive attention in the field of rehabilitation medicine. Wang et al. summarized the classification of bioinspired skin, and then concluded that the characteristics of electronic skin are stimulus response and self-healing ability. More importantly, this review discussed the practical application of bioinspired skin. Therefore, the development of bioinspired superwettable materials has opened new avenues for bioinspired skin. Additionally, wound region caused by skin tissue damage occur from time to time. Controlling the amount of bleeding is identified as the primary task in the four periods of wound healing. Based on this, Zhong et al. summarized the latest progress in superwettable wound dressings and provided a detailed introduction to different materials used for hemostasis and exudate management. Moreover, the management of exudates is also an important means related to wound healing which can avoid the continuous inflammation of the wound. For instance, Lan et al. fabricated an enhanced fractal self-pumping (EFS) hydrogel which can quickly absorb water and discharge it in 0.4 s owing to the introduction of hollow glass microspheres in the hydrogel precursor. By simulating human skin wound models in animal experiments, EFS hydrogel wound dressing can significantly accelerate wound recovery. It is believed that above articles will make readers enthusiastic about learning wound management and are expected to provide design ideas for interface materials for biomedical applications.

In the field of polymer-based organic vapor sensors, higher accuracy and lower detection limit are urgently needed. Inspired by mammalian olfactory recognition system, Zhao et al. proposed a bioinspired polymer array vapor sensor that combines principal component analysis algorithm, which can classify and recognize a variety of common organic compounds (e.g., ethanol, acetone, methylene chloride). The detection ability of the sensor is attributed to the introduction of aggregation-induced emission molecules into the polymer. Malathion is a traditional organophosphorus insecticide component, but the abuse of malathion will lead to life health and ecological environment problems. In order to achieve the detection goal of malathion, Li et al. designed an efficient sensor for malathion with the detection limit of 1.48 g/L and the change can be easily identified by the naked eye. In summary, the above sensors with extremely high accuracy and very low detection limit, are expected to be used for environmental monitoring, agricultural production, medical treatment, and other fields.

Overall, this Research Topic cover several high-profile fields in bio-inspired materials with super wettability, such as fouling prevention, bone tissue recovery, wound healing and sensing detection, which make readers enthusiastic about learning the latest advances in bio-inspired superwettable materials. Although exciting results are achieved one after another, more bioinspired superwettable materials will come into practical applications soon.

Author contributions

All authors listed have made a substantial, direct, and intellectual contribution to the work and approved it for publication.

Acknowledgments

The editors appreciate the contributions of all the authors to this Research Topic, the constructive comments of all the reviewers, and the editorial support from Frontiers throughout the publication process. JM also appreciates the support of the Strategic Priority Research Program of the Chinese Academy of Sciences (XDB 0470201), National Natural Science Foundation of China (22275203).

Conflict of interest

The authors declare that the research was conducted in the absence of any commercial or financial relationships that could be construed as a potential conflict of interest.

Publisher's note

frontiers | Frontiers in Bioengineering and Biotechnology

TYPE Original Research
PUBLISHED 31 October 2022
DOI 10.3389/fbioe.2022.1058404

OPEN ACCESS

EDITED BY
Pengchao Zhang,
Wuhan University of Technology, China

REVIEWED BY
Moyuan Cao,
Nankai University, China
Jinhui Pang,
Jilin University, China

*CORRESPONDENCE
Xiangyu Jiang,
jiangxy@buaa.edu.cn
Dong Wang,
wangdong@ustb.edu.cn

SPECIALTY SECTION
This article was submitted to Biomaterials, a section of the journal Frontiers in Bioengineering and Biotechnology

RECEIVED 30 September 2022
ACCEPTED 11 October 2022
PUBLISHED 31 October 2022

CITATION
Zhao Z, Ge Y, Xu L, Sun X, Zuo J, Wang Z, Liu H, Jiang X and Wang D (2022), Bio-inspired polymer array vapor sensor with dual signals of fluorescence intensity and wavelength shift. *Front. Bioeng. Biotechnol.* 10:1058404. doi: 10.3389/fbioe.2022.1058404

Bio-inspired polymer array vapor sensor with dual signals of fluorescence intensity and wavelength shift

Zhihao Zhao[1,2], Yinghao Ge[3,4], Lingyun Xu[1], Xiaohan Sun[1,3], Jing Zuo[1,3], Zhenglin Wang[1], Hongyang Liu[1], Xiangyu Jiang[1]* and Dong Wang[2]*

[1]Research Institute of Frontier Science, Beihang University, Beijing, China, [2]Department of Materials Physics and Chemistry, School of Materials Science and Engineering, University of Science and Technology Beijing, Beijing, China, [3]Chinese Acad Sci, Tech Institute Phys & Chem, CAS Key Lab Bioinspired Mat & Interfacial Sci, Beijing, China, [4]School of Future Technology, University of Chinese Academy of Sciences, Beijing, China

Organic vapor sensors based on polymer owing to their tunable molecular structures and designable functions have attracted considerable research interest. However, detecting multiple organic vapors with high accuracy and a low detection limit is still challenging. Herein, inspired by the mammalian olfactory recognition system, organic vapor sensors based on one-dimensional microfilament array structures with a wide range of sensing gases are demonstrated. By introducing aggregation-induced emission (AIE) molecules, sensors possess dual-optical sensing mechanisms of variation in fluorescence intensity and wavelength. By virtue of the synergistic effects of dual signals, superb accuracy and incredibly low detection limit are achieved for identifying analytes. In particular, the polymer/AIE microfilament array can detect acetone vapor down to 0.03% of saturated vapor pressure. In the saturated vapor of acetone, the fluorescence intensity of the sensor arrays was reduced by 53.7%, while the fluorescence wavelength was red-shifted by 21 nm. Combined with the principal component analysis (PCA) algorithm, the polymer/AIE molecular sensor arrays accomplished the classification and identification of acetone, ethanol, methylene chloride, toluene, and benzene. This bioinspired approach with dual sensing signals may broaden practical applications to high-performance gas sensors for precise molecular detection.

KEYWORDS

aggregation-induced emission, one-dimensionalization, organic vapor sensor arrays, fluorescent intensity, wavelength shift

1 Introduction

Nowadays, the electronic nose has been intensively studied, and a variety of array sensors have been developed (Lipatov et al., 2013; Rochat and Swager, 2014; Zhang et al., 2017) to detect metal ions, toxic gases, flammable and explosive gases (Zhu Q. et al., 2017), volatile organic compounds and analyze complex mixtures such as fish freshness (Liu et al., 2022) and wine (Han et al., 2022). Traditional chemical sensors use a "lock and key" design strategy to identify analytes, relying on a well-designed highly selective receptor. Such methods are suitable for identifying specific target compounds when the ambient atmosphere is disturbed. However, if the analyte changes, another highly selective receptor must be redesigned, which is very time-consuming and laborious. Therefore, it is still an urgent challenge to develop a universal, effective, wide detection range and low detection limit organic vapor sensor.

Inspired by the superior performance of biological olfactory systems, sensor arrays have been presented to complement traditional chemical sensing methods (Persaud and Dodd, 1982; Li et al., 2019). Mammals perceive the external environment by using the smell system to find food, identify territories and determine enemies. The mammalian olfactory system contains approximately 1,000 different olfactory receptor genes (Mombaerts, 1999; Menini et al., 2004; Buck, 2005). The same receptor can respond to a wide range of analytes but cannot differentiate an analyte accurately. To distinguish specific odors, cross-reactive sensor arrays are formed by a large number of olfactory receptors without specific recognition. Owing to these its-for-recognition arrays, humans can distinguish more than 1 trillion olfactory stimuli (Bushdid et al., 2014). In artificial sensor arrays, which are composed of a series of sensing units without specific recognition capabilities, each element of the sensor array is capable of responding to diverse chemicals or classes of chemicals and do not need to be individually high-selective to any given analyte.

The capillary-bridge-mediated assembly (CBMA) method is an emerging technique to self-assemble materials into a directionally arranged micron filament structure (Feng et al., 2017; Feng et al., 2018; Chen et al., 2021). This ordered quasi-one-dimensional structure allows the sensor to obtain a larger specific surface area than conventional thin-film-like sensors, which will result in better sensor performance (Su et al., 2012; Chen et al., 2013).

Fluorescence sensor arrays, due to their high sensitivity, no need of reference systems, diverse output signals, and ability to image (McDonagh et al., 2008; Wu et al., 2015), have become the research hotspots in recent years. The existing fluorescence sensor response signals are mainly either fluorescence intensity changes (Jiang et al., 2018; Liu et al., 2018; Stevens et al., 2020) or spectral wavelength shifts (Zhu J. et al., 2017; Zhu et al., 2019; Yao et al., 2021). Employing multiple fluorescence response signals for detecting analytes is a feasible strategy to improve the differentiation degree of the sensor arrays (Teo et al., 2009; Koo et al., 2011).

Almost all polymers undergo swelling in the presence of organic vapors. During the swelling process, the macroscopic volume of polymers becomes larger, and the molecular chain gaps subsequently become more spacious. By introducing aggregation-induced emission (AIE) molecules, the volume variant of the polymer can be reflected by the fluorescence signal change (Leung et al., 2014; Mei et al., 2014; Kwok et al., 2015; Gao and Tang, 2017). Different polymers swell to different degrees under the same organic vapor atmosphere, which provides a possibility of designing optical organic vapor sensor arrays with the swelling behavior of macromolecules (Jiang et al., 2018; Jiang et al., 2021).

In this work, one-dimensional arrays containing polymer and AIE molecules have been fabricated by the CBMA method. Based on the polymer swelling principle, organic vapor sensors with two sensing mechanisms of fluorescence intensity change and spectral shift have been obtained. Sensing arrays consisting of four gas sensors with different polymeric substrates were achieved to mimic the olfactory process of mammals. Combined with PCA algorithms, sensor arrays were used to successfully analyze and identify the vapors of five common volatile organic solvents: acetone, ethanol, methylene chloride, benzene, and toluene. Finally, the five different types of organic gases are well separated in the 2D PCA images.

2 Materials and methods

2.1 Materials

Four commercially available polymers, including polystyrene (PS), polyethersulfone (PES), polyvinylpyrrolidone (PVP), and polymethyl methacrylate (PMMA), were purchased from Sinopharm Chemical Reagent Co., Ltd., China and used without purification. 2-[[4'-(Diphenylamino)[1,1′-biphenyl]-4-yl]methylene]propanedinitrile (TPMN) molecules were provided by AIE Institute, China. The photoresist (KMP CP4800) was supplied by Kempur Microelectronics Inc. China. Organic solvents were bought from Shanghai Aladdin Reagent Co. Ltd. Shanghai, China.

2.2 Production of silicon column template

Line-structured silicon column templates were prepared in the following steps. Silicon wafers (100 mm diameter, P-doped, <100> orientation, 400 μm thick) were structured by photolithography and deep reactive ion etching using a direct laser writing device. Then, periodic micropillar structured substrates with a gap of 5 μm between two adjacent columns, a width of 2 μm, and a height of 15 μm were fabricated. The

photoresist was removed by cleaning in a plasma cleaner for 20 min.

2.3 Asymmetric wettability modification of silicon micropillar templates

The template was rinsed with deionized water and acetone in turn, immersed in ethanol for about 5 min, and blown dry with dry nitrogen. Meanwhile, the slides were cleaned with ethanol. The photoresist was spin-coated on the slide using a spin coater (LEBOscience, KW-4A, China). The side with photoresist film was pressed onto the microcolumn template, on which a 10 g weight was placed and left for 20 s. After the silicon template was peeled off, the photoresist was irradiated with 365 nm UV light for 3 min to cure the photoresist. As a result, the top of the silicon column was protected by the photoresist film, while the sidewalls and microstructure gaps of the silicon column were exposed to air. The silicon template was then fumigated in a FAS atmosphere at 60°C for 12 h. In the process, the sidewalls of the silicon micro-pillars and their interstitial surfaces were modified by FAS molecules with low surface energy. The protective film on the top of the silica column was removed to obtain an asymmetric wettability template with a hydrophilic top and hydrophobic side walls, as shown in Supplementary Figure S1.

2.4 Preparation of polymer/AIE molecular microfilament arrays

First, a certain amount of PS and TPMN (mass ratio of 10:1) was dissolved in dichloromethane in various concentrations of 1 g/L, 5 g/L, and 10 g/L. Then, the highly aligned 1D arrays of polymer/AIE were prepared by the CBMA method using a microcolumn silicon template with a width of 2 μm, spacing of 5 μm, and a height of 15 μm. The schematic diagram is shown in Supplementary Figure S2. 10 μL of the polymer/AIE molecules solution was dropped onto the template and covered with a clean quartz sheet to construct a sandwich structure, and then placed in a fume hood for 24 h to slowly evaporate the solvent at room temperature. It was transferred to a vacuum drying oven at 60°C for 2 h to evaporate any possible residual organic solvent. Eventually, highly aligned polymer/AIE molecular microfilament arrays were obtained on quartz sheets.

2.5 Characterization

Bright-field microscopy images were obtained by light microscopy (Olympus, BX53, Japan) and a charge-coupled device (CCD) camera (Olympus, DP80, Japan) under a daylight light source. Meanwhile, fluorescence images were obtained under the excitation of a mercury lamp light source. The morphology of the assembled arrays was observed using a cold-field emission scanning electron microscope (SEM, Hitachi, SU8010, Japan) with an accelerating voltage of 10.0 kV. The dimensions of microstrips arrays were measured *via* a confocal microscope (Olympus, OLS-45-SAF, Japan) with atomic force microscopy (AFM) mode.

2.6 Organic vapor sensing measurement

A micro sampler is used to inject a quantitative amount of organic solvent into a Teflon gas bag containing nitrogen to obtain a specific concentration of organic vapor. The organic vapor was continuously blown into the quartz hood so that the sample was in full contact with the organic vapor. Subsequently, the fluorescence spectra of polymer/AIE molecular microfilament arrays in different gas environments were obtained using a fluorescence spectrometer (Shimadzu, RF-5301pc, Japan) with an excitation wavelength of 480 nm. The changes in fluorescence intensity and peak shifts of polymer/AIE molecules microfilament arrays in different gas atmospheres were then obtained.

3 Results

3.1 Fabrication of 1D polymers/AIE molecules arrays

In order to explore the optimal concentration for the preparation of micron filament arrays by the CBMA method, polymer/AIE molecules solution at different concentrations was formulated. SEM images show that the micron filaments became increasingly smooth as the solution concentration increased (Supplementary Figure S3). At the solution concentration of 10 g/L, the prepared micron filaments possess straight edges and regular arrangement. Therefore, the optimal solution concentration is determined to be 10 g/L. Compared with unmodified templates, arrays prepared using the asymmetric-wettability modification have a larger range of highly aligned arrangements (Supplementary Figure S4). For the unmodified microcolumn templates, the solution contraction is subjected to less induced force and more random, causing aligned microfilament arrays unsuccessfully assembled. As shown in Figure 1A, the obtained polymer/AIE molecules arrays present flat edges and highly parallel arrangements. In the dark-field microscopy image, the sample emits a uniform and bright orange-yellow light, which indicates that the AIE molecules are uniformly distributed in the polymer microfilaments (Figure 1C). To further identify the dimensions of micro stripes, AFM was performed. AFM images demonstrate that the micro stripes in the arrays are uniform in height and similar in width (Figure 1D).

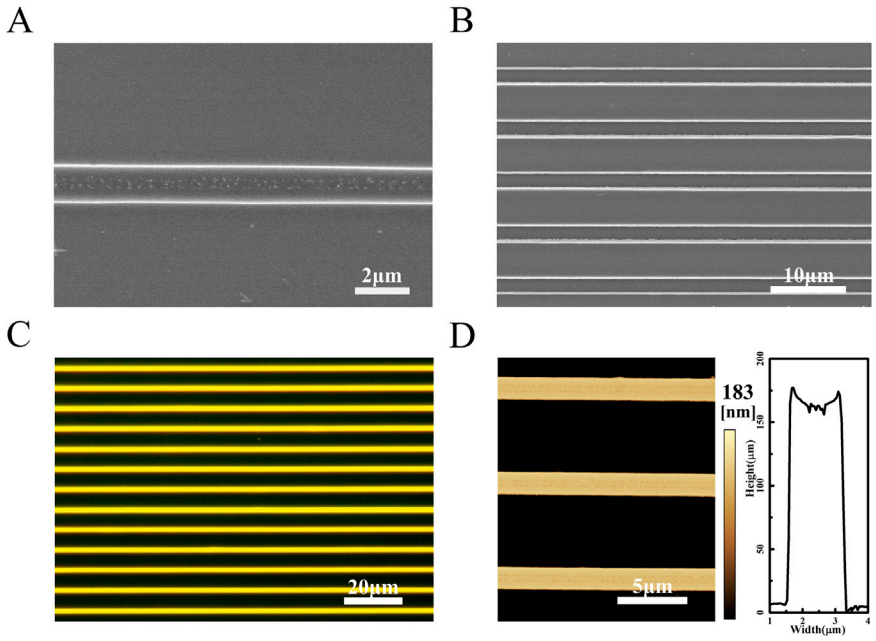

FIGURE 1
(A) SEM image of a single PS/TPMN molecular microfilament array. The width of the microfilaments is 1.41 ± 0.02 μm, and they have flat and smooth edges **(B)** Multiple PS/TPMN molecular microfilament arrays arrange neatly. The spacing between two adjacent microfilaments is 5.44 ± 0.11 μm. The microfilaments are equally spaced and arranged in parallel; **(C)** Dark-field microscopy photograph of the microfilament array with uniform yellow fluorescence emission from the microfilaments; **(D)** AFM photograph of the microfilament array and cross-sectional of the microfilament array. The microfilaments are uniform in height with a height of 183 nm.

3.2 Sensing performances of 1D arrays of polymer/AIE molecules

As shown in Figure 2A, the response of PS/TPMN arrays to acetone vapor was demonstrated. It can be seen that the PS/TPMN sample generates a significant response to acetone vapor. To begin with, its fluorescence spectrum was tested in a laboratory air atmosphere, and the sample emitted the strongest fluorescence at 480 nm excitation light. The samples were then placed in an acetone vapor atmosphere at 100,000 ppm and 300,000 ppm, and the fluorescence intensity was found to be significantly lower. Compared with the fluorescence intensity in the air, the fluorescence intensity decreased by 22.9% and 53.7% in the acetone atmosphere at 100,000 ppm and 300,000 ppm, respectively (Figure 2A). To explain the underlying mechanism of vapor sensing, confocal images of PS/TPMN samples in the air atmosphere and 300000 ppm acetone vapor were taken. The width and height were expanded by 7.18 ± 1.17% and 8.66 ± 0.87% under the acetone atmosphere, respectively (Supplementary Figure S5), which verified that the decrease in fluorescence intensity of the optical gas sensors is due to the swelling effect after adsorption of organic vapors.

The shift in peak position can also be observed along with the change in fluorescence intensity with acetone concentration increased in the ambient atmosphere at the fluorescence spectrum. Compared with the central wavelength of fluorescence in air, the fluorescence intensity was red-shifted by 8.3 nm and 21.0 nm in the acetone atmosphere at 100,000 ppm and 300,000 ppm, respectively. Meanwhile, a change in fluorescence color from yellow to orange and red can be observed in the fluorescence micrographs (Figures 2B–D). Afterward, a test of acetone concentration on the fluorescence wavelength change of PS/TPMN arrays was conducted, and no significant wavelength change was observed at less than 1,000 ppm. Compared with the peak position in the air atmosphere, the wavelength redshift by 0.5 nm in 1,000 ppm acetone atmosphere. With the acetone concentration increased, a good linear relationship between the wave shift and the acetone concentration in the environment was established (Figure 2E). It indicates that the polymer/AIE molecular microfilament array sensor can complement the gas response by using wave peak shift while detecting organic vapor through fluorescence intensity change.

Fluorescence spectroscopy of PS/TPMN arrays under different concentrations of acetone vapor was performed. The results show that the fluorescence intensity change ($\Delta I/I_0$) tends to increase with increasing acetone concentration, where I_0 is defined as the baseline fluorescence intensity of PS/TPMN microfilaments in air, and ΔI indicates the fluorescence intensity difference after and before exposure to acetone vapor. The fluorescence intensity change remained well linear

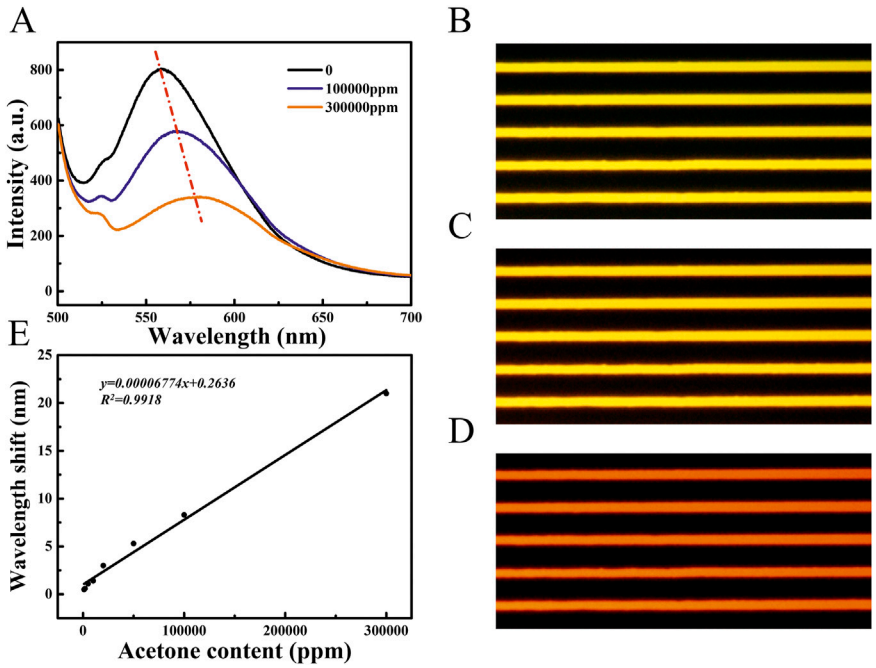

FIGURE 2
(A) Fluorescence spectra of PS/TPMN samples in the gaseous atmosphere at 0, 100000 ppm, and 300000 ppm acetone concentrations. Compared with the acetone concentration of 0, the PS/TPMN samples were red-shifted by 8.3 nm and 21.0 nm in the atmosphere containing 100,000 ppm and 300,000 ppm of acetone vapor, respectively, and the fluorescence intensity was reduced by 22.89 ± 0.81%, and 53.72 ± 1.66%, respectively **(B)** Fluorescence photographs of PS/TPMN samples in the air; **(C)** Fluorescence photographs of PS/TPMN samples in acetone atmosphere at 100000 ppm **(D)** Fluorescence photographs of PS/TPMN samples in 300000 ppm acetone atmosphere; **(E)** Fluorescence photographs of PS/TPMN samples red-shifted in acetone vapor atmosphere at 1,000–300000 ppm, and the degree of red-shift showed a good linear relationship with acetone vapor concentration.

with acetone concentration at less than 1,000 ppm (Figure 3A). With a further increase in acetone concentration, the rising trend of $\Delta I/I_0$ becomes gradually smaller. Figure 3B gives the trend graph of fluorescence intensity variation for the acetone concentration range of 100 ppm–100000 ppm. As shown in Figures 3A,C sensing response time of 73 s for 300,000 ppm acetone vapor was achieved. In addition, the adsorption-desorption cycles of PS/TPMN arrays were conducted and exhibited reliable stability in the saturated vapor of acetone (Figure 3D).

Four different polymer/AIE molecule microfilament array sensors were prepared using four different commercial polymers (PS, PES, PVP, and PMMA) in combination with TPMN. Commonly used organic vapors of acetone, ethanol, methylene chloride, toluene, and benzene were detected by these four polymer/TPMN sensor arrays (all at 10,000 ppm vapor concentration). By collecting fluorescence intensity variation data, the different types of organic vapors were classified using the PCA method. The PCA result shows that the first two principal components, PC1, and PC2, could capture 88.1% of the variation in the data, accounting for 59.4% and 28.7% of the variance, respectively (Figure 4A), and the first two principal components were sufficient for classification. The different types of organic vapors were well separated. Two more sets of data were measured for these seven organic vapors and evaluated whether the sensor could correctly identify organic vapors by the location of the vapors in the PCA plot. A five-nearest points estimation method based on the first two principal components was applied to perform the classification. Specifically, the first two principal component scores for new observations were calculated and plotted. Then, for each new observation, it is determined that the observation belongs to the group with the highest weight of the five-nearest points in the training dataset, as shown in Figure 4B (plotted in sky-blue color). The overall results show that our proposed method can well classify and identify different organic vapors with a classification rate of 100%.

4 Discussion

1D sensors have a larger specific surface area, compared to thin-film sensors, which can achieve fuller contact between the sensor and the environment. Therefore, one-dimensionalization

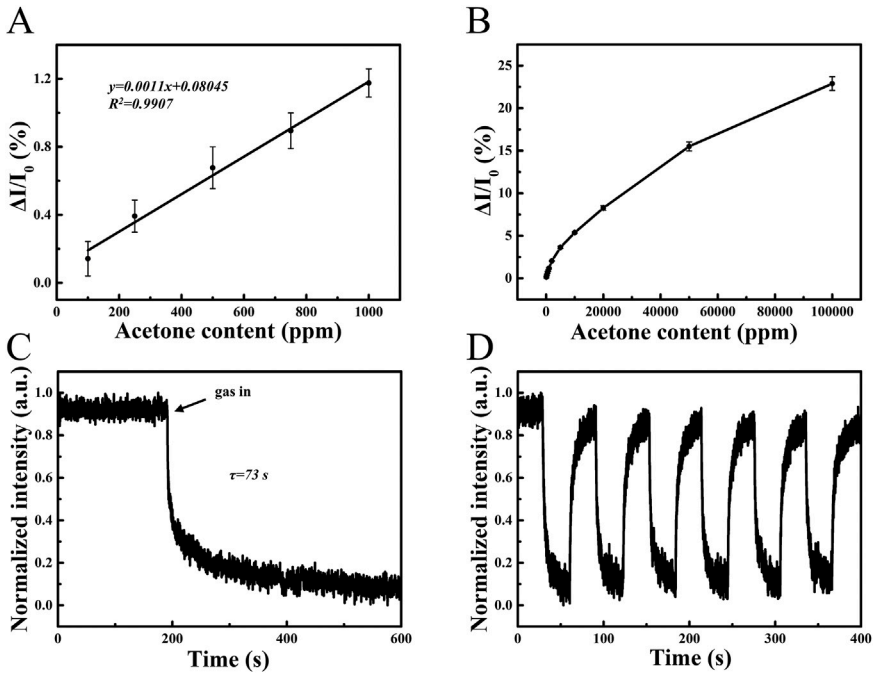

FIGURE 3
(A) Response curves of PS/TPMN samples in acetone vapor at low concentrations. $\Delta I/I_0$ varies linearly with acetone concentration, demonstrating a good linear dependency with low limit of detection of 100 ppm. Error bars, s.d. (n = 10); **(B)** Response curves of PS/TPMN samples in acetone vapor at 100 ppm-100000 ppm. Error bars, s.d. (n = 10) **(C)** Single response curves of PS/TPMN samples in acetone vapor at 300000 ppm. The result indicates the sensor response time is 73 s; **(D)** Continuous multiple response curves of PS/TPMN samples in acetone vapor at 300000 ppm. Demonstrates good reproducibility and stability of the sensor.

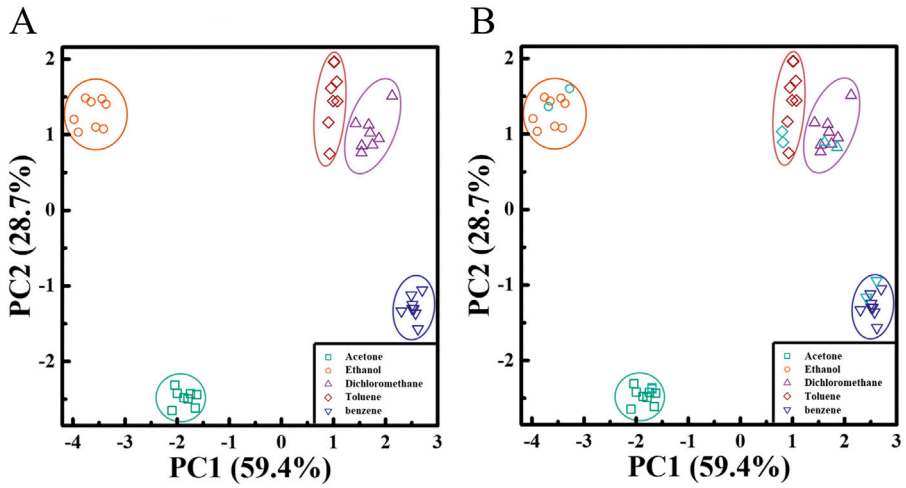

FIGURE 4
Array-based organic vapor sensing and similar organic vapor identification **(A)** PCA plots, calculated from fluorescence intensity variation data obtained for four polymer/TPMN array sensors during exposure to five organic vapors, as shown in the first two main axes of PC1 and PC2. The four commercial polymers used include PS, PMMA, PES, and PVP, and the AIE molecule is TPMN. The PCA algorithm shows that PC1 and PC2 capture 88.1% of the variance of the data, indicating that the different types of organic vapors are well separated. **(B)** Validation of the proposed classification method. Two additional sets of data from these five organic vapors (sky blue) were measured and evaluated, and whether the sensors could correctly identify organic vapors by their vapor locations in the PCA plot. The results show that our proposed method can classify and identify the different organic vapors well.

is a feasible idea to enhance the sensitivity and response speed of sensors. Significant progress has been made in the one-dimensionalization of materials and 1D gas sensors. However, in the fabrication of the 1D materials-based devices, the 1D materials exhibit disordered arrangements with random positions and orientations. By using the CBMA method, we precisely align PS with TPMN fluorescent molecules into 1D micro stripe arrays.

Owing to the precise alignment of 1D structures, which are only confined at the bottom, the sensing material can be fully exposed to ambient gas. Under organic vapors, the microfilaments can expand not only upward but also to the left and right sides. The confocal microscope results show that the width and height of the dissolved 1D structure become larger by 7.18 ± 1.17% and 8.66 ± 0.87%, respectively. In conclusion, the 1D array structures allow for higher sensitivity and a more intense response of the organic vapor sensor based on the swelling principle. The PS/TPMN microfilament arrays can respond to acetone vapor down to 0.03% of the saturation vapor pressure and maintain good linearity between 100 ppm and 1,000 ppm acetone concentration. The polymer/AIE molecule microfilament arrays exhibit good stability when exposed to saturated acetone vapor. A redshift of the wave peak was observed at acetone concentrations up to 2000 ppm. And the central wavelength of sample fluorescence varied linearly with the organic vapor concentration over the acetone concentration range of 2000 ppm–300000 ppm. The polymer/AIE molecule microfilament array sensor can respond to organic vapor with both intensity change and color change. Compared with single-signal organic vapor sensors, it provides more reliable detection results.

Four different polymer/AIE molecular microfilament array sensors were demonstrated using four commercial polymers in combination with TPMN fluorescent molecules. Based on the PCA results, we successfully classified and identified five common organic volatile gas molecules. Among them, two similar organic gases benzene and toluene were still able to be distinguished completely. It proves that the polymer/AIE molecular microfilament sensor arrays based on the polymer swelling principle have good discriminative ability.

5 Conclusion

In conclusion, optical organic vapor sensors have been prepared using the CBMA method, which includes polymer/AIE molecular microfilament arrays with smooth surfaces and uniform dimensions. With the assistance of swelling and AIE effects, obtained sensors can undergo a reversible fluorescence change in an organic vapor atmosphere. Based on the dual-optical sensing response of intensity change and wavelength shift, the optical gas vapor sensors exhibit improved accuracy and broaden detection range. In particular, the fluorescence intensity changes of the PS/TPMN microfilament arrays were observed in acetone vapor from 100 ppm to 100000 ppm, and the fluorescence intensity variation remained well linear with acetone vapor concentration in the low concentration range of 100–1000 ppm. In addition, the fluorescence wavelength shifts of the PS/TPMN microfilament arrays show good linearity in acetone vapor from 1,000 ppm to 300000 ppm. The universality of this technique was verified by adopting four commercial polymers (PS, PES, PVP, and PMMA). Five commonly used organic gases (acetone, ethanol, methylene chloride, toluene, and benzene) were accurately identified by these sensors, especially two similar gases of toluene and benzene. These attractive results demonstrate that polymer arrays with dual optical responses have the potential to be developed into practical and versatile gas sensors in various application fields.

Data availability statement

The original contributions presented in the study are included in the article/Supplementary Material, further inquiries can be directed to the corresponding authors.

Author contributions

XJ and DW conceived the original idea. ZZ and XJ designed and performed the experiments. JZ and YG prepare the materials. ZZ, XS, ZW, and HL analyzed the data. ZZ wrote the original manuscript, LX, XJ, and DW revised it. All authors discussed the results and commented on the manuscript.

Funding

This work was financially supported by the National Natural Science Foundation of China (51973227, 22005011, 21633014, 51901009, 21988102) and the Fundamental Research Funds For the Central Universities.

Acknowledgments

We would like to thank Prof. Shutao Wang's research team for their practical contribution to this work. In addition, we would like to thank Prof. Lei Jiang for advice and proofreading the article before submission.

Conflict of interest

The authors declare that the research was conducted in the absence of any commercial or financial relationships that could be construed as a potential conflict of interest.

Publisher's note

All claims expressed in this article are solely those of the authors and do not necessarily represent those of their affiliated organizations, or those of the publisher, the editors and the reviewers. Any product that may be evaluated in this article, or claim that may be made by its manufacturer, is not guaranteed or endorsed by the publisher.

Supplementary material

The Supplementary Material for this article can be found online at: https://www.frontiersin.org/articles/10.3389/fbioe.2022.1058404/full#supplementary-material

References

Buck, L. B. (2005). Unraveling the sense of smell (nobel lecture). *Angew. Chem. Int. Ed.* 44 (38), 6128–6140. doi:10.1002/anie.200501120

Bushdid, C., Magnasco, M. O., Vosshall, L. B., and Keller, A. (2014). Humans can discriminate more than 1 trillion olfactory stimuli. *Science* 343 (6177), 1370–1372. doi:10.1126/science.1249168

Chen, X., Wong, C. K. Y., Yuan, C. A., and Zhang, G. (2013). Nanowire-based gas sensors. *Sensors Actuators B Chem.* 177, 178–195. doi:10.1016/j.snb.2012.10.134

Chen, Y., Zhu, Z., Jiang, X., and Jiang, L. (2021). Superhydrophobic-substrate-assisted construction of free-standing microcavity-patterned conducting polymer films. *Adv. Sci.* 8 (17), 2100949. doi:10.1002/advs.202100949

Feng, J., Gong, C., Gao, H., Wen, W., Gong, Y., Jiang, X., et al. (2018). Single-crystalline layered metal-halide perovskite nanowires for ultrasensitive photodetectors. *Nat. Electron.* 1 (7), 404–410. doi:10.1038/s41928-018-0101-5

Feng, J., Jiang, X., Yan, X., Wu, Y., Su, B., Fu, H., et al. (2017). Capillary-bridge lithography" for patterning organic crystals toward mode-tunable microlaser arrays. *Adv. Mat.* 29 (1), 1603652. doi:10.1002/adma.201603652

Gao, M., and Tang, B. (2017). Fluorescent sensors based on aggregation-induced emission: Recent advances and perspectives. *ACS Sens.* 2 (10), 1382–1399. doi:10.1021/acssensors.7b00551

Han, J., Kang, M., Jeong, J., Cho, I., Yu, J., Yoon, K., et al. (2022). Artificial olfactory neuron for an in-sensor neuromorphic nose. *Adv. Sci.* 9, 2106017. doi:10.1002/advs.202106017

Jiang, X., Gao, H., Zhang, X., Pang, J., Li, Y., Li, K., et al. (2018). Highly-sensitive optical organic vapor sensor through polymeric swelling induced variation of fluorescent intensity. *Nat. Commun.* 9 (1), 3799. doi:10.1038/s41467-018-06101-8

Jiang, X., Yu, Z., Ma, C., Wang, D., Wu, Y., Shi, C., et al. (2021). Aggregation-induced emission molecule microwire-based specific organic vapor detector through structural modification. *ACS Appl. Mat. Interfaces* 13 (10), 12501–12508. doi:10.1021/acsami.0c22975

Koo, C. K., Samain, F., Dai, N., and Kool, E. T. (2011). DNA polyfluorophores as highly diverse chemosensors of toxic gases. *Chem. Sci.* 2 (10), 1910–1917. doi:10.1039/c1sc00301a

Kwok, R. T. K., Leung, C. W. T., Lam, J. W. Y., and Tang, B. (2015). Biosensing by luminogens with aggregation-induced emission characteristics. *Chem. Soc. Rev.* 44 (13), 4228–4238. doi:10.1039/c4cs00325j

Leung, N. L. C., Xie, N., Yuan, W., Liu, Y., Wu, Q., Peng, Q., et al. (2014). Restriction of intramolecular motions: The general mechanism behind aggregation-induced emission. *Chem. Eur. J.* 20 (47), 15349–15353. doi:10.1002/chem.201403811

Li, Z., Askim, J. R., and Suslick, K. S. (2019). The optoelectronic nose: Colorimetric and fluorometric sensor arrays. *Chem. Rev.* 119 (1), 231–292. doi:10.1021/acs.chemrev.8b00226

Lipatov, A., Varezhnikov, A., Wilson, P., Sysoev, V., Kolmakov, A., and Sinitskii, A. (2013). Highly selective gas sensor arrays based on thermally reduced graphene oxide. *Nanoscale* 5 (12), 5426–5434. doi:10.1039/c3nr00747b

Liu, H., Zhang, Y., Huang, L., and Wang, M. (2022). A colorimetric gas-sensitive array sensor using filter paper for the analysis of fish freshness. *Food Chem.* 377, 132029. doi:10.1016/j.foodchem.2021.132029

Liu, K., Shang, C., Wang, Z., Qi, Y., Miao, R., Liu, K., et al. (2018). Non-contact identification and differentiation of illicit drugs using fluorescent films. *Nat. Commun.* 9 (1), 1695. doi:10.1038/s41467-018-04119-6

McDonagh, C., Burke, C. S., and MacCraith, B. D. (2008). Optical chemical sensors. *Chem. Rev.* 108 (2), 400–422. doi:10.1021/cr068102g

Mei, J., Hong, Y., Lam, J. W. Y., Qin, A., Tang, Y., and Tang, B. (2014). Aggregation-induced emission: The whole is more brilliant than the parts. *Adv. Mat.* 26 (31), 5429–5479. doi:10.1002/adma.201401356

Menini, A., Lagostena, L., and Boccaccio, A. (2004). Olfaction: From odorant molecules to the olfactory cortex. *Physiology* 19, 101–104. doi:10.1152/nips.1507.2003

Mombaerts, P. (1999). Seven-transmembrane proteins as odorant and chemosensory receptors. *Science* 286 (5440), 707–711. doi:10.1126/science.286.5440.707

Persaud, K., and Dodd, G. (1982). Analysis of discrimination mechanisms in the mammalian olfactory system using a model nose. *Nature* 299 (5881), 352–355. doi:10.1038/299352a0

Rochat, S., and Swager, T. M. (2014). Fluorescence sensing of amine vapors using a cationic conjugated polymer combined with various anions. *Angew. Chem. Int. Ed.* 53 (37), 9792–9796. doi:10.1002/anie.201404439

Stevens, D. M., Gray, B. L., Yin, D., Chapman, G. H., and Leznoff, D. B. (2020). Post arrays for the immobilization of vapochromic coordination polymers for chemical sensors. *IEEE Sens. J.* 20 (20), 12102–12108. doi:10.1109/JSEN.2020.3000178

Su, B., Wu, Y., and Jiang, L. (2012). The art of aligning one-dimensional (1D) nanostructures. *Chem. Soc. Rev.* 41 (23), 7832–7856. doi:10.1039/c2cs35187k

Teo, Y. N., Wilson, J. N., and Kool, E. T. (2009). Polyfluorophores on a dna backbone: A multicolor set of labels excited at one wavelength. *J. Am. Chem. Soc.* 131 (11), 3923–3933. doi:10.1021/ja805502k

Wu, J., Kwon, B., Liu, W., Anslyn, E. V., Wang, P., and Kim, J. S. (2015). Chromogenic/fluorogenic ensemble chemosensing systems. *Chem. Rev.* 115 (15), 7893–7943. doi:10.1021/cr500553d

Yao, S., Xu, H., Zheng, T., Liu, S., Chen, J., and Wen, H. (2021). Rare fluorescence red-shifted metal–organic framework sensor for methylamine derived from an N-donor ligand. *Cryst. Growth & Des.* 21 (10), 5765–5772. doi:10.1021/acs.cgd.1c00672

Zhang, D., Liu, J., Jiang, C., Liu, A., and Xia, B. (2017). Quantitative detection of formaldehyde and ammonia gas via metal oxide-modified graphene-based sensor array combining with neural network model. *Sensors Actuators B Chem.* 240, 55–65. doi:10.1016/j.snb.2016.08.085

Zhu, J., Zhao, Z., Li, J., and Zhao, J. (2017a). Fluorescent detection of ascorbic acid based on the emission wavelength shift of CdTe quantum dots. *J. Luminescence* 192, 47–55. doi:10.1016/j.jlumin.2017.06.015

Zhu, Q., Xiong, W., Gong, Y., Zheng, Y., Che, Y., and Zhao, J. (2017b). Discrimination of five classes of explosives by a fluorescence array sensor composed of two tricarbazole-nanostructures. *Anal. Chem.* 89 (22), 11908–11912. doi:10.1021/acs.analchem.7b04083

Zhu, S., Corsetti, S., Wang, Q., Li, C., Huang, Z., and Nabi, G. (2019). Optical sensory arrays for the detection of urinary bladder cancer-related volatile organic compounds. *J. Biophot.* 12 (10), e201800165. doi:10.1002/jbio.201800165

frontiers | Frontiers in Bioengineering and Biotechnology

TYPE Mini Review
PUBLISHED 07 December 2022
DOI 10.3389/fbioe.2022.1106267

OPEN ACCESS

EDITED BY
Pengchao Zhang,
Wuhan University of Technology, China

REVIEWED BY
Baolin Guo,
Xi'an Jiaotong University, China
Xingyu Chen,
Southwest Jiaotong University, China

*CORRESPONDENCE
Ping Shi,
cgscshiping@163.com
Chunmei Ding,
dingcm@scu.edu.cn

SPECIALTY SECTION
This article was submitted to Biomaterials, a section of the journal Frontiers in Bioengineering and Biotechnology

RECEIVED 23 November 2022
ACCEPTED 29 November 2022
PUBLISHED 07 December 2022

CITATION
Zhong D, Zhang H, Ma Z, Xin Q, Lu Y, Shi P, Qin M, Li J and Ding C (2022), Recent advancements in wound management: Tailoring superwettable bio-interfaces. *Front. Bioeng. Biotechnol.* 10:1106267. doi: 10.3389/fbioe.2022.1106267

Recent advancements in wound management: Tailoring superwettable bio-interfaces

Dongsheng Zhong[1], Hongbo Zhang[2], Zhengxin Ma[2], Qiangwei Xin[2], Yongping Lu[1,2], Ping Shi[1]*, Meng Qin[2], Jianshu Li[2] and Chunmei Ding[2]*

[1]Guangyuan Central Hospital, Guangyuan, China, [2]State Key Laboratory of Polymer Materials Engineering, College of Polymer Science and Engineering, Sichuan University, Chengdu, China

Skin tissue suffering from severe damages fail in self-regeneration. Proper wound dressings are highly demanded to protect the wound region and accelerate the healing process. Although large efforts have been devoted, there still exist disturbing dilemmas for traditional dressings. The exquisite design of bio-interface upon superwettable materials opens new avenues and addresses the problems perfectly. However, the advancements in this area have rarely been combed. In light of this, this minireview attempts to summarize recent strategies of superwettable bio-interfaces for wound care. Concentrating on the management of biofluids (blood and exudate), we described superwettable hemostatic bio-interfaces first, and then introduced the management of exudates. Finally, the perspective of this area was given. This minireview gives a comprehensive outline for readers and is believed to provide references for the design of superwettable materials in biomedical area.

KEYWORDS

superwettability, bio-interface, hemostasis, exudates, wound management

Introduction

As the biggest organ in vertebrates, skin functions as the external barrier for the protection of inner organs, regulation of the body temperature etc. (Morgado et al., 2015). Skin tissue suffers from severe damages when high heat, pressure, genetic disorder and other related diseases occur, and might fail in self-regeneration unfortunately (Divyashri et al., 2022). The injured wounds are classified based on the cause, depth, complexity and time of healing (Iacob et al., 2020). Among which, the chronic wound (in comparison with acute wound) usually fails to heal after the treatment for more than 4 weeks, which poses great threat to human health (Sweeney et al., 2012). In consideration of this, proper wound dressings are highly demanded to protect the wound region and accelerate the healing process.

The first wound bandage can be traced back to 4000 years ago, which was made by honey or resin (Farahani and Shafiee, 2021). After thousands of years evolution, a variety of materials have been applied in wound dressing, such as hydrocolloids, films, foam and hydrogel. Ideal wound dressings should meet the requirements of good biocompatibility,

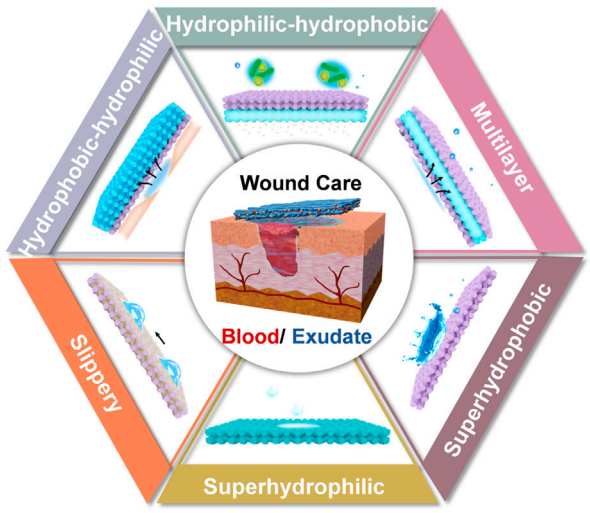

FIGURE 1
Schematic illustration of superwettable bio-interfaces in wound management.

moisture retention, appropriate mechanical property, non-adherent and proper exudate management (Liang et al., 2021). It should be noted that the feasible management of biofluid exerts a crucial role in wound care among all characteristics. Regarding to four phases of wound healing that include hemostasis, inflammation, proliferation, and remodeling, the control of bleeding in hemostasis stage is the primary task, followed by the management of exudates in the inflammatory and proliferative phases (Bernardes et al., 2021; Maleki et al., 2021). Although large efforts have been devoted, there still exist disturbing dilemmas for traditional dressings. For example, materials capable of favorable absorption property usually lead to the ingrowth of clotting and new granulation tissues, which might cause secondary injuries for the routine removal.

The development of superwettable materials opens new avenues for wound dressings. Derived from the natural superwettable phenomena, that include the typical examples of self-cleaning lotus leaf and slippery nepenthes, diverse types of superwetability have been explored: superhyrophilic, amphiphobic and Janus wettability (Ding et al., 2012; Zhu et al., 2017; Sun et al., 2021). Depending on this, the exquisite design of bio-interface can address the problems of existing dilemmas in wound dressing. However, the advancements in this area have rarely been combed. In light of this, the aim of this minireview is to summarize the recent strategies of superwettable bio-interfaces for wound care. Concentrating on the management of biofluids, we divided the content into the control of blood (hemostasis) and exudates. The advantages and disadvantages of each design were interpreted, such as superhydrophilic, superhydrophobic, slippery, inner hydrophilic-outer hydrophobic, inner hydrophobic-outer hydrophilic and multilayer materials (Figure 1). Finally, the perspective of this area was given. We have to state that common hydrogels with the intrinsic hydrophilic characteristic lack the feasible tailoring of wettability, and benefit the wound healing from other viewpoints (injectable, self-healing and smart response). This topic is beyond the scope of this review and will not be discussed here. The readers please refer to previous excellent reviews (Dong and Guo, 2021; Liang et al., 2021; Maleki et al., 2021). We believe this minireview will inspire the design of superwettable interfaces, and expand the application of these materials in other related areas.

Superwettable hemostatic bio-interfaces

The uncontrollable bleeding caused by severe trauma threatens the life of people, haemorrhage control is thus the principal step for wound management (Liu et al., 2022). In an attempt to reduce the high mortality of massive hemorrhage, the development of quick hemostatic materials is in high demand. Normally, the bleeding stops by the formation of blood clot with the main composition of platelets and fibrin (Versteeg et al., 2013). Hydrophilic materials, cotton gauze, as an example, possessing the advantage of high water affinity can absorb water in the blood and accelerate clotting (Zhu et al., 2018). By virtue of this, active hemostatic agents including proteins, polysaccharides and silicon-based materials were widely integrated in hydrophilic substrates for synergistic hemostasis by activating the coagulation cascade, which can be fabricated in the form of membranes, sponges, hydrogels and particles. This topic has been well-summarized by Prof. Guo and will not be discussed here (Liang et al., 2021).

Although large advancements have been achieved, normal hemostatic interfaces constructed by hydrophilic materials generally suffer from the following limitations: 1) massive blood loss due to the rapid capillary drainage of hydrophilic materials; 2) secondary injuries caused by the removal of wound dressing, considering the clotting has formed between bleeding tissue and materials. The delicate design of superwettable bio-interfaces provides an intriguing solution to tackle these problems.

Regarding to the massive blood loss, asymmetric or Janus dressings with superhydrophilic and superhydrophobic properties on two sides were adopted. For example, cotton fabric was endowed with Janus performance by spraying one side with hydrophobic SiO_2 nano-particles and ethyl-α-cyanoacrylate superglue, meanwhile the other side of fabric remained superhydrophilic (Sasaki et al., 2016). The superhydrophilic surface absorbed blood and expedited clotting while the superhydrophobic side prevented the permeation of water and blood. Zhu et al. reported that the

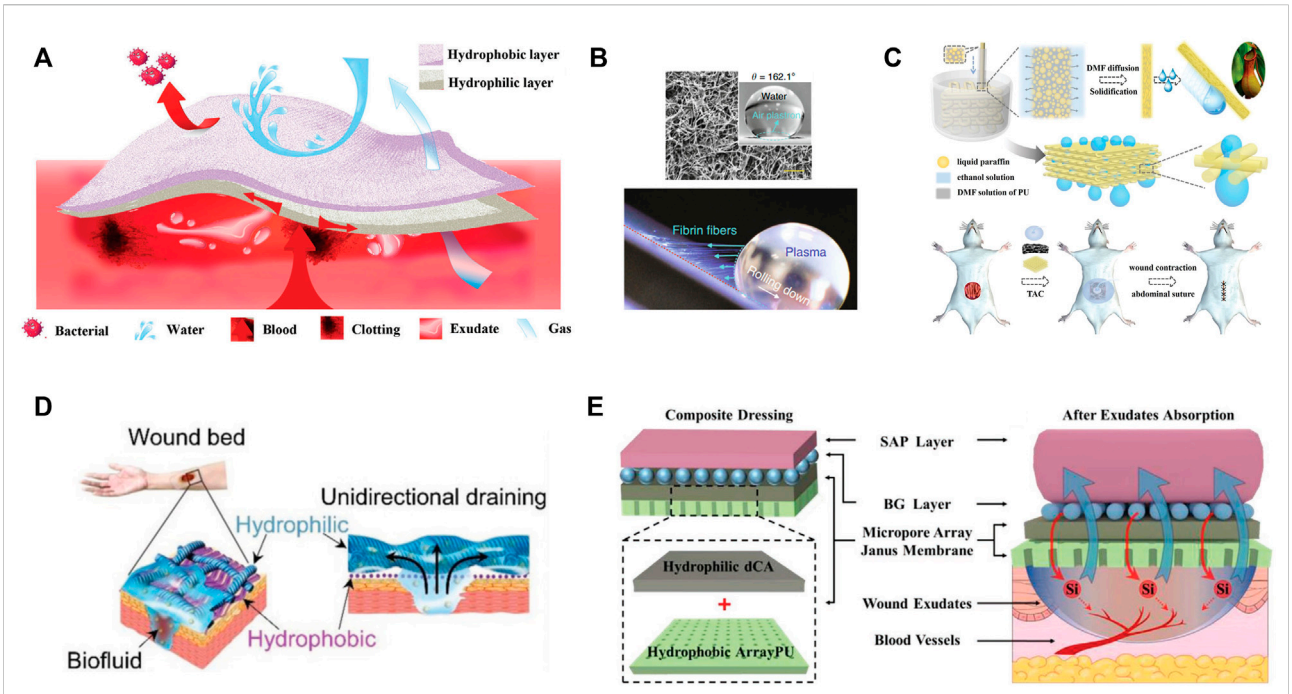

FIGURE 2
(A) Schematic illustration of Janus sponges for wound repair. **(B)** Super-hydrophobic surface with immobilized carbon nanofibers for hemostasis. SEM image and water contact angle of the surface (upper), long fibrin fibers generated when platelet poor plasma droplet rolled down (bottom). **(C)** Schematic illustration of the fabrication process of the 3D-structured slippery polyurethane textile and application in vacuum sealing drainage therapy. **(D)** The design of self-pumping dressing by exudate drainage. **(E)** Scheme of four-layer wound dressing with properties of self-pumping and ion backflow.

Janus fabrics could reduce blood loss more than 50% in comparison with the common superhydrophilic gauzes and prolong the survival time in rat model (Zhu et al., 2018). The similar results were duplicated on Janus cellulose sponges (Cheng et al., 2020). It was explained that the hydrophobic layer prevented the blood penetration and posed proper pressure on the wound, which accounted for efficient blood clotting performance (Figure 2A). This strategy was further verified in self-assembled dipeptide aerogels (Li et al., 2020) and carboxymethyl chitosan/paraffin modified cellulose films (Wang et al., 2020). Moreover, the superhydrophobic external layer, acts as an armor and protects the inner wound from bacterial infection.

To avoid the secondary injuries, the affinity between bleeding tissue and materials should be weakened, and hydrophobic blood-repelling material seems an optimal choice (Liu et al., 2020). However, it should be noted that mere blood repellence fails in the control of massive bleeding. In this case, the active hemostatic agents were simultaneously incorporated. Li and co-workers creatively proposed an approach to address the dilemma of rapid blood coagulation and facial wound-dressing removal (Li Z. et al., 2019). Specifically, a super-hydrophobic surface with immobilized carbon nanofibers (CNFs) was developed, among which CNFs promoted quick fibrin growth and rapid clotting, while the air pocked generated minimal contact area and easy detachment of mature clots (Figure 2B). The peeling tension was 1-2 folds lower than the commercial products. Besides, the commercial zeolite gauze modified with a paraffin coating was rendered with blood repellent property and procoagulant performance as well, which was derived from the retained cation exchange capacity of zeolites (Zhang W. et al., 2021). Very recently, He et al. tailored the hydrophilicity-hydrophobicity balance of cotton gauze by modifying it with catechol compound with flexible long hydrophobic alkyl chain (He H. et al., 2022). The adhesion/blocking effect of catechol groups, blood wicking of cotton and hydrophobic effect of alkyl chains conjointly contributed to the outstanding hemostatic efficiency (rapid hemostatic, low blood loss and no secondary injuries). Following the similar idea, superhydrophilic/superhydrophobic alternate pattern was designed to realize the balance between hemostatic and reduced adhesion (Long et al., 2021).

Superwettable bio-interfaces for exudate management

Apart from the haemorrhage control in the first step of wound care, the management of exudate is also crucial to

wound healing (Sweeney et al., 2012). Wound exudate is defined as the fluid produced around wound in the inflammatory and proliferative phases when haemostasis has been completed (Bernardes et al., 2021). For the acute wounds, the exudate is mainly composed of water electrolytes, protein-digesting enzymes, macrophages, inflammatory mediators and neutrophils, which allows the autolysis of damaged tissue, and provides nutrient for the metabolism of cells (Spear, 2012). The exudate is regarded positive in acute wounds and its production declines with the passage of time. In this case, the dressings should perform the protection and moist control roles (Priya et al., 2016; Shi et al., 2020). By contrast, the composition of chronic wound exudate shows distinct differences: it contains higher concentrations of pro-inflammatory cytokines, matrix metalloproteinases (MMP), and decreased levels of growth factors (Brett, 2006). In addition, the exudate damages peri-wound skin and its production in chronic wounds might be continuous and excessive due to inflammation (Cutting, 2003). Moreover, high-volume exudate could raise the risk of bacterial invasion because the saturated dressing functions as a portal. In this sense, it is of great significance to remove excessive exudate while maintain a moist environment for wound healing.

Water absorbent dressings made by hydrophilic materials supply abundant channels for exudate drainage and are great candidates for exudate management (Varaprasad et al., 2020). In general, the hydrophilic dressings were endowed with other functions including antibacterial and electro-activity (Mayandi et al., 2020; Li et al., 2021; Wang et al., 2022). For instance, superhydrophilic electrospun gelatin nanofibers were loaded with ε-polylysine (a broad-spectrum antibacterial agent) and crosslinked by polydopamine (PDA) for the treatment of second-degree burns (Mayandi et al., 2020). The gelatin mats absorbed the exudates and propelled the migration of early bacterial colonizers into the antibacterial trappers. Li et al. reported nanozyme composite cryogels with the capability of exudate absorption and acid triggered sterilization (Li et al., 2021). The macroporous structure and excellent hydrophilicity of cyogel generated rapid liquid absorption property. Furthermore, taking advantage of the pH-responsive amine groups and switchable Schiff base reaction, on the one hand, the polymer scaffold and Fe-MIL-88NH_2 nanozyme were positively charged to capture microbes through electrostatic interaction in acidic condition. On the other hand, the nanozyme conducted reversible release and rebinding behavior for dynamic killing of microbes. Wang and coworkers opened a new path for the utilization of exudate by transmitting endogenous bioelectricity and motivating the cascade release of growth factors (Wang et al., 2022). To achieve this goal, short nanofibrous sponges were modified by graphene oxide, which was then reduced to conductive graphene under the effect of PDA, and VEGF-carrying liposomes were then loaded. The above works represent the characteristic examples of hydrophilic bio-interfaces, which regulated the biofluid by simple absorption. However, the hygroscopic dressing might overhydrate the wounds and complicate the healing (Schuren et al., 2005). Besides, new granulation tissues grown in the hydrophilic mats further hinder the routine change of dressing. Therefore, other strategies based on superwettbility interfaces have been proposed.

Hydrophobic/slippery surfaces

By contrast with the hydrophilic surfaces, superhydrophobic or slippery interfaces are resistance to biofluid, bacteria and cells, which is also known as great anti-fouling property (Zhang H. et al., 2022). These merits perfectly cope with the adhesion of bacteria and new grown tissue, and have exerted great application in wound management. Zhang and coworkers pioneered the utilization of slippery material by fabricating microfiber textiles with liquid-infused porous surface (Zhang et al., 2020). Benefiting from the super low adhesion of biofluid and cells on surfaces, the wound exudation efficiency could be significantly enhanced with neglectable tissue injury in a vacuum sealing drainage therapy (Figure 2C). This anti-adhesion surface can also be integrated in functional patch to prevent the adhesion of wounded intestine with surrounding tissue (Li et al., 2022), and endowed with bactericidal characteristic by the introduction of antibacterial silver nanoparticles (Shi G. et al., 2019).

Aside from the nepenthes-inspired slippery surface, hydrophobic surface combining the advantage of hydrophilic interface was skillfully constructed by microfluidic-emulsion-templating method (Yao et al., 2020). Porous polyvinyl alcohol hydrogel membrane loaded with zeolitic imidazolate framework-8 not only exhibited good repellence to blood and body fluids, but also enabled the controlled release of zinc irons for the eradication of bacterial and the promotion of angiogenesis and collagen deposition.

Janus materials

Natural human skin is asymmetric with epidermis and dermis arranged from the outer to the inner side (Wu et al., 2016). The epidermis is dense and hydrophobic to resist the bacterial adhesion and avoid excessive dehydration, while the inner dermal layer is sponge-like and hydrophilic to support nutrient exchange and facilitate metabolism. Inspired by this, extensive efforts have been devoted to fabricate asymmetric dressing from the viewpoint of skin tissue engineering. In analogy to natural skin structure, the hydrophilic surfaces resembling that of dermis were normally taken as the inner side for direct interaction with tissue. In order to render the surface with regenerative property, the topological morphology of materials could be engineered to facilitate cell behavior. Besides, growth factors and therapeutic agents were often

loaded to augment the effect. In the meanwhile, the hydrophobic surfaces mimicking epidermis were adopted as the external protective layer to defend against bacterial attack.

As for the bioactive side, fibrous membranes and hydrogels provide supportive environments for drug loading and surface structuration. While the protective side can be constructed by various types of hydrophobic materials. As examples, hydrophilic core/shell fibrous membrane was prepared by coaxial electrospinning with curcumin and antimicrobial peptides loaded in the core and shell respectively. Subsequently, poly (lactic acid) (PLA) beads were electro-sprayed on one side of the membrane for superhydrophobic surface (Li W. et al., 2019). The release of antimicrobial peptides and curcumin favored for the treatment of the acute inflammatory response and mid to late wound healing stages correspondingly. And the superhydrophobic surfaces prohibited the adhesion and invasion of exogenous bacteria. Analogously, pioglitazone-incorporated gelatin and poly (ε-caprolactone) (PCL) were electron-spined on two sides of nylon mesh separately (Yu et al., 2020). This asymmetric composite dressing promoted the healing of full-thickness skin wound in diabetic mice (both type 1 and 2 diabetes). You and coworkers fabricated a Janus patch with resveratrol-loaded hydrogel and hydrophobic polymer (You et al., 2015). Taking advantage of the hydrophobic blocking polymer, the fluid penetration, accompanied with the diffusion of resveratrol was monodirectional, which was beneficial for efficient drug delivery. The hydrogel layer of functional Janus membrane could also be loaded with growth factors and the hydrophobic surface was reported to prevent exudate leaks (An et al., 2017). Interestingly, anisotropic microgrooved hydrogel was designed to facilitate cell behavior (adhesion, proliferation, and oriented migration), and the other side was endowed with anti-adhesive performance by the infusion of liquid paraffin (Zou et al., 2020). This Janus patch avoided adhesion-related complications and promoted the repair of abdominal wall defects in rat. Moreover, superwettable asymmetric polyurethane (PU) sponges were successfully prepared by spraying fluorinated zinc oxide nanoparticles onto one surface of PDA-modified sponge (Chen et al., 2022). It was demonstrated that the durable bacterial barrier of superhydrophobic coatings was conductive to the healing of infected wound.

In contrast to the inner hydrophilic-outer hydrophobic strategy, inner hydrophobic-outer hydrophilic design features the unidirectional transport of exudates and feasible change of wound dressings. This concept was proposed by Shi and coworkers for the first time (Figure 2D), who elaborated the mechanism and key points for the design of self-pumping dressing (Shi L. et al., 2019). The density of hydrophobic nanofiber arrays and the multiple contacting points on hydrophilic microfibers contributed to the rapid transport of biofluids to the hydrophilic side once they were in contact with the hydrophobic fibers. More importantly, the intrinsic hydrophobicity of fabrics resisted the ingrowth of regenerated tissue. Since then, a variety of bio-interfaces including polymeric fibers (Luo et al., 2021), polyurethane sponges (Zhang H. et al., 2021), porous films (Chi et al., 2021), hydrogel composite membrane (Zhang J. et al., 2022) and cotton fabrics (Zhang Z. et al., 2022) have been well-developed. To the best of our knowledge, the absorption and retainment of biofluid is closely associated with the intrinsic property of hydrophilic substrates. In regard to this, the reverse penetration of liquid from the hydrophilic substrate might occur if the water retention capability is not satisfactory. To address this problem, nanofibrous composite aerogel served as the hydrophilic absorption layer to prohibit the reverse liquid penetration (Zhang K. et al., 2021). In brief, quaternized chitosan/polyvinyl alcohol aerogel overcame low water absorption property of traditional compact nanofibers, meanwhile retained the soft mechanical property. After the coverage of hydrophobic curcumin-loaded PCL, the hybrid dressing was utilized for diabetic wound therapy by virtue of antibacterial, antioxidant, and fluid gating characteristics. From another perspective, Qian et al. raised the management of exudate by the collection of wound exudate in the early stage, followed by the cascade release of drug (curcumin) from the hydrophilic substrates (Qian et al., 2022). The inverse effects of the hydrophilic layers in above two works might be attributed to diverse absorption capabilities of hydrophilic substrates and different blocking ability of hydrophobic layer.

Multilayer designs

Superior to single-layer or double-layer dressings, multilayer substrates are designable for the attainment of more complex functions. He et al. reported a three-layer composite dressing consisted of PCL/gelatin nanofiber, collagen/quaternized chitosan sponge and PCL/polystyrene microspheres from the inner to the outer side (He C. et al., 2022). The aligned PCL/gelatin together with curcumin promoted directed cell growth and migration, sponges absorbed exudates, and hydrophobic microspheres inhibited exogenic bacterial adhesion. This strategy enables the antibacterial role of both inner and outer sides. Obeying the same rule, superhydrophilic-hydrophilic-hydrophobic-superhydrophobic four-layer hybrid substrates were developed with the integration of ciprofloxacin and astaxanthin in the hydrophilic layer (Zhang et al., 2023). The combination of fluid absorption, antibacterial, antioxidation and self-cleaning gave rise to potential applications of this membrane in skin tissue engineering.

For the purpose of full utilization of exudates, Chang's group designed a four-layer composite dressing for self-pumping and ion backflow (Bao et al., 2020). PU membrane with micropore arrays served as the bottom layer, while hydrophilic deacetylated cellulose acetate, bioactive silicate bioglass particles and

superabsorbent particles were placed above in sequence (Figure 2E). This system allows for unidirectional transport of abundant exudates from wound bed, and simultaneous backflow of a small amount of fluid (containing bioactive ions). This novel bi-functional transport process benefited the regeneration of diabetic wound. Furthermore, this design can be simplified by sandwich structure: hydrophilic zinc silicate bioceramics encapsuled by hydrophobic PLA in both sides (Zhang Z. et al., 2021). The exudate absorption followed by the release of Zn^{2+} and SiO_3^{2-} ions facilitated the healing of burn wound and regeneration of appendage (hair follicle).

To surmount the low stretching capability of traditional band aids, Xu and coworkers intelligently fabricated a three-layer patch using Janus polydimethylsiloxane layer, filter paper and medical adhesive tape (Xu et al., 2021). Polydimethylsiloxane layer was drilled by femtosecond laser and then single-side modified for Janus property. This patch possessed unidirectional liquid transport on both relaxed and stretched states, indicating the application on moveable skin wounds (stretched or bended skin surface).

Conclusion

In summary, the development of superwettable bio-interfaces motivates the application of these designs in wound care, which exhibit attractive advantages of biofluid management, drug delivery, easy to change etc. In view of the two primary biofluids during healing stages (blood and exudates), superwettable hemostatic bio-interfaces were first described, the management of exudates was then summarized. The blood management requires the quick hemostatic, no blood loss and secondary injuries, and the integration of superhydrophobic bio-interface satisfies the needs. Diverse strategies including hydrophobic/slippery, inner hydrophilic-outer hydrophobic, inner hydrophobic-outer hydrophilic and multilayer surfaces were applied for exudate management. These bio-interfaces all have distinctive merits and were reasonably verified in the specific wound model. Based on the shallow understanding of authors, the perspectives were proposed as follows: 1) The delicate control of exudates (the backflow and purification) needs in-deep investigation, especially the mechanism and accuracy. 2) Almost all chronic animal models in the reported papers differ from that in clinic (non-healing for more than 4 weeks), and the animal model resembling that of real case would be more meaningful. 3) The regeneration of skin appendices and scarless wound healing are still challenging. In a word, tailoring superwettability bio-interfaces provides inspiring solutions to tackle the existing problems in wound management. We hope that this minireview can give a comprehensive outline for readers and provide references for the design of superwettable materials in biomedical area.

Author contributions

CD designed and supervised the manuscript. DZ and CD wrote the manuscript. HZ, ZM, QX, YL, MQ, and PS modified the manuscript. JL reviewed the manuscript. All authors contributed to the article and approved the submitted version.

Acknowledgments

The authors thank the financial support from Natural Science Foundation of Sichuan Province (2022NSFSC1934 and 23NSFSC0317).

Conflict of interest

The authors declare that the research was conducted in the absence of any commercial or financial relationships that could be construed as a potential conflict of interest.

Publisher's note

References

An, Y.-H., Yu, S. J., Kim, I. S., Kim, S.-H., Moon, J.-M., Kim, S. L., et al. (2017). Hydrogel functionalized Janus membrane for skin regeneration. *Adv. Healthc. Mat.* 6 (5), 1600795. doi:10.1002/adhm.201600795

Bao, F., Pei, G., Wu, Z., Zhuang, H., Zhang, Z., Huan, Z., et al. (2020). Bioactive self-pumping composite wound dressings with micropore array modified Janus membrane for enhanced diabetic wound healing. *Adv. Funct. Mat.* 30 (49), 2005422. doi:10.1002/adfm.202005422

Bernardes, B. G., Del Gaudio, P., Alves, P., Costa, R., Garcia-Gonzalez, C. A., and Oliveira, A. L. (2021). Bioaerogels: Promising nanostructured materials in fluid management, healing and regeneration of wounds. *Molecules* 26 (13), 3834. doi:10.3390/molecules26133834

Brett, D. W. (2006). Impact on exudate management, maintenance of a moist wound environment, and prevention of infection. *J. Wound Ostomy Cont. Nurs.* 33, S9–S14. doi:10.1097/01.Won.0000278582.47856.92

Chen, S., Li, S., Ye, Z., Zhang, Y., Gao, S., Rong, H., et al. (2022). Superhydrophobic and superhydrophilic polyurethane sponge for wound healing. *Chem. Eng. J.* 446, 136985. doi:10.1016/j.cej.2022.136985

Cheng, H., Xiao, D., Tang, Y., Wang, B., Feng, X., Lu, M., et al. (2020). Sponges with Janus character from nanocellulose: Preparation and applications in the treatment of hemorrhagic wounds. *Adv. Healthc. Mat.* 9 (17), 1901796. doi:10.1002/adhm.201901796

Chi, J., Shao, C., Shang, L., Zhao, Y., and Ye, F. (2021). Microfluidic droplet templates derived porous patch with anisotropic wettability. *Chem. Eng. J.* 417, 128073. doi:10.1016/j.cej.2020.128073

Cutting, K. F. (2003). Wound exudate: Composition and functions. *Br. J. Community Nurs.* 8 (3), S4–S9. doi:10.12968/bjcn.2003.8.Sup3.11577

Ding, C., Zhu, Y., Liu, M., Feng, L., Wan, M., and Jiang, L. (2012). PANI nanowire film with underwater superoleophobicity and potential-modulated tunable adhesion for no loss oil droplet transport. *Soft Matter* 8 (35), 9064–9068. doi:10.1039/c2sm25987g

Divyashri, G., Badhe, R. V., Sadanandan, B., Vijayalakshmi, V., Kumari, M., Ashrit, P., et al. (2022). Applications of hydrogel-based delivery systems in wound care and treatment: An up-to-date review. *Polym. Adv. Technol.* 33 (7), 2025–2043. doi:10.1002/pat.5661

Dong, R., and Guo, B. (2021). Smart wound dressings for wound healing. *Nano Today* 41, 101290. doi:10.1016/j.nantod.2021.101290

Farahani, M., and Shafiee, A. (2021). Wound healing: From passive to smart dressings. *Adv. Healthc. Mat.* 10 (16), 2100477. doi:10.1002/adhm.202100477

He, C., Yu, B., Lv, Y., Huang, Y., Guo, J., Li, L., et al. (2022a). Biomimetic asymmetric composite dressing by electrospinning with aligned nanofibrous and micropatterned structures for severe burn wound healing. *ACS Appl. Mat. Interfaces* 14 (29), 32799–32812. doi:10.1021/acsami.2c04323

He, H., Zhou, W., Gao, J., Wang, F., Wang, S., Fang, Y., et al. (2022b). Efficient, biosafe and tissue adhesive hemostatic cotton gauze with controlled balance of hydrophilicity and hydrophobicity. *Nat. Commun.* 13 (1), 552. doi:10.1038/s41467-022-28209-8

Iacob, A.-T., Drăgan, M., Ionescu, O.-M., Profire, L., Ficai, A., Andronescu, E., et al. (2020). An overview of biopolymeric electrospun nanofibers based on polysaccharides for wound healing management. *Pharmaceutics* 12 (10), 983. doi:10.3390/pharmaceutics12100983

Li, W., Yu, Q., Yao, H., Zhu, Y., Topham, P. D., Yue, K., et al. (2019a). Superhydrophobic hierarchical fiber/bead composite membranes for efficient treatment of burns. *Acta Biomater.* 92, 60–70. doi:10.1016/j.actbio.2019.05.025

Li, X., Li, Q., Fei, J., Jia, Y., Xue, H., Zhao, J., et al. (2020). Self-assembled dipeptide aerogels with tunable wettability. *Angew. Chem. Int. Ed.* 59 (29), 11932–11936. doi:10.1002/anie.202005575

Li, Y., Li, G., Chen, Y., Zhao, X., Wang, Y., Liu, J., et al. (2022). Gradient modulus tissue adhesive composite for dynamic wound closure. *Adv. Funct. Mat.* 32, 2207306. doi:10.1002/adfm.202207306

Li, Y., Wang, D., Wen, J., Yu, P., Liu, J., Li, J., et al. (2021). Chemically grafted nanozyme composite cryogels to enhance antibacterial and biocompatible performance for bioliquid regulation and adaptive bacteria trapping. *ACS Nano* 15 (12), 19672–19683. doi:10.1021/acsnano.1c06983

Li, Z., Milionis, A., Zheng, Y., Yee, M., Codispoti, L., Tan, F., et al. (2019b). Superhydrophobic hemostatic nanofiber composites for fast clotting and minimal adhesion. *Nat. Commun.* 10 (1), 5562. doi:10.1038/s41467-019-13512-8

Liang, Y., He, J., and Guo, B. (2021). Functional hydrogels as wound dressing to enhance wound healing. *ACS Nano* 15 (8), 12687–12722. doi:10.1021/acsnano.1c04206

Liu, J., Ye, L., Sun, Y., Hu, M., Chen, F., Wegner, S., et al. (2020). Elastic superhydrophobic and photocatalytic active films used as blood repellent dressing. *Adv. Mat.* 32 (11), 1908008. doi:10.1002/adma.201908008

Liu, Y., Niu, H., Wang, C., Yang, X., Li, W., Zhang, Y., et al. (2022). Bio-inspired, bio-degradable adenosine 5′-diphosphate-modified hyaluronic acid coordinated hydrophobic undecanal-modified chitosan for hemostasis and wound healing. *Bioact. Mat.* 17, 162–177. doi:10.1016/j.bioactmat.2022.01.025

Long, C., Qing, Y., Li, S., Cui, M., Han, M., An, K., et al. (2021). Asymmetric composite wound nanodressing with superhydrophilic/superhydrophobic alternate pattern for reducing blood loss and adhesion. *Compos. Part B Eng.* 223, 109134. doi:10.1016/j.compositesb.2021.109134

Luo, Z., Jiang, L., Xu, C., Kai, D., Fan, X., You, M., et al. (2021). Engineered Janus amphipathic polymeric fiber films with unidirectional drainage and anti-adhesion abilities to accelerate wound healing. *Chem. Eng. J.* 421, 127725. doi:10.1016/j.cej.2020.127725

Maleki, A., He, J., Bochani, S., Nosrati, V., Shahbazi, M.-A., and Guo, B. (2021). Multifunctional photoactive hydrogels for wound healing acceleration. *ACS Nano* 15 (12), 18895–18930. doi:10.1021/acsnano.1c08334

Mayandi, V., Wen Choong, A. C., Dhand, C., Lim, F. P., Aung, T. T., Sriram, H., et al. (2020). Multifunctional antimicrobial nanofiber dressings containing ε-polylysine for the eradication of bacterial bioburden and promotion of wound healing in critically colonized wounds. *ACS Appl. Mat. Interfaces* 12 (14), 15989–16005. doi:10.1021/acsami.9b21683

Morgado, P. I., Aguiar-Ricardo, A., and Correia, I. J. (2015). Asymmetric membranes as ideal wound dressings: An overview on production methods, structure, properties and performance relationship. *J. Memb. Sci.* 490, 139–151. doi:10.1016/j.memsci.2015.04.064

Priya, S. G., Gupta, A., Jain, E., Sarkar, J., Damania, A., Jagdale, P. R., et al. (2016). Bilayer cryogel wound dressing and skin regeneration grafts for the treatment of acute skin wounds. *ACS Appl. Mat. Interfaces* 8 (24), 15145–15159. doi:10.1021/acsami.6b04711

Qian, S., Wang, J., Liu, Z., Mao, J., Zhao, B., Mao, X., et al. (2022). Secretory fluid-aggregated Janus electrospun short fiber scaffold for wound healing. *Small* 18, 2200799. doi:10.1002/smll.202200799

Sasaki, K., Tenjimbayashi, M., Manabe, K., and Shiratori, S. (2016). Asymmetric superhydrophobic/superhydrophilic cotton fabrics designed by spraying polymer and nanoparticles. *ACS Appl. Mat. Interfaces* 8 (1), 651–659. doi:10.1021/acsami.5b09782

Schuren, J., Becker, A., and Gary Sibbald, R. (2005). A liquid film-forming acrylate for peri-wound protection: A systematic review and meta-analysis (3Mtm cavilontm no-sting barrier film). *Int. Wound J.* 2 (3), 230–238. doi:10.1111/j.1742-4801.2005.00131.x

Shi, C., Wang, C., Liu, H., Li, Q., Li, R., Zhang, Y., et al. (2020). Selection of appropriate wound dressing for various wounds. *Front. Bioeng. Biotechnol.* 8, 182. doi:10.3389/fbioe.2020.00182

Shi, G., Wang, Y., Derakhshanfar, S., Xu, K., Zhong, W., Luo, G., et al. (2019a). Biomimicry of oil infused layer on 3D printed poly(dimethylsiloxane): Non-fouling, antibacterial and promoting infected wound healing. *Mater. Sci. Eng. C* 100, 915–927. doi:10.1016/j.msec.2019.03.058

Shi, L., Liu, X., Wang, W., Jiang, L., and Wang, S. (2019b). A self-pumping dressing for draining excessive biofluid around wounds. *Adv. Mat.* 31, 1804187. doi:10.1002/adma.201804187

Spear, M. (2012). Wound exudate-the good, the bad, and the ugly. *Plast. Surg. Nurs.* 32 (2), 77–79. doi:10.1097/PSN.0b013e318256d638

Sun, L., Guo, J., Chen, H., Zhang, D., Shang, L., Zhang, B., et al. (2021). Tailoring materials with specific wettability in biomedical engineering. *Adv. Sci. (Weinh).* 8 (19), 2100126. doi:10.1002/advs.202100126

Sweeney, I. R., Miraftab, M., and Collyer, G. (2012). A critical review of modern and emerging absorbent dressings used to treat exuding wounds. *Int. Wound J.* 9 (6), 601–612. doi:10.1111/j.1742-481X.2011.00923.x

Varaprasad, K., Jayaramudu, T., Kanikireddy, V., Toro, C., and Sadiku, E. R. (2020). Alginate-based composite materials for wound dressing application:A mini review. *Carbohydr. Polym.* 236, 116025. doi:10.1016/j.carbpol.2020.116025

Versteeg, H. H., Heemskerk, J. W. M., Levi, M., and Reitsma, P. H. (2013). New fundamentals in hemostasis. *Physiol. Rev.* 93 (1), 327–358. doi:10.1152/physrev.00016.2011

Wang, J., Lin, J., Chen, L., Deng, L., and Cui, W. (2022). Endogenous electric-field-coupled electrospun short fiber via collecting wound exudation. *Adv. Mat.* 34 (9), 2108325. doi:10.1002/adma.202108325

Wang, Y., Xiao, D., Zhong, Y., Zhang, L., Chen, Z., Sui, X., et al. (2020). Facile fabrication of carboxymethyl chitosan/paraffin coated carboxymethylated cotton fabric with asymmetric wettability for hemostatic wound dressing. *Cellulose* 27 (6), 3443–3453. doi:10.1007/s10570-020-02969-2

Wu, C., Chen, T., Xin, Y., Zhang, Z., Ren, Z., Lei, J., et al. (2016). Nanofibrous asymmetric membranes self-organized from chemically heterogeneous electrospun mats for skin tissue engineering. *Biomed. Mat.* 11 (3), 035019. doi:10.1088/1748-6041/11/3/035019

Xu, B., Li, A., Wang, R., Zhang, J., Ding, Y., Pan, D., et al. (2021). Elastic Janus film for wound dressings: Unidirectional biofluid transport and effectively promoting wound healing. *Adv. Funct. Mat.* 31 (41), 2105265. doi:10.1002/adfm.202105265

Yao, X., Zhu, G., Zhu, P., Ma, J., Chen, W., Liu, Z., et al. (2020). Omniphobic ZIF-8@Hydrogel membrane by microfluidic-emulsion-templating method for wound healing. *Adv. Funct. Mat.* 30 (13), 1909389. doi:10.1002/adfm.201909389

You, J. B., Choi, A. Y., Baek, J., Oh, M. S., Im, S. G., Lee, K. E., et al. (2015). Application of monodirectional Janus patch to oromucosal delivery system. *Adv. Healthc. Mat.* 4 (15), 2229–2236. doi:10.1002/adhm.201500416

Yu, B., He, C., Wang, W., Ren, Y., Yang, J., Guo, S., et al. (2020). Asymmetric wettable composite wound dressing prepared by electrospinning with bioinspired micropatterning enhances diabetic wound healing. *ACS Appl. Bio Mat.* 3 (8), 5383–5394. doi:10.1021/acsabm.0c00695

Zhang, H., Chen, C., Zhang, H., Chen, G., Wang, Y., and Zhao, Y. (2021a). Janus medical sponge dressings with anisotropic wettability for wound healing. *Appl. Mat. Today* 23, 101068. doi:10.1016/j.apmt.2021.101068

Zhang, H., Chen, G., Yu, Y., Guo, J., Tan, Q., and Zhao, Y. (2020). Microfluidic printing of slippery textiles for medical drainage around wounds. *Adv. Sci.* 7 (16), 2000789. doi:10.1002/advs.202000789

Zhang, H., Xu, X., Wu, M., Zhao, Y., Sun, F., Xin, Q., et al. (2022a). Virus-like iron oxide minerals inspired by magnetotactic bacteria: Towards an outstanding photothermal superhydrophobic platform on universal substrates. *Adv. Funct. Mat.* 32 (29), 2201795. doi:10.1002/adfm.202201795

Zhang, J., Liu, B., Liu, X., Wang, D., Dong, B., Zhang, Y., et al. (2022b). Laser ablated Janus hydrogel composite membrane for draining excessive blood and biofluid around wounds. *Macromol. Mat. Eng.* 307 (8), 2200026. doi:10.1002/mame.202200026

Zhang, K., Jiao, X., Zhou, L., Wang, J., Wang, C., Qin, Y., et al. (2021b). Nanofibrous composite aerogel with multi-bioactive and fluid gating characteristics for promoting diabetic wound healing. *Biomaterials* 276, 121040. doi:10.1016/j.biomaterials.2021.121040

Zhang, W., Guan, X., Qiu, X., Gao, T., Yu, W., Zhang, M., et al. (2023). Bioactive composite Janus nanofibrous membranes loading Ciprofloxacin and Astaxanthin for enhanced healing of full-thickness skin defect wounds. *Appl. Surf. Sci.* 610, 155290. doi:10.1016/j.apsusc.2022.155290

Zhang, W., Wu, J., Yu, L., Chen, H., Li, D., Shi, C., et al. (2021c). Paraffin-Coated hydrophobic hemostatic zeolite gauze for rapid coagulation with minimal adhesion. *ACS Appl. Mat. Interfaces* 13 (44), 52174–52180. doi:10.1021/acsami.1c10891

Zhang, Z., Li, W., Liu, Y., Yang, Z., Ma, L., Zhuang, H., et al. (2021d). Design of a biofluid-absorbing bioactive sandwich-structured Zn–Si bioceramic composite wound dressing for hair follicle regeneration and skin burn wound healing. *Bioact. Mat.* 6 (7), 1910–1920. doi:10.1016/j.bioactmat.2020.12.006

Zhang, Z., Wang, T., Chen, S., Lv, C., Zhuang, X., and Wang, S. (2022c). Fabrication of antibacterial Janus bandages with high wound healing performances by facile single-side electrospray PDMS coating. *Surf. Interfaces* 34, 102392. doi:10.1016/j.surfin.2022.102392

Zhu, T., Wu, J., Zhao, N., Cai, C., Qian, Z., Si, F., et al. (2018). Superhydrophobic/superhydrophilic Janus fabrics reducing blood loss. *Adv. Healthc. Mat.* 7 (7), 1701086. doi:10.1002/adhm.201701086

Zhu, Z., Tian, Y., Chen, Y., Gu, Z., Wang, S., and Jiang, L. (2017). Superamphiphilic silicon wafer surfaces and applications for uniform polymer film fabrication. *Angew. Chem. Int. Ed.* 56, 5720–5724. doi:10.1002/anie.201700039

Zou, M., Zhao, X., Zhang, X., Zhao, Y., Zhang, C., and Shi, K. (2020). Bio-inspired multiple composite film with anisotropic surface wettability and adhesion for tissue repair. *Chem. Eng. J.* 398, 125563. doi:10.1016/j.cej.2020.125563

frontiers | Frontiers in Bioengineering and Biotechnology

TYPE Review
PUBLISHED 19 January 2023
DOI 10.3389/fbioe.2023.1117944

OPEN ACCESS

EDITED BY
Jianxun Ding,
Changchun Institute of Applied Chemistry (CAS), China

REVIEWED BY
Jun-Bing Fan,
Southern Medical University, China
Shuaishuai Yuan,
Qingdao University of Science and Technology, China
Yang Wu,
Lanzhou Institute of Chemical Physics (CAS), China
Rong Wang,
Ningbo Institute of Materials Technology and Engineering (CAS), China
Zhe Sun,
Soochow University, China
Weifeng Zhao,
Sichuan University, China

*CORRESPONDENCE
Shutao Wang,
stwang@mail.ipc.ac.cn
Jingxin Meng,
mengjx628@mail.ipc.ac.cn

†These authors have contributed equally to this work

SPECIALTY SECTION
This article was submitted to Biomaterials, a section of the journal Frontiers in Bioengineering and Biotechnology

RECEIVED 07 December 2022
ACCEPTED 05 January 2023
PUBLISHED 19 January 2023

CITATION
Zhang Z, Zhao R, Wang S and Meng J (2023), Recent advances in bio-inspired ionic liquid-based interfacial materials from preparation to application. *Front. Bioeng. Biotechnol.* 11:1117944. doi: 10.3389/fbioe.2023.1117944

Recent advances in bio-inspired ionic liquid-based interfacial materials from preparation to application

Zhe Zhang[1,2†], Ran Zhao[1,2†], Shutao Wang[1,2,3*] and Jingxin Meng[1,2,3,4*]

[1]CAS Key Laboratory of Bio-inspired Materials and Interfacial Science, Technical Institute of Physics and Chemistry, Chinese Academy of Sciences, Beijing, China, [2]University of Chinese Academy of Sciences, Beijing, China, [3]Qingdao Casfuture Research Institute Co., Ltd., Qingdao, China, [4]Binzhou Institute of Technology, Binzhou, China

Natural creatures always display unique and charming functions, such as the adhesion of mussels and the lubrication of Nepenthes, to maintain their life activities. Bio-inspired interfacial materials infused with liquid, especially for ionic liquids (ILs), have been designed and prepared to meet the emerging and rising needs of human beings. In this review, we first summarize the recent development of bio-inspired IL-based interfacial materials (BILIMs), ranging from the synthesis strategy to the design principle. Then, we discuss the advanced applications of BILIMs from anti-adhesive aspects (e.g., anti-biofouling, anti-liquid fouling, and anti-solid fouling) to adhesive aspects (e.g., biological sensor, adhesive tape, and wound dressing). Finally, the current limitations and future prospects of BILIMs are provided to feed the actual needs.

KEYWORDS

bio-inspired, ionic liquid, interfacial, adhesion, regulation

1 Introduction

In nature, the structure and function of biotas provide continuous inspiration for technological development and material fabrication. Learning from nature, a series of bio-inspired interfacial materials have been developed for meeting actual needs, such as lotus leaf-inspired self-cleaning materials (Feng et al., 2002), cactus-inspired water-collecting materials (Ju et al., 2012), sharklet skin-inspired drag-reducing materials (Bechert et al., 1997), and polar bear hair-inspired thermal insulation materials (Chen et al., 2016; Cui et al., 2018). The scientific studies of bio-inspired interfacial materials provide new insights into crucial fields, including energy conservation, environment protection, and information transfer.

Inspired by pitcher plants, a liquid-infused material was developed for antifouling and anti-corrosion by preventing direct contact between fouling and the substrate through the liquid barrier layer on the surface. Ionic liquid (IL) is a liquid organic salt composed of organic cations and inorganic or organic anions. In the 1970s and 1980s, the first generation of ILs with non-volatility and thermal stability was established. To meet practical needs, the second generation of ILs with adjusted and specific physicochemical properties was developed in 1992. In the early 21st century, the third generation of biocompatible ILs attracted more research interest. The fourth generation of ILs with unique and unpredictable properties in solution or after mixing with other molecular liquids was first proposed in 2018. As a non-volatile lubricant, IL has attracted significant attention for extending the durability of liquid-infused surfaces. In

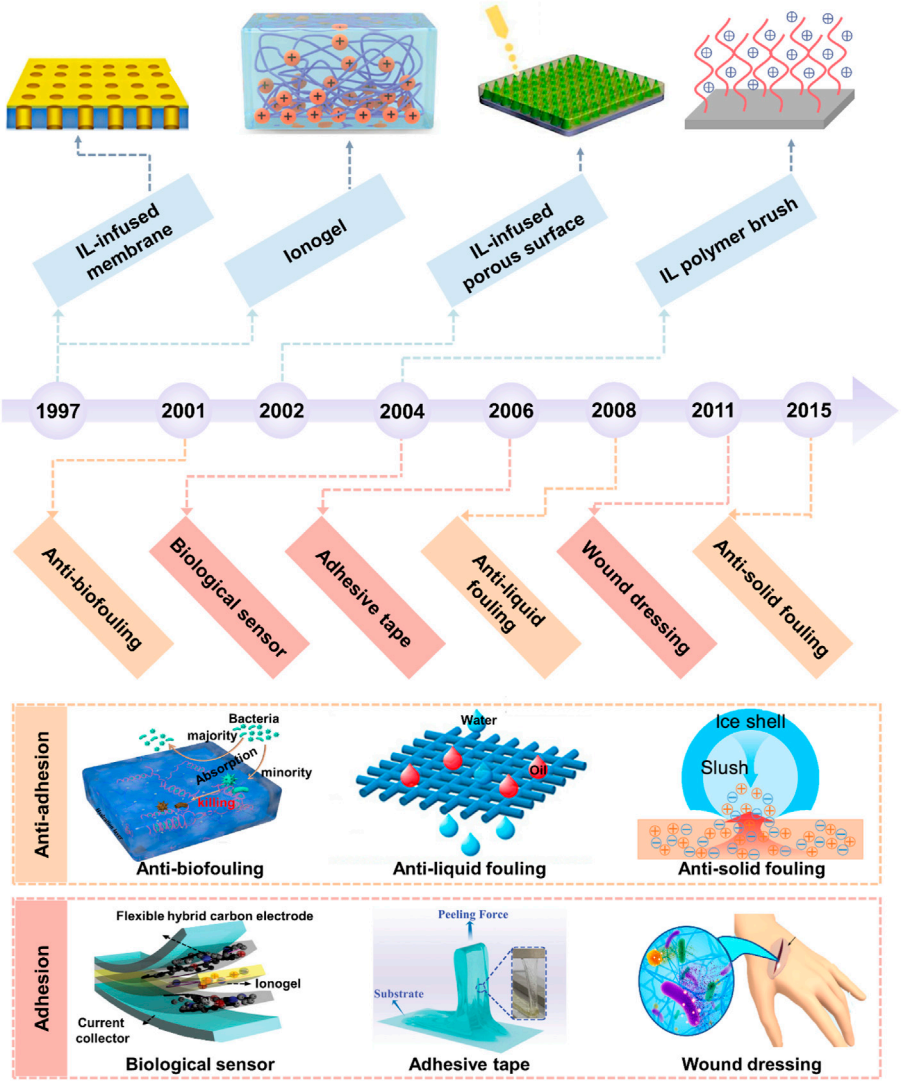

FIGURE 1
Milestones of the development and application of BILIM. The development of ILs has gone through three generations ranging from the first generation of unstable ILs and the second generation of stable ILs to the third generation of functional ILs. There are four main forms of IL-based interfacial materials, including 1D IL polymer brush, 2D IL-infused porous surface and supported membrane, and 3D ionogel. The applications of BILIMs are mainly divided into anti-adhesion (anti-biofouling, anti-scaling, and anti-icing) and adhesion (biological sensor, adhesive tape, and wound dressing). Reproduced with permission (Zhang et al., 2019). Copyright 2019, American Chemical Society. Reproduced with permission (Zhuo et al., 2020). Copyright 2020, American Chemical Society. Reproduced with permission (Deng et al., 2020). Copyright 2020, American Chemical Society. Reproduced with permission (Cho et al., 2020). Copyright 2020, WILEY-VCH Verlag GmbH & Co. KGaA, Weinheim. Reproduced with permission (Yao et al., 2022). Copyright 2022, Wiley-VCH GmbH. Reproduced with permission (Wang et al., 2020). Copyright 2020, American Chemical Society.

contrast, the IL-based interfacial materials exhibit strong adhesion when the IL is tightly bonded within the polymer network. Meanwhile, the lubricity and adhesion of IL-based interfacial materials can be controlled intelligently by regulating the state of IL on the surface or inside the polymer. Therefore, the potential applications of advanced IL-based interfacial materials can be improved and enriched by employing appropriate ILs because of their attractive advantages such as adjustable wettability, structural variability, and desirable electrochemical stability.

Distinct from the previous reviews on IL materials, this review mainly reexamines the development history of bio-inspired IL-based interfacial materials (BILIMs), as shown in Figure 1. First, we summarize the synthesis strategy and design principle of BILIMs. Then, we introduce the recent advances of BILIM applications from anti-adhesion (e.g., anti-biofouling, anti-liquid fouling, and anti-solid fouling) to adhesion (e.g., biological sensor, adhesive tape, and wound dressing). Finally, we discuss the limitation and future development of BILIM applications.

2 Preparation method of BILIMs

Inspired by nature, four main types of BILIMs divided by spatial dimension have been prepared, ranging from one-dimensional (1D) IL polymer brush, 2D IL-infused porous surface, and supported membrane to 3D ionogel (Figure 1).

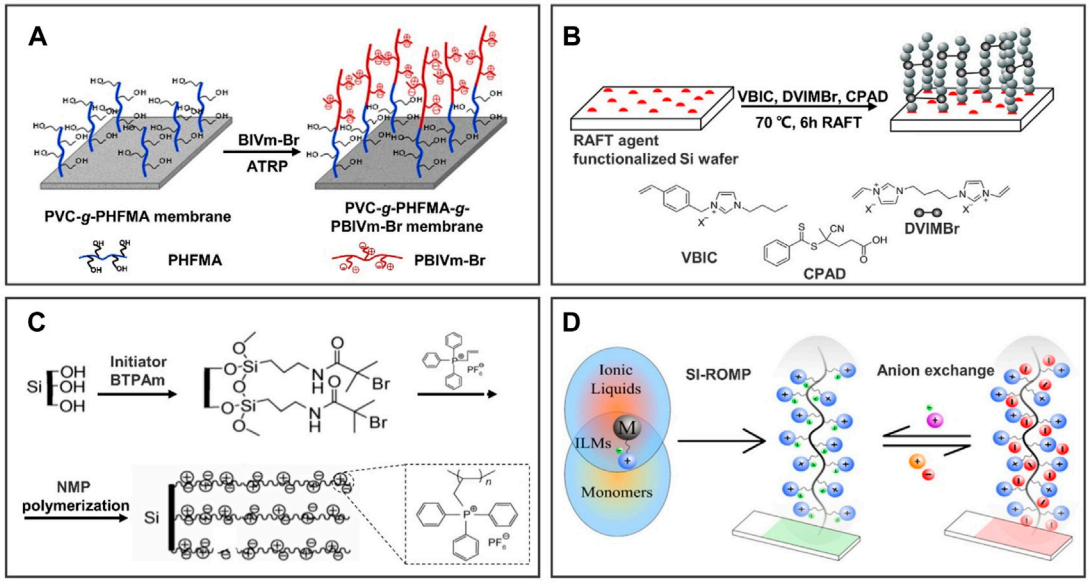

FIGURE 2
Preparation methods of 1D IL polymer brushes by chemical reaction. Numerous studies have reported on the preparation methods of ILs polymer brushes; four general preparation methods are introduced in brief as follows: **(A)** atom transfer radical polymerization (ATRP); **(B)** reversible addition-fragmentation chain transfer (RAFT); **(C)** ring-opening metathesis polymerization (ROMP); and **(D)** nitroxide-mediated radical polymerization (NMP). **(A)** reproduced with permission (Cheng et al., 2018). Copyright 2017, John Wiley and Sons, Ltd; **(B)** reproduced with permission (Demirci et al., 2020). Copyright 2020, American Chemical Society; **(C)** reprinted with permission (Njoroge et al., 2017). Copyright 2017, American Chemical Society; **(D)** reproduced with permission (Yang et al., 2010). Copyright 2010, Science China Press and Springer-Verlag Berlin Heidelberg.

2.1 IL polymer brush

By linking one end of the IL polymer chain, a 1D IL polymer brush can be formed on the surface of various substrates, thereby integrating excellent chemical and physical properties of ILs into these substrates (Washiro et al., 2004; Laloyaux et al., 2010; Buddingh et al., 2021). However, traditional free radical polymerization meets with the difficulty of controlling the polymer structure and molecular weight. To overcome this problem, four main methods with controlled radical polymerization are introduced in brief as follows: atom transfer radical polymerization (ATRP), reversible addition-fragmentation chain-transfer (RAFT), nitroxide-mediated radical polymerization (NMP), and ring-opening metathesis polymerization (ROMP). These methods rely on the reversible storage of active radicals to reduce termination events relative to the total number of polymer chains. Thus, this allows for better control not only of molecular weight and dispersion but also of the end composition of the chain, allowing the construction of a specialized graft structure of the chain.

Generally, the IL polymer brush was prepared on the surface of substrates by forming active free radicals and then polymerization such as ATRP, RAFT, and NMP. ATRP was performed by utilizing organic halides as initiators and transition metal complexes as halogen atom carriers to form a fast conversion "free ion to silyl ketene acetal" equilibrium system through a redox reaction, thus realizing the control of polymerization reaction. ATRP has been widely used in the preparation of modified IL membranes due to its strong controllability. For example, Figure 2A shows that Cheng et al. (2018) grafted poly(1-butyl-3-vinylimidazolium bromide) (PBVIm-Br) onto the surface of poly(vinyl chloride) (PVC) membrane by ATRP. The hydrophilicity of the poly(ionic liquid) (PIL) polymer brush-modified membrane is significantly enhanced by positive charge, which has a potential application in membrane separation. In addition, a special chain transfer agent with a high chain transfer constant is added to the polymerization system, which enables the degenerate transfer between the growing free radical and the chain transfer agent, reduces the concentration of free radicals, narrows the molecular weight distribution, and enables the polymerization to reflect the controllable/"active" characteristics. This reaction process is called RAFT, which has a promising application because of its wide range of monomers. However, RAFT also has many shortcomings, such as a complex preparation process, difficulty obtaining commercial reagents, easily caused chain termination, and other problems. To obtain the homogeneous brush layer on the substrate, as shown in Figure 2B, 1,4-di(3-vinylimidazolium)butane dibromide (DVIMBr) as the crosslinker was used to graft 1-vinylbenzyl-3-butylimidazolium bromide (VBIC) onto the membrane through RAFT (Demirci et al., 2020). Additionally, Figure 2C shows that a PIL-grafted silicon surface was prepared by NMP, and the wettability of the surface can be changed from hydrophilicity to hydrophobicity by changing the anion type through ion exchange (Yang et al., 2010). In essence, NMP generates free radicals from nitrogen–oxygen compounds and forms dormant species of monomer free radicals in the process of polymerization, thereby achieving controlled polymerization. Although this method has the advantages of being environmentally friendly and simple, it remains a challenge in scalable applications.

Different from the abovementioned methods, the double bond contained in the monomer is still retained in the polymer obtained by ROMP. ROMP is the ring-opening polymerization of ring alkenes. Its

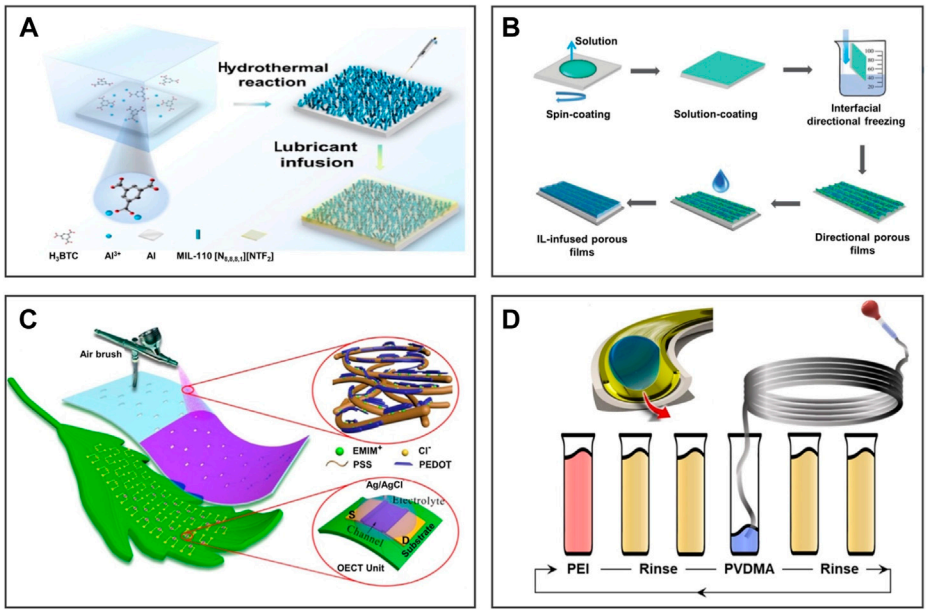

FIGURE 3
Preparation methods of 2D IL-infused porous surfaces. Schematic diagram of the IL-infused porous surface obtained *via* the hydrothermal method, freeze–drying, spraying, and layer-by-layer method. **(A)** The hydrothermal method is a process of precursor chemical reaction on the substrate under high temperature and high-pressure conditions. **(B)** The interfacial directional freezing technique is usually used to prepare porous materials with anisotropic interfaces. **(C)** Spraying–deposition is a process of spraying solution to the substrate surface through a spray gun to obtain coating. **(D)** The layer-by-layer suction flow method is suitable for a pipe, which uses an external injection apparatus to slowly and evenly infuse solution into the pipe. **(A)** is reproduced with permission (Li et al., 2022). Copyright 2021, Elsevier Inc.; **(B)** reproduced with permission (Wang Z. et al., 2018). Copyright 2018, WILEY-VCH Verlag GmbH and Co. KGaA, Weinheim; **(C)** reprinted with permission (Wu et al., 2020). Copyright 2020, American Chemical Society; **(D)** reproduced with permission (Agarwal et al., 2021). Copyright 2021, American Chemical Society.

occurrence requires the following four aspects: the presence of ring alkenes, carbene complex catalysts, the breaking of double bonds, and the end-to-end connection. For instance, Njoroge et al. (2017) grafted 3-[(bicyclo[2.2.1]hept-5-en-2-yl)methyl]-1,2-dimethylimidazol-3-ium hexafluorophosphate ($[N_1$-dMIm$][PF_6]$ to Au or silicon substrates through ROMP as shown in Figure 2D. As a result of the simple and efficient preparation process, ROMP has been widely used for preparing an IL polymer brush-modified surface.

Although IL polymer brushes strengthen the interfacial interaction between ILs and substrate, it still confronts some problems such as the uncontrollable accurate density of grafted ILs and the limited types of available ILs (Men et al., 2013). At present, IL brushes are basically grafted onto the substrate by a polymerization reaction.

2.2 IL-infused porous surface

To solve the fouling problem of pollutants, the slippery liquid-infused porous surface (SLIPS) has been developed by Aizenberg due to the existence of the lubricant layer. However, the SLIPS often face a problem caused by the loss of lubricant from the coating surface, and durability is still a challenge for the SLIPS. The loss of lubricant is a common phenomenon that may lead to the failure of SLIPS coating. Due to their advantages (e.g., adjusted surface energy and negligible vapor pressure), ILs as one of the lubricants may alleviate this failure. The IL-infused porous surface was prepared by superwetting of the ILs on the surface through the capillary interaction or the hydrophobic interaction between the micro-/nanostructure and the ILs (Liang et al., 2002; Salbaum et al., 2021). To obtain excellent antifouling properties, porous surfaces can be prepared by many promising methods, such as the hydrothermal method, freeze–drying, spraying, and layer-by-layer suction flow methods.

The hydrothermal method is a process of precursor chemical reaction on the substrate under high-temperature and high-pressure conditions. For example, Li et al. (2022) prepared a MOF-based surfactant with dual functions of contact killing and fouling release on an aluminum sheet by the one-step hydrothermal reaction as shown in Figure 3A. IL-$[N_{8,8,8,1}][NTf_2]$ was captured by the Al-MIL-110 porous surface to obtain an anti-biofouling coating with excellent stability and low lipopolysaccharide adsorption capacity. It as a novel synergistic coating has potential applications for the degradation and release of pollutants. Compared with the traditional *in situ* synthesis method, the hydrothermal method only needs to place the substrate directly into the precursor solution to obtain a porous surface. However, the hydrothermal method also has some obvious disadvantages, such as the need for high temperature and high pressure and other harsh conditions, which makes it more dependent on production equipment, which also hinders the universality of preparing porous surfaces on any substrate. Moreover, the mechanical robust and long-term properties of this coating are still a challenge in practical application.

The interfacial directional freezing technique is usually used to prepare porous materials with anisotropic interfaces. For instance, on the basis of the anisotropic porous film, Figure 3B shows that Wang X. et al. (2018)prepared the smooth surface with a photoelectric

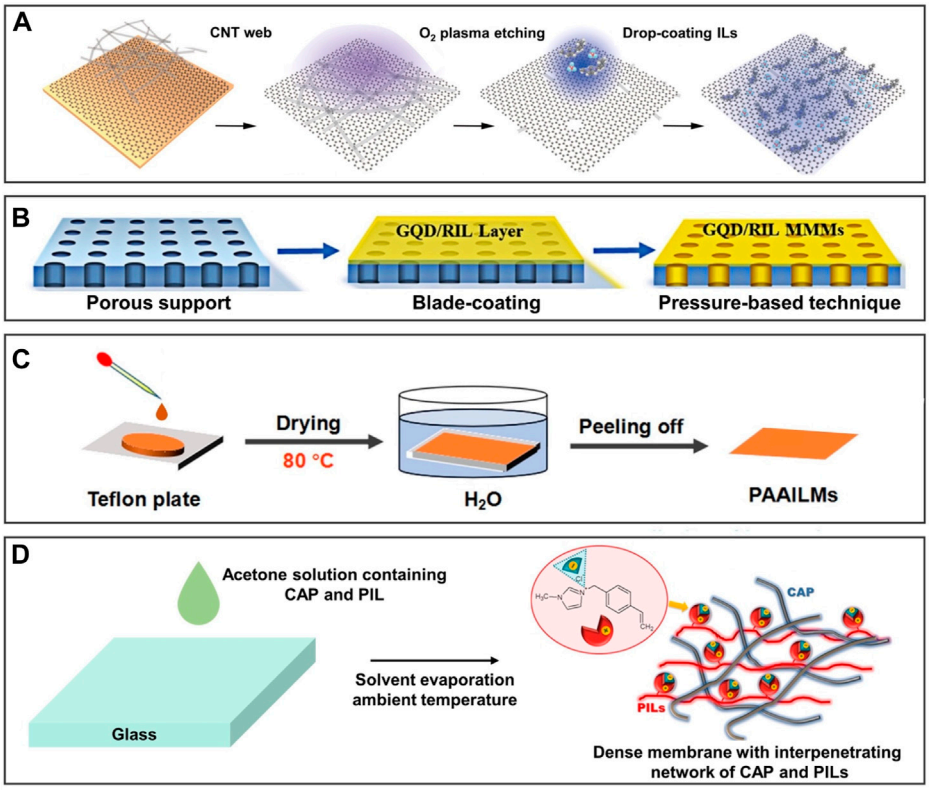

FIGURE 4
Preparation methods of 2D IL-infused membranes. Schematic diagram of IL polymer brushes grafted surfaces. **(A)** Impregnating ILs into the pores of the graphene-based membrane by capillary force for separating CO_2 and N_2. **(B)** Impregnating ILs into the membrane by pressure difference and capillary force for separating ethylene/ethane. **(C)** Reducing the viscosity of PAAILs by heating at 80 °C to impregnate the PVDF-based membrane for separation of amino acids. **(D)** Reducing the viscosity of impregnating 1-methyl-3-(4-vinylbenzyl)-1H-imidazol-3-ium chloride by dissolving in solvent to impregnate the membrane based on cellulose acetate propionate for dehydration of propan-2-ol. **(A)** is reproduced with permission (Guo et al., 2020). Copyright 2020, American Chemical Society; **(C)** reprinted with permission (Dou et al., 2021). Copyright 2020, Wiley-VCH GmbH; **(B)** reproduced with permission (Liu L. et al., 2021). Copyright 2021 Elsevier Inc; **(D)** reproduced with permission (Rynkowska et al., 2017). Copyright 2020, Wiley-VCH GmbH.

synergistic response using the interfacial directional freezing technology of the poly(3-hexylthiophene-2,5-diyl)/[6,6]-phenyl-C_{61}-butyric acid methyl ester (P3HT/PCBM) binary system. Compared to the porous material prepared by the traditional directional freezing technology, the porous material prepared by the interface directional freezing technology exhibits anisotropy from bulk to the interface. However, this method is expensive and difficult to scalable manufacturing.

Spraying–deposition is a process of spraying solution to the substrate surface through a spray gun to obtain coating. As shown in Figure 3C, Wu et al. (2020) demonstrated a simple spray–deposition method to prepare an organic electrochemical transistor (OECT) made of IL-doped poly(3,4-ethylenedioxythiophene): poly(styrene sulfonate) (PEDOT: PSS). The spray–deposition technology provides a convenient way to prepare high-performance OECT channels with scalable manufacturing, excellent stability, high yield, and low cost. However, spraying–deposition is difficult to coat evenly when it comes to the inner surface of objects with a narrow inner cavity, such as the pipe wall with a small inner diameter. The layer-by-layer suction flow method remedies this deficiency, which uses an external injection apparatus to slowly and evenly infuse solution into the pipe. For instance, Agarwal et al. (2021) produced a uniform smooth coating on the inner surface of narrow pipes as shown in Figure 3D. The coating can be applied to pipes of any size and length for inhibiting the blockage of the pipe. This method provides an opportunity to manufacture coating on the inner surface with various shapes.

These methods merely provide porous surfaces, but the successful preparation of IL-infused surfaces requires suitable interactions between the IL and the porous surface. Also, the function of the IL-infused porous surface depends on the characteristics of the IL existing on the surface, such as repellency, lubricity, wetting properties, and self-healing. Although many efforts have been made to improve the affinity between ILs and porous surfaces, the attractive force is still weak, and the content of ILs trapped by micro-/nanostructures is limited, leading to poor mechanical stability and easy to fail in extreme conditions (Howell et al., 2018). At present, the IL-infused surface still has the dilemma of failure after the loss of surface lubricant.

2.3 IL-infused supported membrane

The IL-based supported membrane was prepared by loading ILs into membrane internal channels (Carlin and Fuller, 1997; Branco et al., 2002; Noble et al., 2011; Sasikumar et al., 2018). Compared with

traditional supported liquid membranes, ILs with high viscosity can enhance the capillary force between ILs and the supported membrane for improving stability (Sprugis et al., 2019). At present, the reported methods for preparing the IL-infused supported membrane mainly include the impregnation method, pressure difference method, reducing viscosity by heating, and reducing viscosity by solvent.

The IL-infused supported membrane is usually used to separate mixtures such as CO_2/N_2, ethylene/ethane, amino acids, and propan-2-ol/H_2O. For example, the IL/graphene hybrid membrane was prepared by impregnating ILs into the pores of the film by capillary force (Guo et al., 2020), which can dynamically adjust the chemical affinity of ILs and nanopores for achieving the high permeability of the membrane to separate CO_2 and N_2 (Figure 4A). The preparation of this IL-infused supported membrane is simple but limited by the viscosity of ILs and the pore size. ILs impregnate non-uniformly into a large pore size due to weak capillary force, which causes defects and affects the function of the membrane. In addition to the active impregnation method, the passive pressure difference method can also be used to prepare the IL-infused supported membrane. Figure 4B shows that analogous mixed matrix membranes were obtained by the pressure difference method and impregnation method for ethylene/ethane separation (Dou et al., 2021). The non-covalent interactions between ILs and nanofillers induce the arrangement of ILs to form dense mass transfer interface paths for efficient separation. The membrane prepared by this method can overcome the problem of hardly impregnating the channels because of its high viscosity. However, this preparation method is difficult to achieve when the viscosity of ILs is too high.

To solve the problem of high viscosity, raising the temperature or adding solvent seems to achieve reduced viscosity. Mixing poly(amino acid ionic liquids) (PAAILs) with polyvinylidene fluoride (PVDF) and reducing the viscosity of PAAILs by heating at 80°C to prepare the IL-infused supported membrane for separation amino acids in Figure 4C (Liu L. et al., 2021). However, IL-infused supported membranes prepared by increasing temperature and reducing viscosity are limited by the temperature tolerance range of the supported membrane, causing the limited application range. Additionally, the reduced viscosity of ILs by dissolving in solvents allows them to easily penetrate the channel of the supported membrane. As exhibited in Figure 4D, Rynkowska et al. (2017) added 1-methyl-3-(4-vinylbenzyl)-1H-imidazol-3-ium chloride to acetone solution to obtain dense membranes based on cellulose acetate propionate for dehydration of propan-2-ol. This method becomes a promising candidate for preparing IL-infused supported membranes for the advantages of being simple, stable, and uniform.

The multifunctional IL-infused supported membrane can be prepared by employing ILs with tunable properties such as density, viscosity, wettability, and chemical affinity (Hirota et al., 2017). However, huge challenges for the IL-infused supported membrane remained such as the stability under harsh conditions and the preparation on large scale.

2.4 Ionogel

Ionogel was formed by infusing ILs into the polymer matrix (Fuller et al., 1997; Lu et al., 2009). In contrast with the IL polymer brush and IL-infused porous surface, the IL content of ionogel increases significantly due to the swelling property of the polymer matrix, which offers significant advantages in terms of durability. Many existing studies have reviewed the preparation methods of ionogels from three main kinds: physical crosslinking method, chemical crosslinking method, and their combinations.

2.4.1 Physical crosslinked ionogel

Ionogel can be mainly formed between the IL and the polymer chain by the physical crosslinking method through hydrogen bonds, electrostatic interaction, and host–guest interaction. The hydrogen bond was formed by the combination of H atoms and high-electronegative atoms in molecules, endowing ionogel with good reversibility and controllable crosslinked strength. For instance, Liu Y. et al. (2021) prepared conductive hydrogel by a simple physical crosslinking method. As shown in Figure 5A, PVA/EMImAc/H_2O hydrogels exhibit the advantages of robustness, high flexibility, and elasticity under the effect of hydrogen bonds, but it is prone to failure in extreme environments. In order to solve this problem, the electrostatic interaction based on chemical bonds between anions and cations can be further introduced. For instance, Ding et al. (2017) used the electrostatic interaction to lock 1-ethyl-3-methylimidazolium dicyandiamide ([EMIm][DCA]) into poly(2-acrylamide-2-methyl-1-propanesulfonic acid) (PAMPS) in Figure 5B. Moreover, its durability may be solved by the host–guest interaction, which is the self-assembly of monomer molecules through the host–guest recognition characteristics. For instance, Zhang et al. (2015) prepared ionogel in Figure 5C by taking advantage of the host–guest interaction between b-cyclodextrin (b-CD) and bisimidazolium ILs (Bis-C_{12}(mim)Br). Under the effect of the host–guest interaction, the ionogel can be used as a quasi-solid electrolyte for dye-sensitized solar cells with excellent long-term stability.

The polymer chain entanglement of physically crosslinked ionogel is instantaneously reversible (Sprugis et al., 2019), but the heat-resistance and solvent-resistance are poor, and the permanent deformation is also serious.

2.4.2 Chemical crosslinked ionogel

The chemical crosslinking method mainly includes photopolymerization crosslinking and thermal polymerization crosslinking. Photopolymerization is a typical free-radical polymerization method by activating monomer molecules with light to conduct chain polymerization. This method has the strength of controllability, low polymerization temperature, and high reaction selectivity. For instance, Xu et al. (2021) prepared a multifunctional ionogel through a one-pot photopolymerization, as shown in Figure 5D. This method requires the participation of ultraviolet light, which is difficult to apply in scenarios without light. Fortunately, thermal polymerization makes up for the defects of photopolymerization. Chain polymerization can be conducted by activating monomer molecules in the way of thermal initiation. As illustrated in Figure 5E, Lan et al. (2020) developed a stretchable transparent dual-network ionogel by a simple one-pot thermal polymerization method. However, both photo-initiated polymerization and thermal-initiated polymerization require the input of external energy, making it difficult to synthesize the desired ionogel in a mild environment. Accordingly, Ran et al. prepared IL-click ionogel under mild conditions based on the ionic crosslinking and covalent crosslinking methods in Figure 5F. Click

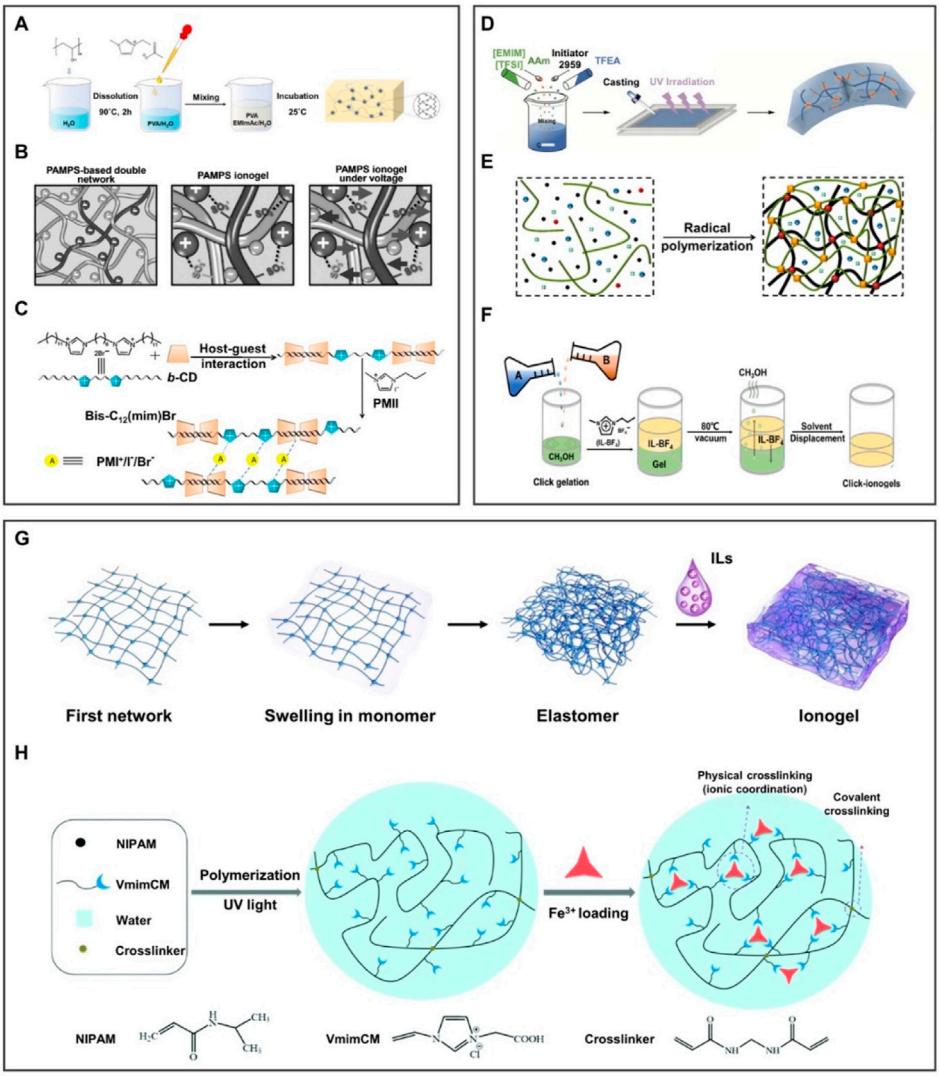

FIGURE 5
Preparation methods of 3D ionogels. **(A–C)** Schematic diagram of ionogel obtained by physical crosslinking. **(A)** Hydrogen bond was formed by the combination of H atoms and high-electronegative atoms in molecules, endowing ionogel good reversibility and controllable crosslinked strength. **(B)** Electrostatic interaction is chemical bonds formed by the charges interaction between anions and cations. **(C)** Host–guest interaction is the self-assembly of monomer molecules through the recognition of characteristics between the host and the guest. **(A)** is reproduced with permission (Liu Y. et al., 2021). Copyright 2021, American Chemical Society; **(B)** reproduced with permission (Ding et al., 2017). Copyright 2017, WILEY-VCH Verlag GmbH and Co. KGaA, Weinheim; **(C)** reproduced with permission (Zhang et al., 2015). Copyright 2015, Elsevier Ltd. **(D–F)** Schematic diagram of ionogel obtained by chemical crosslinking. **(D)** Photoinitiated polymerization under the participation of ultraviolet light. **(E)** Thermal polymerization under the participation of thermal. **(F)** Click chemistry under the reaction of click-functional groups to form stable conjugates in mild conditions. Image **(D)** is reproduced with permission (Xu et al., 2021). Copyright 2021, Wiley-VCH GmbH; **(E)** reproduced with permission (Lan et al., 2020). Copyright 2020, American Chemical Society; **(F)** reproduced with permission (Ren et al., 2019). Copyright 2019, Science. **(G,H)** Schematic diagram of ionogel obtained by the combination of physical and chemical crosslinking through **(G)** hydrogen bonding and thermal polymerization; **(H)** ionic coordination and photopolymerization. Image **(G)** reproduced with permission (Cao et al., 2020). Copyright 2020, The Royal Society of Chemistry; **(H)** reproduced with permission (Sun et al., 2018). Copyright 2018, The Royal Society of Chemistry.

chemistry is a reaction in which a pair of click-functional groups rapidly and selectively reacts with each other to form stable conjugates under mild conditions. Since the click reaction is highly efficient under mild conditions, ionogels can be prepared by simply mixing PEGDA and poly(1-butyl-3vinyl imidazolium fluoborite) (PIL-BF_4) methanol solutions without additional oxygen, humidity, or heating condition (Ren et al., 2019).

The chemically crosslinked ionogel contains permanent connections formed by covalent bonds, offering ionogel high strength and controllable crosslinked degree.

2.4.3 Physical–chemical crosslinked ionogel

The physical–chemical crosslinking method combines the reversibility of physical crosslinking with the stability of chemical crosslinking. In Figure 5G, the ionogel was prepared through hydrogen bonds and thermal polymerization, which possess transparent, mechanically robust, and high ionic conductivity (Cao et al., 2020). Sun et al. prepared a stimuli-responsive ionogel (Figure 5H), comprising chemically crosslinked polymer poly(*N*-isopropylacrylamide) (PNIPAM), physically crosslinked iron ions, and a carboxyl group. Physical crosslinking formed by

ion coordination can improve the mechanical strength of ionogel, making it controllable between the strong coordination of Fe^{3+} and the weak coordination of Fe^{2+}. In addition, covalent crosslinked PNIPAM and conductive ILs are used as thermal switches to obtain thermal/redox dual stimuli-responsive ionogel (Sun et al., 2018).

Physically and chemically crosslinked ionogels can make up for the shortcomings of a single physically crosslinked or chemically crosslinked ionogel, but the challenge is the rational design of experiments to determine the key performance of ionogels.

In brief, ILs can be physically trapped into the polymer matrix (Mantravadi et al., 2016; Cao et al., 2017; Singh et al., 2017), the weak interfacial force result in poor mechanical properties, but it has good physical properties such as stretchability and self-healing. In addition, ILs can also react with the polymer matrix and be fixed in the polymer matrix through polymerization (Muldoon and Gordon, 2004; Ohno, 2007; Zgrzeba et al., 2015), which strengthens the mechanical properties of ionogel. Meanwhile, the strong crosslinking prevents losing ILs from the surface to the environment. However, ionogel is usually prepared by free radical polymerization, which is limited by the reaction conditions and the type of polymer matrix and ILs. To design required ionogels, the physical–chemical crosslinking method can endow ionogels with excellent physical properties by controlling the crosslinked degree. In addition, ionogels can reversibly expand and contract under external stimuli (e.g., light and heat), which has great potential in the intelligent control system.

3 Principle of stable existence of BILIM

BILIMs were divided into three dimensions. The thin layer of IL forms the 1D coating by intermolecular chemical action between IL grafted onto the substrate, and the 2D coating was manufactured by capturing IL through the capillary action or hydrophobic action formed by micro-nano structures on the substrate surface. The inherent porosity of the 3D polymer network and the swelling nature of the network enable the storage of IL. Due to the wide variety of ILs, the properties of ILs also change with the species, such as from hydrophilic to hydrophobic, so the choice of ILs plays a decisive role in the performance of the three coatings. Based on the stable BILIMs, the solid substrate must preferentially wet the IL and repel ambient fluids; meanwhile, the IL and ambient fluids should not dissolve the substrate (Smith et al., 2013).

To ensure the stability of BILIMs in different fluids, the thermodynamic state of coatings can be determined by the contact angles, spread coefficient, and interfacial tension. First, the superwetting of ILs in the air on the substrate surface can be expressed in the following equation:

$$S_{sl(a)} = \gamma_{sa} - \gamma_{sl} - \gamma_{la}, \tag{1}$$

where s, a, and l represent the substrate, air, and IL, respectively. If $S_{sl(a)} \geq 0$, the IL-based coating was successfully manufactured by the infusion of IL into the substrate; otherwise, IL would remain at top of the substrate at a certain contact angle. Even if the IL-based coating can be stabilized in the air, there is a new criterion for stability when placed in water:

$$S_{sl(w)} = \gamma_{sw} - \gamma_{sl} - \gamma_{lw}, \tag{2}$$

where w refers to water. IL was captured by the solid texture without being replaced by water when $S_{sl(w)} \geq 0$. If $S_{sl(w)} < 0$, water will extrude the IL into the solid texture. Except for the displacement behavior of water, there is also the behavior of IL in the texture-cloaking water droplets causing IL exhaustion:

$$S_{lw(a)} = \gamma_{sw} - \gamma_{sl} - \gamma_{lw}. \tag{3}$$

If $S_{lw(a)} < 0$, the IL will cloak the water droplet resting on the IL-based coating, which may cause the loss of ILs in the aqueous environment (Peppou-Chapman et al., 2020). In addition, the IL must be insoluble in the working fluid. Based on the aforementioned requirements, there is no best choice of ILs because of their wide varieties, but the types of ILs should be selected according to the actual needs to achieve an excellent performance of the IL-based coating. In general, low surface energy ILs can be injected into textured surfaces while avoiding miscibility with water. ILs do not evaporate quickly in the air because they have almost no saturated vapor pressure. The interfacial tension in the aforementioned equation can be calculated by the following formula:

$$\gamma_{ij} = \left(\sqrt{\gamma_i^{LW}} - \sqrt{\gamma_j^{LW}}\right)^2 + 2\left(\sqrt{\gamma_i^{+}\gamma_i^{-}} + \sqrt{\gamma_j^{+}\gamma_j^{-}} - \sqrt{\gamma_i^{+}\gamma_j^{-}} - \sqrt{\gamma_i^{-}\gamma_j^{+}}\right). \tag{4}$$

For the surface energy component of the substrate, the surface energy parameters of the standard liquid can be obtained from the previous report (Meng and Wang, 2019), measuring the contact angle of the standard liquid on the solid surface and calculating the surface energy using Lewis acid–base theory.

$$\gamma_s = \gamma_s^{LW} + \gamma_s^{AB}, \tag{5}$$

$$\gamma_s^{AB} = 2\sqrt{(\gamma_s^{+}\gamma_s^{-})}, \tag{6}$$

$$\gamma_L(\cos\theta + 1) = 2\sqrt{\gamma_L^{LW}\gamma_S^{LW}} + 2\sqrt{\gamma_L^{+}\gamma_S^{-}} + 2\sqrt{\gamma_L^{-}\gamma_S^{+}}, \tag{7}$$

where γ^{AB} represents the polar acid–base (AB) component of the surface energy, γ^{+} represents Lewis acid parameters of the surface energy, γ^{-} represents Lewis base parameters of the surface energy, γ^{LW} represents the non-polar Lifshitz–van der Waals (LW) component of the surface energy, and θ represents the contact angle formed by the standard liquid on the substrate surface.

4 Applications

4.1 Anti-adhesive application

Undesired adhesion on the surface may damage the surface function and further lead to surface failure. Pitcher plants utilize their slippery characteristics to capture insects as their main source of nitrogen. Corals secrete natural antibacterial substances to resist the attachment of fouling organisms in the sea (Jin et al., 2022). The mucus on fish scales traps water to resist oil pollution. Learning from nature life, BILIM can be widely used in self-cleaning, marine antifouling, biomedical, and other fields because it can inhibit the adhesion of bacteria, oil, scale, and ice.

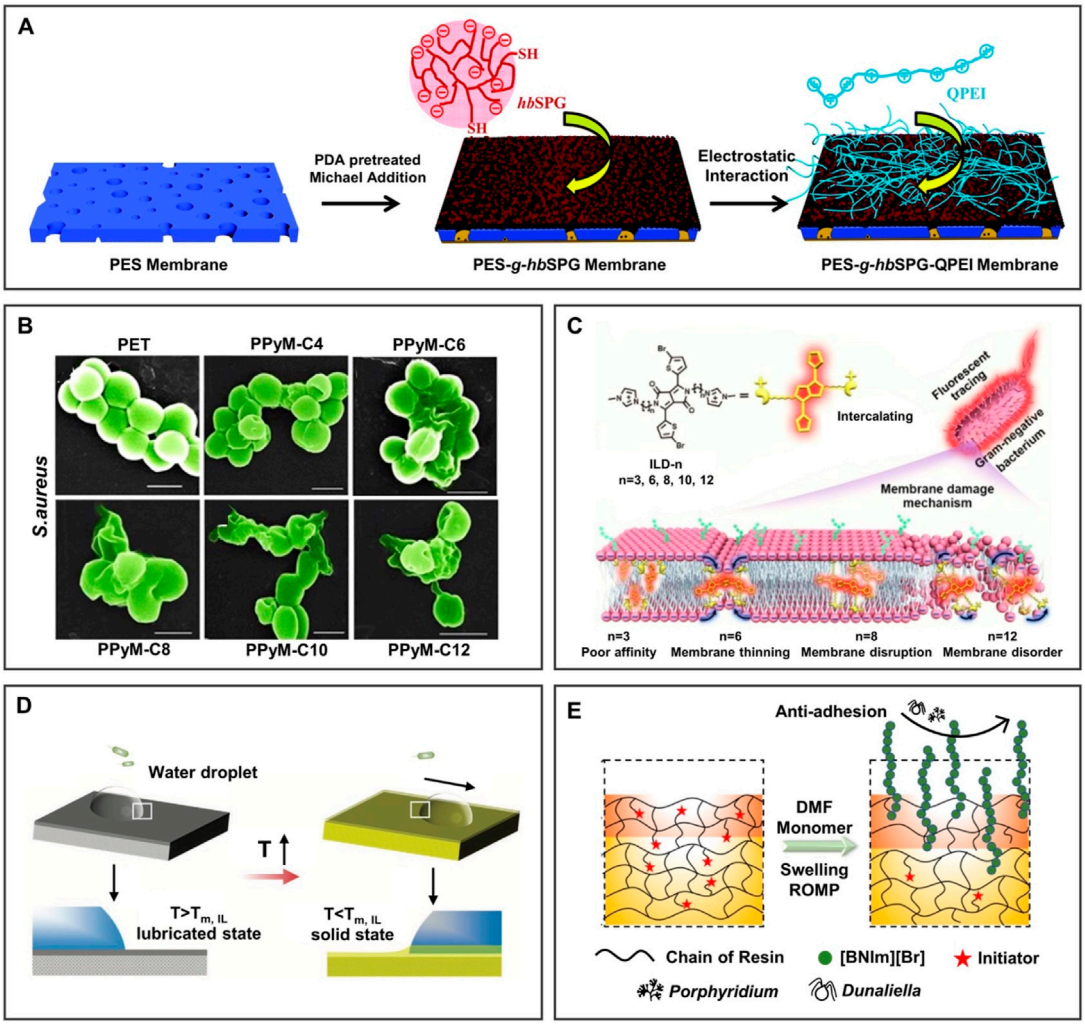

FIGURE 6
BILIMs for anti-biofouling. **(A)** PILs modified membrane decreased the adsorption of protein obviously after soaking in wastewater for 2 months. Reproduced with permission (Li et al., 2019). Copyright 2019, The Royal Society of Chemistry. **(B)** Antibacterial efficiency of PILs against Gram-positive bacteria increased with the increase of the alkyl chain length of substituents because of hydrophobic segments inserted into bacterial membranes, leading to bacterial death. Reproduced with permission (Qin et al., 2017). Copyright 2017, American Chemical Society. **(C)** The antibacterial efficiency of pyrrolidinium-type IL against *Staphylococcus aureus* increases with the increase of the alkyl chain length of substituents, resulting in instability of the lipid bilayer and further promoting antibacterial activity. Reproduced with permission (Zheng et al., 2020). Copyright 2020, American Chemical Society. **(D)** Responsive self-replenishing ionogel with renewable anti-biofouling properties. Reproduced with permission (Ye et al., 2019). Copyright 2019, WILEY-VCH Verlag GmbH and Co. KGaA, Weinheim. **(E)** Bio-inspired sharklet surface can remove algae and shows good anti-biofouling performance. Reproduced with permission (He et al., 2021). Copyright 2021, Elsevier B.V.

4.1.1 Anti-biofouling

In 2016, the World Health Organization published a set of alarming data. Approximately 700,000 deaths are attributable to "superbug" infection every year, and the annual number of deaths may increase to 10 million by 2050. The traditional antibacterial materials have developed drug resistance so the need for an alternative and sufficiently powerful antibacterial material so that bacteria never develop resistance is urgent (Wei et al., 2020). Due to the electrostatic effect on disturbing bacterial membranes, IL-based antibacterial materials have attracted extensive research interest (Zhao et al., 2014). Recently, the antibacterial mechanism and intelligent IL-based antibacterial materials have developed rapidly (Zhao et al., 2015).

As shown in Figure 6A, the anionic sulfonated hyperbranched polyglycerol (hbSPG) and cationic quaternized polyethylenimine (QPEI) were introduced onto the poly(ether sulfone) (PES) membrane (Li et al., 2019). The membrane showed anti-protein adsorption through the surface hydration network, preventing the adsorption of hydrophobic impurities and antibacterial performance because of its hierarchical architecture and the free quaternary ammonium base after being immersed in wastewater for 2 months, showing great potential in the application of anti-protein pollution.

Moreover, the antibacterial mechanism of BILIMs and the effect of chain length on antibacterial ability were further studied. In Figure 6B, Qin et al. (2017) showed that the antibacterial efficiency of PILs against Gram-positive bacteria

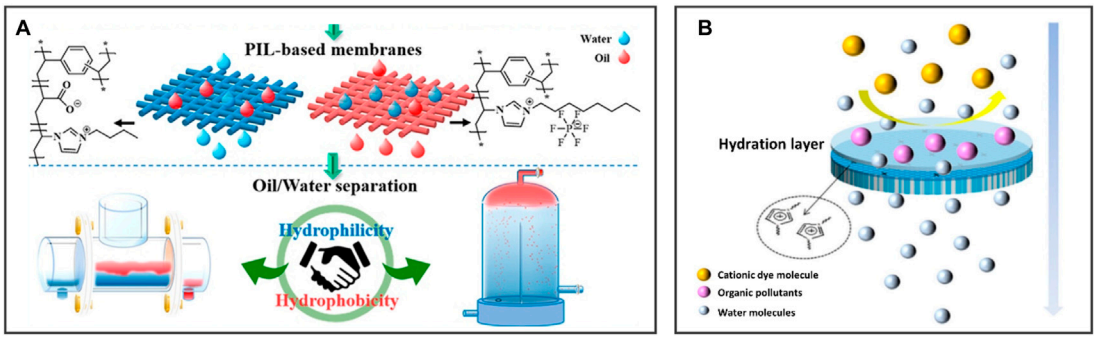

FIGURE 7
BILIMs for anti-liquid fouling. **(A)** Oil/water separation membrane with adjustable surface wettability realizes continuous oil/water separation without polluted by oil. Reproduced with permission (Deng et al., 2020). Copyright 2020, American Chemical Society. **(B)** ILs modified membrane can separate dyes and purify wastewater containing organic pollutant. Reproduced with permission (Liu et al., 2022). Copyright 2022, Springer Nature.

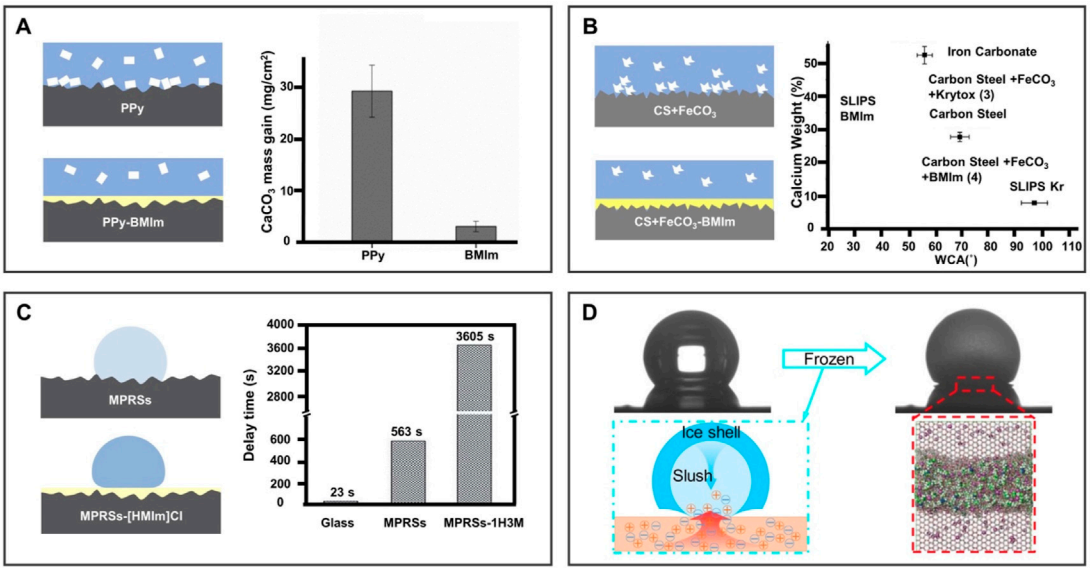

FIGURE 8
BILIMs for anti-solid fouling. **(A)** Low surface energy lubricant and BMIm were injected into the porous polypyrrole coating to reduce scaling. Reproduced with permission (Charpentier et al., 2015). Copyright 2015, Elsevier Inc. **(B)** BMIm-infused $FeCO_3$ layer of carbon steel increases hydrophobicity and reduces scale formation. Reproduced with permission (Saul et al., 2021). Copyright 2021, Informa United Kingdom Limited. **(C)** BMIm[PF_6] doped polyvinylidene fluoride nanofibers delay the freezing time of water droplets and reduced the crystallization temperature and ice adhesion strength of water droplets. Reproduced with permission (Rao et al., 2019). Copyright 2019, The Royal Society of Chemistry. **(D)** Ionogel surface inhibits ice nucleation, growth, and adhesion. Reproduced with permission (Zhuo et al., 2020). Copyright 2020, American Chemical Society.

increased with the increase of the alkyl chain length of substituents, the reason may be that hydrophobic segments are more easily inserted into bacterial membranes, leading to bacterial death. Furthermore, the antibacterial mechanism was systematically explored at the molecular level (Zheng et al., 2020). As shown in Figure 6C, ILs were readily embedded into the bacterial membrane as the molecular size increases, resulting in the instability of the lipid bilayer and further promoting antibacterial performance. This work demonstrated the electrostatic interactions between molecular sizes of IL-based materials and Gram-negative bacteria with the effect of an antibacterial ability. Moreover, the responsive self-replenishing coating offers an idea strategy for the renewable anti-biofouling surface. In Figure 6D, Ye et al. (2019) mixed the solid/liquid binary mixture of ILs with a semicrystalline polymer. After heating, the surface of the ionogel changes from a solid to a liquid-infused state, which promotes the removal of biofilm/bacteria. After the surface is damaged, ILs released from the inside to the surface and crystallized on the surface to realize the self-replenishment of ILs on the surface. This work provides an opportunity for ionogels to be used as a functional coating with renewable anti-biofouling properties.

In addition to killing bacteria, algae pollution can be resisted by preparing a multi-scale IL polymer brush-modified antifouling surface (He et al., 2021). 1-(1H-Benzotriazolyl) methyl-

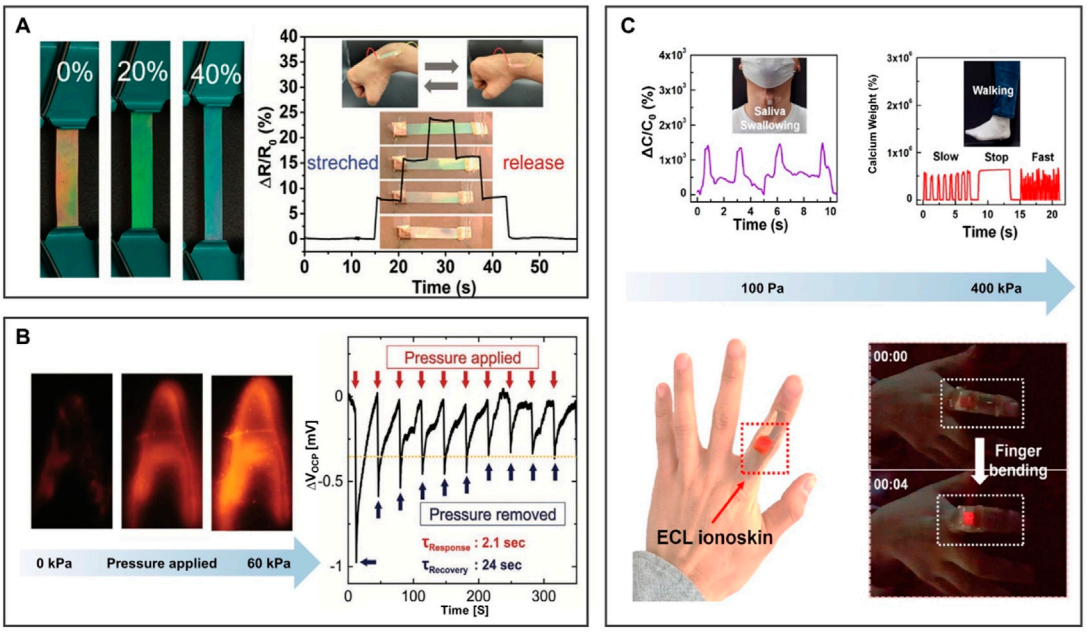

FIGURE 9
BILIMs for a biological sensor. **(A)** Bionic interactive visible ion skin. Reproduced with permission (Lyu et al., 2021). Copyright 2021, Wiley-VCH GmbH. **(B)** Electrochemiluminescence skin with the piezoelectric ion effect. Reproduced with permission (Lee et al., 2021). Copyright 2021, Wiley-VCH GmbH. **(C)** Photoelectric dual output high-performance wearable ion skin. Reproduced with permission (Kwon et al., 2021). Copyright 2021, American Chemical Society.

3norbornene methyl-1H-imidazolium bromide ([BNIm][Br]) was grafted onto the bio-inspired sharklet substrate prepared by 3D printing of acrylic resin (Figure 6E). Compared to the bare sharklet substrate, the removal rate of *Porphyridium* increased from 40.7% to 60.1%. Therefore, ILs can be grafted onto the substrate surface or infused into a porous surface to obtain antibacterial function (Ye et al., 2012), which can be adjusted by the length of the ILs alkyl chain, hydrophobicity, and molecular size.

4.1.2 Anti-liquid fouling

Some organic substances such as protein and grease contained in wastewater will cause deposition on the surface and corrosion of water treatment equipment (Wei et al., 2018), which poses a real threat to the environment (Wei et al., 2022). Many physical and chemical methods (such as distillation and electromagnetic radiation) have been developed for organic pollutants separation in wastewater but have the problems of low efficiency and high energy consumption (Zhang X. et al., 2020). To overcome the defects of the aforementioned methods, the antifouling coating inspired by nature can reduce the deposition of these organic substances and maintain the initial function of the equipment surface.

Deng *et al.* prepared a series of PIL-based oil/water separation membranes with adjustable surface wettability using *N*-vinylimidazolium IL and divinylbenzene (Figure 7A). The hydrophilic poly(1-vinyl-3-butylimidazolium acrylate)-based membrane (PILM-1) transports water and retains oil, while the hydrophobic poly(1-vinyl-3-octylimidazolium hexafluorophosphate)-based membrane (PILM-5) removes oil and retains water. Two types of membranes with opposite wettability show excellent oil/water separation efficiency (over 99%) during the treatment process and realize continuous oil/water separation of 46 L/12 h (Deng et al., 2020). Additionally, Liu et al. (2022) prepared an IL-modified membrane by grafting 1-butyl-3-vinylimidazole bromide IL onto PVDF for improving the wettability and antifouling performance of the membrane (Figure 7B), demonstrating excellent separation performance for cationic dyes in wastewater.

The development of bio-inspired coatings is a promising strategy to solve the increasingly serious problem of organic fouling, which has the advantages of reliable service life, effective cost reduction, and broad application prospects in water treatment equipment.

4.1.3 Anti-solid fouling

Some adhesion of solids (e.g., mineral scale and ice) can pose serious problems to humans in daily production and life. Undesired scale adhesion in pipes will cause fuel waste due to decreased heat transfer efficiency. Furthermore, once ice forms on a surface (e.g., aircraft), it will seriously endanger the normal operation of the equipment and put humans in danger. Therefore, dealing with the solid adhesion problem is of great significance to ensure normal operation. BILIM has achieved success in antifouling and anti-icing applications due to the existence of the liquid barrier layer on the surface.

Compared to the Fluorinert FC-70-infused surface, the IL-infused surface is more stable on the coating surface because of its moderate surface energy than with fluorinated lubricating oil. Using IL-BMIm as a liquid layer, Charpentier et al. (2015) developed a polypyrrole coating on a stainless-steel substrate using a potentiostatic deposition method in Figure 8A. Due to the slippery and low adhesion properties of the liquid-infused surface, calcium carbonate ($CaCO_3$) was significantly reduced by 18 times, offering a novel solution for anti-scaling. In addition, Saul et al. (2021) infused IL-BMIm into the $FeCO_3$ layer on X65 carbon steel to prepare a novel

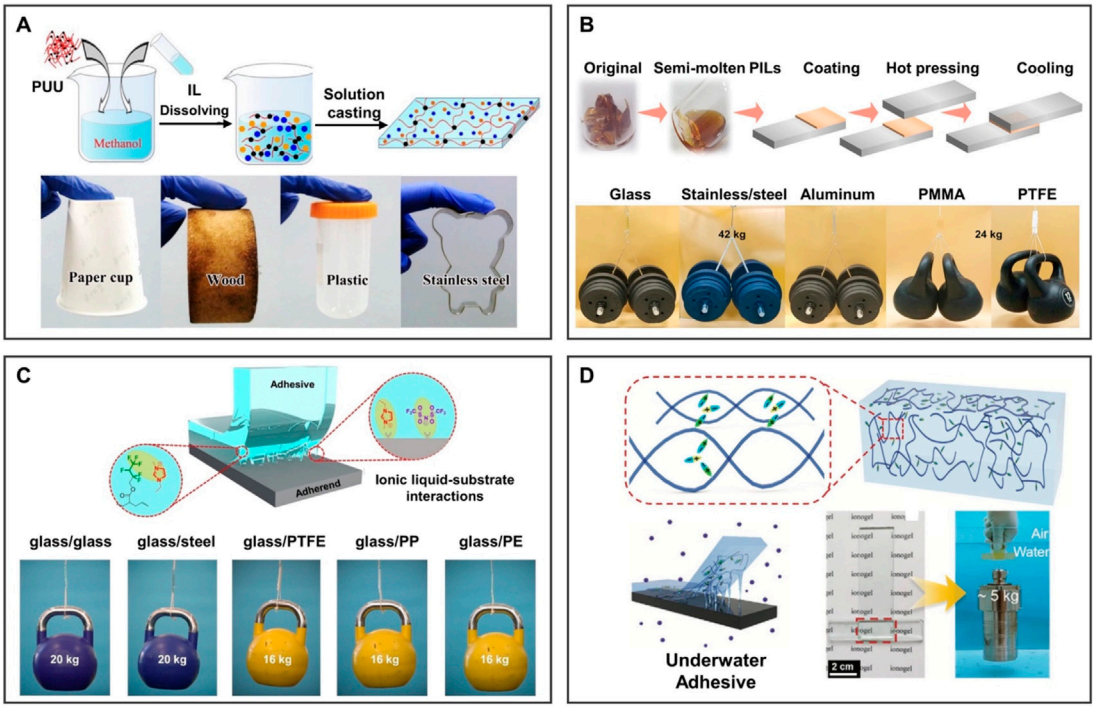

FIGURE 10
BILIMs for adhesive tape. **(A)** PUU polymer hydrogen bonding and amphiphilicity enable ionogels to adhere to any substrate, thus realizing the university of adherence to substrates. Reproduced with permission (Chen and Guo, 2021). Copyright 2021, American Chemical Society. **(B)** Flexible alkoxy chains are introduced into the cationic backbone of PILs, enabling strong hydrogen bonding and electrostatic interactions while contributing to high cohesive energy and interfacial adhesive energy to obtain high-efficiency adhesive. Reproduced with permission (Zhang et al., 2021). Copyright 2021, Wiley-VCH GmbH. **(C)** Ion-dipole interactions between P(HFBA-*co*-MMA) and hydrophobic ILs for higher adhesion strength and reversible adhesion. Reproduced with permission (Huang et al., 2021). Copyright 2021, American Chemical Society. **(D)** Ionogel soaked in the salt solution can discharge the salt ions on the surface of the substrate to adhere to the substrate, and the adhered substrate can lift a heavy object up to 5 kg, realizing reversible and strong adhesion. Reproduced with permission (Yu and Wu, 2021). Copyright 2021, Wiley-VCH GmbH.

kind of BILIM (Figure 8B). There is no need to use a functional layer between the substrate and the lubricant interface and shows enhanced anti-scaling ability against $CaCO_3$.

In addition to the adhesion of scales, the adhesion of ice may also cause surface failure or even serious accidents. Therefore, many efforts have been made to reduce the formation and adhesion of ice on the surface. As shown in Figure 8C, the smooth surface obtained by infusing [HMIm]Cl into the polymer has excellent anti-icing performance compared to the bare glass and the polymer surface without an IL infusion. The surface extends the icing time to 3605s and reduces the adhesion of ice (Rao et al., 2019). In addition, Zhuo et al. (2020) developed a novel anti-icing ionogel to inhibit the growth of ice to mitigate the harm caused by accretion ice, as illustrated in Figure 8D. The ionogel demonstrated an outstanding ability to inhibit the growth of ice and prevent the formation of frost in a humidified environment. It is observed that the positive and negative ions of [BMIm]Br separate at the front interface of ice growth, creating an electric field that prevents ice growth due to the formed interface liquid layer with poor adhesion to the substrate.

Although the research on ILs in anti-scaling and anti-icing is small, the existing literature has shown great potential in removing undesired adhesion. It is expected to lead the scientific research wave in anti-scaling and anti-icing by utilizing the lubricating properties and freezing tolerance properties of ILs.

4.2 Adhesive materials

There are many interesting adhesion phenomena in nature, such as snails, abalone, mussels, and geckos. Inspired by nature, the interfacial interaction forces formed by the contact between the gecko's foot and the solid wall provide adhesion for the gecko to walk on a vertical wall, the non-covalent interaction between the adhesive secreted by mussels and the solid substrate is settled on the rock for survival. For BILIMs, their adhesion performance can be adjusted by rationally designing ILs, thus expanding the application range of materials. Due to the high adhesion from the electrostatic effect, IL-based adhesive materials have made innovations in biological sensors, adhesive tape, and wound dressing.

4.2.1 Biological sensor

The rapid rise of the internet has popularized the use of electronic products and improved the life quality of humans. However, traditional electronic devices suffer from limited toughness and poor self-healing properties, while IL-based electronic devices have excellent performances such as flexibility, self-healing property, and reconfigurable property caused by charge effect and high conductivity. Therefore, many research studies have paid attention to building new multi-functional electronic devices based on ILs. The unique mechanical properties of ILs make them promising for various biological sensors.

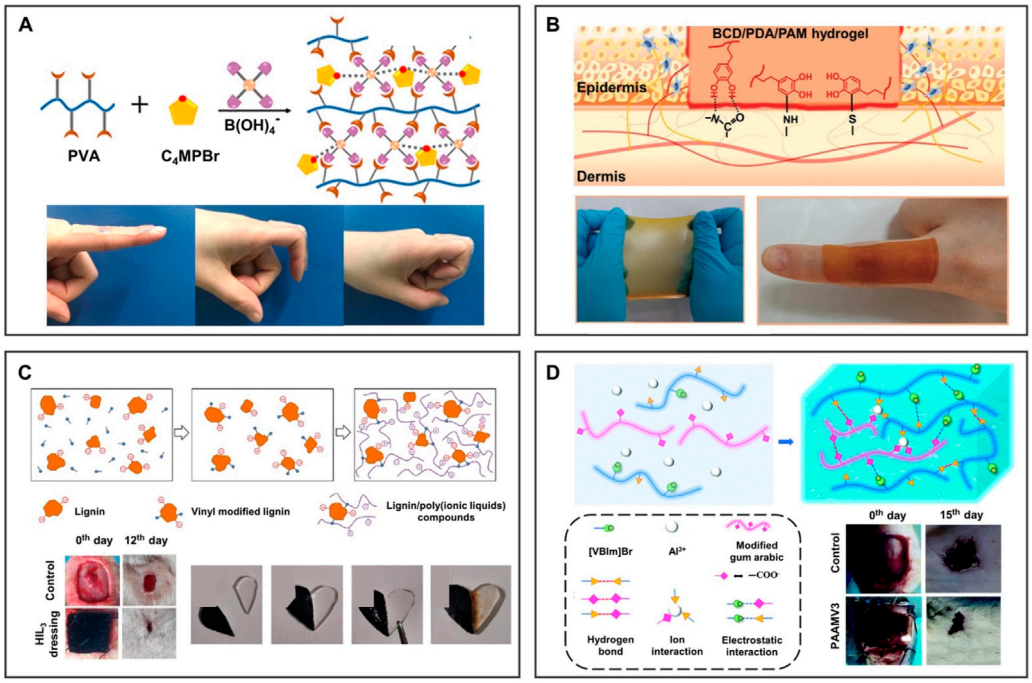

FIGURE 11
BILIMs for wound dressing. **(A)** Incorporation of pyrrolidine to provide ionogel adhesion for application in wound dressings. Reproduced with permission (Yu et al., 2020). Copyright 2020, Elsevier B.V. **(B)** After the introduction of PDA containing abundant catechol groups, ionogel can be attached to the areas where the body moves greatly and realize the treatment of special regional wounds. Reproduced with permission (Yang et al., 2021). Copyright 2021, Wiley-VCH GmbH. **(C)** Lignin with a three-dimensional network structure and antioxidant activity was introduced into ionogel, which showed good antibacterial activity and promoted wound healing. Reproduced with permission (Zhang X. et al., 2020). Copyright 2020, Elsevier B.V. **(D)** After combining ILs with hydrogel dressing containing migratable ions, dressing promotes the migration of ions, thus promoting self-healing performance. Reproduced with permission (Li et al., 2021). Copyright 2021, The Royal Society of Chemistry.

To obtain photonic ionogels (PIGs) with good stability and synergistic sensitivity, Lyu et al. (2021) developed an ion skin by locking 1-ethyl-3-methylimidazolium bis-(trifluoromethylsulfonyl) imide ([EMIm][TFSI]) into poly(ethylene glycol) phenyl ether acrylate (PEGPEA) polymer elastomer as shown in Figure 9A. Under a slight tensile strain, the PIGs immediately changed from orange to green. When the strain reached 40%, the PIGs changed to blue, showing excellent mechanochromic performance. They can be used for ion skin sensors and photoelectric interactive devices.

The deformable electronic skin device was designed to convert local stress into a spatially resolved optical signal (Lee et al., 2021). The electrochemical performance of the composite material is controlled by the electrochemiluminescence (ECL)-active material (ECL: $Ru(bpy)_3)[PF_6]_2$, IL: [EMIm][TFSI]), and the mechanical performance is controlled by polyurethane matrix (Figure 9B). When pressure is applied to the film from the top, cations leave and anions are retained due to the difference in the mobility rate of anions and cations, thereby appearing negative charge layer and positive charge layer on the film. When the pressure was removed, the electrical potential will slowly return to its original value until a uniform ion distribution is obtained. For the aforementioned reasons, the ECL skin device platform can convert mechanical stimuli into visual readings, laying the foundation for the design of tactile sensors for human–machine interaction with electronic skin. In addition, the structural changes of porous ionogels can also be used to visualize electronic signals.

As described in Figure 9C, Kwon et al. (2021) prepared porous ionogel by *in situ* crosslinking polymerization of PEA-g-PS-g-PDVB and [EMIm][TFSI]. After applying pressure, the elastic porous ionogel collapsed and the pores closed. Therefore, the contact area between the gel and the electrode increases, resulting in a higher ECL capacitance. The applied pressure can be directly displayed by the brightness of the emitted light, and it is expected to become an important part of high-performance, functional ion electronics. Additionally, molding soft BILIMs into specific structures with strong adhesion and high conductivity by utilizing 3D printing has prospects for intelligent devices such as biosensors, wearable electronic devices, and smart robotics (Chen et al., 2022).

Electronic devices based on ILs have made innovations in the development and application of flexible wearable devices (Wang et al., 2022). IL-based electronic devices are mainly in the form of ionogel, which confines the ILs in an elastic polymer matrix. ILs have excellent properties such as conductivity and electrochemical stability, thereby improving the electrochemical performance of electronic devices. In addition, conductive additives such as carbon-based materials and metal nanoparticles were introduced into the polymer network to improve high conductivity and mechanical properties. However, most of the research is still in the theoretical research or basic research stage and generally has problems with stability and durability. The future research direction is to continue to optimize the performance of biological devices to obtain high-performance devices.

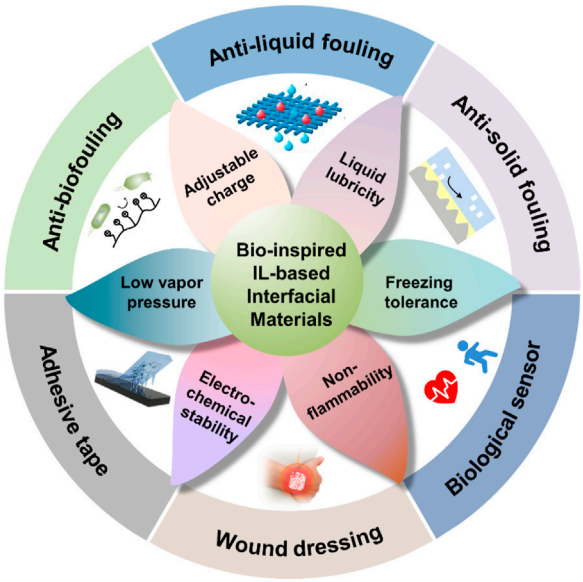

FIGURE 12
Unique properties and applications of BILIMs. BILIM inherits the advantages of ILs, such as charge adjustability and electrochemical stability, and shows promising potential applications in anti-adhesion (anti-biofouling, anti-liquid fouling, and anti-solid fouling) and adhesion (biological sensor, adhesive tape, and wound dressing). Reproduced with permission (Zhang et al., 2019). Copyright 2019, American Chemical Society. Reproduced with permission (Cho et al., 2020). Copyright 2020, WILEY-VCH Verlag GmbH & Co. KGaA, Weinheim. Reproduced with permission (Wang et al., 2020). Copyright 2020, American Chemical Society. Reproduced with permission (Yao et al., 2022). Copyright 2022, Wiley-VCH GmbH (Deng et al., 2020). Copyright 2020, American Chemical Society.

4.2.2 Adhesive tape

Underwater adhesion generally has problems such as poor adhesion and instability, which seriously affect the efficacy and service life of adhesive materials in practical applications. IL-based adhesive tape has broad application prospects due to its underwater stability and adhesion, the adhesive strength of which can be adjusted by changing the types of ILs. In addition, physical interaction can be introduced into adhesive tape based on ionogel to further enhance the adhesion strength.

As a common physical interaction, hydrogen bonds can be used to enhance the adhesion of the tape. As shown in Figure 10A, Guo et al.2020 developed supramolecular hydrogel containing poly(urethane-urea) (PUU) and ILs (Chen 2021 Guo, 2021). The hydrogen bond endows the ionogel with excellent adhesion, which can be adhered to any substrate. It can be attached to a human's skin as a sensor to monitor various movements. Additionally, an efficient adhesive tape was prepared by simply introducing flexible alkoxy into the cationic skeleton of PILs containing $TFSI^-$ anion (Figure 10B). The strong hydrogen bond and electrostatic interaction between flexible alkoxy chains and PILs both contribute to high cohesive energy and interfacial adhesion energy (Zhang et al., 2021). Alkoxy PILs can adhere to various substrates such as glass, ceramic, and stainless steel.

In addition to the hydrogen bond, the effect of a charge also enhances adhesion. The transparent ionogel adhesive tape was composed of hydrophobic ILs and poly(hexafluorobutyl acrylate-*co*-methyl methacrylate) (Huang et al., 2021). The ionogel adhesive tape achieved high adhesive strength through an ion-dipole interaction, which can be reversibly adhered to various substrates, such as glass, steel, and PTFE, and the adhesive strength of ionogel was higher than that of most commercial adhesive tapes (Figure 10C). Cations of the ionogel can repel salt ions from the substrate surface, and quickly and firmly adhere to various substrates in salt solution (Yu and Wu, 2021) (Figure 10D). The ionogel possesses the performance of high ionic conductivity, underwater adhesion, self-healing, and stretchability, which can lift an object up to 5 kg underwater and repeatedly adhere to the substrate for sensors.

IL-based adhesive tapes take full advantage of the characteristics of ILs and polymer networks to obtain high adhesive strength through physical interaction including hydrogen bonds and charge interaction. The adhesive strength, self-healing ability, stretchability, optical transparency, electrical conductivity, and other properties of IL-based adhesive tape can be controlled by reasonably designing the structure of ILs.

4.2.3 Wound dressing

Many efforts have been made to apply adhesive materials to wound dressings; however, little attention has been paid to combining high adhesion with antibacterial/antiinflammatory functions in existing solutions. The incorporation of ILs brings high adhesion to antibacterial wound dressings, which makes up for the aforementioned problem. As shown in Figure 11A, Yu et al. (2020) designed an antibacterial hydrogel containing pyrrole ILs, which showed effective antibacterial activity against Gram-negative and Gram-positive bacteria. The antibacterial and adhesive properties of ionogel give it potential in wound dressing applications. Inspired by the bio-adhesion of mussel dopamine, Yang et al. (2021) fabricated an adhesive hydrogel dressing containing PDA. As shown in Figure 11B, PDA components are rich in catechol groups, so they can adhere to various surfaces, especially in special areas requiring large movements, which can be used as a wound dressing. Inspired by trees, Zhang Y. et al. (2020) synthesized a novel type of lignin/PILs composite hydrogel dressing. As shown in Figure 11C, self-healing hydrogel obtained by the supramolecular interaction between lignin and PILs can promote wound healing in rats. The introduction of lignin with a three-dimensional network structure can significantly improve the mechanical property and antioxidant activity of hydrogel dressing. The IL-based hydrogel dressing with excellent antibacterial performance can promote skin wound healing wonderfully. As depicted in Figure 11D, (Li et al. (2021) grafted positively charged IL 1-vinyl-3-butylimidazolium ([VBIm]Br) and Al^{3+} onto the main chain of hydrogel through covalent interaction. On the one hand, ILs can promote the hydrophobic interaction between hydrophobic segments of hydrogel, which can show the good mechanical properties of hydrogel after absorbing water. On the other hand, charged ILs can promote the migration of Al^{3+}, improving the self-healing performance of hydrogel and accelerating the self-healing of rat wounds. The synergistic effect of strong adhesion and antibacterial properties of the IL-based wound dressing will play a huge role in wound healing.

Considering the biosafety of BILIMs in bio-adhesion and wound dressing, numerous studies have shown that choline, some ammonium ions, and glycine betaine can be utilized as cations to obtain biological ILs with biodegradable and low toxicity (Gomes et al., 2019). IL-based wound dressing possesses a good bactericidal

effect on common bacilli, cocci, and fungi, which has good biocompatibility without destroying the normal cell structure. In addition, the introduction of charged ILs endows IL-based wound dressing with good mechanical properties and adhesion, which is conducive to promoting the self-healing of the wound. Therefore, BILIM provides a broad application prospect in wound dressing.

5 Summary and outlook

Due to the negligible vapor pressure, adjustable charge, liquid lubricity, freezing tolerance, non-flammability, and electro-chemical stability of ILs (Figure 12), BILIMs have attracted the interest of scientific researchers, making them considerably important in antifouling, anti-liquid fouling, anti-solid fouling, adhesive tape, wound dressing, and biological sensors. Although great achievements have been made in various applications of ILs, there are still some challenges to be solved in BILIMs.

Although BILIMs have been used for anti-microbial purposes, the mechanism is still unclear: the increase in the alkyl chain length of ILs does not increase the antibacterial ability for all bacterial species, and the effect of structural changes on their antimicrobial capacity has not been widely discussed. The currently accepted mechanism is the interaction between the negatively charged bacterial cell membrane and the positive charges of the ILs disturbing the cell membrane, the hydrophobic segment of the ILs is inserted into the cell membrane, resulting in the death of bacteria. However, this theory has not yet been confirmed, and the antibacterial mechanism of ILs should be clarified in the future. Of course, with IL as an ideal lubrication layer, the loss of the IL layer on the porous surface is an inevitable problem when it is in a complex fluid environment. In future development, improving the stability and durability of the IL-infused coating is the primary problem to be solved and may be considered from the aspects of intelligent control of the state of the IL layer on the surface and intelligent release.

The existing IL-based electronic devices may have undesired chemical reactions under high pressure, which may cause a decrease in conductivity and short circuits, thus leading to the failure of these electronic devices. Encapsulating ILs can alleviate this failure mechanism to some extent, yet brings problems of compatibility with the package interface, such as poor adhesion, poor toughness, and difficulty in bonding. Therefore, it is necessary to further explore the internal composition and crosslinking forms of ILs materials to improve the electrochemical performance, durability, stability, and compatibility of biological sensors.

Due to the diversity and the adjustment of anions and cations, IL-based stimuli-responsive materials can achieve controllable physical and chemical properties as well as functions by reasonably designing ionic species anion, cation, hydrophilicity, and hydrophobicity of ILs. Although many efforts have been made to develop various IL-based smart devices, it is necessary to systematically study the mechanism between the properties of ILs and the stimuli-responsive performance of ILs. From the perspective of practical applications, there are still many challenges and opportunities.

Author contributions

ZZ and RZ wrote the draft manuscript, JM, SW, and RZ contributed to the manuscript revision, and JM and SW provided funding. All authors read and approved the submitted version.

Funding

This work was supported by the National Key R&D Program of China (2019YFA0709300) and the National Natural Science Foundation of China (22275203, 21875269, 21972155, and 22035008).

Conflict of interest

SW and JM were employed by Qingdao Casfuture Research Institute Co., Ltd.

The remaining authors declare that the research was conducted in the absence of any commercial or financial relationships that could be construed as a potential conflict of interest.

Publisher's note

References

Agarwal, H., Nyffeler, K. E., Blackwell, H. E., and Lynn, D. M. (2021). Fabrication of slippery liquid-infused coatings in flexible narrow-bore tubing. *ACS Appl. Mat. Interfaces* 13, 55621–55632. doi:10.1021/acsami.1c14662

Bechert, D. W., Bruse, M., Hage, W., VanderHoeven, J. G. T., and Hoppe, G. (1997). Experiments on drag-reducing surfaces and their optimization with an adjustable geometry. *J. Fluid Mech.* 338, 59–87. doi:10.1017/s0022112096004673

Branco, L. C., Crespo, J. G., and Afonso, C. A. M. (2002). Highly selective transport of organic compounds by using supported liquid membranes based on ionic liquids. *Angew. Chem. Int. Ed.* 41, 2771–2773. doi:10.1002/1521-3773(20020802)41:15<2771:aid-anie2771>3.0.co;2-u

Buddingh, J. V., Hozumi, A., and Liu, G. (2021). Liquid and liquid-like surfaces/coatings that readily slide fluids. *Prog. Polym. Sci.* 123, 101468–101497. doi:10.1016/j.progpolymsci.2021.101468

Cao, Y., Morrissey, T. G., Acome, E., Allec, S. I., Wong, B. M., Keplinger, C., et al. (2017). A transparent, self-healing, highly stretchable ionic conductor. *Adv. Mat.* 29, 1605099–1605107. doi:10.1002/adma.201605099

Cao, Z., Liu, H., and Jiang, L. (2020). Transparent, mechanically robust, and ultrastable ionogels enabled by hydrogen bonding between elastomers and ionic liquids. *Mat. Horiz.* 7, 912–918. doi:10.1039/c9mh01699f

Carlin, R., and Fuller, J. (1997). Ionic liquid-polymer gel catalytic membrane. *Chem. Commun.* 15, 1345–1346. doi:10.1039/a702195j

Charpentier, T. V., Neville, A., Baudin, S., Smith, M. J., Euvrard, M., Bell, A., et al. (2015). Liquid infused porous surfaces for mineral fouling mitigation. *J. Colloid Interface Sci.* 444, 81–86. doi:10.1016/j.jcis.2014.12.043

Chen, H., Ge, P., Yan, Z., Chen, M., Dai, X., Zhuo, H., et al. (2022). 3D printable, biomimetic adhesive, and self-healing acrylic elastomers for customized attachable strain sensor. *Chem. Eng. J.* 430, 133111–133120. doi:10.1016/j.cej.2021.133111

Chen, H., Zhang, P., Zhang, L., Liu, H., Jiang, Y., Zhang, D., et al. (2016). Continuous directional water transport on the peristome surface of Nepenthes alata. *Nature* 532, 85–89. doi:10.1038/nature17189

Chen, L., and Guo, M. (2021). Highly transparent, stretchable, and conductive supramolecular ionogels integrated with three-dimensional printable, adhesive, healable, and recyclable character. *ACS Appl. Mat. Interfaces* 13, 25365–25373. doi:10.1021/acsami.1c04255

Cheng, Y. Y., Du, C. H., Wu, C. J., Sun, K. X., and Chi, N. P. (2018). Improving the hydrophilic and antifouling properties of poly(vinyl chloride) membranes by atom transfer radical polymerization grafting of poly(ionic liquid) brushes. *Polym. Adv. Technol.* 29, 623–631. doi:10.1002/pat.4172

Cho, K., Kim, H., Jang, S., Kyung, H., Kang, M., Lee, K., et al. (2020). Optimizing electrochemically active surfaces of carbonaceous electrodes for ionogel based supercapacitors. *Adv. Funct. Mat.* 30, 2002053. doi:10.1002/adfm.202002053

Cui, Y., Gong, H., Wang, Y., Li, D., and Bai, H. (2018). A thermally insulating textile inspired by polar bear hair. *Adv. Mat.* 30, e1706807. doi:10.1002/adma.201706807

Demirci, S., Kinali-Demirci, S., and VanVeller, B. (2020). Surface-grafted polymeric ionic liquids with tunable morphology *via* in/*ex situ* cross-linking methods. *ACS Macro Lett.* 9, 1806–1811. doi:10.1021/acsmacrolett.0c00632

Deng, X., Zhang, J., Zhang, L., Cheng, G., Chen, B., Zhang, Y., et al. (2020). Poly(ionic liquid)-coated meshes with opposite wettability for continuous oil/water separation. *Ind. Eng. Chem. Res.* 59, 6672–6680. doi:10.1021/acs.iecr.0c00554

Ding, Y., Zhang, J., Chang, L., Zhang, X., Liu, H., and Jiang, L. (2017). Preparation of high-performance ionogels with excellent transparency, good mechanical strength, and high conductivity. *Adv. Mat.* 29, 1704253–1704259. doi:10.1002/adma.201704253

Dou, H., Xu, M., Wang, B., Zhang, Z., Luo, D., Shi, B., et al. (2021). Analogous mixed matrix membranes with self-assembled interface pathways. *Angew. Chem. Int. Ed.* 60, 5864–5870. doi:10.1002/anie.202014893

Feng, L., Li, S. H., Li, Y. S., Li, H. J., Zhang, L. J., Zhai, J., et al. (2002). Super-hydrophobic surfaces: From natural to artificial. *Adv. Mat.* 14, 1857–1860. doi:10.1002/adma.200290020

Fuller, J., Breda, A. C., and Carlin, R. T. (1997). Ionic liquid-polymer gel electrolytes. *J. Electrochem. Soc.* 144, L67–L70. doi:10.1149/1.1837555

Gomes, J. M., Silva, S. S., and Reis, R. L. (2019). Biocompatible ionic liquids: Fundamental behaviours and applications. *Chem. Soc. Rev.* 48, 4317–4335. doi:10.1039/c9cs00016j

Guo, W., Mahurin, S. M., Unocic, R. R., Luo, H., and Dai, S. (2020). Broadening the gas separation utility of monolayer nanoporous graphene membranes by an ionic liquid gating. *Nano Lett.* 20, 7995–8000. doi:10.1021/acs.nanolett.0c02860

He, B., Du, Y., Wang, B., Wang, X., Ye, Q., and Liu, S. (2021). Grafting embedded poly(ionic liquid) brushes on biomimetic sharklet resin surface for anti-biofouling applications. *Prog. Org. Coat.* 157, 106298–106305. doi:10.1016/j.porgcoat.2021.106298

Hirota, Y., Maeda, Y., Yamamoto, Y., Miyamoto, M., and Nishiyama, N. (2017). Organosilica membrane with ionic liquid properties for separation of toluene/H_2 mixture. *Materials* 10, 901–907. doi:10.3390/ma10080901

Howell, C., Grinthal, A., Sunny, S., Aizenberg, M., and Aizenberg, J. (2018). Designing liquid-infused surfaces for medical applications: A review. *Adv. Mat.* 30, e1802724. doi:10.1002/adma.201802724

Huang, S., Wan, Y., Ming, X., Zhou, J., Zhou, M., Chen, H., et al. (2021). Adhering low surface energy materials without surface pretreatment via ion-dipole interactions. *ACS Appl. Mat. Inter.* 13, 41112–41119. doi:10.1021/acsami.1c11822

Jin, H., Tian, L., Bing, W., Zhao, J., and Ren, L. (2022). Bioinspired marine antifouling coatings: Status, prospects, and future. *Prog. Mat. Sci.* 124, 100889–100941. doi:10.1016/j.pmatsci.2021.100889

Ju, J., Bai, H., Zheng, Y., Zhao, T., Fang, R., and Jiang, L. (2012). A multi-structural and multi-functional integrated fog collection system in cactus. *Nat. Commun.* 3, 1247–1252. doi:10.1038/ncomms2253

Kwon, J. H., Kim, Y. M., and Moon, H. C. (2021). Porous ion gel: A versatile ionotronic sensory platform for high-performance, wearable ionoskins with electrical and optical dual output. *ACS Nano* 15, 15132–15141. doi:10.1021/acsnano.1c05570

Laloyaux, X., Fautre, E., Blin, T., Purohit, V., Leprince, J., Jouenne, T., et al. (2010). Temperature-responsive polymer brushes switching from bactericidal to cell-repellent. *Adv. Mat.* 22, 5024–5028. doi:10.1002/adma.201002538

Lan, J., Li, Y., Yan, B., Yin, C., Ran, R., and Shi, L. Y. (2020). Transparent stretchable dual-network ionogel with temperature tolerance for high-performance flexible strain sensors. *ACS Appl. Mat. Interfaces* 12, 37597–37606. doi:10.1021/acsami.0c10495

Lee, J. I., Choi, H., Kong, S. H., Park, S., Park, D., Kim, J. S., et al. (2021). Visco-poroelastic electrochemiluminescence skin with piezo-ionic effect. *Adv. Mat.* 33, e2100321. doi:10.1002/adma.202100321

Li, D., Fei, X., Wang, K., Xu, L., Wang, Y., Tian, J., et al. (2021). A novel self-healing triple physical cross-linked hydrogel for antibacterial dressing. *J. Mat. Chem. B* 9, 6844–6855. doi:10.1039/d1tb01257f

Li, H., Yan, M., and Zhao, W. (2022). Designing a MOF-based slippery lubricant-infused porous surface with dual functional anti-fouling strategy. *J. Colloid Interface Sci.* 607, 1424–1435. doi:10.1016/j.jcis.2021.09.052

Li, J. L., Zhang, Y., Zhang, S., Liu, M., Li, X., and Cai, T. (2019). Hyperbranched poly(ionic liquid) functionalized poly(ether sulfone) membranes as healable antifouling coatings for osmotic power generation. *J. Mat. Chem. A* 7, 8167–8176. doi:10.1039/c8ta10484k

Liang, C. D., Yuan, C. Y., Warmack, R. J., Barnes, C. E., and Dai, S. (2002). Ionic liquids: A new class of sensing materials for detection of organic vapors based on the use of a quartz crystal microbalance. *Anal. Chem.* 74, 2172–2176. doi:10.1021/ac011007h

Liu, H., Xie, J., Zhao, J., Xue, P., Lv, X., and Sun, S. (2022). Hydrophilic ionic-liquid grafted poly(vinylidene fluoride) membranes with excellent cationic dye and oil-water emulsion removal performance. *J. Mat. Sci.* 57, 4876–4894. doi:10.1007/s10853-022-06911-8

Liu, L., Xiong, S., Zeng, L., Cai, C., Li, F., and Tan, Z. (2021). Two birds with one stone: Porous poly(ionic liquids) membrane with high efficiency for the separation of amino acids mixture and its antibacterial properties. *J. Colloid Interface Sci.* 584, 866–874. doi:10.1016/j.jcis.2020.10.018

Liu, Y., Wang, W., Gu, K., Yao, J., Shao, Z., and Chen, X. (2021). Poly(vinyl alcohol) hydrogels with integrated toughness, conductivity, and freezing tolerance based on ionic liquid/water binary solvent systems. *ACS Appl. Mat. Interfaces* 13, 29008–29020. doi:10.1021/acsami.1c09006

Lu, J., Yan, F., and Texter, J. (2009). Advanced applications of ionic liquids in polymer science. *Prog. Polym. Sci.* 34, 431–448. doi:10.1016/j.progpolymsci.2008.12.001

Lyu, Q., Wang, S., Peng, B., Chen, X., Du, S., Li, M., et al. (2021). Bioinspired photonic ionogels as interactively visual ionic skin with optical and electrical synergy. *Small* 17, e2103271. doi:10.1002/smll.202103271

Mantravadi, R., Chinnam, P. R., Dikin, D. A., and Wunder, S. L. (2016). High conductivity, high strength solid electrolytes formed by *in situ* encapsulation of ionic liquids in nanofibrillar methyl cellulose networks. *ACS Appl. Mat. Interfaces* 8, 13426–13436. doi:10.1021/acsami.6b02903

Men, Y., Drechsler, M., and Yuan, J. (2013). Double-stimuli-responsive spherical polymer brushes with a poly(ionic liquid) core and a thermoresponsive shell. *Macromol. Rapid Commun.* 34, 1721–1727. doi:10.1002/marc.201300628

Meng, J., and Wang, S. (2019). Advanced antiscaling interfacial materials toward highly efficient heat energy transfer. *Adv. Funct. Mat.* 30, 1904796–1904813. doi:10.1002/adfm.201904796

Muldoon, M., and Gordon, C. (2004). Synthesis of gel-type polymer beads from ionic liquid monomers. *Sci. Pol. Chem.* 42, 3865–3869. doi:10.1002/pola.20299

Njoroge, I., Matson, M. W., and Jennings, G. K. (2017). Dynamic anion-adaptive poly(ionic liquid) films via surface-initiated ring-opening metathesis polymerization. *J. Phys. Chem. C* 121, 20323–20334. doi:10.1021/acs.jpcc.7b05834

Noble, R. D., Gin, D. L., and Gin, D. L. (2011). Perspective on ionic liquids and ionic liquid membranes. *J. Membr. Sci.* 369, 1–4. doi:10.1016/j.memsci.2010.11.075

Ohno, H. (2007). Design of ion conductive polymers based on ionic liquids. *Macromol. Symp.* 249, 551–556. doi:10.1002/masy.200750435

Peppou-Chapman, S., Hong, J. K., Waterhouse, A., and Neto, C. (2020). Life and death of liquid-infused surfaces: A review on the choice, analysis and fate of the infused liquid layer. *Chem. Soc. Rev.* 49, 3688–3715. doi:10.1039/d0cs00036a

Qin, J., Guo, J., Xu, Q., Zheng, Z., Mao, H., and Yan, F. (2017). Synthesis of pyrrolidinium-type poly(ionic liquid) membranes for antibacterial applications. *ACS Appl. Mat. Interfaces* 9, 10504–10511. doi:10.1021/acsami.7b00387

Rao, Q., Li, A., Zhang, J., Jiang, J., Zhang, Q., Zhan, X., et al. (2019). Multi-functional fluorinated ionic liquid infused slippery surfaces with dual-responsive wettability switching and self-repairing. *J. Mat. Chem. A* 7, 2172–2183. doi:10.1039/c8ta08956f

Ren, Y., Guo, J., Liu, Z., Sun, Z., Wu, Y., Liu, L., et al. (2019). Ionic liquid–based click-ionogels. *Sci. Adv.* 5, eaax0648. doi:10.1126/sciadv.aax0648

Rynkowska, E., Dzieszkowski, K., Lancien, A., Fatyeyeva, K., Szymczyk, A., Kujawa, J., et al. (2017). Physicochemical properties and pervaporation performance of dense membranes based on cellulose acetate propionate (CAP) and containing polymerizable ionic liquid (PIL). *J. Membr. Sci.* 544, 243–251. doi:10.1016/j.memsci.2017.09.031

Salbaum, T., Galvan, Y., Haumann, M., Wasserscheid, P., Zarraga, R., and Vogel, N. (2021). Enduring liquid repellency through slippery ionic liquid-infused organogels. *J. Mat. Chem. A* 9, 2357–2366. doi:10.1039/d0ta10237g

Sasikumar, B., Arthanareeswaran, G., and Ismail, A. F. (2018). Recent progress in ionic liquid membranes for gas separation. *J. Mol. Liq.* 266, 330–341. doi:10.1016/j.molliq.2018.06.081

Saul, A., Barker, R., Baraka-Lokmane, S., Le Beulze, A., Charpentier, T., Tangparitkul, S., et al. (2021). Corrosion derived lubricant infused surfaces on X65 carbon steel for improved inorganic scaling performance. *J. Adhes. Sci. Technol.* 36, 632–722. doi:10.1080/01694243.2021.1932315

Singh, G., Singh, G., Damarla, K., Sharma, P. K., Kumar, A., and Kang, T. S. (2017). Gelatin-based highly stretchable, self-healing, conducting, multiadhesive, and antimicrobial ionogels embedded with Ag_2O nanoparticles. *ACS Sustain. Chem. Eng.* 5, 6568–6577. doi:10.1021/acssuschemeng.7b00719

Smith, J. D., Dhiman, R., Anand, S., Reza-Garduno, E., Cohen, R. E., McKinley, G. H., et al. (2013). Droplet mobility on lubricant-impregnated surfaces. *Soft Matter* 9, 1772–1780. doi:10.1039/c2sm27032c

Sprugis, E., Vaivars, G., and Merijs Meri, R. (2019). A study of mechanical properties of polymer composite membranes with various ionic liquids at elevated temperatures. *Mat. Sci.* 25, 66–70. doi:10.5755/j01.ms.25.1.18933

Sun, N., Sun, P., Wu, A., Qiao, X., Lu, F., and Zheng, L. (2018). Facile fabrication of thermo/redox responsive hydrogels based on a dual crosslinked matrix for a smart on-off switch. *Soft Matter* 14, 4327–4334. doi:10.1039/c8sm00504d

Wang, K., Wang, J., Li, L., Xu, L., Feng, N., Wang, Y., et al. (2020). Novel nonreleasing antibacterial hydrogel dressing by a one-pot method. *ACS Biomater. Sci. Eng.* 6, 1259–1268. doi:10.1021/acsbiomaterials.9b01812

Wang, X., Gu, C., Wang, L., Zhang, J., and Tu, J. (2018). Ionic liquids-infused slippery surfaces for condensation and hot water repellency. *Chem. Eng. J.* 343, 561–571. doi:10.1016/j.cej.2018.03.045

Wang, Z., Cui, H., Liu, M., Grage, S. L., Hoffmann, M., Sedghamiz, E., et al. (2022). Tough, transparent, 3D-printable, and self-healing poly(ethylene glycol)-gel (PEGgel). *Adv. Mat.* 34, e2107791–e2107804. doi:10.1002/adma.202107791

Wang, Z., Liu, Y., Guo, P., Heng, L., and Jiang, L. (2018). Photoelectric synergetic responsive slippery surfaces based on tailored anisotropic films generated by interfacial directional freezing. *Adv. Funct. Mat.* 28, 1801310–1801319. doi:10.1002/adfm.201801310

Washiro, S., Yoshizawa, M., Nakajima, H., and Ohno, H. (2004). Highly ion conductive flexible films composed of network polymers based on polymerizable ionic liquids. *Polymer* 45, 1577–1582. doi:10.1016/j.polymer.2004.01.003

Wei, R., Guo, J., Jin, L., He, C., Xie, Y., Zhang, X., et al. (2020). Vapor induced phase separation towards anion-/near-infrared-responsive pore channels for switchable anti-fouling membranes. *J. Mat. Chem.* 8, 8934–8948. doi:10.1039/d0ta02154g

Wei, R., Yang, B., He, C., Jin, L., Zhang, X., and Zhao, C. (2022). Versatile and robust poly(ionic liquid) coatings with intelligent superhydrophilicity/superhydrophobicity switch in high-efficient oil-water separation. *Sep. Purif. Technol.* 282, 120100–120113. doi:10.1016/j.seppur.2021.120100

Wei, R., Yang, F., Gu, R., Liu, Q., Zhou, J., Zhang, X., et al. (2018). Design of robust thermal and anion dual-responsive membranes with switchable response temperature. *ACS Appl. Mat. Interfaces* 10, 36443–36455. doi:10.1021/acsami.8b12887

Wu, X., Surendran, A., Moser, M., Chen, S., Muhammad, B. T., Maria, I. P., et al. (2020). Universal spray-deposition process for scalable, high-performance, and stable organic electrochemical transistors. *ACS Appl. Mat. Interfaces* 12, 20757–20764. doi:10.1021/acsami.0c04776

Xu, L., Huang, Z., Deng, Z., Du, Z., Sun, T. L., Guo, Z. H., et al. (2021). A transparent, highly stretchable, solvent-resistant, recyclable multifunctional ionogel with underwater self-healing and adhesion for reliable strain sensors. *Adv. Mat.* 33, e2105306. doi:10.1002/adma.202105306

Yang, W., He, X., Gao, J., Guo, H., He, X., Wan, F., et al. (2010). Synthesis, characterization, and tunable wettability of poly(ionic liquid) brushes via nitroxide-mediated radical polymerization (NMP). *Chin. Sci. Bull.* 55, 3562–3568. doi:10.1007/s11434-010-3288-z

Yang, Z., Huang, R., Zheng, B., Guo, W., Li, C., He, W., et al. (2021). Highly stretchable, adhesive, biocompatible, and antibacterial hydrogel dressings for wound healing. *Adv. Sci.* 8, 2003627–2003638. doi:10.1002/advs.202003627

Yao, X., Zhang, S., Qian, L., Wei, N., Nica, V., Coseri, S., et al. (2022). Super stretchable, self-healing, adhesive ionic conductive hydrogels based on tailor-made ionic liquid for high-performance strain sensors. *Adv. Funct. Mat.* 32, 2204565. doi:10.1002/adfm.202204565

Ye, L., Chen, F., Liu, J., Gao, A., Kircher, G., Liu, W., et al. (2019). Responsive ionogel surface with renewable antibiofouling properties. *Macromol. Rapid Commun.* 40, e1900395. doi:10.1002/marc.201900395

Ye, Q., Gao, T., Wan, F., Yu, B., Pei, X., Zhou, F., et al. (2012). Grafting poly(ionic liquid) brushes for anti-bacterial and anti-biofouling applications. *J. Mat. Chem.* 22, 13123–13131. doi:10.1039/c2jm31527k

Yu, Y., Yang, Z., Ren, S., Gao, Y., and Zheng, L. (2020). Multifunctional hydrogel based on ionic liquid with antibacterial performance. *J. Mol. Liq.* 299, 112185–112192. doi:10.1016/j.molliq.2019.112185

Yu, Z., and Wu, P. (2021). Underwater communication and optical camouflage ionogels. *Adv. Mat.* 33, e2008479. doi:10.1002/adma.202008479

Zgrzeba, A., Andrzejewska, E., and Marcinkowska, A. (2015). Ionic liquid-containing ionogels by thiol–ene photopolymerization. Kinetics and solvent effect. *RSC Adv.* 5, 100354–100361. doi:10.1039/c5ra21254e

Zhang, J., Chen, Z., Zhang, Y., Dong, S., Chen, Y., and Zhang, S. (2021). Poly(ionic liquid)s containing alkoxy chains and bis(trifluoromethanesulfonyl)imide anions as highly adhesive materials. *Adv. Mat.* 33, e2100962. doi:10.1002/adma.202100962

Zhang, J., Shen, B., Chen, L., Chen, L., Mo, J., and Feng, J. (2019). Antibacterial and antifouling hybrid ionic-covalent hydrogels with tunable mechanical properties. *ACS Appl. Mat. Interfaces* 11, 31594–31604. doi:10.1021/acsami.9b08870

Zhang, J., Zhang, W., Guo, J., Yuan, C., and Yan, F. (2015). Ultrahigh ionic liquid content supramolecular ionogels for quasi-solid-state dye sensitized solar cells. *Electrochim. Acta* 165, 98–104. doi:10.1016/j.electacta.2015.02.244

Zhang, X., Chen, Q., Wei, R., Jin, L., He, C., Zhao, W., et al. (2020). Design of poly ionic liquids modified cotton fabric with ion species-triggered bidirectional oil-water separation performance. *J. Hazard. Mat.* 400, 123163–123178. doi:10.1016/j.jhazmat.2020.123163

Zhang, Y., Yuan, B., Zhang, Y., Cao, Q., Yang, C., Li, Y., et al. (2020). Biomimetic lignin/poly(ionic liquids) composite hydrogel dressing with excellent mechanical strength, self-healing properties, and reusability. *Chem. Eng. J.* 400, 125984–125993. doi:10.1016/j.cej.2020.125984

Zhao, W., Ye, Q., Hu, H., Wang, X., and Zhou, F. (2015). Fabrication of binary components based on a poly(ionic liquid) through "grafting" and "clicking" and their synergistic antifouling activity. *RSC Adv.* 5, 100347–100353. doi:10.1039/c5ra23391g

Zhao, W., Ye, Q., Hu, H., Wang, X., and Zhou, F. (2014). Grafting zwitterionic polymer brushes via electrochemical surface-initiated atomic-transfer radical polymerization for anti-fouling applications. *J. Mat. Chem. B* 2, 5352–5357. doi:10.1039/c4tb00816b

Zheng, L., Li, J., Yu, M., Jia, W., Duan, S., Cao, D., et al. (2020). Molecular sizes and antibacterial performance relationships of flexible ionic liquid derivatives. *J. Am. Chem. Soc.* 142, 20257–20269. doi:10.1021/jacs.0c10771

Zhuo, Y., Xiao, S., Håkonsen, V., He, J., and Zhang, Z. (2020). Anti-icing ionogel surfaces: Inhibiting ice nucleation, growth, and adhesion. *ACS Mat. Lett.* 2, 616–623. doi:10.1021/acsmaterialslett.0c00094

frontiers | Frontiers in Bioengineering and Biotechnology

TYPE Original Research
PUBLISHED 03 February 2023
DOI 10.3389/fbioe.2023.1142095

OPEN ACCESS

EDITED BY
Pengchao Zhang,
Wuhan University of Technology, China

REVIEWED BY
Xueliang Huang,
Hunan Normal University, China
Pangkuan Chen,
Beijing Institute of Technology, China

*CORRESPONDENCE
Zhenyu Pan,
zn000382@whu.edu.cn
Aixi Yu,
yuaixi@whu.edu.cn

†These authors have contributed equally to this work

SPECIALTY SECTION
This article was submitted to Biomaterials, a section of the journal Frontiers in Bioengineering and Biotechnology

RECEIVED 11 January 2023
ACCEPTED 26 January 2023
PUBLISHED 03 February 2023

CITATION
Liu Q, Liu C, Wang W, Yuan L, Wang Y, Yi X, Pan Z and Yu A (2023), Bioinspired strontium magnesium phosphate cement prepared utilizing the precursor method for bone tissue engineering.
Front. Bioeng. Biotechnol. 11:1142095.
doi: 10.3389/fbioe.2023.1142095

Bioinspired strontium magnesium phosphate cement prepared utilizing the precursor method for bone tissue engineering

Qiaoyun Liu[1†], Changjiang Liu[1†], Weixing Wang[1], Liangjie Yuan[2], Yu Wang[1,3], Xinzeyu Yi[1], Zhenyu Pan[1*] and Aixi Yu[1*]

[1]Department of Orthopedics Trauma and Microsurgery, Zhongnan Hospital of Wuhan University, Wuhan, Hubei, China, [2]College of Chemistry and Molecular Sciences, Wuhan University, Wuhan, Hubei, China, [3]16th Department, Plastic Surgery Hospital, Chinese Academy of Medical Sciences, Peking Union Medical College, Beijing, China

Bioinspired strontium magnesium phosphate cements for bone tissue engineering were prepared using a new, facile, environmentally friendly and high yielding (98.5%) precursor method. The bioinspired SMPCs have uniform particle distributions, excellent mechanical strengths and high biocompatibilities. The *in vitro* responses of bone marrow stromal cells to the SMPCs, including viability, osteogenic differentiation and alkaline phosphatase activity, were evaluated. The results show that the SMPC containing 0.5 mol of strontium (referred to as SMPC-2) has a higher degradation rate and biological activity than magnesium phosphate cements and the other SMPCs. In addition, the synergistic effect of strontium and magnesium ion release from SMPC-2 creates a conducive environment for cell proliferation, mineralized calcium deposition and new bone formation. These observations demonstrate the feasibility of using the new precursor method to generate SMPCs and the utility of these biologically compatible and highly effective cements for bone tissue engineering.

KEYWORDS

bioinspired, precursor method, strontium magnesium phosphate, bone tissue engineering, biological activity

1 Introduction

Most of bone defects caused by trauma and tumor do not readily heal, and as a result, formation of bone non-union occurs (Dabiri et al., 2019). An effective method to rapidly restore the physiological function of defective bone tissue involves the use of appropriate bone graft materials (Pina et al., 2015; Nabiyouni et al., 2018). Inspired by the unique components of natural bones, magnesium phosphate cement (MPC) has been developed as a promising material for bone tissue engineering owing to its high mechanical strength, rapid curing propensity and good degradability (Babaie et al., 2017; Kanter et al., 2018; Yang et al., 2019). However, MPC is usually prepared by traditional methods involving hydration reactions of magnesium oxide and phosphate salts. A cement formed in this manner typically has a very short setting time and poor biocompatibility (Qiao et al., 2012). Consequently, methods for preparation of MPC that have practical clinical applications need to be devised. In one effort aimed at this goal, Yu et al. observed that the compressive strength of MPC rolled (23–58 MPa) and setting time (12–16 min) can be controlled by including $Ca(H_2PO_4)_2{\cdot}H_2O$ in the reaction mixture (Yu et al., 2019). Also, Wang et al. observed that the injectability and biocompatibility of MPC can be regulated by addition of citric acid (Wang et al., 2019). Moreover, Zhao et al.

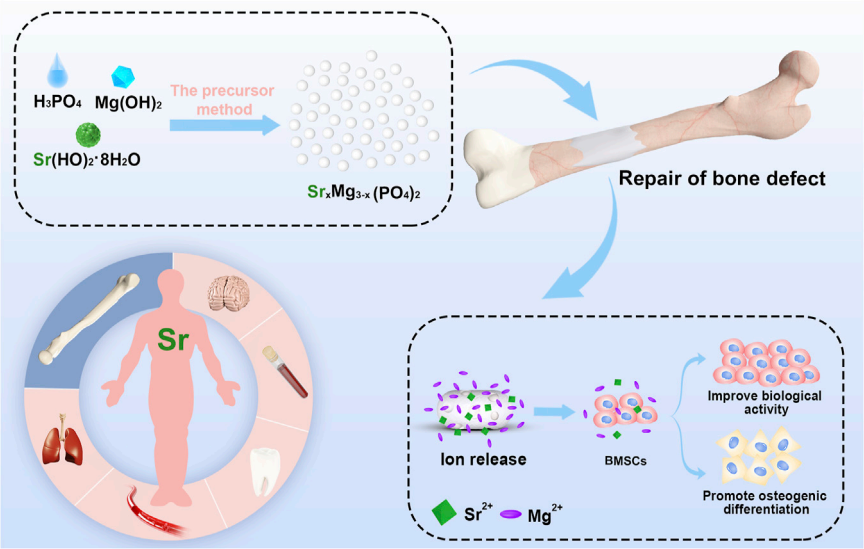

GRAPHICAL ABSTRACT

found that inclusion of gelatin microspheres (GM) and $Ca(H_2PO_4)_2{\cdot}H_2O$ improves the physicochemical, biodegradation and biocompatibility properties of MPC (Zhao et al., 2021).

Strontium (Sr) and magnesium belong to the alkaline earth metal family. As a trace element in human body, Sr not only promotes absorption of mineralized bone tissue by osteoclasts, it also causes an increase in the number of osteoblasts and induces osteoblasts to form bone matrix that leads to mineralized bone tissue generation (Arepalli et al., 2016; Liu et al., 2016; Kargozar et al., 2017). Early studies have shown that strontium has a dose-dependent effect on bone, which at certain dose levels can be beneficial to bones. Schorr et al. found that strontium promotes an increase of vertebral bone mass in patients with osteoporosis (Shorr and Carter, 1952). However, when strontium concentrations exceed the ideal levels, an adverse effect can take place on mineralization in the bone reconstruction process. For example, using histological and radiological methods, Matsunoto et al. found that administration of high-doses of strontium to rat tibia delays bone growth and the rate of endochondral ossification lysis (Matsumoto, 1976).

Based on these observations, it is reasonable to expect that by adding an appropriate amount of strontium the osteogenesis and repair of bone defects by MPC would be improved. At present, limited numbers of research efforts have focused on the bone repair properties of strontium doped MPCs and their clinical applications. In one investigation, He et al. observed that strontium modified magnesium phosphate bioceramics can be fabricated by employing a high-temperature (1,200°C) solid-state method and confirmed that this bone repair material inhibits the formation of osteoclasts (He et al., 2019). However, the material synthesized in this way had a fixed shape so that it was only suitable for repairing defects in bones having the same shape.

In the current study, a precursor method was developed for large scale synthesis of bioinspired strontium doped magnesium phosphate cement (SMPC) for use in bone tissue engineering. This method is widely used in the preparation of materials for lithium-ion batteries because it is both green and controllable (Xie et al., 2019; Liu et al., 2021). The precursor (P-SMP) used in this approach is generated by mixing magnesium hydroxide, strontium hydroxide with phosphoric acid. P-SMP has small particle sizes, uniformly distributed components, a large surface energy, and high activity and biocompatibility. The precursor method, which involves heating the P-SMPs to 800°C followed by mixing the formed strontium doped magnesium phosphates (SMPs) with KH_2PO_4 and MgO. Preparation of the cements has a low energy consumption and high yield, both of which make it suitable for large-scale synthesis. In addition, the SPMCs generated in this manner have a suitable setting time at room temperature and they can be arbitrarily shaped to meet the varying needs of bone defect patients. In addition, effects of using different amounts of Sr on the properties of the SMPCs were explored and a survey was made of key biological properties of this cement. The results of this investigation should promote interest in practical use of SMPC in bone repair engineering.

2 Materials and methods

2.1 Materials

$Mg(OH)_2$ (AR) and $Sr(OH)_2{\cdot}8H_2O$ (AR) were purchased from Aladdin Inc., China. H_3PO_4 (AR, ≥85 wt%.), $(MgCO_3)_4{\cdot}Mg(OH)_2{\cdot}5H_2O$ (AR) and KH_2PO_4 (AR) were purchased from Sinopharm Chemical Reagent Co., Ltd. All chemicals were used as received.

2.2 Preparation of bioinspired MPC and SMPCs

2.2.1 Preparation of the precursors P-MP and P-SMPs

To 800 g of stirred water (200 rpm) was added 174 g of $Mg(OH)_2$. After stirring for about 5 min the magnesium hydroxide became evenly dispersed in the water. Following

TABLE 1 Contents of MP and SMP.

Sample	Content of Sr/moL	Composition	Theoretical weight/g	Yield/g	% yield
MP	0	$Mg_3(PO_4)_2$	262.86	259.65	98.78
SMP-1	0.25	$Mg_{2.75}Sr_{0.25}(PO_4)_2$	278.69	274.87	98.63
SMP-2	0.5	$Mg_{2.5}Sr_{0.5}(PO_4)_2$	294.55	290.74	98.71
SMP-3	0.75	$Mg_{2.25}Sr_{0.75}(PO_4)_2$	310.34	307.31	99.02
SMP-4	1.0	$Mg_2Sr(PO_4)_2$	326.17	321.29	98.50

increasing the stirring speed to 300 rpm, 230.6 g of H_3PO_4 was added dropwise to the solution over a 10 min period. Stirring was continued for 10 min, at which time the pH of the solution was 7.5. The formed solid was separated by filtration and the formed filter cake was dried for 10 h at 100°C to give the precursor P-MP. The same procedure was utilized to prepare the Sr containing precursors P-SMP-1, P-SMP-2, P-SMP-3 and P-SMP-4 with the exception that 0.25, 0.5, 0.75 and 1.0 mol, respectively, of $Sr(OH)_2{\cdot}8H_2O$ were used in place of $Mg(OH)_2$.

2.2.2 Preparation of MP and SMPs

P-MP was heated in a muffle furnace to 800°C at a rate of 3°C/min and then at 800°C for 2 h to yield MP. The SMPs, SMP-1, SMP-2, SMP-3 and SMP-4 were generated using the same heat treatment method. The contents of these materials are given in Table 1.

2.2.3 Preparation of bioinspired MPC and SMPCs

MgO was generated by sintering magnesium carbonate ($(MgCO_3)_4{\cdot}Mg(OH)_2{\cdot}5H_2O$) at 800°C for 2 h. MP or the SMPs, KH_2PO_4 and MgO were mixed in the mass ratio of 2.62:4.08: 0.80 at room temperature. Addition of deionized water in the mass ratio of 1.5:1 and standing for 2 min led to production of MPC or the SMPCs. Cylindrical samples of these materials, obtained letting each cement to stand in a polytetrafluoroethylene cylindrical mold (6 mm diameter, 12 mm height) for 7 d at 37°C and 100% humidity, were subjected to strength tests. Cements with dimensions of 6 mm diameter and 2 mm height were subjected to disinfection under high temperature and pressure, and then used to assess cell viability, *in vitro* degradation performance, alkaline phosphatase (ALP) activity, and for alizarin Red S and cell living/death staining.

2.3 Characterization

All materials prepared in this effort were analyzed using thermogravimetry (TG) with a Netzsch STA449 thermal analyzer (Netzsch, Germany) at a heating rate of 10°C/min in flowing air. P-MP, P-SMP, MP, SMP, MPC and SMPC were also studied using X-ray diffractometry (XRD), to identify their crystalline phases. XRD measurements were carried out using a Rigaku Miniflex600 diffractometer (Rigaku, Japan) with Cu Ka radiation (k = 1.54178 Å) at a scanning rate of 6°/min. Registrations were performed in the 10°–80°, 2(θ) range. To determine morphologies, and particle sizes and distributions, scanning election microscope (SEM) images were recorded using a JSM-6510 scanning election microscope (JEOL, Japan).

2.4 Setting time and compressive strength

The setting time was measured using a Vicat instrument, which was defined as the time taken before the needle cannot penetrate the sample by 1 mm. Compressive strengths of the materials were measured at a loading rate of 1 mm/min using a universal testing machine (Instron 5,967, United States) according to BS EN 12390–3:2009 (British Standard Institution, 2009). Five replicates of each measurement were made.

2.5 pH variation and cement degradation

In triplicate measurements, the initial weights (W_0, based on solid/liquid mass ratio of 0.2 g/g) of disc samples of each material were recorded and then each disc is immersed in oscillating (100 rpm) Tris HCl buffer (pH = 7.4) at 37°C. Tris HCl buffer was refreshed once a day in the first week and once a week later. Disc samples were removed on the 1st, 3rd, 7th, 14th, 21st and 28th day, and the pH of the Tris HCl buffer was determined (FE-28, Mettler, China). The removed disc samples were rinsed with deionized water, dried at 80°C for 2 h, and then weighed (W_t). Percent weight loss was calculated using following Eq. 1.

$$\text{Weight loss } (\%) = \frac{W_0 - W_t}{W_0} \times 100\% \quad (1)$$

2.6 $Mg^{2+}$and Sr^{2+} release

In triplicate experiments, discs in Tris HCl buffer, produced in the above manner, were removed on the 1st, 3rd, 7th, 14th, 21st and 28th d to give remaining clear liquids whose Mg^{2+} and Sr^{2+} concentrations were determined using inductively coupled plasma mass spectrometery (QP-MS, Jena AG, Germany).

2.7 Extract solutions and cell culture

Each disc sample was placed in complete medium (from Procell). The resulting system was oscillated at 100 rpm and 37°C for 24 h (Wang et al., 2019). The complete medium (referred to as extracted complete medium) was collected for later cell culture experiments. In a separate experiment, complete medium containing the discs were replaced by osteogenic inducing medium, the extracted osteogenic inducing

medium (extracted OIM) was used to study osteogenic induced differentiation.

Rat mesenchymal bone marrow stem cells (BMSCs) (from Procell) were cultured under 5% CO_2 in complete medium at 37°C. The extracted complete medium was replaced every third day. In the study of osteogenic differentiation, after the BMSCs culturing at 37°C under 5% CO_2 for 1 d, complete medium was replaced by extracted complete medium. When the density of the BMSCs reached 90%, the complete medium was replaced by extracted OIM which renewed every third day.

2.8 Cytotoxicity analysis

The *in vitro* cytotoxicity of disc samples of each material was evaluated in quintuplicate using a CCK-8 assay. BMSCs in complete medium were seeded in 96 well plates at a density of 1×10^5 cells/well, and then cultured at 37°C under 5% CO_2 for 1 d. Complete medium was replaced by extracted complete medium and complete medium was used as control. After culturing for 1, 3 and 5 d, extracted complete medium in each well was removed and replaced by 90 μL complete culture medium containing 10 μL CCK-8 reagent. After 2 h incubation, the optical density (OD) at 450 nm in each well was determined using a microplate reader (FC, ThermoFisher, United States). Cell viability was calculated using the following Eq. 2.

$$\text{Cell viability (\%)} = \frac{\text{OD (dose)} - \text{OD (blank)}}{\text{OD (0 dose)} - \text{OD (blank)}} \times 100\% \quad (2)$$

2.9 Live/dead cell ratio

BMSCs in complete medium were seeded in 24 well plates at a density of 5×10^5 cells/well, and then cultured at 37°C with 5% CO_2 for 1 d. Complete medium was replaced by extracted complete medium and then after 5 d the extracted complete culture medium was removed. According to the procedure provided by the kit manufacturer, 150 μL of a solution of 4′,6-diamidino-2-phenylindole (dead cells: red fluorescence light) and calcein acetoxymethyl ester (live cells: green fluorescence light) was added to each well, which were incubated for 30 min. Distributions of live/dead cells were determined by using a fluorescence microscope (ICX41, SOPTOP, China).

2.10 Alkaline phosphatase activity

The activity of alkaline phosphatase (ALP) was analyzed determined using the Alkaline Phosphatase Assay Kit (Beyotime, China). BMSCs in complete medium were seeded in 24 well plates at a density of 5×10^5 cells/well and then cultured at 37°C with 5% CO_2 for 1 d. Complete medium was replaced by extracted OIM, which was removed after BMSCs culturing for 7 and 14 d. According to the procedure provided by the kit's manufacturer, 50 μL western and IP cell lysate was added to each well for 1–2 min. The lysates were mixed with *p*-nitrophenyl phosphate (PNPP) and incubated for 30 min. Optical densities (OD) at 405 nm were determined using a microplate reader (FC, ThermoFisher, United States).

2.11 Alizarin red S staining

BMSCs in complete medium were seeded in 24 well plates at a density of 5×10^5 cells/well, and then cultured at 37°C with 5% CO_2 for 1 d. Complete medium was replaced by extracted OIM. After 14 and 28 d, extracted OIM was removed, and the cells were treated with 4% neutral formaldehyde for 30 min, placed in an Alizarin red staining solution for 30 min and washed twice with PBS. Analysis of the stained cells was accomplished using a microscope (ICX41, SOPTOP, China).

2.12 Statistical analysis

All data is presented as means ± standard deviation. Data from each group were analyzed by using GraphPad Prism eight statistical software using one-way analysis of variance (ANOVA). When *p*-value <0.05, the data were considered had statistical difference.

3 Results and discussion

3.1 Synthesis and characterization

Analysis of the XRD patterns (Figure 1A) shows that the major components in P-MP and P-SMP is $Mg_3(PO_4)_2{\cdot}5H_2O$ (PDF# 35–0329), and that as the amount of strontium in the P-SMPs increases the degree of crystallinity becomes lower. Also, the presence of strontium does not affect the crystalline phases of the P-SMPs, likely because at room temperature used for their preparation strontium exists as an amorphous substance.

In Figure 1B are displayed TG curves of P-MP and P-SMP-4. The weight loss profiles of these precursors are similar and that thermal decomposition of these materials takes place in two steps. The first step, corresponding to about a 15% weight loss, occurs from 25°C to 200°C, which is associated with volatilization of water from $Mg_3(PO_4)_2{\cdot}5H_2O$. The second step takes place from 200°C to 550°C and it corresponds to respective weight losses form P-MP and P-SMP-4 of about 11% and 8%. This step is associated with decomposition of the amorphous component in each precursor. No weight changes occur above 550°C as is expected for the produced MP and SMP. Based on these results, combustion temperatures of above 200°C, can possibly be used for the heat treatment of P-MP and P-SMP. Considering other factors including compressive strength and setting time, 800°C for 2 h is preferrable for generating MP and SMP from the respective precursors.

X-ray diffraction analysis was performed to investigate the effects of strontium on the crystalline phases of the SMPs (Figure 1C). The pattern of pristine MP is completely consistent with the one in the database for $Mg_3(PO_4)_2$ (PDF# 35–0329). As the content of Sr in the SMPs.

Increases, the XRD pattern begins to increasingly include peaks associated with $SrMg_2(PO_4)_2$ (PDF# 52–1,590). In addition, no other impurity peaks derived from impurities are present in the XRD patterns. The results demonstrate that MP and the SMPs, prepared using the precursor method, have high crystallinities and purities. In

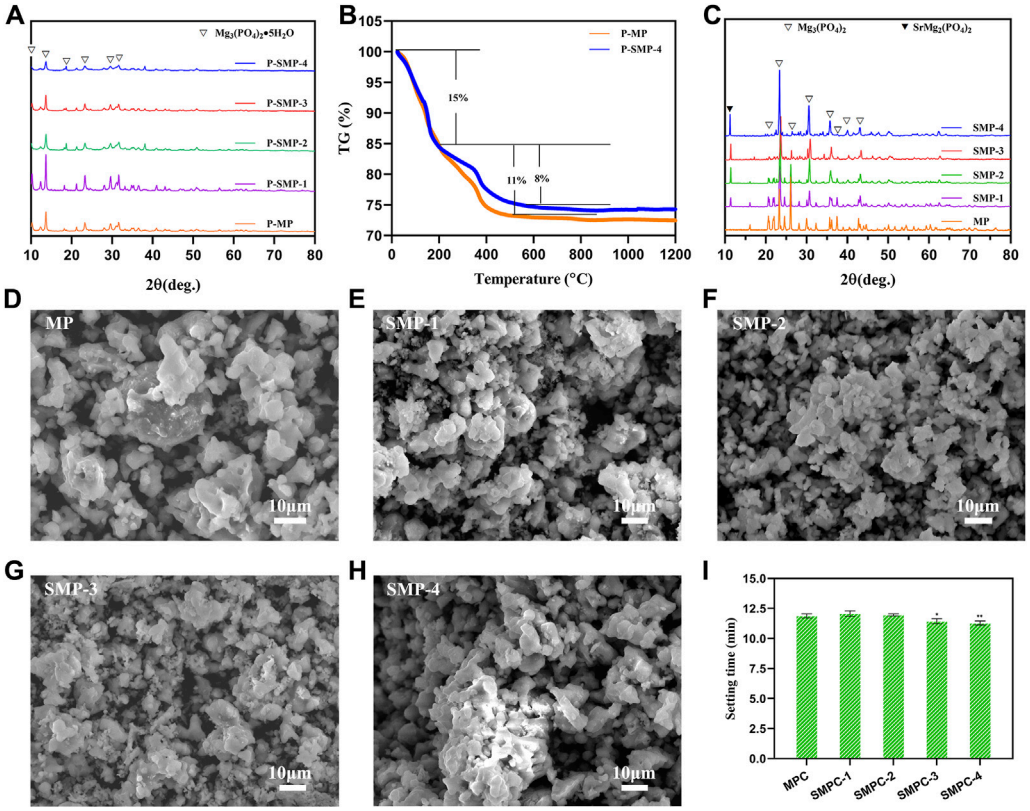

FIGURE 1
Materials characterization. **(A)** The XRD patterns of precursor P-MP and the P-SMPs. **(B)** TG curves of P-MP and P-SMP-4. **(C)** XRD patterns of MP and SMP. **(D–H)** SEM morphologies of the MP and the SMPs. **(I)** Setting time of the cements MPC and the SMPCs; the data are presented as mean ± SD (*p <0.05; **p <0.01; vs. MPC).

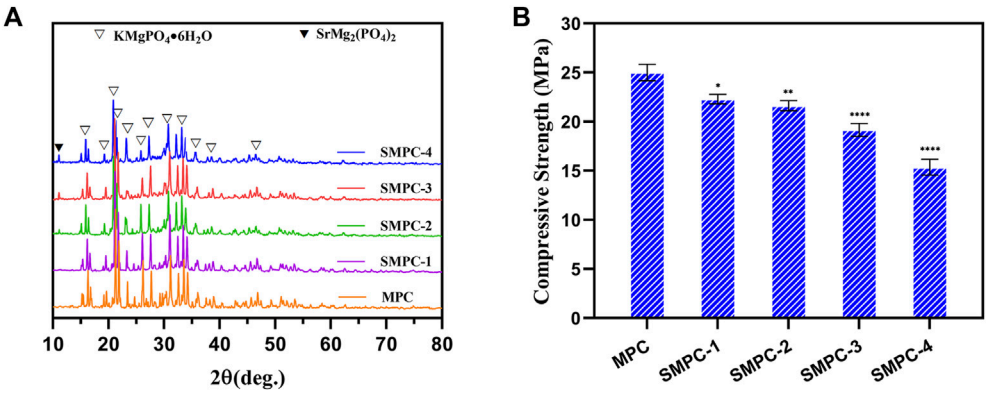

FIGURE 2
(A) XRD patterns of the MPC and SMPCs. **(B)** Compressive strength of the cements MPC and the SMPCs; the data are presented as mean ± SD (*p <0.05; **p <0.01; ****p <0.0001; vs. MPC).

addition, the precursor method is simple, environmentally friendly, and high yielding (98.50%–99.02%) (Table 1).

The morphologies of MP and the SMPs were assessed using scanning electron microscopy (Figures 1D–H). The results show that the basic morphology of MP remains unchanged when strontium is included, but increases in Sr content leads to creation of more uniformly distributed small particles with sizes less than 4 μm. In particular, the particle distribution in SMP-2 is more uniform, and 50% of the particles have sizes less than 2 μm, which may be conducive to the release of Sr^{2+} during the *in vitro* degradation (Arepalli et al., 2016). The setting time of the cements, MPC and the SMPCs was measured (Figure 1I). The results show that the setting time of MP is

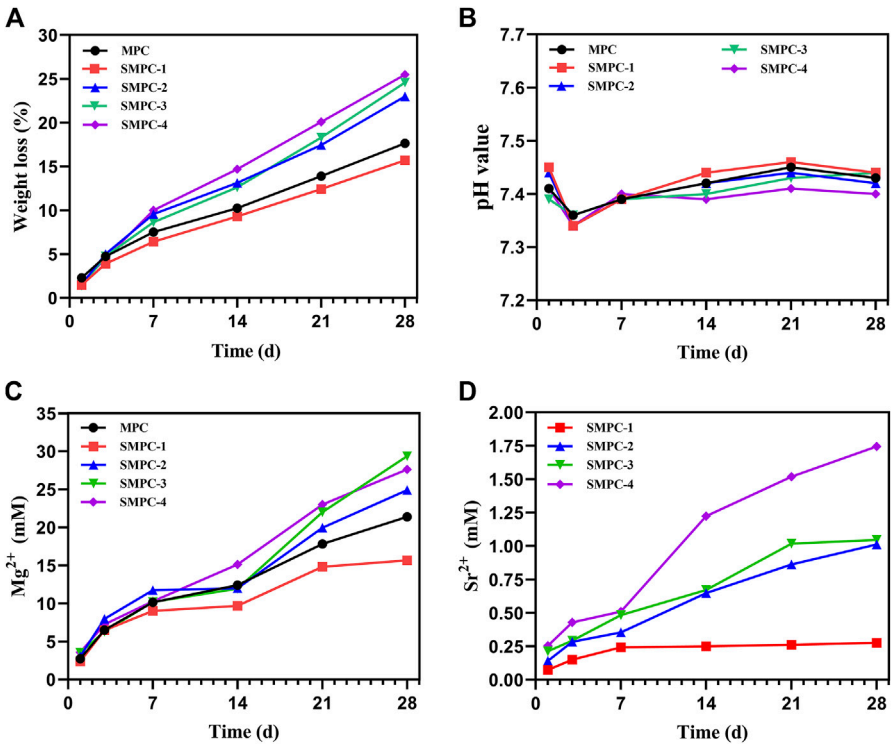

FIGURE 3
In vitro degradation propensities of MPC and the SMPCs soaking in Tris HCl (pH = 7.4) buffer: **(A)** Weight loss of the MCP and SMPC cements. **(B)** The pH of the MCP and SMPCs. **(C)** Mg^{2+} cumulative content released from MCP and SMPCs. **(D)** Sr^{2+} cumulative content released from SMPCs.

about 12.08 min, and that the setting time of SMPCs decreased slightly with Sr content, but the difference was not significant. The setting time of MPC and SMPCs ranged from 11.23 min to 12.08 min, meeting the requirement of clinical bone repair materials for setting time of 8–15 min (Khairoun et al., 1998).

XRD patterns of cements, MPC and the SMPCs, cured at 37°C for 7 d are displayed in Figure 2A. It should be noted that because the hydration product of MPC is $KMgPO_4{\cdot}6H_2O$ the XRD peaks of MPC correspond to those of the mixed K and Mg containing phosphate (PDF# 35–0812). The presence of Sr does not affect the crystallinity of the SMPC cements. Moreover, SMP does not become hydrated during the process of bone cement formation so that XRD spectra of the SPMCs contain peaks associated with both $KMgPO_4{\cdot}6H_2O$ and $SrMg_2(PO_4)_2$. Also, analysis of the XRD patterns in Figure 2A indicates that unreacted MgO does not remain in MPC and SMPC after bone cement formation. As a result, these cements should have better biocompatibility than MPC prepared from dead burned MgO (Mestres and Ginebra, 2011; Qiao et al., 2012). The compressive strengths of the cements, MPC and the SMPCs were determined after curing at 37°C for 7 d (Figure 2B). The results show that the compressive strength of MP is about 25 MPa, and that the compressive strength decreases as the amount of strontium increases from 0.25 mol to 1.0 mol. Importantly, when the strontium content is 0.5 mol (SMPC-2), the compressive strength is 22.5 MPa, which meets the requirements for bone repair materials. The compressive strength changes likely result from the fact that the radius of Sr^{2+} is slightly larger than that of Mg^{2+}, and that this difference causes a change in the lattice structure of the MPC.

3.2 *In vitro* degradability and cytotoxicity of MPC and the SMPCs

Biodegradability is critical requirement of artificial bone repair materials, because it leads to cell infiltration and better *in vivo* absorption (Zhai et al., 2018). Thus, the *in vitro* biodegradation properties of MPC and the SMPCs were evaluated. In Figures 3A, B are plots of the respective time dependencies of weight loss percentages and pH occurring upon immersing the bone cements in Tris HCl (pH = 7.4) buffer for 1, 3, 7, 14, 21 and 28 d. The *in vitro* degradation trends

Of all cements are similar and degradation in the first week is significantly larger than those occurring during longer time periods (Figure 3A). The total weight loss of MPC is 17.6% after 28 d of the *in vitro* degradation. When the strontium content is 0.25 mol (SMPC-1), the rate of *in vitro* degradation is slightly lower that of MPC. When the amount of strontium is 1.0 mol (SMPC-4), *in vitro* degradation after 28 d is 25.5%, suggesting that the biodegradability of bone cement is strongly promoted by strontium. The high *in vitro* degradation performance is likely caused by the replacement of magnesium by strontium, which weakens the crystal structure that is conducive to the release of metal ions.

As shown in Figure 3B, the pH values of media containing MPC and the SMPCs decrease slightly during the 1st-3rd day period but then undergo slight increases as the soaking time is extended. During the soaking periods, pH values of media containing MPC and the SMPCs are similar in the 7.35–7.45 range that is conducive to cell growth. In a previous study, a solid-phase method utilizing excess MgO was employed to prepare MPC at a high temperature. This approach generates a cement whose degradation

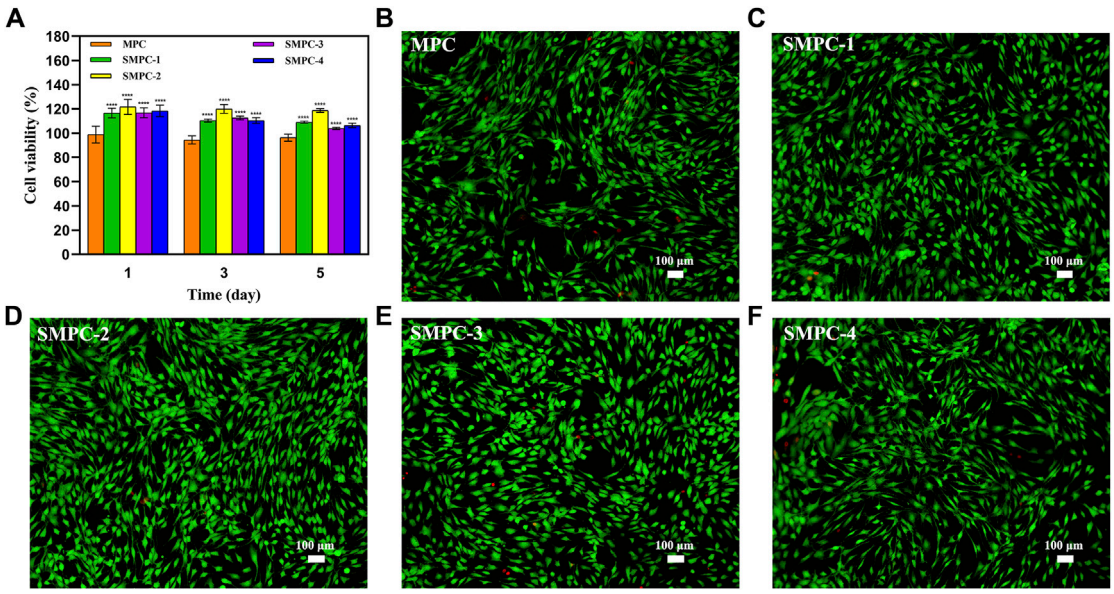

FIGURE 4
(A) Results of CCK-8 assays of BMSC bioactivities in the presence of MPC and the SMPCs after culturing for 1, 3, and 5 d. Data are presented as mean ± SD (****p <0.0001; vs. MPC). **(B–F)** Fluorescence microscope images of 4′,6-diamidino-2-phenylindole and calcein acetoxymethyl ester stained BMSCs cultured in the presence of MPC and the SMPCs for 5 d (green: viable cells; red: dead cells).

creates an alkaline environment (pH > 7.5), which has an adverse effect on cell growth (Qiao et al., 2012). In the newly developed precursor method, only 6.4% of active MgO is used for cement formation considering mechanical strength and setting time and as a result, no unreacted MgO remains, as demonstrated by the results of XRD analysis (Figure 2).

To investigate metal ion release from MPC and SMPCs during under cell culture conditions, the contents of Mg^{2+} and Sr^{2+} in the Tris HCl solution after 1–28 d were determined using inductively coupled plasma mass spectrometery. (Figures 3C, D). The rate of release of Mg^{2+} from MPC in the first 7 d period is significantly higher than it is during the later time periods (Figure 3C). The content of Mg^{2+} in the medium arising from soaking MPC for 28 d is 15.66 mM. Interestingly, the rate of release of Mg^{2+} from all SMPCs except SMPC-1 increases with Sr content. This phenomenon could be associated with weakening of lattice structure brought about by replacement of Mg^{2+} by Sr^{2+}. By inspection of Figure 3D it can be seen that the rate of Sr^{2+} release from the SMPCs also increases as the Sr content increases and that the total amount of Sr^{2+} released from SMPC-2 after 28 d is 0.14–1.01 mM. The results are consistent with those arising from the *in vitro* degradation studies (Figure 3A). Based on the above results, it can be concluded that the SMPCs prepared using the precursor method display good degradation performances *in vitro* and provide a proper environment for cell growth.

The CCK-8 assay can be employed to evaluate the effects of MPC and the SMPCs on BMSC viability. The results (Figure 4A) show that activities of the of SMPC treated cells over a 1–5 d period are larger than those of cells treated with MPC, suggesting that $Sr2^{+}$ promotes cell proliferation. For example, the activity of SMPC-2 treated cells is 120% during the 3 d period, indicating that it has the highest biocompatibility. This finding suggests that a cooperative effect occurs at $Sr2^{+}$ concentrations of 0.14–1.01 mM and $Mg2^{+}$ concentrations of 2.74–21.39 mM to enhance the synthesis of intracellular proteins and DNA, which are considered to be key regulators of cell proliferation and differentiation (Rubin, 1975).

For evaluation of the effects of MPC and the SMPCs on the live/dead cell ratio, fluorescence microscope images of 4′,6-diamidino-2-phenylindole and calcein acetoxymethyl ester stained BMSC were obtained after a 5 d culture period (Figures 4B–F). Inspection of the images shows that when SMPCs are present in the incubation mixture, the density of live BMSCs is significantly enhanced relative to that for cells grown in the presence of MPC. In addition, only a small number of dead cells form in the SMPCs treated mixture. Moreover, SMPC-2 (0.5 mol Sr) promotes formation of the greatest number of viable BMSCs and lowest number of dead cells. The results show that a defined amount of Sr in the cement (e.g., SMPC-2) leads to an improvement of cell viability, which is consistent with the CCK-8 assay results in Figure 4A. Overall, these experiments suggest that SMPCs prepared using the precursor method more potently promote cell growth and proliferation.

3.3 Osteogenic differentiation

Mineralized calcium content is a key marker for osteoblast proliferation and differentiation, as well as the osteogenic potential of bone tissue. The results of osteoblast proliferation studies using the Alizarin Red S staining method are given in the form of microscope images of stained BMSCs in Figure 5. Alizarin red combines with calcium ions to form a stable red complex, which can detect the mineralization degree of osteoblasts. The adsorption amount of Alizarin red dye is in direct proportion to the calcium content (Wang et al., 2016). The results show that inclusion of Sr in the MPC cement used to treat these cells facilitates osteogenic induction and.

Differentiation after incubation for 14 and 28 d, and that the enhancement is dependent on the Sr content of the SMPCs and the

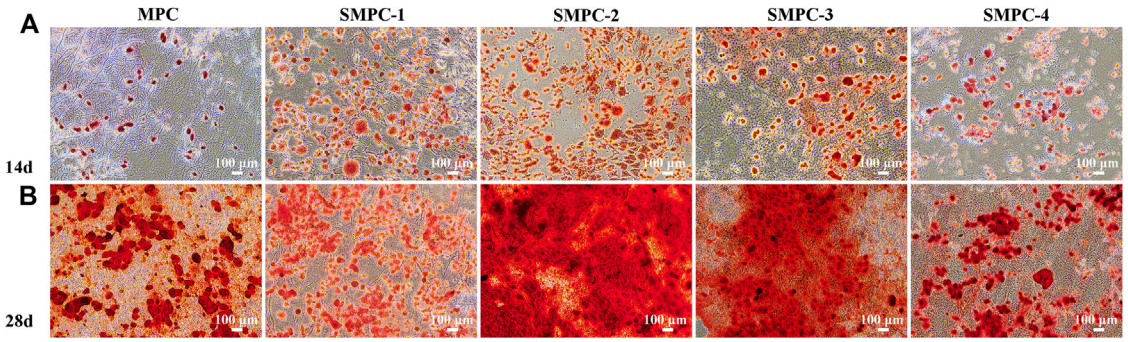

FIGURE 5
BMSCs stained with alizarin red S solution after culturing 14 d **(A)** and 28 d **(B)** in the presence of MPC and the SPMCs.

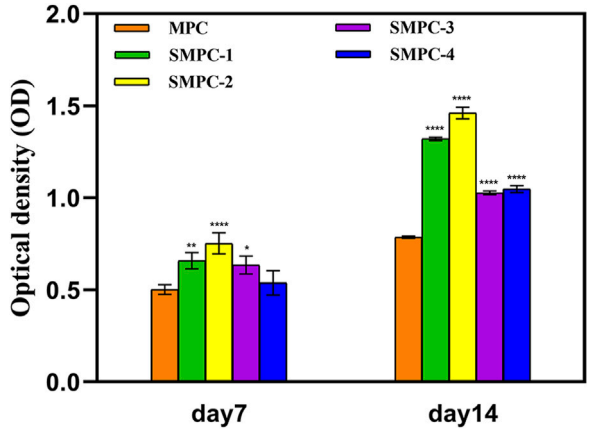

FIGURE 6
ALP activities in the form of optical densities in assays of BMSCs cultured for 7 and 14 d in the presence of MPC and the SPMCs. Data are presented as mean ± SD (*p <0.05; **p <0.01; ****p <0.0001; vs. MPC).

incubation time. Specifically, after 14 d, the mineralization effect initially increases with Sr content, reaches a plateau at a 0.5 mol Sr (SMPC-2) and then decreases (Figure 5A), and in all cases the enhancement effects are greatly magnified at 28 d (Figure 5B). These observations are consistent with a previous study which showed that Sr alone induces bone marrow mesenchymal stem cells to osteogenesis (Arepalli et al., 2016).

The content of alkaline phosphatase (ALP) directly reflects the activity of osteoblasts, which positively correlates with the mineralization ability of osteoblasts. The bar graphs in Figure 6 show alkaline phosphatase activities in BMSCs first increase and then decreases with increasing Sr content in the SMPCs. This finding is consistent with the mineralization results given in Figure 5, and the combined results indicate that SMPC-2 has the best osteogenic differentiation effect. It has been reported that when the $Sr2^{+}$ concentration is in the 0.34–1.0 mM range, differentiation activity and osteoclast mediated resorption reduction of bone or bone substitutes takes place (Gentleman et al., 2010; Montesi et al., 2017). The observations definitively demonstrate that Mg^{2+} in the concentration range of 14.36–26.27 mM has an up-regulating effect on osteoblast proliferation (Wu et al., 2015), and inclusion of 0.14–1.01 mM Sr^{2+} further promotes osteogenic differentiation of stem cells (Gentleman et al., 2010).

4 Conclusion

In this study, bioinspired strontium magnesium phosphate cements (SMPCs) possessing various Sr contents (0–1.0 mol) were prepared by using a newly developed precursor method. The synthetic process utilizing this protocol is simple and environment-friendly, and high yielding (98.5%). The SMPCs were found to have and uniform particle distributions, and high crystallinities, purities and compressive strengths. Compared to MPC, the SMPCs have higher rates of biodegradation to form both free $Sr2^{+}$ and $Mg2^{+}$ and, as a result, they create a more favorable environment for growth of BMSCs. Particularly significant is the observation that shows that SMPC-2 containing 0.5 mol of Sr has the highest bioactivity. The synergistic effect of $Sr2^{+}$ and $Mg2^{+}$ release from SMPC-2 creates a more conducive environment for promoting cell proliferation, mineralized calcium deposition and bone tissue formation. These properties make the SMPCs promising cements for damaged bone repair applications. In the future, investigations will be carried out to improve the mechanical properties of the SMPCs, to enhance the understanding of the foundation of their *in vivo* repair effects, and finally to apply these cements in clinical environments.

Data availability statement

The raw data supporting the conclusions of this article will be made available by the authors, without undue reservation.

Author contributions

QL: Investigation, Formal analysis, Data Curation, Visualization, Writing-original draft. CL: Investigation, Formal analysis, Data Curation, Visualization, Writing-original draft. WW: Methodology, Validation, Data Curation, Visualization. LY: Investigation, Data curation, Validation, Formal analysis. YW: Data curation, Validation, Methodology, Software. XY: Data curation, Formal analysis, Software, Methodology. ZP: Conceptualization, Supervision, Project

administration, Writing-review and editing, Methodology. AY: Conceptualization, Supervision, Project administration, Writing-review and editing, Funding acquisition.

Funding

This study was supported by the Medical Leading Talent Project of Hubei Province (LJ20200405).

Acknowledgments

We thank the members of the AY groups for the helpful discussions and the Wuhan University Testing Center for their help in testing.

Conflict of interest

The authors declare that the research was conducted in the absence of any commercial or financial relationships that could be construed as a potential conflict of interest.

Publisher's note

All claims expressed in this article are solely those of the authors and do not necessarily represent those of their affiliated organizations, or those of the publisher, the editors and the reviewers. Any product that may be evaluated in this article, or claim that may be made by its manufacturer, is not guaranteed or endorsed by the publisher.

References

Arepalli, S., Tripathi, H., Hira, S., Manna, P. P., Pyare, R., and Singh, S. P. (2016). Enhanced bioactivity, biocompatibility and mechanical behavior of strontium substituted bioactive glasses. *Mater. Sci. Eng. C* 69, 108–116. doi:10.1016/j.msec.2016.06.070

Babaie, E., Lin, B., and Bhaduri, S. B. (2017). A new method to produce macroporous Mg phosphate bone growth substitutes. *Mater. Sci. Eng. C* 75, 602–609. doi:10.1016/j.msec.2017.02.111

British Standard Institution (2009). Testing hardened concrete, compressive strength of test specimens. Available at: https://cis.ihs.com/cis/document/326874.BS EN 12390-3.

Dabiri, S., Lagazzo, A., Aliakbarian, B., Mehrjoo, M., Finocchio, E., and Pastorino, L. (2019). Fabrication of alginate modified brushite cement impregnated with antibiotic: Mechanical, thermal, and biological characterizations. *J. Biomed. Mater. Res. A* 107, 2063–2075. doi:10.1002/jbm.a.36719

Gentleman, E., Fredholm, Y. C., Jell, G., Lotfibakhshaiesh, N., O'Donnell, M. D., Hill, R. G., et al. (2010). The effects of strontium-substituted bioactive glasses on osteoblasts and osteoclasts *in vitro*. *Biomaterials* 31, 3949–3956. doi:10.1016/j.biomaterials.2010.01.121

He, F., Lu, T., Fang, X., Qiu, C., Tian, Y., Li, Y., et al. (2019). Study on $Mg_xSr_{3-x}(PO_4)_2$ bioceramics as potential bone grafts. *Colloids Surf. B* 175, 158–165. doi:10.1016/j.colsurfb.2018.11.085

Kanter, B., Vikman, A., Bruckner, T., Schamel, M., Gbureck, U., and Ignatius, A. (2018). Bone regeneration capacity of magnesium phosphate cements in a large animal model. *Acta Biomater.* 69, 352–361. doi:10.1016/j.actbio.2018.01.035

Kargozar, S., Lotfibakhshaiesh, N., Ai, J., Mozafari, M., Brouki Milan, P., Hamzehlou, S., et al. (2017). Strontium- and cobalt-substituted bioactive glasses seeded with human umbilical cord perivascular cells to promote bone regeneration via enhanced osteogenic and angiogenic activities. *Acta Biomater.* 58, 502–514. doi:10.1016/j.actbio.2017.06.021

Khairoun, I., Boltong, M. G., Driessens, F. C., and Planell, J. A. (1998). Limited compliance of some apatitic calcium phosphate bone cements with clinical requirements. *J. Mater. Sci. Mater. Med.* 9, 667–671. doi:10.1023/a:1008939710282

Liu, H., Liu, L., and Din, C. (2021). A quick microwave-assisted rheological phase reaction route for preparing $Cu_3Mo_2O_9$ with excellent lithium storage and supercapacitor performance. *J. Alloy. Compd.* 867, 159061. doi:10.1016/j.jallcom.2021.159061

Liu, J., Simon, C., Linson, R., and Fortune, F. (2016). Strontium-substituted bioactive glasses *in vitro* osteogenic and antibacterial effects. *Dent. Mater.* 32, 412–422. doi:10.1016/j.dental.2015.12.013

Matsumoto, A. (1976). Effect of strontium on the epiphyseal cartilage plate of rat tibiae-histological and radiographic studies. *Jap. J. Pharmacol.* 26, 675–681. doi:10.1254/jjp.26.675

Mestres, G., and Ginebra, M. (2011). Novel magnesium phosphate cements with high early strength and antibacterial properties. *Acta Biomater.* 7, 1853–1861. doi:10.1016/j.actbio.2010.12.008

Montesi, M., Panseri, S., Dapporto, M., Tampieri, A., and Sprio, S. (2017). Sr-substituted bone cements direct mesenchymal stem cells, osteoblasts and osteoclasts fate. *PLoS One* 12, e0172100. doi:10.1371/journal.pone.0172100

Nabiyouni, M., Bruckner, T., Zhou, H., Gbureck, U., and Bhaduri, S. B. (2018). Magnesium based bioceramics in orthopedic applications. *Acta Biomater.* 66, 23–43. doi:10.1016/j.actbio.2017.11.033

Pina, S., Oliveira, J. M., and Reis, R. L. (2015). Natural-based nanocomposites for bone tissue engineering and regenerative medicine: A review. *Adv. Mater.* 27, 1143–1169. doi:10.1002/adma.201403354

Qiao, F., Chau, C., and Li, Z. (2012). Calorimetric study of magnesium potassium phosphate cement. *Mater. Struct.* 45, 447–456. doi:10.1617/s11527-011-9776-z

Rubin, H. (1975). Central role for magnesium in coordinate control of metabolism and growth in animal cells. *Proc. Natl. Acad. Sci.USA* 72, 3551–3555. doi:10.1073/pnas.72.9.3551

Shorr, E., and Carter, A. C. (1952). The usefulness of strontium as an adjuvant to calcium in the remineralization of the skeleton in man. *Bulletin* 13, 59–66.

Wang, S., Xu, C., Yu, S., Wu, X., Jie, Z., and Dai, H. (2019). Citric acid enhances the physical properties, cytocompatibility and osteogenesis of magnesium calcium phosphate cement. *J. Mech. Behav. Biomed.* 94, 42–50. doi:10.1016/j.jmbbm.2019.02.026

Wang, Y., Zhu, G., Wang, J., and Chen, J. (2016). Irradiation alters the differentiation potential of bone marrow mesenchymal stem cells. *Mol. Med. Rep.* 13, 213–223. doi:10.3892/mmr.2015.4539

Wu, L., Feyerabend, F., Schilling, A., Willumeit, R., and Luthringer, B. (2015). Effects of extracellular magnesium extract on the proliferation and differentiation of human osteoblasts and osteoclasts in coculture. *Acta Biomater.* 27, 294–304. doi:10.1016/j.actbio.2015.08.042

Xie, X., Hu, G., Cao, Y., Du, K., Gan, Z., Xu, L., et al. (2019). Rheological phase synthesis of $Fe_2P_2O_7$/C composites as the precursor to fabricate high performance $LiFePO_4$/C composites for lithium-ion batteries. *Ceram. Int.* 45, 12331–12336. doi:10.1016/j.ceramint.2019.03.149

Yang, J., Wang, L., and Zhang, J. (2019). Experimental study on the deformation characteristics of magnesium potassium phosphate cement paste at early hydration ages. *Cem. Concr. Compos.* 103, 175–182. doi:10.1016/j.cemconcomp.2019.05.003

Yu, S., Liu, L., Xu, C., and Dai, H. (2019). Magnesium phosphate based cement with improved setting, strength and cytocompatibility properties by adding $Ca(H_2PO_4)_2{\cdot}H_2O$ and citric acid. *J. Mech. Behav. Biomed.* 91, 229–236. doi:10.1016/j.jmbbm.2018.12.004

Zhai, Q., Han, F., He, Z., Shi, C., Zhou, P., Zhu, C., et al. (2018). The "magnesium sacrifice" strategy enables PMMA bone cement partial biodegradability and osseointegration potential. *Int. J. Mol. Sci.* 19, 1746. doi:10.3390/ijms19061746

Zhao, Y., Yu, S., Wu, X., Dai, H., Liu, W., Tu, R., et al. (2021). Construction of macroporous magnesium phosphate-based bone cement with sustained drug release. *Mater. Des.* 200, 109466. doi:10.1016/j.matdes.2021.109466

frontiers | Frontiers in Bioengineering and Biotechnology

TYPE Original Research
PUBLISHED 27 February 2023
DOI 10.3389/fbioe.2023.1161192

OPEN ACCESS

EDITED BY
Hongliang Liu,
Yantai University, China

REVIEWED BY
Dan Lu,
Peking University, China
Hui Li,
Beijing Normal University, China

*CORRESPONDENCE
Shengjie Jiang,
kqjiangshengjie@bjmu.edu.cn

†These authors have contributed equally to this work and share first authorship

SPECIALTY SECTION
This article was submitted to Biomaterials, a section of the journal Frontiers in Bioengineering and Biotechnology

RECEIVED 08 February 2023
ACCEPTED 17 February 2023
PUBLISHED 27 February 2023

CITATION
Guo X, Zheng H, Guo Y, Heng BC, Yang Y, Yao W and Jiang S (2023), A three-dimensional actively spreading bone repair material based on cell spheroids can facilitate the preservation of tooth extraction sockets.
Front. Bioeng. Biotechnol. 11:1161192.
doi: 10.3389/fbioe.2023.1161192

A three-dimensional actively spreading bone repair material based on cell spheroids can facilitate the preservation of tooth extraction sockets

Xinwei Guo[1†], Huimin Zheng[1†], Yusi Guo[1†], Boon Chin Heng[1], Yue Yang[2], Weitong Yao[3] and Shengjie Jiang[1,4*]

[1]Beijing Laboratory of Biomedical Materials, Department of Geriatric Dentistry, Peking University School and Hospital of Stomatology, Beijing, China, [2]Department of Prosthodontics, The First Clinical Division, Peking University School and Hospital of Stomatology, Beijing, China, [3]Hubei Jiangxia Laboratory, Wuhan, China, [4]Guangdong Provincial Key Laboratory of Stomatology, Hospital of Stomatology, Sun Yat-Sen University, Guangzhou, Guangdong, China

Introduction: Achieving a successful reconstruction of alveolar bone morphology still remains a challenge because of the irregularity and complex microenvironment of tooth sockets. Biological materials including hydroxyapatite and collagen, are used for alveolar ridge preservation. However, the healing effect is often unsatisfactory.

Methods: Inspired by superwetting biomimetic materials, we constructed a 3D actively-spreading bone repair material. It consisted of photocurable polyether F127 diacrylate hydrogel loaded with mixed spheroids of mesenchymal stem cells (MSCs) and vascular endothelial cells (ECs).

Results: Biologically, cells in the spheroids were able to spread and migrate outwards, and possessed both osteogenic and angiogenic potential. Meanwhile, ECs also enhanced osteogenic differentiation of MSCs. Mechanically, the excellent physical properties of F127DA hydrogel ensured that it was able to be injected directly into the tooth socket and stabilized after light curing. *In vivo* experiments showed that MSC-EC-F127DA system promoted bone repair and preserved the shape of alveolar ridge within a short time duration.

Discussion: In conclusion, the novel photocurable injectable MSC-EC-F127DA hydrogel system was able to achieve three-dimensional tissue infiltration, and exhibited much therapeutic potential for complex oral bone defects in the future.

KEYWORDS

actively spreading material, site preservation, cell spheroid, polyether F127 diacrylate, mesenchymal stem cell

1 Introduction

Tooth extraction is a common dental surgical procedure to deal with teeth that have lost restoration value and normal physiological functions. Missing teeth may seriously impair masticatory function and patients' esthetic appearance, so they need to be repaired as soon as possible. However, after tooth extraction, osteoclasts are usually activated due to trauma and inflammatory granulation tissue within the tooth socket, resulting in continuous bone

resorption (Jung et al., 2018). Studies have shown that alveolar bone is resorbed rapidly in both the horizontal and vertical directions within 3–6 months after tooth extraction, and that the resorption rate slows down after 6 months. Unfortunately, the whole process is irreversible (Tomlin et al., 2014). Statistics have shown that 50% of the buccolingual alveolar bone were resorbed during the first year after tooth extraction (Araújo and January 2011). If appropriate measures are not taken, rapid bone resorption can compromise prosthodontic rehabilitation. Alveolar ridge preservation (ARP) is a surgical procedure to slow down alveolar bone resorption by implanting bone increment materials into the socket, and covering it with barrier membrane materials immediately after tooth extraction (G. Avila-Ortiz et al., 2020; Majzoub et al., 2019). The most commonly used implant materials are hydroxyapatite, bio-ceramic and collagen (Kim et al., 2016; Avila-Ortiz et al., 2019). However, these materials only offer structural support in the tooth socket, and exert only very limited pro-osteogenic effects because of their inadequate biocompatibility. Moreover, implants might be treated as foreign objects by the body and trigger specific immune responses *in situ*, resulting in immune exclusion effect and even bone resorption. In recent years, stem cell therapy has been proposed to effectively reduce immune exclusion effect. Studies have shown that stem cells preferentially migrate to the defect area that displays the increased expression of inflammatory chemokines (Liesveld, 2020). Furthermore, they have the potential to differentiate into multiple lineages, such as the osteogenic and angiogenic lineages. Hence, after tooth extraction, stem cells are able to migrate to the tooth socket and play a key role in bone repair (Meng et al., 2022). Exogenous mesenchymal stem cell transplantation can speed up the repair process, but requires a large number of stem cells so that prior *ex vivo* cell expansion is necessary. However, current 2D adherent cultures often lead to rapid cell senescence after successive passage, and impair their multipotent differentiation potential (Turinetto et al., 2016), which ultimately results in reduced proliferation and osteogenic capacity after transplantation. Moreover, because of gravity, the transplanted stem cells often converge at the lowest position and cannot make full contact with the bone defect in a three-dimensional (3D) manner. In order to overcome these problems, inspired by previous studies on biomimetic superwetting materials (Jiang et al., 2021; Yang et al., 2022), we fabricated a 3D actively-spreading bone repair material. The photocurable polyether F127 diacrylate hydrogel loaded with mixed spheroids of mesenchymal stem cells (MSCs) and vascular endothelial cells (ECs) was injected into the alveolar bone defect to accelerate bone regeneration.

Biomimetic superwetting materials take inspiration from the natural structures of living organisms, therefore they have strong hydrophobicity and high biocompatibility *in vivo* (Li et al., 2021). The most imitated structure is the lotus leaf, which surface is abundant in micron-level protrusions, making itself highly hydrophobic and self-cleanable. Water can form beads on the lotus leaves, easily roll off afterwards and carry away dust (Farzam et al., 2022). Cell membranes are also hydrophobic, because it is mainly composed of a phospholipid bilayer. Due to its hydrophobic effect, it can isolate intracellular fluid from extracellular fluid, ensuring the relative stability of the cellular internal environment. Studies have shown that the hydrophobicity of cell membranes facilitates cell adhesion and infiltration. The more hydrophobic the cells are, the stronger the infiltration and adhesion will be (Rosenberg, 1991). Cell spheroids are growth forms of large numbers of cells aggregating into a 3D spherical structure. The cell spheroid itself can be used as a biologically-active infiltrating material, because the hydrophobic area of the cell membrane is expanded, allowing better infiltration within the tooth extraction socket filled with blood and saliva. Furthermore, previous studies have shown that cell spheroids have the active spreading ability, as cells inside the spheroid can migrate in all directions by budding (Yin et al., 2022). Therefore, implanting biomaterials containing cell spheroids into the complex microenvironment of tooth sockets can ensure a higher degree of cell contact with the bone wall (Maritan et al., 2017). Cell spheroid also helps preserve the "stemness" of stem cells. Compared with cells in 2D culture, MSCs cultured spherically in 3D always maintain good multipotent differentiation and proliferative potentials (Yan et al., 2014). Studies have also shown that 2D co-culture of endothelial progenitor cells with MSCs enhance the osteogenic biomarker expression of MSCs (Peng et al., 2019). On this basis, we hypothesize that 3D cultures of ECs with MSCs to form a mixed ECs-MSCs spheroid can enhance the osteogenic potential of MSCs, facilitate early vascular reconstruction in the defect area, and promote socket healing.

Biocompatible scaffolds are also required for the implantation of cell spheroids into the socket. Here, we selected polyether F127 diacrylate (F127DA), an acrylacylated polyethylene glycol—polypropylene glycol—polyethylene glycol triblock copolymer, as the 3D scaffold for spheroid implantation. F127DA has demonstrated a good biosafety record and excellent mechanical properties (Ren et al., 2019). Additionally, F127DA hydrogel is temperature-sensitive before light curing, forming a gelatinous shape at higher temperatures, and returning to the liquid state at lower temperatures. The internal temperature of the mouth is always maintained at about 37°C, and the fluidity of F127DA is reduced at this temperature, impeding it from flowing out of the socket after injection. With photo-initiator added into the system, it can be quickly cross-linked into hydrogels under ultraviolet or visible light of a certain wavelength, which can be easily operated in the dental clinic. In all, we constructed a 3D actively-spreading material incorporated with EC-MSC mixed spheroids, which demonstrated promising clinical application potential and is expected to be a favorable biomaterial for the treatment of complex oral bone defects in the future.

2 Materials and methods

2.1 Preparation and harvest of spheroids

ECs and MSCs were first cultured in T75 culture flasks. When the cell confluence reached 80%, ECs and MSCs were dissociated with trypsin. Then the cell suspension was centrifuged at a speed of 1,200 rpm. The supernatant was discarded, and cells were resuspended with fresh medium. AggreWell™400 24-well plate (STEMCELL Technologies, Canada) was prepared in an ultra-clean cabinet. The Anti-Adhesion Rinsing Solution (STEMCELL

Technologies, Canada) was then added to the plate with aliquots of 500 μL per well. Then the plate was centrifuged at 1,300 g for 5 min. Microscopy observations were used to assess whether the bubbles at the bottom of the plate disappeared. If not, the plate would be re-centrifuged. Next, the Anti-Adhesion Rinsing Solution was aspirated, and the plate was then rinsed with pre-heated medium. ECs and MSCs was counted to 1.2–2.4 × 10^6 cells per well. Cell suspensions with a volume of 2 mL were added to each well. The suspension was gently dispersed by pipetting to ensure that the cells were evenly distributed in the microwell. Then the plate was centrifuged at 100 g for 3 min, and was incubated at 37°C, 5% CO_2 and 95% humidity for 24 or more hours. Finally, whether any spheroid was formed in the micro-well, was evaluated by observation under a microscope.

When harvesting spheroids, the supernatant was carefully aspirated from each well. 2 mL of fresh medium was added, and pipetted repeatedly to make sure that spheroids were suspended from the bottom of microwells. Medium containing spheroids was collected into a centrifuge tube. The centrifuge tube was then placed on the test-tube stand for more than half an hour, waiting for the spheroids to settle down naturally. It should be noted that the cell spheroids cannot be centrifuged, or their shape may be damaged. Then the supernatant was discarded. The remaining sediments were the target spheroids.

2.2 Observations of spheroid spreading behavior

The harvested MSC spheroids and MSC-EC mixed spheroids were cultured in 48-well plates. The budding of spheroids was observed and photographed every 2 h. The image processing software ImageJ FIJI was used to calculate the number and length of the budding, so as to calculate the spreading area of the spheroids at different time points.

2.3 RT-qPCR

The spheroids were lysed by 1 mL TRIzol (Thermo Fisher, The United States), pipetted several times and left to stand on ice for 10 min. Then 200 μL of chloroform was added into the centrifuge tube. The mixture was then centrifuged at a speed of 12,000 g at 4°C for 10 min. The supernatant at the top layer was carefully transferred to another centrifuge tube, followed by the addition of 500 μL isopropanol into the supernatant. After being rotated up and down for 10 min, the tube was centrifuged at a speed of 12,000 g at 4°C for 15 min. Then the supernatant was discarded. The RNA was washed and precipitated twice with 75% ethanol, centrifuged at the speed of 7,500 g for 5 min each time. The target RNA was then dried for 10 min at room temperature until the color turned completely transparent.

20 μL of RNase free water was then added into the centrifuge tube to dissolve RNA. A nanodrop (Thermo Fisher, The United States.) was used to measure the RNA concentration. RNA was then reverse transcribed into cDNA by a reverse transcription kit (Takara, Japan) and PCR thermal cycler (Takara, Japan). Transparent 96 well plates (Thermo Fisher, The United States.) and a real-time fluorescent quantitative PCR system (ABI, The United States.) were used for qPCR detection. The qPCR mixture with a total volume of 10 μL per well includes 5 μ L FastStart universal SYBR Green Master Mix (Roche, Germany), 3 μ L RNase free water, 1 μ L template cDNA, and 1 μ L primer. The experimental results were analyzed by relative quantitative methods. Primer sequences utilized for qRT-PCR are shown in Table 1.

TABLE 1 Primer sequences utilized for qRT-PCR.

GAPDH	TCTCTGCTCCTCCCTGTTC	ACACCGACCTTCACCATCT
OPG	GGTAATGACACGATCACTCC	TGACACGATCACTCC
CD31	CAGCCATTACGACTCCCAGA	GAGCCTTCCGTTCTCTTGGT

2.4 Alkaline phosphatase qualitative staining

Spheroids cultured for 3 days were harvested and cultured on 24 well plate. After 24 h, 1 mL neutral formaldehyde was added into each well to fix cells for 10 min. Then the plate was washed twice with deionized water. An alkaline phosphatase (ALP) qualitative kit (Beyotime, China) was used to stain the spheroids.

2.5 Alizarin red staining

Spheroids cultured for 10 days were harvested and cultured on 24 well plates. After 24 h, 1 mL of neutral formaldehyde was added into each well to fix cells for 10 min. Then the plate was washed twice with deionized water. The spheroids were then stained with 500 μL of alizarin red solution incubated on a shaker at room temperature for 15 min, and finally rinsed by deionized water again.

2.6 Immunofluorescence

Spheroids were seeded in a 24-well plate with glass bottom for laser confocal microscopy. The sample was rinsed with PBS and fixed with neutral formaldehyde solution for 10 min 0.5% (w/v) Triton X-100 (Sigma, The United States) was used to permeabilize the cells for 10 min. Then 3% (w/v) bovine serum albumin (BSA, Solarbio, China) was used for blocking at 4°C for 20 min. The antibodies were added to the sample and incubated overnight. Antibodies used include: Anti-CD34 antibody (ab198395, abcam, United Kingdom.), and Anti-BMP2 antibody (ab276041, abcam, United Kingdom). The cell nuclei were stained with 4′, 6-diamidino-2-phenylindole (DAPI; Sigma, The United States). The cell spheroids were observed under laser confocal microscopy and photographic images were captured.

2.7 Preparation of F127DA hydrogel

PBS was used to dissolve the photo-initiator. The solution was heated by water bath at 40°C–50°C for 15 min. Then the photo-initiator solution was added to the F127DA powder. The mixture

was stored at 2°C–8°C for 30 min, and vibrated several times during the period. It is noted that the concentration of F127DA solution is 3%–30% (w/v). The final solution was then stored in the dark after complete dissolution. When curing, a light source with a wavelength of 405 nm was used to irradiate the F127DA solution containing the photo-initiator for 30 s.

2.8 Hydrogel loading with spheroids

Millex Syringe Filters (Millipore, The United States) was used to filter the F127DA solution. Spheroids were collected and resuspended within the F127DA solution. Then the spheroid suspension was added to 24 well plates. Each well was irradiated by a light source with a wavelength of 405 nm for 30 s. An appropriate volume of medium was added to each well after the light curing. Finally, the plate was incubated at 37°C.

2.9 Hydrogel degradation

The cell strainer was weighed with an analytical balance, and the weight was recorded as M0. The F127DA hydrogel after light curing was placed into the cell strainer and immersed into the PBS solution at 37°C. The cell strainer containing hydrogel was taken out of the PBS every 24 h, dried with filter paper to absorb water on its surface, and the overall weight was weighed as Mt. The weight measured at the first 24 h is M1. The calculation formula of degradation rate (Dt) at each time point is: Dt=(Mt-M0)/(M1-M0).

2.10 Rheological measurements

The rheometer (Andonpa MCR302, China) was set to shock mode, with a constant frequency of 1 Hz, the strain variation range of 0.01%–100%, and the test temperature of 25°C. The fixture was a parallel plate. Before testing, the uncured liquid hydrogel was added to the plate with a hollow round mold. Then the liquid was light cured. Next, the mold was removed.

2.11 Compression strength test

The compression strength was measured with the universal mechanical testing machine (SHIMADZU, Japan). The tested hydrogel was molded into a cylinder with a height of 4 mm and a diameter of 10 mm. The compression rate is 5 mm/min. Then the stress-strain curve was calculated according to the displacement and the primary load measurement was automatically recorded by a computer.

2.12 Animal experiment

The animal experiment was approved by the Biomedical Ethics Committee of Peking University (approval number: PUIRB-LA2022688). Specific pathogen-free male Wistar rats were divided into a blank control group (Ctrl group), F127DA hydrogel group (Gel group), hydrogel loaded with MSC spheroid group (MSC group), and hydrogel loaded with MSC-EC mixed spheroids group (Mix group), according to the random number table method. The maxillary first molars were extracted intact after intraperitoneal injection of pentobarbital at a concentration of 10 mg/mL and local injection of 2% (w/v) lidocaine plus 0.1% (w/v) epinephrine hydrochloride. Spheroids and hydrogel were injected into the extraction sockets of the corresponding groups. The extraction sockets were irradiated with a light source at 405 nm for 30 s. After 3 weeks, the rats were culled by over-anesthesia, and the maxillae were explanted and scanned by Micro CT. We chose this time point because new bone gradually began to form after 3 weeks, which was conducive to comparing the differences between groups. Then the maxillae were decalcified with a 10% (w/v) EDTA solution for 2 weeks, and then sequentially dehydrated, waxed, embedded, sectioned. Hematoxylin-eosin (HE) staining, Masson staining and immunohistochemical staining of CD31 (ab182981, abcam, United Kingdom) and COL1 (ab270993, abcam, United Kingdom) were performed afterwards.

3 Results

Figure 1 illustrates the principle and procedure of the study. MSC-EC mixed spheroids were added to the uncured hydrogel to form a flowable, injectable hydrogel suspension. After injection of the suspension into the alveolar sockets, the hydrogel became more viscous at 37°C due to the temperature-sensitive property of F127DA, so that it could not flow out of the sockets easily. The hydrogels were immediately light cured to acquire a further retention. Then, cells in the spheroids actively spread in a 3D direction gradually, enhancing osteogenesis and angiogenesis, and thus promoting socket healing.

Our experiment showed that the MSC-EC mixed spheroids had active spreading, osteogenesis and angiogenesis capacities. Moreover, the mixed spheroids had stronger osteogenic ability than the single MSC spheroids. In the budding experiment, light microscopy showed that only a small number of cells spread out of the spheroid at 6 h, but the length and number of buddings increased at 24 h in both groups (Figure 2A). Quantitative analysis showed that the spheroid spreading area of the two groups gradually increased with the passage of time, and reached twice at 48 h as much as that at 24 h (Figure 2B). No significant difference was found between two group at all time points. Immunofluorescence staining of cytoskeleton also showed an overall tendency of outward infiltration of the spheroids (Supplementary Figure S1). The above results indicated that mixed spheroids had the same spreading ability as the single MSC spheroids. Then, angiogenic and osteogenic potential of the spheroids was studied. PCR results showed that osteogenic and angiogenic gene markers OPG and CD31 were significantly more highly expressed in mixed spheroids (Figure 2C). ALP and alizarin red staining showed that more mature osteoblasts and calcium deposits were formed in the Mix group (Figure 2D). Immunofluorescence showed a stronger BMP-2 expression in the mixed spheroid with the introduction of $CD34^+$ ECs. Interestingly, we also found that BMP-2 positive osteoblastic cells were mainly distributed at the periphery of the spheroids, while $CD34^+$

10.3389/fbioe.2023.1161192

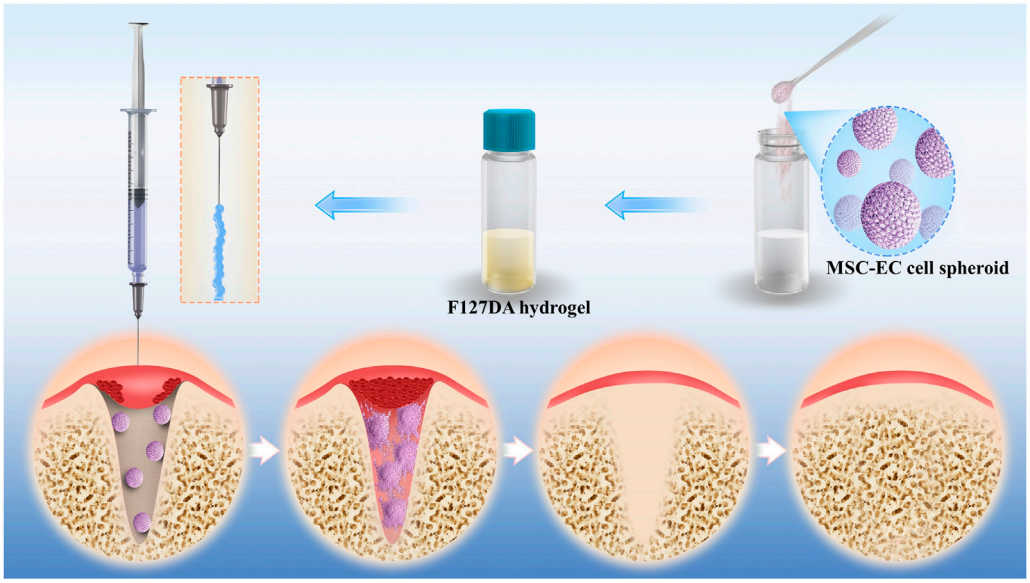

FIGURE 1
Schematic illustration of F127DA hydrogel loading with MSC-EC spheroids promoting tooth extraction socket healing.

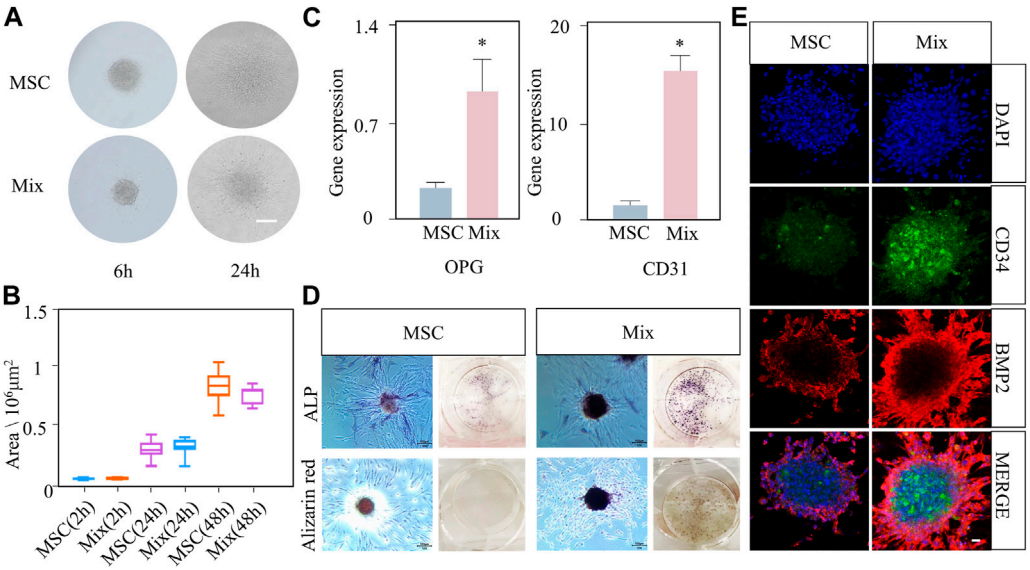

FIGURE 2
The active spreading and osteogenic abilities of MSC-EC mixed spheroids (Mix) were stronger than that of MSC spheroids. **(A, B)** Light microscope images of budding experiment, and the statistical data of spheroid area change with time in the Mix and MSC groups. Scale bar: 100 μm. **(C)** qPCR results of OPG and CD31 gene expression at 3 days of culture. **(D)** ALP staining and alizarin red staining images taken at 3 or 10 days of spheroid culture. **(E)** Immunofluorescence exhibiting the expression of CD34 and BMP2 in the Mix and MSC groups. Scale bar: 10 μm * ($p < 0.05$) indicate statistically significant differences.

endothelial cells were mainly located at the center. Together, they exhibited a special cooperative spatial distribution pattern (Figure 2E).

Based on its mechanical properties, F127DA hydrogel is an ideal scaffold material because it can support the socket, prevent bone collapse, and allow the spheroids to grow and spread. In order to test the fluidity of F127DA visually, the vial containing hydrogel was inverted upside down for seconds and was then put upright quickly. It became more difficult for F127DA solution to flow down at 60°C rather than at 4°C (Figure 3A). After light curing, F127DA hydrogel turned into a semi-solid state and could not flow down after being inverted (Figure 3A). When injecting F127DA into water at 25°C or

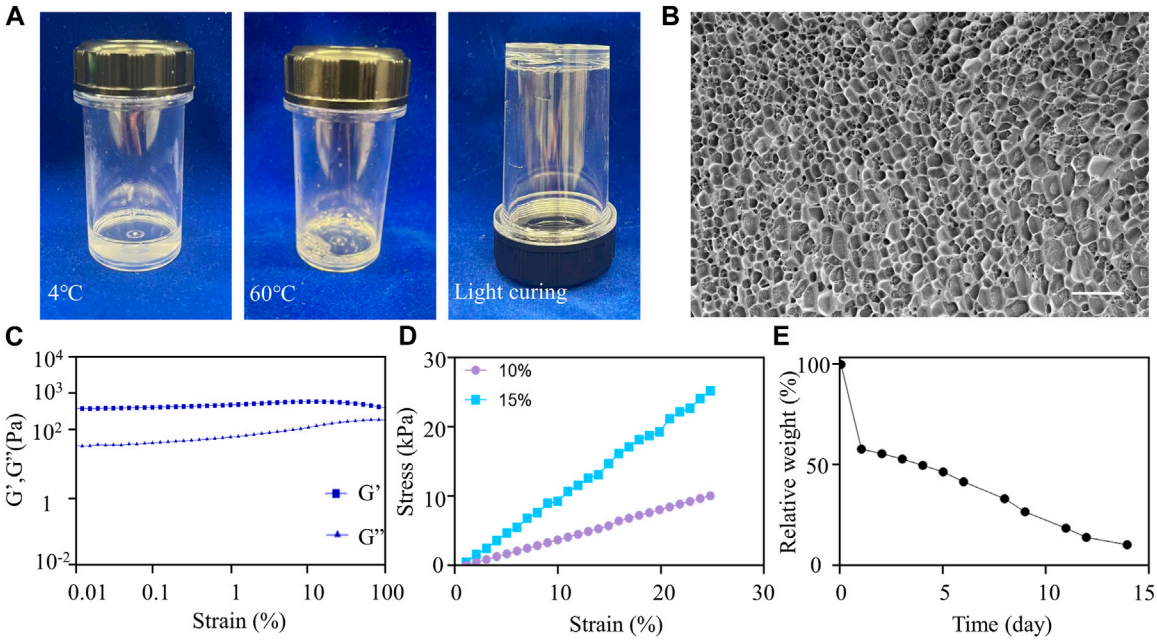

FIGURE 3
Material characterization of F127DA. **(A)** F127DA became viscous as the temperature increased and could be light cured. **(B)** Cryo-scanning electron microscope image showing the inside structure of the hydrogel. Scale bar: 10 μm. **(C)** Rheological tests showing that the hydrogel exhibited elastic solid behavior. **(D)** The compressive strength test showing the relationship between stress and strain of 10% and 15% F127DA hydrogel. **(E)** The variation curve of relative weight of the hydrogel with time at 37°C.

60°C respectively, the hydrogel became more colloidal at higher temperature (Supplementary Figure S2A). The above results indicated that F127DA hydrogel is thermosensitive, light curable and injectable. Cryo-scanning electron microscopy showed that F27DA hydrogel had a loose and porous structure. The average size of inside pores was about 4 μm (Figure 3B). The rheological test demonstrated elastic solid behavior (Figure 3C). Moreover, F127DA exhibited a strong compressive strength. The relationship between stress and strain was close to linear, so the material underwent elastic deformation with complete recovery (Figure 3D). Supplementary Figure S2B also showed good bendable and tensile properties of light cured F127DA hydrogel. The degradation experiment showed that F127DA slowly degraded at 37°C, with 50% weight of hydrogel degraded on the fourth day, and nearly 100% at the 14th day (Figure 3E). Hence, F127DA has enough time to support cell spreading, and avoids hindering bone repair due to material occupancy as well. Supplementary Figures S2C, SD showed the 3D state of spheroids in the hydrogel under light microscopy and scanning electron microscopy. It can be seen that the spheroid grew in a spherical shape and was embedded with surrounding hydrogel fibers.

After being loaded with MSC-EC mixed spheroids, the hydrogel was immediately implanted into the alveolar fossa of rats. We found that this MSC-EC-F127DA actively-spreading material can facilitate vascular regeneration and bone repair *in vivo*. In both Ctrl and Gel groups, Micro CT images showed poor regeneration effects and low bone density in the fossa area, and obvious bone depression could be seen by 3D reconstruction; On the other hand, the sockets of MSC group recovered well, but the level of the alveolar ridge was quite low; The restoration effect was the best in the Mix group, with the maximum bone mass and the highest alveolar ridge level at the same time. Bone mineral density (BMD) measurement also showed that BMD of the Mix group was the highest. In a word, the restoration and healing effects of MSC-EC mixed spheroids implantation was the best (Figure 4). HE staining showed that the trabeculae of the Ctrl and Gel group were loose, and there were many spaces in between; In the MSC group, the trabecular structure was more complete, bug still not dense enough; In the Mix group, the bone trabeculae were much more densely arranged and closely connected. Masson staining also showed more collagen fibers in the alveolar fossa of the Mix group. Immunohistochemical images demonstrated a higher expression of angiogenic and osteogenic markers CD31 and COL1 in the Mix group (Figure 5). All these data indicate that MSC-EC-F127DA material enhances osteogenesis and angiogenesis, and thus promote the healing of sockets.

4 Discussion

We developed a new superwetting material, which consists of photocurable polyester F127 diacrylate hydrogel loaded with MSC-EC mixed cell spheroids. This new material system can effectively promote bone regeneration after being injected into the tooth socket. According to previous studies, the horizontal absorption of alveolar ridge averaged 3.8 mm in width and 1.24 mm in vertical height at 6 months after tooth extraction. Moreover, the resorption of labial

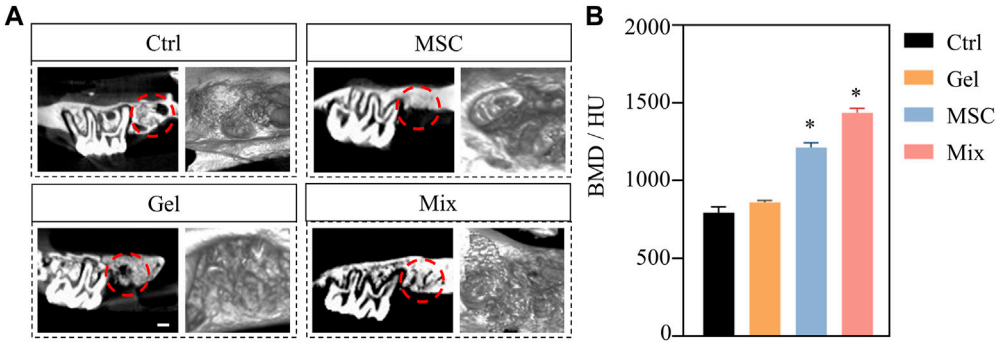

FIGURE 4
(A) Micro CT images of rat maxillae of Ctrl, MSC, Gel and Mix groups at 3 weeks after implantation. Scale bar: 500 μm. **(B)** The statistical results of bone mineral density (BMD) values. * ($p < 0.05$) indicate statistically significant differences.

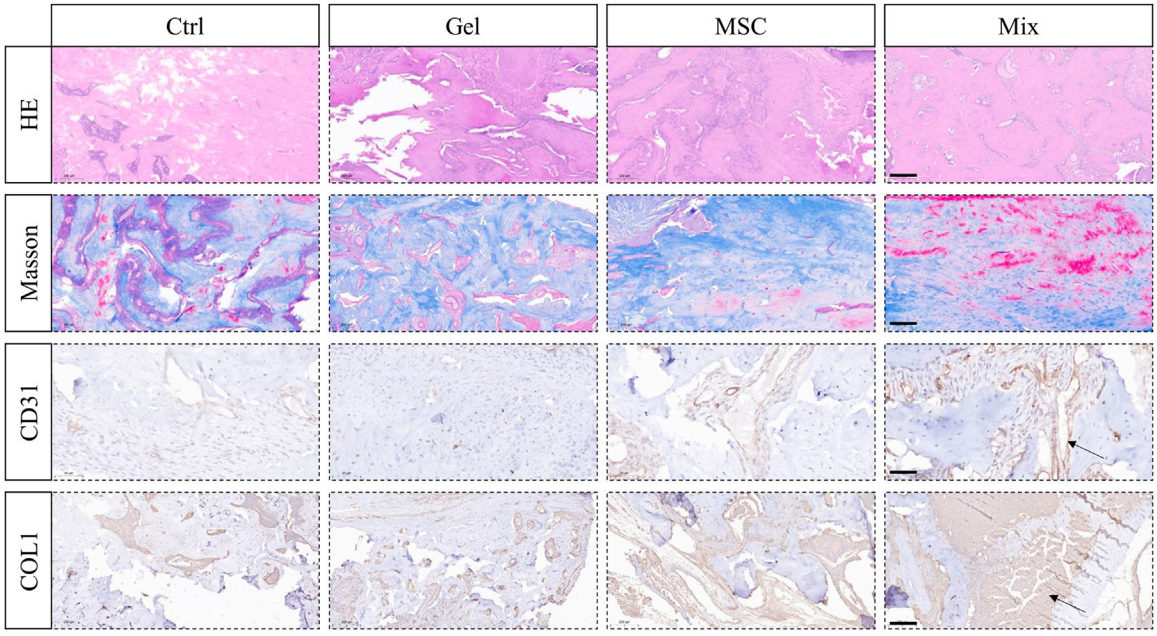

FIGURE 5
HE and Masson staining showing the trabeculae structure and collagen forming in the tooth sockets; Immunohistochemical staining of angiogenic marker CD31 and osteogenic marker COL1 in order to observe angiogenesis and osteogenesis effects. Scale bar: 200 μm (HE, Masson, COL1); 50 μm (CD31). The arrow sign: positive expression tissue.

and buccal cortical bone becomes more significant without tooth. However, it is crucial for implantation therapy to maintain good bone contour and quality. The lack of bone contour support will often lead to attachment loss and gingival recession. Furthermore, bone quality is also crucial for determining the osseointegration effect (Isoda et al., 2012). In this study, the micro-CT results showed that the highest area ratio of woven bone was observed in the Mix group, as compared to Ctrl, Gel and MSC groups. This type of bone tissue is composed of porous bone trabecular layers, red bone marrow tissues and blood vessels, and will gradually mature into cortical bone at a later stage (Mercado-Pagán et al., 2015). In addition, we also observed that the trabecula near the alveolar crest could undergo cortical transformation, and bridge the buccal and lingual cortical bones to form a closed tooth socket. This would provide a favorable site for subsequent implantation. Histomorphology results showed that the Mix group exhibited the highest neovascularization at 3 weeks post-implantation. The generation of new blood vessels and the establishment of vascular networks are among the most important driving forces for tissue healing (Rouwkema and Khademhosseini, 2016). Adequate blood supply can provide oxygen, minerals and nutrients to the surrounding tissues, laying a solid foundation for subsequent

bone healing (Percival and Richtsmeier, 2013). In conclusion, this novel superwetting material system has a strong ability to promote osteogenesis and angiogenesis, accelerate bone healing and preserve alveolar ridge after tooth extraction.

After further evaluation of the properties of this material, we found that the hydrogel has good biocompatibility, and can undergo full degradation within half a month. Moreover, the material is temperature-sensitive and gradually becomes viscous with increase of temperature. Additionally, it is also photocurable and has high strength. Hydrogels have similar biological structural characteristics to natural extracellular matrix (ECM), such as high water content, good biodegradability, high porosity and good biocompatibility (Seliktar, 2012). Therefore, hydrogels can provide a conducive microenvironment for implanted cells to colonize, grow and differentiate. Moreover, F127DA hydrogel is also slowly biodegradable, which avoids space occupation and allows bone formation. Additionally, F127DA is flowable and injectable at room temperature, and becomes more viscous at 37°C, so that the hydrogel stays in the tooth socket more easily. By light curing for 30 s, which is quite accessible at dental clinic, F127DA becomes solidified and achieves good mechanical strength. Due to its injectable and light-curable properties, the hydrogel can fill in irregular defects and provide good support for bone and soft tissue. Injection administration is also less invasive than surgeries and avoids secondary trauma caused by traditional bone transplantation (Piantanida et al., 2019). In conclusion, F127DA hydrogel is an ideal scaffold material for alveolar ridge preservation owing to its outstanding physical properties.

F127DA hydrogel is also a good scaffold for 3D cell culture. It can be seen from SEM that the hydrogel is loose and porous, and the cell spheroid can be chimed with the micelle. This structure favors the spheroids to spread outwards along the micelle. The directed migration of cell populations is the basis for cell development, wound healing and tissue regeneration (Su et al., 2018). On one hand, the excellent diffusion ability of the cell spheroids in F127DA may be due to the hydrophobic micelles, which are uneven and cross-linked with each other at the nanoscale. This structure is similar to the mastoid of the lotus leaf, and is thus beneficial for the infiltration and spreading of the spheroid. On the other hand, after bone injury, BMSCs can migrate to the damaged site and promote structural and functional recovery (Abkowitz et al., 2003). As can be seen from the immunofluorescence images, the MSC-EC mixed cell spheroids not only help reconstruct blood vessels, but also promote MSCs migration and colonization. At the same time, ECs within the spheroid improved osteogenic function of MSCs, which further enhanced bone regeneration within the tooth socket.

Compared with two-dimensional cell culture, 3D spherical cultures of MSCs can promote the release of growth factors such as Oct4, Sox2 and Nanog, which play key roles in maintaining self-renewal and multi-directional differentiation potential of stem cells (Tsai et al., 2017). In addition, MSCs express anti-apoptotic gene Bcl-2 at high levels and pro-apoptotic gene Bax at low levels during 3D spherical culture (Cheng et al., 2013). Therefore, implantation of cell spheroids instead of 2D-cultured cells prevents problems like decreased "stemness" and weak proliferative capacity. On the other hand, when the stage of restoration initiates and replace inflammatory stage during the healing process of tooth socket, mature monocytes/macrophages will differentiate into osteoclasts. The stability of osteoclast function is crucial for starting bone remodeling (Kubatzky et al., 2018). By reducing secretion of IL-1β and TNF-a, MSC spheroids decrease pro-inflammatory M1 phenotype polarization of macrophages, thereby reducing immune rejection and physiological bone resorption (Zhang et al., 2020). However, implanting MSC spheroids along cannot fully activate the osteogenic potential of MSCs and achieve satisfactory osteogenesis effect. Conventional *in vitro* osteogenic induction drugs, such as β-sodium glycerophosphate and dexamethasone, exert certain cytotoxic effects *in vivo*. Therefore, it is crucial to seek a bio-safe induction method. Some studies have shown that the joint transplantation of HUVECs and BMSCs into mice bone defects can accelerate bone healing and promote angiogenesis (Böhrnsen et al., 2021). Therefore, we hypothesized implanting MSC-EC mixed spheroids can potentially enhance osteogenesis in tooth sockets. The *in vivo* results showed that the osteogenic and angiogenic gene markers in the Mix group were significantly upregulated. The interaction between ECs and MSCs in the spheroids provides a cell-guided co-migration mechanism, and a specific pro-osteogenic and pro-angiogenic microenvironment for bone repair.

In summary, we have successfully developed a superwetting material system based on F127DA hydrogel and MSC-EC spheroids. The spheroids in this system have strong 3D active spreading capacity, and can effectively promote bone and blood vessel remodeling. The injectability, mechanical durability, and strength of the F127DA make it readily amenable and convenient for clinical applications. The MSC-EC-F127DA system, as a pro-healing material for tooth sockets, has demonstrated its potential as a supramolecular biomaterial, and can be applied to various biomedical engineering applications in the future.

Data availability statement

The original contributions presented in the study are included in the article/Supplementary Material, further inquiries can be directed to the corresponding author.

Ethics statement

The animal study was reviewed and approved by Biomedical Ethics Committee of Peking University (approval number: PUIRB-LA2022688).

Author contributions

XG contributed to administrate the project, data curation, investigation, and the original draft. HZ contributed to the original draft. YG contributed to investigation and the original draft. BH contributed to language editing. YY and WY contributed to language editing and supervised the writing. SJ conceptualized the idea, supervised the writing, reviewed, and edited the draft.

Funding

This work was supported by the National Natural Science Foundation of China (82101072, 82100979), China Postdoctoral Science Foundation (2022T150024), Open Funding of Guangdong Provincial Key Laboratory of Stomatology (KF2021120101) and Peking University School of Stomatology Fund for Distinguished Young Scholars (PKUSS20210111).

Conflict of interest

The authors declare that the research was conducted in the absence of any commercial or financial relationships that could be construed as a potential conflict of interest.

Publisher's note

Supplementary material

The Supplementary Material for this article can be found online at: https://www.frontiersin.org/articles/10.3389/fbioe.2023.1161192/full#supplementary-material

References

Abkowitz, J. L., Robinson, A. E., Kale, S., Long, M. W., and Chen, J. (2003). Mobilization of hematopoietic stem cells during homeostasis and after cytokine exposure. *Blood* 102 (4), 1249–1253. doi:10.1182/blood-2003-01-0318

Araújo, M. G., and Jan, L. (2011). Socket grafting with the use of autologous bone: An experimental study in the dog: Socket grafting with the use of autologous bone. *Clin. Oral Implants Res.* 22 (1), 9–13. doi:10.1111/j.1600-0501.2010.01937.x

Avila-Ortiz, G., Chambrone, L., and Vignoletti, F. (2019). Effect of alveolar ridge preservation interventions following tooth extraction: A systematic review and meta-analysis. *J. Clin. Periodontology* 46, 195–223. doi:10.1111/jcpe.13057

Avila-Ortiz, G., Gubler, M., Romero-Bustillos, M., Nicholas, C. L., ZimmermanandC, M. B., and Barwacz, A. (2020). Efficacy of alveolar ridge preservation: A randomized controlled trial. *J. Dent. Res.* 99 (4), 402–409. doi:10.1177/0022034520905660

Böhrnsen, F., Melsheimer, P., Natorp, M., Rolf, H., Schminke, B., Kauffmann, P., et al. (2021). Cotransplantation of mesenchymal stromal cells and endothelial cells on calcium carbonate and hydroxylapatite scaffolds *in vivo*. *J. Cranio-Maxillofacial Surg.* 49 (3), 238–245. doi:10.1016/j.jcms.2020.03.001

Cheng, N-C., Chen, S-Y., Li, J-R., and Young, T-H. (2013). Short-term spheroid formation enhances the regenerative capacity of adipose-derived stem cells by promoting stemness, angiogenesis, and chemotaxis. *Stem Cells Transl. Med.* 2 (8), 584–594. doi:10.5966/sctm.2013-0007

Farzam, M., Beitollahpoor, M., Solomon, S. E., Ashbaughand, H. S., and Pesika, N. S. (2022). Advances in the fabrication and characterization of superhydrophobic surfaces inspired by the Lotus leaf. *Biomimetics* 7 (4), 196. doi:10.3390/biomimetics7040196

Isoda, K., Ayukawa, Y., Tsukiyama, Y., Sogo, M., Matsushita, Y., and Koyano, K. (2012). Relationship between the bone density estimated by cone-beam computed tomography and the primary stability of dental implants: Relationship between bone density and implant stability. *Clin. Oral Implants Res.* 23 (7), 832–836. doi:10.1111/j.1600-0501.2011.02203.x

Jiang, S., Li, H., Zeng, Q., Xiao, Z., Zhang, X., Xu, M., et al. (2021). The dynamic counterbalance of RAC1-YAP/OB-cadherin coordinates tissue spreading with stem cell fate patterning. *Adv. Sci.* 8 (10), 2004000. doi:10.1002/advs.202004000

Jung, R. E., Alexis, I., ChristophDaniel, H. F. H. S. T., and Thoma, D. S. (2018). Alveolar Ridge preservation in the esthetic zone. *Periodontology* 77 (1), 165–175. doi:10.1111/prd.12209

Kim, R-W., Kim, J-H., and Moon, S-Y. (2016). Effect of hydroxyapatite on critical-sized defect. *Maxillofac. Plastic Reconstr. Surg.* 38 (1), 26. doi:10.1186/s40902-016-0072-2

Kubatzky, K. F., Uhle, F., and Eigenbrod, T. (2018). From macrophage to osteoclast – how metabolism determines function and activity. *Cytokine* 112, 102–115. doi:10.1016/j.cyto.2018.06.013

Li, D., Fan, Y., Guocai, H., and Zhiguang, G. (2021). Multibioinspired janus membranes with superwettable performance for unidirectional transportation and fog collection. *Chem. Eng. J.* 404, 126515. doi:10.1016/j.cej.2020.126515

Liesveld, J. L., Naman, S., and Omar, S. A. (2020). Stem cell homing: From physiology to therapeutics. *Stem Cells* 38 (10), 1241–1253. doi:10.1002/stem.3242

Majzoub, J., Ravida, A., Starch-Jensen, T., Tattan, M., and Suarez-Lopez del Amo, F. (2019). Thomas Starch-Jensen, Mustafa TattanandFernando Suárez-López del AmoThe Influence of Different Grafting Materials on Alveolar Ridge Preservation: a Systematic Review. *J. Oral Maxillofac. Res.* 10 (3), e6. doi:10.5037/jomr.2019.10306

Maritan, S. M., Lianand, E. Y., and Mulligan, L. M. (2017). An efficient and flexible cell aggregation method for 3D spheroid production. *J. Vis. Exp.* 121, 55544. doi:10.3791/55544

Meng, L., Wei, Y., Liang, Y., Qin, H., and Xie, H. (2022). Stem cell homing in periodontal tissue regeneration. *Front. Bioeng. Biotechnol.* 10, 1017613. doi:10.3389/fbioe.2022.1017613

Mercado-Pagán, A. E., Stahl, A. M., Shanjani, Y., and Yang, Y. (2015). Vascularization in bone tissue engineering constructs. *Ann. Biomed. Eng.* 43 (3), 718–729. doi:10.1007/s10439-015-1253-3

Peng, J., Chen, L., Peng, K., Chen, X., Wu, J., He, Z., et al. (2019). Bone marrow mesenchymal stem cells and endothelial progenitor cells Co-culture enhances large segment bone defect repair. *J. Biomed. Nanotechnol.* 15 (4), 742–755. doi:10.1166/jbn.2019.2735

Percival, C. J., and Richtsmeier, J. T. (2013). Angiogenesis and intramembranous osteogenesis: Angiogenesis and intramembranous osteogenesis. *Dev. Dyn.* 242 (8), 909–922. doi:10.1002/dvdy.23992

Piantanida, E., Alonci, G., Alessandro, B., and De Cola, L. (2019). Design of nanocomposite injectable hydrogels for minimally invasive surgery. *Accounts Chem. Res.* 52 (8), 2101–2112. doi:10.1021/acs.accounts.9b00114

Ren, P., Zhang, H., Zhong, D., Ren, F., Wu, Y., Hou, R., et al. (2019). Stiff micelle-crosslinked hyaluronate hydrogels with low swelling for potential cartilage repair. *J. Mater. Chem. B* 7 (36), 5490–5501. doi:10.1039/C9TB01155B

Rosenberg, M. (1991). Basic and applied aspects of microbial adhesion at the hydrocarbon: Water interface. *Crit. Rev. Microbiol.* 18 (2), 159–173. doi:10.3109/10408419109113512

Rouwkema, J., and Khademhosseini, A. (2016). Vascularization and angiogenesis in tissue engineering: Beyond creating static networks. *Trends Biotechnol.* 34 (9), 733–745. doi:10.1016/j.tibtech.2016.03.002

Seliktar, D. (2012). Designing cell-compatible hydrogels for biomedical applications. *Science* 336 (6085), 1124–1128. doi:10.1126/science.1214804

Su, P., Tian, Y., Yang, C., Ma, X., Wang, X., Pei, J., et al. (2018). Mesenchymal stem cell migration during bone formation and bone diseases therapy. *Int. J. Mol. Sci.* 19 (8), 2343. doi:10.3390/ijms19082343

Tomlin, E. M., Shelby, J. N., and Rossmann, J. A. (2014). ridge preservation for implant therapy: A review of the literature. *Open Dent. J.* 8 (1), 66–76. doi:10.2174/1874210601408010066

Tsai, A-C., Liu, Y., Yuan, X., Chella, R., and Ma, T. (2017). Aggregation kinetics of human mesenchymal stem cells under wave motion. *Biotechnol. J.* 12 (5), 1600448. doi:10.1002/biot.201600448

Turinetto, V., Vitale, E., and Giachino, C. (2016). Senescence in human mesenchymal stem cells: Functional changes and implications in stem cell-based therapy. *Int. J. Mol. Sci.* 17 (7), 1164. doi:10.3390/ijms17071164

Yan, X-Z., Jeroen, J., van den Beucken, J. P., Both, S. K., Yang, P-S., and John, A. (2014). Biomaterial strategies for stem cell maintenance during *in vitro* expansion. *Tissue Eng. Part B Rev.* 20 (4), 340–354. doi:10.1089/ten.teb.2013.0349

Yang, Y., Huang, C., Zheng, H., Meng, Z., Chin, B. H., Zhou, T., et al. (2022). Superwettable and injectable GelMA-MSC microspheres promote cartilage repair in temporomandibular joints. *Front. Bioeng. Biotechnol.* 10, 1026911. doi:10.3389/fbioe.2022.1026911

Yin, L., Li, J., Zhang, Y., Yang, Q., Yang, C., Yi, Z., et al. (2022). Changes in progenitors and differentiated epithelial cells of neonatal piglets. *Anim. Nutr.* 8, 265–276. doi:10.1016/j.aninu.2021.10.008

Zhang, J., Yin, C., Zhao, Q., Zhao, Z., Wang, J., Richard, J., et al. (2020). Anti-inflammation effects of injectable platelet-rich fibrin via macrophages and dendritic cells. *J. Biomed. Mater. Res. Part A* 108 (1), 61–68. doi:10.1002/jbm.a.36792

frontiers | Frontiers in Bioengineering and Biotechnology

TYPE Original Research
PUBLISHED 03 March 2023
DOI 10.3389/fbioe.2023.1165724

OPEN ACCESS

EDITED BY
Jingxin Meng,
Technical Institute of Physics and Chemistry (CAS), China

REVIEWED BY
Liang Cui,
Zhejiang Sci-Tech University, China
Leiliang He,
Zhengzhou University, China

*CORRESPONDENCE
Jiahao Huang,
jhuangaf@connect.ust.hk

†These authors have contributed equally to this work and share first authorship

SPECIALTY SECTION
This article was submitted to Biomaterials, a section of the journal Frontiers in Bioengineering and Biotechnology

RECEIVED 14 February 2023
ACCEPTED 23 February 2023
PUBLISHED 03 March 2023

CITATION
Li P, Zhan H, Tao S, Xie Z and Huang J (2023), Bio-inspired aptamers decorated gold nanoparticles enable visualized detection of malathion.
Front. Bioeng. Biotechnol. 11:1165724.
doi: 10.3389/fbioe.2023.1165724

Bio-inspired aptamers decorated gold nanoparticles enable visualized detection of malathion

Peng Li[1,2†], Haonan Zhan[1†], Sijian Tao[1†], Zhuohao Xie[1,2] and Jiahao Huang[1,2*]

[1]School of Biomedical Engineering, Southern Medical University, Guangzhou, China, [2]Department of Critical Care Medicine, Affiliated Hospital of Guangdong Medical University, Zhanjiang, China

Biosensors always respond to the targets of interest in a specific manner, employing biological or bio-mimic recognition elements such as antibodies and aptamers. Inspired by target recognition in nature, an aptamer-mediated, gold nanoparticle-based sensing approach is developed in this work for effective determination of malathion. The sensing system consists of negatively charged aptamer probes, and polycationic proteins, protamine, as well as exceptional colorimetric nanoprobes, barely gold nanoparticles (AuNPs). Protamine molecules bound to aptamer probes hinder the aggregation of AuNPs, while no such inhibition is maintained when aptamer-specific malathion is introduced into the solution, thus leading to the solution colour change from red to blue observable by the naked eye. The assay is accomplished *via* a mix-and-measure step within 40 min with a detection limit as low as 1.48 μg/L (3σ/s rule). The assay method also exhibits high selectivity and good applicability for the quantification of malathion in tap water with recovery rates of 98.9%–109.4%. Additionally, the good detection accuracy is also confirmed by the high-performance liquid chromatography method. Therefore, the non-enzymatic, label- and device-free characteristics make it a robust tool for malathion assay in agricultural, environmental, and medical fields.

KEYWORDS

bio-inspired recognition components, super-hydrophilic nanomaterial, biosensor, enzyme-free system, colorimetric assay

1 Introduction

In living system, biological particles, such as cells and virus, always respond to their relevant receptors in a specific manner by employing target recognition elements such as antibodies and aptamers. Inspired by the target recognition in biological particles, an aptamer-decorated super-hydrophilic gold nanoparticle-based sensing approach is developed in this work for effective determination of malathion. Malathion, as one of the most frequently used and broad-spectrum organophosphate pesticides (OPs) (Vasseghian et al., 2022), has a great impact on improving the productivity of crops, including wheat, grain, rice, and peanuts, and so forth. However, many studies have demonstrated that malathion is strongly related to the occurrence of many diseases, such as Alzheimer's disease (Venkatesan et al., 2017), systemic toxicity (Abdo et al., 2021), and cancer (Anjitha et al., 2020). The excessive use of OPs has brought about many serious problems and aroused great public concern in environmental protection, ecological balance, food safety, and human health. According to the Guidelines for Canadian

Drinking Water Quality, the maximum acceptable concentration (MAC) of malathion in drinking water is set at 290 μg/L. And the government in China has also issued the standard of malathion in drinking water (GB 5749-2006) at 250 μg/L (Sang et al., 2022). It is thereby urgently demanded to develop effective methods for malathion quantification (Albuquerque and Poppi, 2015; Zhang et al., 2018; Wang et al., 2019).

A variety of conventional methods have been utilized for the determination of malathion at trace level, including gas chromatography (GC) (Bavcon et al., 2003), high-performance liquid chromatography (HPLC) (Bazmandegan-Shamili et al., 2017), gas chromatography-mass spectrometry (GC-MS) (Latifah et al., 2011), and so on. Nevertheless, they suffer from certain drawbacks, since these methods are highly dependent on the applications of costly and sophisticated equipment, which always need to be operated by skilled personnel in a relatively time-consuming fashion. Considerable effort has thus devoted to developing fast and accurate approaches for malathion analyses. Enzyme-linked immunosorbent assays (ELISA) (Brun et al., 2005; Tamarit-López et al., 2011) represent one of the most typical and powerful strategies among them. In ELISA, antibodies are indispensable for analyte recognition and subsequent signal reporting in ELISA for malathion detection. However, antibodies are difficult to obtain, highly expensive, and easily denatured. ELISA also involves many tedious washing and separation steps (Jaria et al., 2020). Furthermore, sensitive biosensors have been constructed for malathion assay *via* the utilization of acetylcholinesterase (AChE) (Raghu et al., 2014; He et al., 2018; Bao et al., 2019; Chen et al., 2021), which serves as important analyte recognition element due to the remarkable activity inhibition of AChE by malathion. However, the sensing mechanisms are always established in a turn-off manner, which easily causes undesired false results. Other than this, the AChE activity is easily affected by many unexpected factors, such as high temperature and harsh buffer solution, which may ruin the detection reliability. Therefore, enzyme-free strategies are superior in terms of assay cost, simplicity of experimental procedures, and detection reliability.

To circumvent the potential problems mentioned above, aptamer can provide an ideal solution. Aptamer is single-strand oligonucleotide probe achieved by *in vitro* selection process called systematic evolution of ligands by exponential enrichment (SELEX) (Meng et al., 2015), which targets to a wide range of analytes, such as small molecules (Lou et al., 2019; Luo et al., 2019), metal ions (Raducanu et al., 2020), proteins (Lo et al., 2021), tumor markers (Li et al., 2022), and even the whole cells (Lv et al., 2021). Aptamer possesses many advantages, such as ease of synthesis and modification, small size, high affinity, low cost, high thermal stability, wide types of targets, and compatible for many signal reporting techniques. The last decade has witnessed the great progress in the development of aptasensors for malathion monitoring, which are usually coupled with colorimetric (Bala et al., 2016; Bala et al., 2017), fluorescent (Bala et al., 2018; Huang et al., 2021), electrochemical (Xu et al., 2019; Xu et al., 2021b), and chemiluminescent (Wu et al., 2021) techniques. Colorimetric detection methods have attracted special attention due to the instrument-free, easy-to-use, and low-cost features (Guo et al., 2021; Wu et al., 2022). It is thus of great importance to develop simple yet robust methods for malathion analysis.

Toward this goal, we herein propose an efficient colorimetric aptasensor for malathion detection, which is an antibody- and enzyme-free sensing system and can be performed in a washing- and device-free fashion. There are three species in the sensing system, including aptamer probes, protamine molecules, and unmodified gold nanoparticles (AuNPs). Aptamer probes are used as specific ligands for malathion recognition, and AuNPs serving as extremely sensitive colorimetric indicators. Furthermore, protamine molecules play an essential role in modulating the interaction among AuNPs, aptamer probes, as well as malathion. The presence of malathion breaks the absorption balance between aptamer probes and protamine molecules, which subsequently induces aggregation of AuNPs followed by an obvious colour change ready for visual detection. The sensing of malathion is conducted in a mix-and-measure manner and response signals can be monitored by using the naked eye. The assay can be completed within 40 min with a detection limit of 1.48 μg/L, which is far below the standards of malathion in drinking water issued by the Chinese and Canadian governments. Therefore, we report a novel sensing method for malathion analysis, which is ease-to-use, inexpensive, and selective. The present work may find potential applications in agriculture, food safety, and human health.

2 Experimental section

2.1 Chemicals and materials

Chloroauric acid trihydrate ($HAuCl_4$) and trisodium citrate were both purchased from Macklin Biochemical Co. (Shanghai, China). Protamine sulfate salt was purchased from Sigma-Aldrich Co. (St. Louis, MO, United States). Organophosphorus pesticides, including malathion, acetamiprid, carbaryl, chlorpyrifos, methamidophos, and imidacloprid, were all obtained from Alta Scientific Co. (Tianjin, China). The aptamer probes of malathion with the sequences of 5′-AGC TTG CTG CAG CGA TTC TTG ATC GCC ACA GAG CT-3′, were ordered from Sangon Biotechnology Co. (Shanghai, China). All the reagents used were of analytical grade and were used as obtained without further purification. All the solution was prepared by using ultrapure water (resistivity≥18.2 MΩ cm) supplied by a Thermo Fisher Scientific GenPure water purification system (United States). The glassware was rinsed with aqua regia prior to use.

UV-vis absorption spectra were recorded using a Thermo Fisher Scientific Evolution 300 spectrophotometer (United States). UV-vis absorption spectra were scanned from 400 nm to 800 nm and then collected for further analysis. Dynamic light scattering (DLS) data and Zeta potential were obtained using a Brookhaven Instruments NanoBrook 90PlusZeta (United States). The transmission electron microscope (TEM) analyses were conducted by utilizing Hitachi H7800 microscope (Japan).

2.2 Synthesis of AuNPs

AuNPs were synthesized following the trisodium citrate reduction method with slight modifications (Grabar et al., 1995;

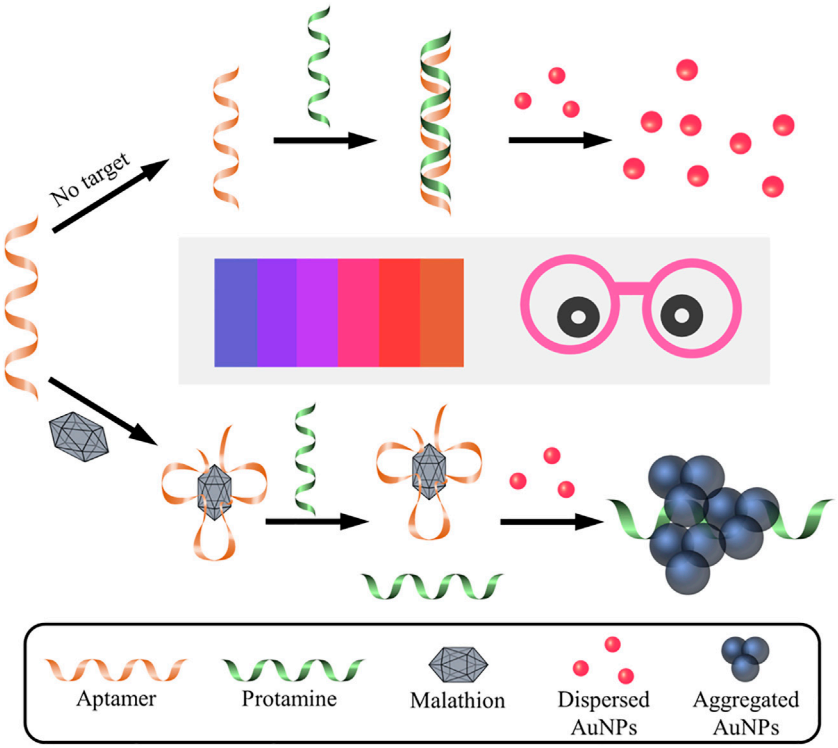

FIGURE 1
Schematic illustration of colorimetric aptasensor for malathion assay based on the utilization of protamine and AuNPs. Without the presence of malathion, aptamer probe is absorbed by protamine *via* electrostatic interactions, which makes it difficult for protamine to trigger the aggregation of AuNPs. As a result, the AuNPs remain well dispersed and exhibit red in color. On the contrary, the existence of malathion exhibits preferential binding affinity to aptamer, which is then unable to combine with protamine molecule. Consequently, protamine tends to mediate the aggregation of AuNPs and cause the color change to blue. It is noted that Pro, Apt, and Mal represent protamine, aptamer, and malathion, respectively. The color change of AuNPs solution can easily visualized by the naked eye and is closely related to the concentration of malathion in the solution.

Elghanian et al., 1997). Briefly, an aqueous of 0.01% $HAuCl_4$ (100 mL) solution was heated to boiling before 3 mL 1% trisodium citrate solution was quickly introduced under vigorous stirring (450 rpm). The mixture solution kept boiling for an additional 20 min. The solution colour gradually changed from pale yellow to light gray and eventually turned into wine red. This indicated the generation of AuNPs. The mixture was naturally cooled at room temperature with stirring and then stored in dark bottles at 4°C for further use. The UV-vis absorption spectra and Zeta potential were recorded to indicate the properties of AuNPs. DLS data and TEM image were used to determine the average size of the AuNPs.

2.3 Detection of malathion

The serial dilutions of malathion were prepared by introducing stock solution of malathion in acetone into phosphate buffer solution (pH 7.2) and then stored at −20°C before use. For malathion assay, malathion-specific aptamer (3 μL, 25 μM) was mixed with various concentrations of malathion, diluted with phosphate buffer, and then incubated for 10 min at room temperature. Next, protamine (3 μL, 50 μg/mL) was added and incubated for another 20 min. Finally, AuNPs (400 μL) were introduced into the above mixture and remained still for 10 min. Afterward, the absorption spectra were collected by using UV-vis spectrophotometer. The images of reaction samples were also taken for comparison. Moreover, the particle sizes were characterized and recorded. To study the assay selectivity, various un-specific organophosphorus pesticides such as acetamiprid, carbaryl, chlorpyrifos, methamidophos, and imidacloprid were also used as analogues to test the detection performance of the strategy.

2.4 Determination of malathion in spiked sample

Tap water directly taken from laboratory water outlet at Southern Medical University was chosen to evaluate the validity of the proposed strategy for real application. After filtered through a 0.45 μm membrane, the filtered tap water was spiked with malathion with concentrations of 10 μL and 50 μg/L to prepared the spiked samples. The as-prepared positive samples were then analysed according to the experimental procedure described above. And the theoretical values were calculated according to the established standard calibration curve.

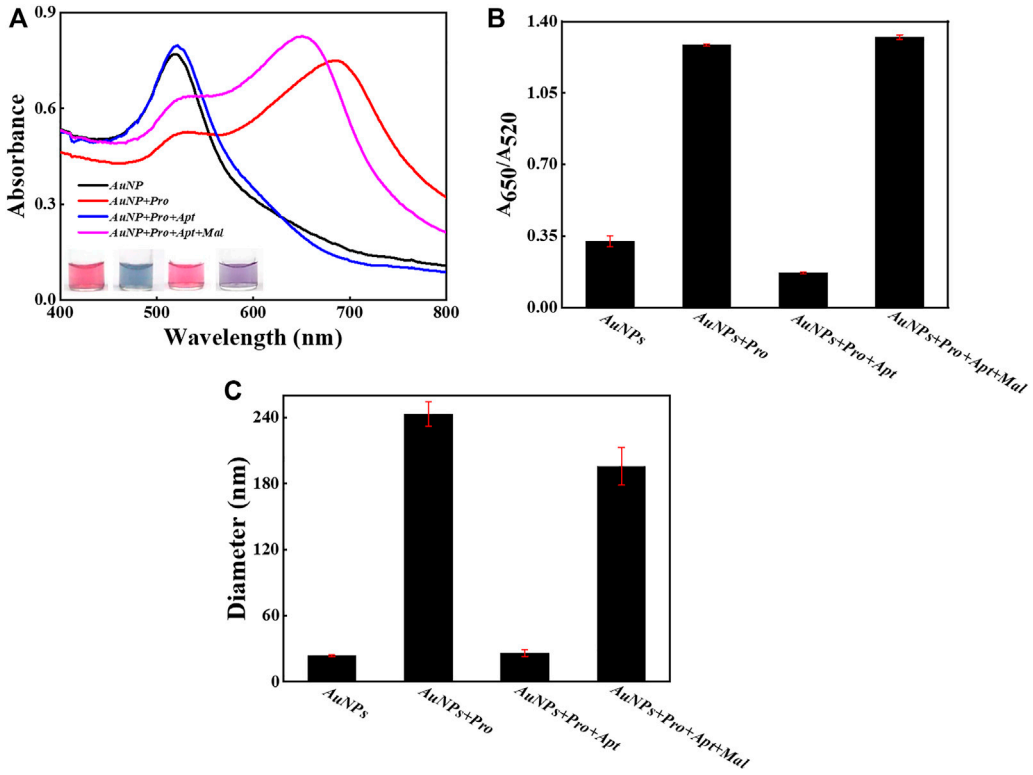

FIGURE 2
The feasibility examination. **(A)** The UV-Vis spectra of AuNPs and sample images with and without the introduction of malathion. **(B)** The values of A_{650}/A_{520} in different samples. **(C)** The DLS results in different samples. The error bars represent the standard deviation of three independent measurements.

3 Results and discussion

3.1 Working mechanism

The working mechanism of the designed aptasensor is depicted in Figure 1. In the absence of target malathion, the electrostatic absorption effect between the negatively charged aptamer probes and the polycation protamine molecules make it easy for them to form stable aptamer/protamine complex. The protamine molecules are then unable to interact with negatively charged AuNPs, which thus remain well dispersed in the solution with a red color. Nevertheless, the presence of malathion would consume the aptamer probes *via* the formation of malathion/aptamer complexes due to high affinity of aptamer towards malathion. The liberated polycation protamine would then be ready to induce the aggregation of AuNPs, imparting a color change from red to blue. There are several merits in the present sensing system for visual detection of malathion. Firstly, the sensing system is very simple, since there are no antibodies or enzymes involved. What are really demanded are only aptamer probes, protamine molecules, and unmodified AuNPs. Furthermore, the assay is easily performed with one mix-and-measure step, without the requirement of repeated washing and separation procedures. More importantly, the response signal can be readily observed by using the naked eye. Consequently, it is an enzyme- and device-free method for sensitive and rapid detection of malathion.

3.2 Characterization of AuNPs

AuNPs were synthesized by employing classic chemical methodology, in which trisodium citrate served a dual purpose, reduction agent and capping agent. AuNPs were then characterized by using UV-Vis spectrophotometer, visual detection, DLS, and TEM, as demonstrated in Supplementary Figure S1. The AuNP solution displayed red and had a strong absorption at around 520 nm (Supplementary Figure S1A). The hydrodynamic diameter of AuNPs was estimated to be 18.47 nm (Supplementary Figure S1B). As shown in Supplementary Figure S1C, the size of AuNPs determined by TEM was about 13 nm. Furthermore, AuNPs beard a negative surface charge and a Zeta potential of −37.31 mV was recorded (Supplementary Figure S1D), which was attributed to the coverage of citrate layer. All the results suggest that AuNPs with desired properties were fabricated and ready for further use.

3.3 Feasibility confirmation

To verify the detection principle as demonstrated in Figure 1, several samples were intentionally prepared and their response signals were carefully compared and analyzed (Figure 2). As shown in Figure 2A, the absorption peak of bare AuNPs was around 520 nm, and it shifted to about 690 nm upon the

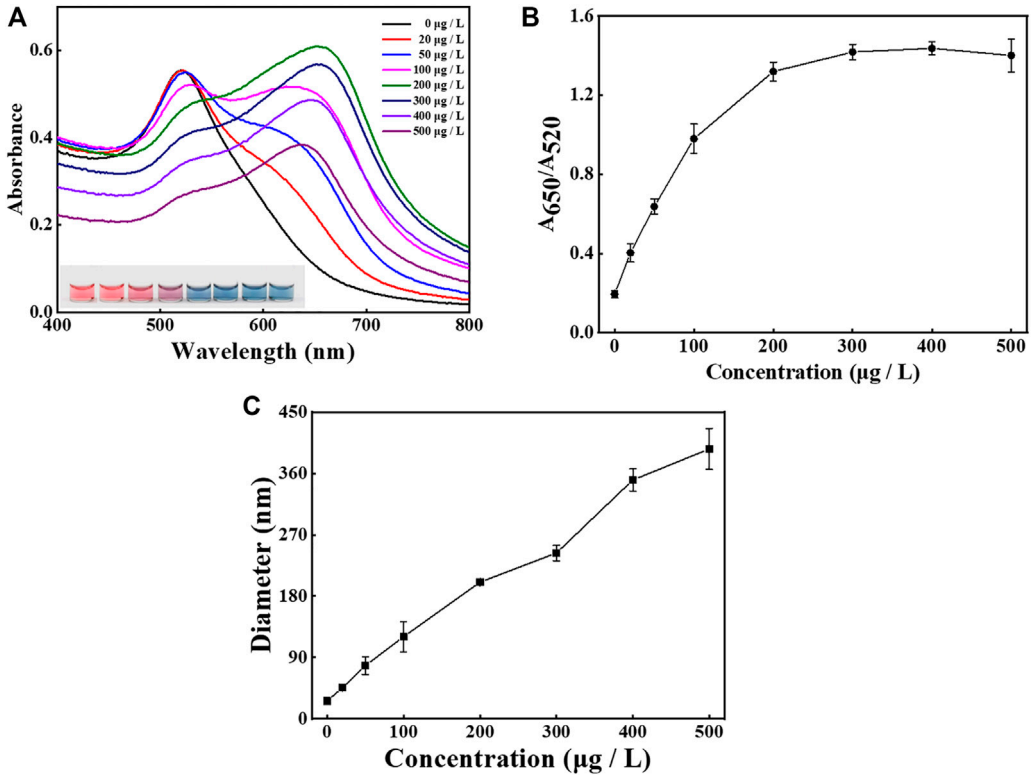

FIGURE 3
Condition investigation. The effect of protamine concentration (from 0 to 500 μg/L) on the sensing performance. **(A)** The UV-Vis spectra of AuNPs and sample images after the addition of protamine with varying concentrations. **(B)** The values of A_{650}/A_{520} after the addition of protamine with varying concentrations. **(C)** The DLS sizes of AuNPs after the addition of protamine with varying concentrations. The error bars represent the standard deviation of three independent measurements.

introduction of protamine molecules, which suggests that AuNPs aggregated due to the electrostatic interactions between protamine and AuNPs. Interestingly, the absorption peak went back to about 520 nm after the addition of aptamer probes, which indicates that aptamer probes were able to reverse the aggregation behaviors of AuNPs. More importantly, the absorption peak moved to about 650 nm after the introduction of malathion, which confirmed the formation of AuNPs aggregation. The images of samples also revealed the status and color changes of AuNPs upon different stimulus. These visual detection results were consistent with those indicated by UV-vis spectra. The ratio of optical density between 650 nm and 520 nm is a typical indicator to illustrate the dispersion status of AuNPs. The results of A650/A520 (Figure 2B) support the fact that malathion was able to induce the aggregation of AuNPs. Moreover, the sizes of these samples were measured (Figure 2C). The AuNPs alone reported a hydrodynamic size of about 24 nm, and then grew to about 243 nm after mixing with protamine molecule. However, the hydrodynamic size returned back to around 26 nm upon the introduction of aptamer probes into the mixture containing AuNPs and protamine. The addition of malathion then permitted the AuNPs to aggregate with a hydrodynamic size of 196 nm. The results together verify that the working principle depicted in Figure 1 worked well as designed.

3.4 Condition optimization

To achieve the optimal performance, several important experimental parameters in the sensing system were optimized, including the concentrations of protamine (Figure 3) and aptamer probes (Figure 4), as well as the incubation time between the aptamer and malathion (Supplementary Figure S2). To study the effect of protamine concentration, AuNPs were mixed with varied protamine concentrations ranging from 0 to 500 μg/L. As shown in Figure 3, the UV-Vis spectra, actual images, and DLS measurements were recorded and plotted for further analyses. The UV-Vis spectra shifted red with the growing of protamine concentration (Figure 3A). Meanwhile, the color of samples changed from pink to blue as the protamine increased, and then remained unchanged after the concentration reached 300 μg/L. As presented in Figure 3B, the value of A_{650}/A_{520} gradually rose and then stabilized when the protamine concentration arrived at 300 μg/L. Consequently, 300 μg/L was chosen for subsequent experiments. It is also observed from Figure 3C that the sizes of AuNPs had a linear dependence on the concentrations of protamine molecules.

The effect of aptamer amounts on the dispersion of AuNPs and the performance of the method was also examined, as shown in Figure 4. The UV-Vis spectra shifted blue as the concentration of aptamer increased (Figure 4A), and the images reveal that the solution color varied from blue to pink. As presented in

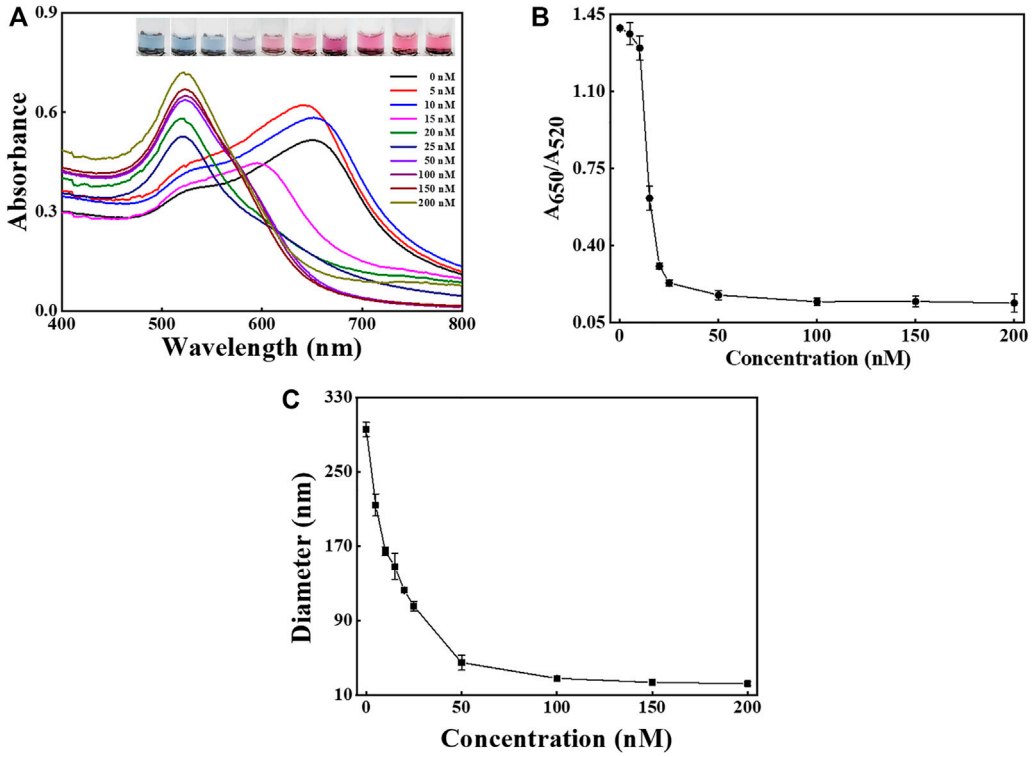

FIGURE 4
Condition investigation. The effect of aptamer amounts (from 0 to 200 nM) on the sensing performance. **(A)** The UV-Vis spectra and sample images of AuNPs after the addition of aptamer with different concentrations. **(B)** The values of A_{650}/A_{520} after the addition of aptamer with different concentrations. **(C)** The DLS sizes of AuNPs after the addition of aptamer with different concentrations. The error bars represent the standard deviation of three independent measurements.

Figure 4B the ratio of A_{650}/A_{520} gradually decreased and became stable at aptamer concentration higher than 150 nM. The result indicates that 150 nM was sufficiently high to protect the stability of AuNPs. The DLS results suggest that the hydrodynamic diameter of AuNPs sharply dropped when the aptamer amounts rose and then levelled off at about 150 nM (Figure 4C).

In order to keep a good balance between the effective binding and rapid detection, the incubation time between malathion and aptamer probes was also investigated, as shown in Supplementary Figure S2. The UV-Vis spectra of several time points kept unchanged (Supplementary Figure S2A) and the A_{650}/A_{520} was stable (Supplementary Figure S2B). The results demonstrate that the interaction between malathion and the corresponding aptamer might be completed within 10 min. As a result, 10 min was chosen for the subsequent experiments.

3.5 Sensitivity and specificity evaluation

After careful evaluation of optimized reaction conditions, the sensing performance of the aptasensor was assessed by utilizing UV-vis spectroscopy, visual observation, and DLS. To study the sensitivity of the designed method, the malathion with concentration ranging from 1 to 1,000 μg/L was added followed by the signal recording under the optimized experimental conditions (Figure 5). As seen in Figure 5A, when the concentrations of malathion grew higher, the absorption spectrums decreased at 520 nm and meanwhile increased at 650 nm. The color of samples also changed from red to blue. The dependency of A_{650}/A_{520} with the malathion levels was plotted in Figure 5B. A_{650}/A_{520} increased linearly with the concentrations of malathion varying from 1 to 50 μg/L, as shown in Figure 5C. The limit of detection (LOD) was theoretically calculated as 1.48 μg/L with a regression coefficient R^2 = 0.9931 based on the 3σ/s rule, in which σ is the standard deviation of the background signal and s stands for the slope of the calibration plot. It is noted that the LOD is below the maximum residue limit of malathion (10 μg/L) set by China's Agriculture Ministry (GB 2736-2021). The performance of the current assay method was compared with previously reported approaches (Table 1). It is noted that the detection limit of the current method is poorer than some other strategies, such as fluorescent (Chen et al., 2020), electrochemical (He et al., 2018), and chemiluminescent sensors (Wu et al., 2021). Fortunately, it is still sufficiently sensitive to meet the application requirement for malathion monitoring in drinking water. As reported in previous research, GNP-based DLS methods are able to achieve significantly enhanced sensitivities for the detection of DNA (Dai et al., 2008), proteins (Jans et al., 2009), and As(III) ions (Kalluri et al., 2009). But unlike the unmodified GNPs used in this work, the surfaces of GNPs need to be further functionalized to realize the assay.

The specificity was accessed by challenging the system with potential interfering agents such as acetamiprid, carbaryl,

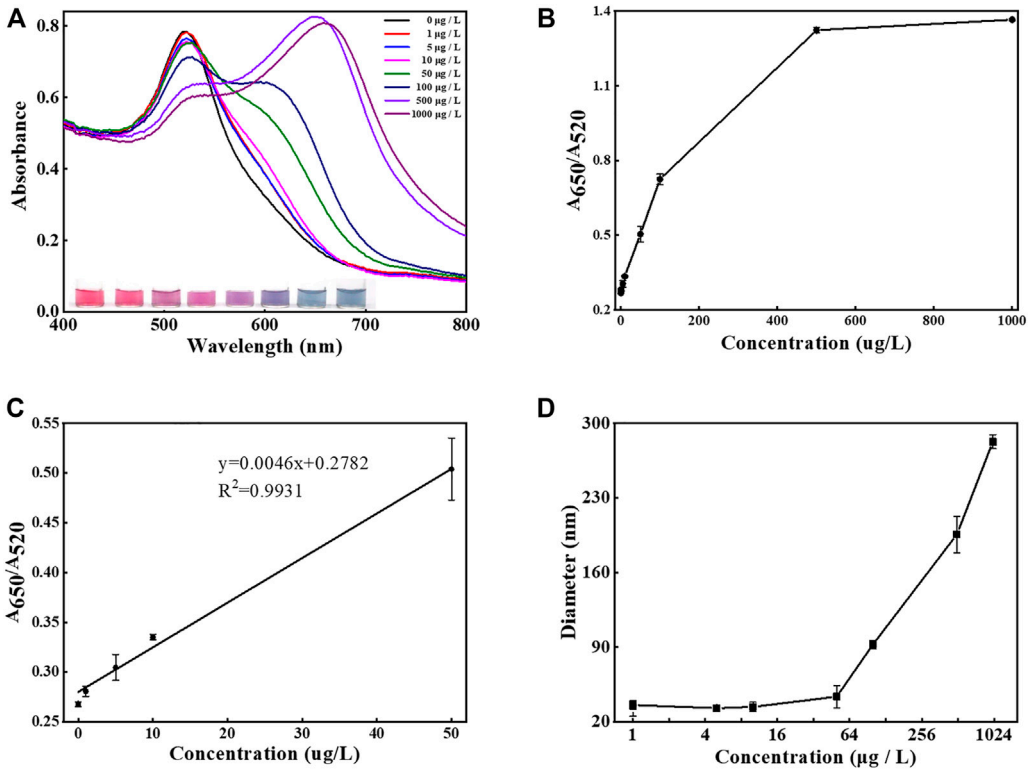

FIGURE 5
Sensitivity determination. **(A)** The UV-Vis spectra and images recorded after the introduction of malathion with concentrations from 0 to 1,000 μg/L. **(B)** The dependence of the values of A_{650}/A_{520} against various target concentrations from 0 to 1,000 μg/L. **(C)** The linear relationship between the values of A_{650}/A_{520} and the concentration of malathion from 0 to 50 μg/L. **(D)** The dependence of the DLS sizes of AuNPs in solution against various target concentrations from 0 to 1,000 μg/L. The error bars represent the standard deviation of three independent measurements.

TABLE 1 The performance comparison of malathion detection methods.

Methodology	Linear range (μg/L)	LOD (μg/L)	Ref
electrochemical	—	6.7	Wang et al. (2016)
	1-10000	0.16	He et al. (2018)
fluorescence	100-25000	10	Wang et al. (2019)
	3.3-330	0.47	Chen et al. (2020)
surface-enhanced Raman scattering	167-3333	167	Nie et al. (2018)
	—	123	Albuquerque et al. (2015)
resonance Rayleigh scattering	12-800	1.7	Huang et al. (2019)
chemiluminescence	—	1.57×10^{-4}	Wu et al. (2021)
localized surface plasmon resonance	—	1.8×10^{3}	Dissanayake et al. (2019)
colorimetric	10-120	3.1	Xu et al. (2021a)
	16.6-233	3.93	Li et al. (2019)
	8.3-5333	7.5	Liu et al. (2021)
	1-5000	14	Faghiri et al. (2021)
	0-50	1.48	This work

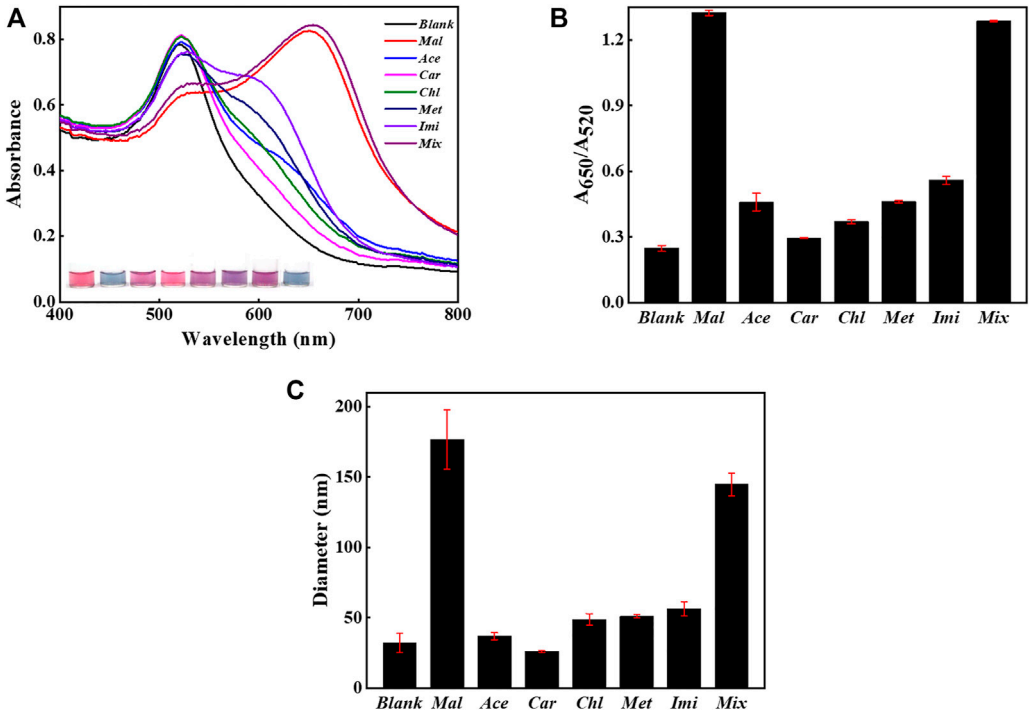

FIGURE 6
Selectivity evaluation. The sensing method when challenged with 1,000 μg/L non-specific substances alone or coexisting with the presence of 500 μg/L malathion. **(A)** The UV-Vis spectra of AuNPs and sample images after the introduction of non-specific analytes with or without the presence of malathion. **(B)** The values of A_{650}/A_{520} in different samples. **(C)** The DLS sizes of AuNPs in different samples. The error bars represent the standard deviation of three independent measurements.

TABLE 2 The recovery tests of malathion spiked in tap water using the current method.

Sample	Target added (μg/L)	Target found (μg/L)	Recovery (%)
1	10	9.9 ± 3.3	98.9
2	50	54.7 ± 5.9	109.4

chlorpyrifos, methamidophos, and imidacloprid, as displayed in Figure 6. The presence of malathion alone or co-existing with interfering agents caused a significant change in the UV-Vis spectra and solution color (Figure 6A). But the sensing system did not have response upon the addition of non-specific targets, since the UV-Vis spectra and solution color remained unchanged compared with the blank sample. Additionally, the value of A_{650}/A_{520} clearly distinguished the signal produced by malathion from those caused by the other competitive organophosphorus pesticides, as found from Figure 6B. The co-existence of non-specific pesticides did not affect the sensing of malathion. As demonstrated in Figure 6C, the samples containing malathion also reported considerably higher sizes than those involving un-specific analytes. All these results confirm that the constructed sensing strategy was highly specific for malathion due to the high affinity of aptamer to malathion. Moreover, the sensing system was highly stable even in the presence of a great number of interfering agents, which guarantees the detection reliability.

3.6 Practical application

In order to assess the capability of the detection method for real sample, the malathion in tap water was also detected and analyzed. Malathion with various concentration (10 μg/L and 50 μg/L) were individually spiked into tap water, The results were given in Table 2. It is shown that the acceptable recovery rates ranging from 98.9% to 109.4% were achieved. The data indicates that the proposed aptasensor had a promising potential in real applications.

To confirm the detection accuracy, HPLC method was used for the built of calibration curve (Supplementary Figure S3A) and the recovery rates of several concentrations of malathion spiked into tape water were determined, and the results could be found from Supplementary Figure S3b; Table 3. The data reveals that the present method was accurate for malathion assay in real sample and held a promising for further applications.

There are some limitations in the current work. First of all, although barely GNPs are easily synthesized and serve as excellent color indicators, their colloidal stability is highly sensitive to the

TABLE 3 The recovery tests of malathion spiked in tap water using HPLC.

Sample	Malathion added (μg/L)	Malathion detected (μg/L)	Recovery rate (%)
1	150	150.3 ± 15.3	100.2
2	300	320.4 ± 19.5	106.8
3	600	691.3 ± 45.7	115.2

choice of buffer, salt concentration, and pH values. To improve their stability and avoid undesired aggregation, surface functionalization may provide an effective solution to this issue. Moreover, the length of aptamer probes is also an important factor that may influence the stability and eventually the sensing performance for malathion assay. Therefore, the choice of aptamer strands and the reaction buffer is an essential step in the construction of this kind of colorimetric sensors.

4 Conclusion

Aptamers, a superior alternative to antibodies, have emerged as powerful bio-inspired receptors for the design and applications of new biosensors, especially combining with nanomaterials. Inspired by target recognition in nature, an aptamer-mediated, gold nanoparticle-based sensing approach was deployed to quantify malathion in a robust and selective fashion. The assay of malathion could be conducted within 40 min in a add-and-observe manner by using the naked eye. This label-, antibody-, and device-free method was able to detect malathion as low as 1.48 μg/L (0-50 μg/L) and held a promising potential for monitoring malathion in drinking water. The detection accuracy was also verified by the HPLC method. By selecting proper aptamer probes for relevant targets of interest, the sensing concept in this work can be easily extended for the detection of other analytes. This will be our future concern. The construction of powerful aptasensor may open a new path for efficient reporting of pesticides, which benefits the development of agriculture, environmental protection, food control, and public health.

Data availability statement

The original contributions presented in the study are included in the article/Supplementary Material, further inquiries can be directed to the corresponding author.

Author contributions

PL: Methodology, validation, and writing-original draft. HZ: Methodology, investigation, and writing-original draft. ST: Data curation, investigation, and methodology. ZX: Writing-review and editing. JH: Conceptualization, supervision, writing-review and editing, and funding acquisition.

Funding

This work was supported by the National Natural Science Foundation of China under Grant No. 21975117.

Conflict of interest

The authors declare that the research was conducted in the absence of any commercial or financial relationships that could be construed as a potential conflict of interest.

Publisher's note

All claims expressed in this article are solely those of the authors and do not necessarily represent those of their affiliated organizations, or those of the publisher, the editors and the reviewers. Any product that may be evaluated in this article, or claim that may be made by its manufacturer, is not guaranteed or endorsed by the publisher.

Supplementary material

The Supplementary Material for this article can be found online at: https://www.frontiersin.org/articles/10.3389/fbioe.2023.1165724/full#supplementary-material

References

Abdo, W., Elmadawy, M. A., Abdelhiee, E. Y., Abdel-Kareem, M. A., Farag, A., Aboubakr, M., et al. (2021). Protective effect of thymoquinone against lung intoxication induced by malathion inhalation. *Sci. Rep.* 11, 2498. doi:10.1038/s41598-021-82083-w

Albuquerque, C. D. L., and Poppi, R. J. (2015). Detection of malathion in food peels by surface-enhanced Raman imaging spectroscopy and multivariate curve resolution. *Anal. Chim. Acta* 879, 24–33. doi:10.1016/j.aca.2015.04.019

Anjitha, R., Antony, A., Shilpa, O., Anupama, K. P., Mallikarjunaiah, S., and Gurushankara, H. P. (2020). Malathion induced cancer-linked gene expression in human lymphocytes. *Environ. Res.* 182, 109131. doi:10.1016/j.envres.2020.109131

Bala, R., Dhingra, S., Kumar, M., Bansal, K., Mittal, S., Sharma, R. K., et al. (2017). Detection of organophosphorus pesticide–Malathion in environmental samples using peptide and aptamer based nanoprobes. *Chem. Eng. J.* 311, 111–116. doi:10.1016/j.cej.2016.11.070

Bala, R., Kumar, M., Bansal, K., Sharma, R. K., and Wangoo, N. (2016). Ultrasensitive aptamer biosensor for malathion detection based on cationic polymer and gold nanoparticles. *Biosens. Bioelectron.* 85, 445–449. doi:10.1016/j.bios.2016.05.042

Bala, R., Swami, A., Tabujew, I., Peneva, K., Wangoo, N., and Sharma, R. K. (2018). Ultra-sensitive detection of malathion using quantum dots-polymer based fluorescence aptasensor. *Biosens. Bioelectron.* 104, 45–49. doi:10.1016/j.bios.2017.12.034

Bao, J., Huang, T., Wang, Z. N., Yang, H., Geng, X. T., Xu, G. L., et al. (2019). 3D graphene/copper oxide nano-flowers based acetylcholinesterase biosensor for sensitive detection of organophosphate pesticides. *Sens. Actuat B-Chem.* 279, 95–101. doi:10.1016/j.snb.2018.09.118

Bavcon, M., Trebse, P., and Zupancic-Kralj, L. (2003). Investigations of the determination and transformations of diazinon and malathion under environmental conditions using gas chromatography coupled with a flame ionisation detector. *Chemosphere* 50, 595–601. doi:10.1016/s0045-6535(02)00643-4

Bazmandegan-Shamili, A., Shabani, A. M. H., Dadfarnia, S., Moghadam, M. R., and Saeidi, M. (2017). Preparation of magnetic mesoporous silica composite for the solid-phase microextraction of diazinon and malathion before their determination by high-performance liquid chromatography. *J. Sep. Sci.* 40, 1731–1738. doi:10.1002/jssc.201601339

Brun, E. M., Garces-Garcia, M., Banuls, M. J., Gabaldon, J. A., Puchades, R., and Maquieira, A. (2005). Evaluation of a novel malathion immunoassay for groundwater and surface water analysis. *Environ. Sci. Technol.* 39 (8), 2786–2794. doi:10.1021/es048945u

Chen, Q. S., Sheng, R., Wang, P. Y., Ouyang, Q., Wang, A. C., Ali, S., et al. (2020). Ultra-sensitive detection of malathion residues using FRET-based upconversion fluorescence sensor in food. *Spectrochim. Acta. A.* 241, 118654. doi:10.1016/j.saa.2020.118654

Chen, Y., Zhu, Y. Y., Zhao, Y. H., and Wang, J. (2021). Fluorescent and colorimetric dual-response sensor based on copper (II)-decorated graphitic carbon nitride nanosheets for detection of toxic organophosphorus. *Food Chem.* 345, 128560. doi:10.1016/j.foodchem.2020.128560

Dai, Q., Liu, X., Coutts, J., Austin, L., and Huo, Q. (2008). A one-step highly sensitive method for DNA detection using dynamic light scattering. *J. Am. Chem. Soc.* 130, 8138–8139. doi:10.1021/ja801947e

Dissanayake, N. M., Arachchilage, J. S., Samuels, T. A., and Obare, S. O. (2019). Highly sensitive plasmonic metal nanoparticle-based sensors for the detection of organophosphorus pesticides. *Talanta* 200, 218–227. doi:10.1016/j.talanta.2019.03.042

Elghanian, R., Storhoff, J. J., Mucic, R. C., Letsinger, R. L., and Mirkin, C. A. (1997). Selective colorimetric detection of polynucleotides based on the distance-dependent optical properties of gold nanoparticles. *Science* 277, 1078–1081. doi:10.1126/science.277.5329.1078

Faghiri, F., Hajjami, M., and Ghorbani, F. (2021). Development of a sensing system based on coupling magnetic solid phase extraction and colorimetric detection for determination of organophosphorus pesticides in fruit extract and environmental sample. *Sens. Actuat B-Chem.* 343, 130157. doi:10.1016/j.snb.2021.130157

Grabar, K. C., Freeman, R. G., Hommer, M. B., and Natan, M. J. (1995). Preparation and characterization of Au colloid monolayers. *Anal. Chem.* 67, 735–743. doi:10.1021/ac00100a008

Guo, W. F., Zhang, C. X., Ma, T. T., Liu, X. Y., Chen, Z., Li, S., et al. (2021). Advances in aptamer screening and aptasensors' detection of heavy metal ions. *J. Nanobiotechnol* 10, 166. doi:10.1186/s12951-021-00914-4

He, L. H., Cui, B. B., Liu, J. M., Song, Y. P., Wang, M. H., Peng, D. L., et al. (2018). Novel electrochemical biosensor based on core-shell nanostructured composite of hollow carbon spheres and polyaniline for sensitively detecting malathion. *Sens. Actuat B-Chem.* 258, 813–821. doi:10.1016/j.snb.2017.11.161

Huang, N. N., Hu, X. T., Li, W. T., Mwakosya, A. W., Guo, Z. Q., Xu, Y. W., et al. (2021). Fluorescence and colorimetric dual-mode sensor for visual detection of malathion in cabbage based on carbon quantum dots and gold nanoparticles. *Food Chem.* 343, 128494. doi:10.1016/j.foodchem.2020.128494

Huang, Y. M., Yang, J. D., Cheng, J. W., Zhang, Y. H., and Yuan, H. Y. (2019). A novel spectral method for determination of trace malathion using EryB as light scattering probe by resonance Rayleigh scattering technique. *Spectrochim. Acta. A.* 213, 104–110. doi:10.1016/j.saa.2019.01.022

Jans, H., Liu, X., Austin, L., Maes, G., and Huo, Q. (2009). Dynamic light scattering as a powerful tool for gold nanoparticle bioconjugation and biomolecular binding studies. *Anal. Chem.* 81, 9425–9432. doi:10.1021/ac901822w

Jaria, G., Calisto, V., Otero, M., and Esteves, V. I. (2020). Monitoring pharmaceuticals in the aquatic environment using enzyme-linked immunosorbent assay (ELISA)-a practical overview. *Anal. Bioanal. Chem.* 412, 3983–4008. doi:10.1007/s00216-020-02509-8

Kalluri, J., Arbneshi, T., Khan, S. A., Neely, A., Candice, P., Varisli, B., et al. (2009). Use of gold nanoparticles in a simple colorimetric and ultrasensitive dynamic light scattering assay: Selective detection of arsenic in groundwate. *Angew. Chem. Int. Ed.* 121, 9848–9851. doi:10.1002/ange.200903958

Latifah, A. M., Musa, R. D., and Latiff, P. A. (2011). Gas chromatography mono spectrometry study of malathion residues in *Centella asiatica*. *Iran. J. Environ. Healt* 8, 57–64.

Li, D. X., Wang, S., Wang, L., Zhang, H., and Hu, J. D. (2019). A simple colorimetric probe based on anti-aggregation of AuNPs for rapid and sensitive detection of malathion in environmental samples. *Anal. Bioanal. Chem.* 411, 2645–2652. doi:10.1007/s00216-019-01703-7

Li, P., Li, W. Q., Xie, Z. H., Zhan, H. N., Deng, L. H., and Huang, J. H. (2022). A label-free and signal-amplifiable assay method for colorimetric detection of carcinoembryonic antigen. *Biotechnol. Bioeng.* 119, 504–512. doi:10.1002/bit.28003

Liu, P., Li, X., Xu, X. C., Niu, X. H., Wang, M. Z., Zhu, H. J., et al. (2021). Analyte-triggered oxidase-mimetic activity loss of Ag_3PO_4/UiO-66 enables colorimetric detection of malathion completely free from bioenzymes. *Sens. Actuat B-Chem.* 338, 129866. doi:10.1016/j.snb.2021.129866

Lo, Y., Cheung, Y. W., Wang, L., Lee, M., Figueroa-Miranda, G., Liang, S. L., et al. (2021). An electrochemical aptamer-based biosensor targeting Plasmodium falciparum histidine-rich protein II for malaria diagnosis. *Biotechnol. Bioeng.* 192, 113472. doi:10.1016/j.bios.2021.113472

Lou, Y. F., Peng, Y. B., Luo, X. W., Yang, Z. M., Wang, R. F., Sun, D. W., et al. (2019). A universal aptasensing platform based on cryonase-assisted signal amplification and graphene oxide induced quenching of the fluorescence of labeled nucleic acid probes: Application to the detection of theophylline and ATP. *Microchim. Acta* 186, 494. doi:10.1007/s00604-019-3596-1

Luo, X. W., Chen, Z. F., Li, H. F., Li, W. Q., Cui, L., and Huang, J. H. (2019). Exploiting the application of L -aptamer with excellent stability: An efficient sensing platform for malachite green in fish samples. *Analyst* 144, 4204–4209. doi:10.1039/c9an00332k

Lv, Z. X., Wang, Q. Q., and Yang, M. H. (2021). Multivalent duplexed-aptamer networks regulated a CRISPR-cas12a system for circulating tumor cell detection. *Anal. Chem.* 93, 12921–12929. doi:10.1021/acs.analchem.1c02228

Meng, H. M., Fu, T., Zhang, X. B., and Tan, W. H. (2015). Cell-SELEX-based aptamer-conjugated nanomaterials for cancer diagnosis and therapy. *Natl. Sci. Rev.* 2, 71–84. doi:10.1093/nsr/nwv001

Nie, Y. H., Teng, Y. J., Li, P., Liu, W. H., Shi, Q. W., and Zhang, Y. C. (2018). Label-free aptamer-based sensor for specific detection of malathion residues by surface-enhanced Raman scattering. *Spectrochim. Acta. A.* 191, 271–276. doi:10.1016/j.saa.2017.10.030

Raducanu, V. S., Rashid, F., Zaher, M. S., Li, Y. Y., Merzaban, J. S., and Hamdan, S. M. (2020). A direct fluorescent signal transducer embedded in a DNA aptamer paves the way for versatile metal-ion detection. *Sens. Actuat B-Chem.* 304, 127376. doi:10.1016/j.snb.2019.127376

Raghu, P., Reddy, T. M., Reddaiah, K., Swamy, B. E. K., and Screedhar, M. (2014). Acetylcholinesterase based biosensor for monitoring of malathion and acephate in food samples: A voltammetric study. *Food Chem.* 142, 188–196. doi:10.1016/j.foodchem.2013.07.047

Sang, C. H., Yu, Z. Y., An, W., Sørensen, P. B., Jin, F., and Yang, M. (2022). Development of a data driven model to screen the priority control pesticides in drinking water based on health risk ranking and contribution rates. *Environ. Int.* 158, 106901. doi:10.1016/j.envint.2021.106901

Tamarit-López, J., Morais, S., Puchades, R., and Maquieira, Á. (2011). Direct hapten-linked multiplexed immunoassays on polycarbonate surface. *Biosens. Bioelectron.* 26, 2694–2698. doi:10.1016/j.bios.2010.08.066

Vasseghian, Y., Almomani, F., Van, T. L., Moradi, M., and Dragoi, E. N. (2022). Decontamination of toxic Malathion pesticide in aqueous solutions by Fenton-based processes: Degradation pathway, toxicity assessment and health risk assessment. *J. Hazard Mater* 423, 127016. doi:10.1016/j.jhazmat.2021.127016

Venkatesan, R., Park, Y. U., Ji, E., Yeo, E. J., and Kim, S. Y. (2017). Malathion increases apoptotic cell death by inducing lysosomal membrane permeabilization in N2a neuroblastoma cells: A model for neurodegeneration in alzheimer's disease. *Cell Death Discov.* 3, 17007. doi:10.1038/cddiscovery.2017.7

Wang, M., Su, K., Cao, J., She, Y. X., Abd Ei-Aty, A. M., Hacımüftüoğlu, A., et al. (2019). Off-On" non-enzymatic sensor for malathion detection based on fluorescence resonance energy transfer between β-cyclodextrin@Ag and fluorescent probe. *Talanta* 192, 295–300. doi:10.1016/j.talanta.2018.09.060

Wang, T., Reid, R. C., and Minteer, S. D. (2016). A paper-based mitochondrial electrochemical biosensor for pesticide detection. *Electroanal* 28, 854–859. doi:10.1002/elan.201500487

Wu, D., Gordon, C. K. L., Shin, J. H., Eisenstein, M., and Soh, H. T. (2022). Directed evolution of aptamer discovery technologies. *Acc. Chem. Res.* 55, 685–695. doi:10.1021/acs.accounts.1c00724

Wu, H., Wu, J., Wang, H. Y., Liu, Y. L., Han, G. Q., and Zou, P. (2021). Sensitive and label-free chemiluminescence detection of malathion using exonuclease-assisted dual signal amplification and G-quadruplex/hemin DNAzyme. *J. Hazard. Mat.* 411, 124784. doi:10.1016/j.jhazmat.2020.124784

Xu, D., Li, R. Y., Wang, Q. S., Yang, Y. Q., Zhu, H. Y., and Li, Z. J. (2021a). A NiAg-graphene quantum dot-graphene hybrid with high oxidase-like catalytic activity for sensitive colorimetric detection of malathion. *New J. Chem.* 45, 7129–7137. doi:10.1039/d1nj00621e

Xu, G. L., Hou, J. Z., Zhao, Y. N., Bao, J., Yang, M., Fa, H. B., et al. (2019). Dual-signal aptamer sensor based on polydopamine-gold nanoparticles and exonuclease I for ultrasensitive malathion detection. *Sens. Actuat B-Chem.* 287, 428–436. doi:10.1016/j.snb.2019.01.113

Xu, G. L., Huo, D. Q., Hou, J. Z., Zhang, C., Zhao, Y. N., Hou, C. J., et al. (2021b). An electrochemical aptasensor of malathion based on ferrocene/DNA-hybridized MOF, DNA coupling-gold nanoparticles and competitive DNA strand reaction. *Microchem. J.* 162, 105829. doi:10.1016/j.microc.2020.105829

Zhang, Y. F., Bromberg, L., Lin, Z., Brown, P., Voorhis, T. V., and Hatton, T. A. (2018). Polydiacetylene functionalized with charged termini for device-free colorimetric detection of malathion. *J. Colloid. Interf. Sci.* 528, 27–35. doi:10.1016/j.jcis.2018.04.098

frontiers | Frontiers in Bioengineering and Biotechnology

TYPE Original Research
PUBLISHED 03 April 2023
DOI 10.3389/fbioe.2023.1183799

OPEN ACCESS

EDITED BY
Feilong Zhang,
Nanyang Technological University,
Singapore

REVIEWED BY
Wenxin Fu,
Institute of Chemistry Chinese Academy of Sciences, China
Huan Liu,
Beihang University, China

*CORRESPONDENCE
Ye Tian,
tianyely@iccas.ac.cn

SPECIALTY SECTION
This article was submitted to Biomaterials, a section of the journal Frontiers in Bioengineering and Biotechnology

RECEIVED 10 March 2023
ACCEPTED 17 March 2023
PUBLISHED 03 April 2023

CITATION
Hao D, Li X, Yang E, Tian Y and Jiang L (2023), Barnacle inspired high-strength hydrogel for adhesive.
Front. Bioeng. Biotechnol. 11:1183799.
doi: 10.3389/fbioe.2023.1183799

Barnacle inspired high-strength hydrogel for adhesive

Dezhao Hao[1,2], Xingchao Li[1,2], Enfeng Yang[1,2], Ye Tian[1,2,3]* and Lei Jiang[1,2]

[1]CAS Key Laboratory of Bio-inspired Materials and Interfacial Science, Technical Institute of Physics and Chemistry, Chinese Academy of Sciences, Beijing, China, [2]School of Future Technology, University of Chinese Academy of Sciences, Beijing, China, [3]Beijing Institute of Future Science and Technology on Bioinspired Interface, Beijing, China

Barnacle exhibits high adhesion strength underwater for its glue with coupled adhesion mechanisms, including hydrogen bonding, electrostatic force, and hydrophobic interaction. Inspired by such adhesion mechanism, we designed and constructed a hydrophobic phase separation hydrogel induced by the electrostatic and hydrogen bond interaction assembly of PEI and PMAA. By coupling the effect of hydrogen bond, electrostatic force and hydrophobic interaction, our gel materials show an ultrahigh mechanical strength, which is up to 2.66 ± 0.18 MPa. Also, benefit from the coupled adhesion forces, as well as the ability to destroy the interface water layer, the adhesion strength on the polar materials can be up to 1.99 ± 0.11 MPa underwater, while that of the adhesion strength is about 2.70 ± 0.21 MPa under silicon oil. This work provides a deeper understanding of the underwater adhesion principle of barnacle glue. Furthermore, our bioinspired strategy would provide an inspiration for the fabrication of high mechanical gel materials, and the rapid strong adhesive used in both water and organic solvents.

KEYWORDS

barnacle, hydrogel, bio-inspired, phase separation, under water and oil adhesive

Introduction

Barnacle, a very common marine organism, has a very strong underwater adhesion ability. It can cause serious surface damage to many natural and artificial materials in the sea (Aldred and Clare, 2008; Murosaki et al., 2011; Kamino, 2013), and even can firmly adhere to the skin or shell of some animals (Pugliese et al., 2012). Barnacle cement is considered to be the most durable and hardest connection among aquatic organisms (Abbott, 1990). Adhesive is a protein material (>90% protein), while the rest is composed of carbohydrates, ash and trace lipids (Walker, 1999). The barnacle adhesion protein can rapidly self-assemble in water and adhere the barnacle itself to various substrates (Cheung et al., 1977; Wiegemann and Watermann, 2003). Among barnacle adhesive proteins, there are only common amino acids, and there is no special adhesive chemical like L-dopa in the mussel (Wilker, 2011; Kord Forooshani and Lee, 2017). The hydrogen bond and ionic bond in barnacle cement are considered to be weak and cannot realize the main cross-linking mechanism. Due to the resistance of the adhesive to thioglycolate, disulfide bonds are also excluded (Naldrett, 1993). On the contrary, researchers (Barnes and Blackstock, 1976) showed that the anionic detergent sodium dodecyl sulfate (SDS) containing the reducing agent 2-mercaptoethanol was sufficient to dissolve the cement, which led to the hypothesis that hydrophobic interaction and sulfur crosslinking were the key components of the cement matrix.

Other evidence shows that the high hydrophobicity of barnacle proteins is the main reason for the insolubility of these proteins (Naldrett and Kaplan, 1997).

However, the key problem to achieve effective adhesion underwater is how to break through the water layer on the solid surface (Waite, 1987; Maier et al., 2015). The water film will prevent the effective contact between various adhesives and the surface, and it will also occupy a certain volume and is difficult to be discharged after the adhesive is cured (Shao and Stewart, 2010; Akdogan et al., 2014; Zhao et al., 2016; Zhao et al., 2017). Therefore, it is very important to study the competitive forces between adhesive molecules and interfacial water on the surface (Narayanan et al., 2021). At present, the strategies of underwater and organic solvent adhesion are mainly divided into the following categories: 1) underwater adhesion is achieved by using stronger hydrogen bonds, such as L-dopa or dopamine based adhesives (Ryu et al., 2011; Wang et al., 2015; Cui et al., 2019) and Phragmatopoma californica (Zhao et al., 2005). But the adhesion strength that can be achieved is relatively low; 2) The adhesion between water and organic solvent is realized by solvent exchange (Zhao et al., 2016; Xu et al., 2020; Wan et al., 2023). The adhesion strength is still very limited; 3) Underwater adhesion can be achieved by hydrophobic interaction, such as PDMS tape (Wan et al., 2019) and organogel coating (Li et al., 2020); 4) It is still difficult to achieve high adhesion strength by extruding the water layer with special structures, such as the suction cups of octopi (Baik et al., 2017), clingfish (Ping et al., 2018), etc. Compared with natural underwater adhesives, it is still a challenge to design and prepare an adhesive that has both the adhesion strength and the convenience under water and specially under organic solvents.

Here, we imitate the solidification and interface interaction principle of barnacle glue, and use two hydrophilic polymers PMAA and PEI to form a relatively hydrophobic polymer network through hydrogen bonding and electrostatic self-assembly hydrogel in aqueous solution. In this gel, there are hydrogen bond, electrostatic force and hydrophobic interaction, and these water-soluble monomers can diffuse and mix with the interface water to destroy the interface water layer. We plan to test the gel to carry out underwater and organic solvent adhesion tests in imitation of the underwater adhesion process of barnacles.

Chemicals and materials

Polyethylene imine (PEI, 50% aqueous solution, molecular weight Mw 70000), methacrylic acid (MAA), Dimethyl silicone oil (viscosity 10 mPa s), ammonium persulfate, guanidine thiocyanate (GT), sodium dodecyl sulfate, sodium fluorescein, the above reagents were purchased from Macklin Biochemical Technology; Hydrochloric acid (36 wt%), sodium carbonate, sodium bicarbonate, ethyl acetate, ethanol, n-hexane, and the above reagents are purchased from Sinopharm chemicals; 1,1′-Dioctadecyl-3,3,3′,3′-tetramethylindocarbocyanine perchlorate (DiI, purchased form Sigma-Aldrich). The above reagents are directly used without purification in the experiment.

Preparations of hydrogel

First, dilute 30 g of 50% PEI aqueous solution with 70 g of water, then add 30 g of methacrylic acid, then stir evenly and remove bubbles in it by ultrasonic for 10 min. During polymerization, add 0.3 g ammonium persulfate and quickly stir it evenly, then pour the mixed solution into the mold and wait for curing at room temperature. For other proportions of gel, please refer to Supplementary Table S1 in the Supplementary Material.

Characterizations of hydrogel structures and wettability

Before testing SEM, hydrogel samples need to be freeze-dried first, then sprayed with gold, and then put into an electron microscope (Hitachi, SU8010) to observe its porous structure. The voltage is 10 kV, and the magnification is 200-10000 times.

The surface wettability of gel samples was tested by the contact angle tester OCA-20 machine (Dataphysics Germany). Use 2 μL of pure water for each test. Change different positions after each test, take 5 data values from each sample and average them.

The water-soluble fluorescein sodium and oil-soluble DiI water and n-hexane were prepared into 10 nM solution respectively, and then the samples were put into them for dyeing, and then the dyed samples were put into Nikon Confocal Microscopes C2 system for observation.

Mechanical tests

The sample for mechanical test is prepared with a PTFE mold, as shown in Supplementary Figure S1. The width of the test part is 6 mm, the thickness is 2 mm, and the cross-sectional area is 12 mm^2. The model of tension machine is CTM2100/1KN (Xie Qiang Instrument Manufacturing (Shanghai) Co., Ltd.), the test range of the sensor is 0-1000 N.

Adhesive properties

Adhesion test samples use the basement sized 1 cm × 2.5 cm. Place one adhesive substrate in water or organic solvent, and then add pre-gel solution 500 μL. Then, another adhesive substrate is pressed on the adhesive substrate with hydrogel pre-gel solution in water or organic solvent, and the included angle between the two substrates is kept at 90° until the hydrogel is cured. The adhesion area of all adhesive samples obtained is 1 cm^2.

Results and discussion

Chemical structure design and self-assembly mechanism

Barnacle glue contains a lot of charged amino acids and hydrophobic components, which can be self-assembled by

10.3389/fbioe.2023.1183799

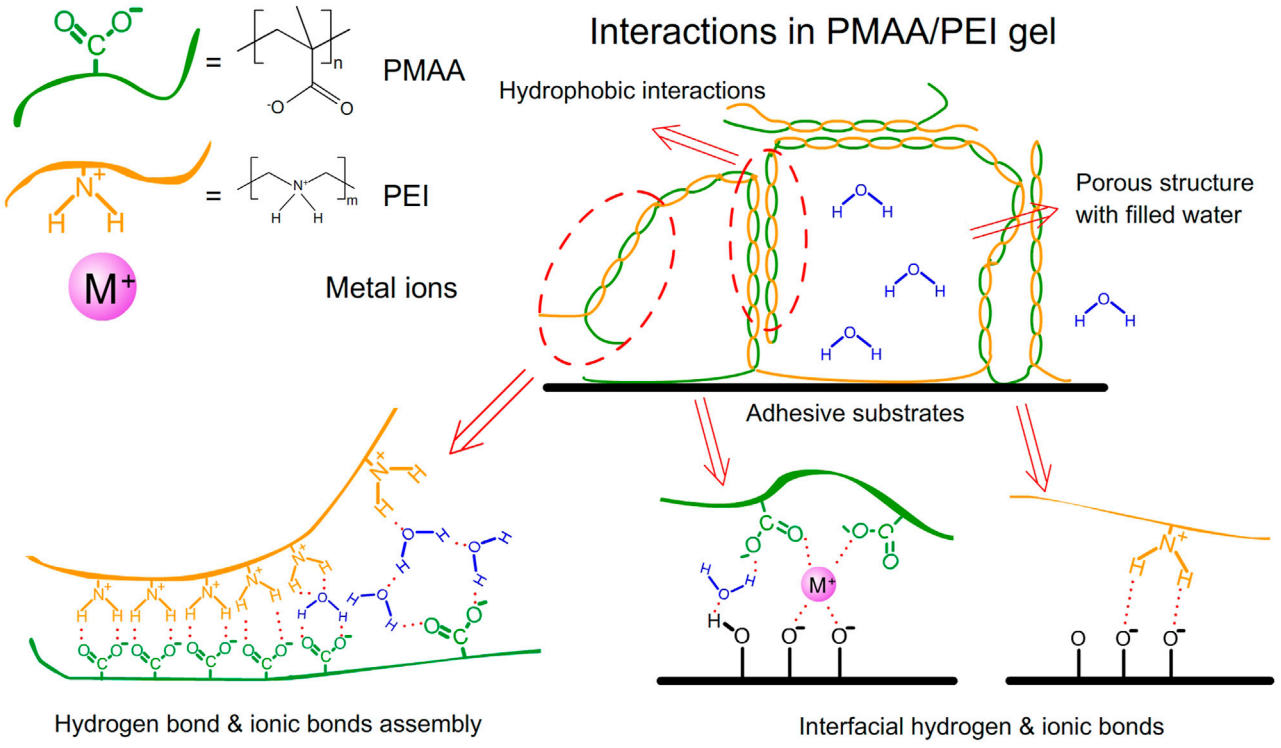

FIGURE 1
Interactions in PMAA/PEI gel.

electrostatic and hydrophobic interactions to form barnacle glue with underwater adhesion (Kamino et al., 2000; Kamino, 2001; Yan et al., 2020). Inspired by barnacle, we designed a hydrogel with a large number of amino and carboxyl groups, which contains the polyethyleneimine (PEI) and the monomer methacrylic acid (MAA). The polymerization is initiated by ammonium persulfate (APS). After polymerization, these two polymers can form high-strength PMAA/PEI self-assembled hydrogel (hereinafter referred to as PMAA/PEI gel, as shown in Figure 1) by electrostatic and hydrogen bonding. Additionally, when the molar ratio of the two polymer units is close to 1:1, MAA and PEI in PMAA/PEI gel can form a self-assembly structure relying on the internal hydrogen bond and ionic bond and can shield the charge, so that the electrostatic interaction and external hydrogen bond interaction are weakened and the assembly becomes hydrophobic, and then the hydrophobic interaction continues to assemble to obtain a phase separation structure. Figures 2A–C shows the polymerization process of gel. It can be seen that gel is polymerized by clear and transparent solution at room temperature, and can be completely solidified into white and hard gel in only about 180 s. Figure 2D explains the polymerization principle of gel. On the one hand, PEI can act as an accelerator of persulfate, which can form a large number of free radicals to promote polymerization when reacting with persulfate at room temperature; On the other hand, PEI is positively charged in solution, which will rely to electrostatic force to attract negatively charged methacrylic acid anions, so it is very conducive to the rapid polymerization of methacrylic acid and the formation of assembly.

PMAA/PEI gel contains no chemical cross-linker, but only relies on the electrostatic, hydrogen bond and hydrophobic interaction between the two polymers to form gel. Therefore, the final properties of gel are very related to the proportion of the two substances. Figure 3A and Supplementary Video S1 shows the photos of PMAA/PEI gel with different polymer unit mole ratios (The ratio of amino groups in PEI to carboxyl groups in PMAA). When PMAA: PEI = 0.5, the gel network is positively charged as a whole. Due to the good hydrophilicity of PEI, the gel remains transparent and has low strength, but has an elongation at break of more than 3,000%, as illustrated in Figure 3B. When PMAA: PEI = 1, the two polymers in the gel can just be assembled 1:1, and the strength of the gel also reaches the highest, as shown in Figure 3C. When the proportion of PMAA is further increased, the gel is acidic in the case of excessive PMAA. The hydrophilicity of PMAA will decline, so the gel can still keep a good hydrophobic assembly phase separation state, and the strength will only decrease slightly. Based on the above experimental results, PMAA: PEI = 1 gel was used as the research object in all subsequent studies.

Wettability study

PMAA/PEI gel has very obvious hydrophobicity. As shown in Figure 4A, when the gel is dyed with hydrophilic dyes (sodium fluorescein, yellow fluorescence) and hydrophobic dyes (DiI, red fluorescence) respectively, it can be observed under the laser

10.3389/fbioe.2023.1183799

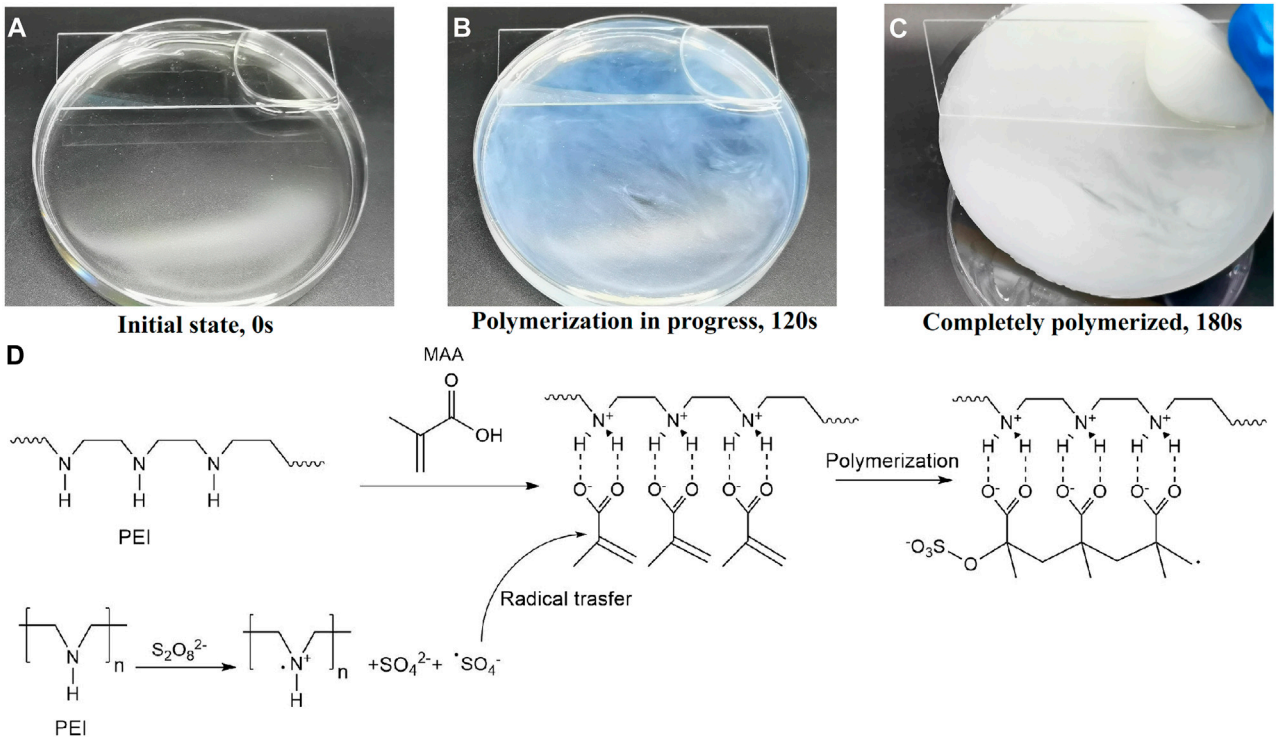

FIGURE 2
The polymerization process of PMAA/PEI gel. **(A–C)** The photograph of the polymerization progress. **(D)** The principle of room temperature thermal polymerization.

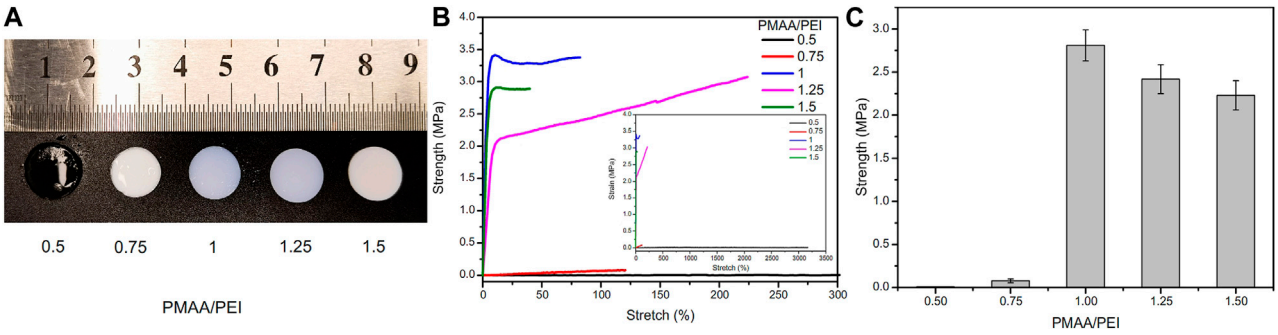

FIGURE 3
Hydrogel samples at different PMAA/PEI molar ratios. **(A)** Photos of these samples, of which PMAA/PEI = 0.5 is still transparent, while other samples are white, indicating that these samples have shown relatively obvious phase separation; **(B)** Elongation curves of several samples, the illustration of which is a complete force curve, in which the elongation at break of the sample with PMAA. PEI = 0.5 exceeds 3,000%; **(C)** The breaking strength of gel with several ratios, of which the gel with PMAA/PEI molar ratio of 1:1 has the best performance, and this ratio is used by default in subsequent experiments.

confocal microscope that the gel section is almost completely red. So, it is dyed by hydrophobic dyes. However, the surface of PMAA/PEI gel can be dyed by hydrophilic dyes, indicating that there is a hydrophilic layer on the surface of gel. Supplementary Figure S2 shows the contact angle of PMAA/PEI gel in air and the contact angle of silicone oil under water. The contact angles of silicone oil on the surface and inside of gel show obvious differences, which are 138.4 ± 7.0° and 115.5 ± 8.1°, respectively. This shows that the interior of gel has stronger oleophilicity. This is because the incompletely assembled polymer chains on the gel surface which can make the gel surface more hydrophilic. The interior of gel cannot be observed because it is opaque. The illustration in Figure 4A shows the water contact angle of PMAA/PEI gel in the air, which has reached more than 70°, exceeding the hydrophobic/hydrophilic limit (Vogler, 1998; Tian and Jiang, 2013). Therefore,

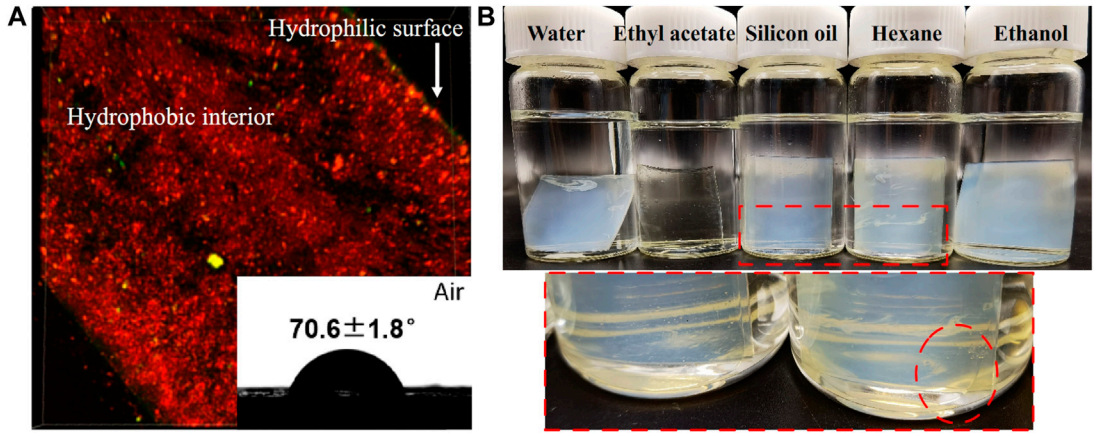

FIGURE 4
The wettability and solvent displacement test of PMAA/PEI gel. **(A)** The cross section of gel dyed by sodium fluorescein and DiI is mainly oleophilic but shows hydrophilic on the surface. The contact angle of water on the flat surface reaches 70.6 ± 1.8°; **(B)** The photo of PMAA/PEI gel soaked in water, ethyl acetate, silicone oil, n-hexane and ethanol for 72 h show that it becomes transparent when soaked in ethyl acetate, while part of the water in the gel soaked in silicone oil and n-hexane can be replaced by organic solvents.

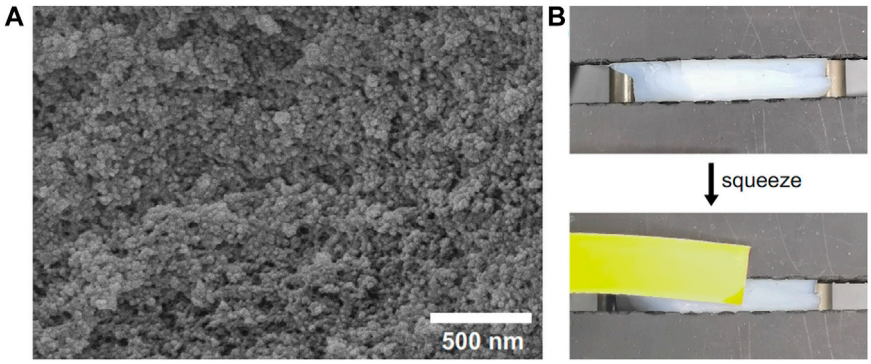

FIGURE 5
PMAA/PEI gel has a porous structure and can extrude water. **(A)** Porous structure of gel; **(B)** Under the action of external force, the water in the pore structure of gel can be squeezed out.

it can be considered that the surface of PMAA/PEI gel is hydrophobic. During the preparation of gel, its surface and interior were not treated differently, so it can be inferred that the interior of gel is also hydrophobic. However, the internal network of PMAA/PEI gel actually contains a lot of water (about 65%), and the two polymers that make up the gel are also hydrophilic, which indicates that the two polymer networks inside the gel have strong assembly ability and can completely wrap water. In Figure 4B, we carried out the solvent displacement experiment of gel. The experiment confirmed that the water in PMAA/PEI gel can be replaced by some organic solvents, such as ethyl acetate, silicone oil, n-hexane, etc. For ethyl acetate, it can even obviously enter the gel network, and make the gel transparent. The above experiments confirmed that there are a large number of hydrophobic networks in the gel, which has better affinity for many organic solvents than water.

Structure of hydrogel

As a hydrophobic PMAA/PEI gel containing a lot of water, there is an obvious phase separation structure in it. Figure 5A shows that PMAA/PEI gel material has a nano-sized porous structure. This shows that the polymer in the gel has been assembled into a relatively rigid hydrophobic network, while the original water is filled in the porous structure formed by nano-sized phase separation. In addition, a large number of water filled porous structures in PMAA/PEI gel can also be deformed under external force extrusion, and the water filled in the porous structure will be partially squeezed, as shown in Figure 5B and Supplementary Video S2. Since the gel used in the test is a 1:1 M ratio of PEI and PMAA, it can be completely assembled without residue in water. The inspection result of the pH test paper used to test the pH of the extruded water in the experiment is close to pH = 7, which also proves that

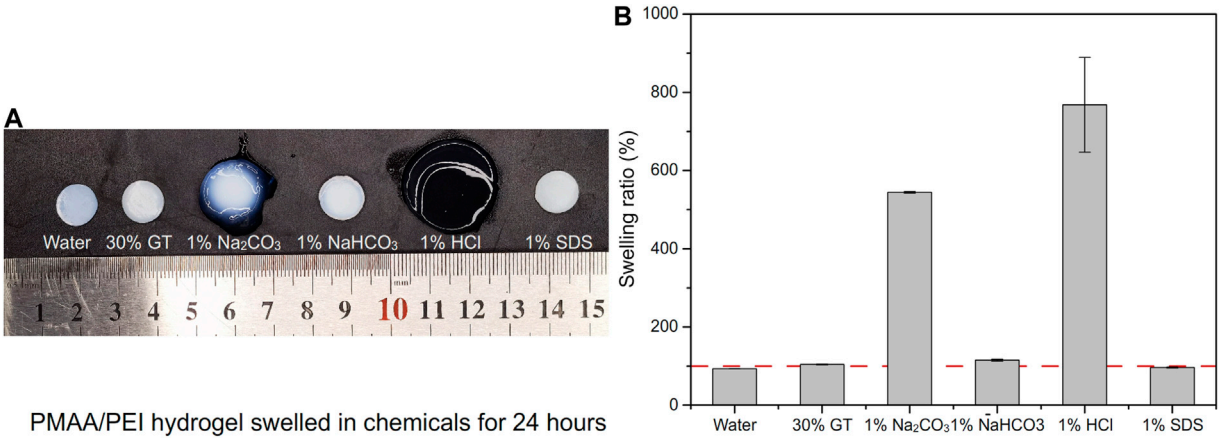

FIGURE 6
The swelling of PMAA/PEI gel in several solutions. **(A)** Photos of PMAA/PEI gel after swelling in water, 30% GT, 1% sodium carbonate, 1% sodium bicarbonate, 1% hydrochloric acid and 1% SDS solution for 24 h. The swelling is very obvious in hydrochloric acid and sodium carbonate solution; **(B)** Swelling rate data in several solutions. The gel swells severely in hydrochloric acid and sodium carbonate solutions, shrinks slightly in water and SDS, and swells slightly in 30% GT and sodium bicarbonate solutions.

there is almost no excess PEI or PMAA residue in the extruded water, that is, the water in the pores is almost pure water.

Interactions in hydrogel

PMAA/PEI gel, as a hydrogel that does not consist chemical crosslinkers but only relies on hydrogen bonds, ionic bonds and hydrophobic interactions, has shown strong resistance to a variety of destructive agents. As shown in Figure 6A, PMAA/PEI gel shows different swelling states after soaking in water, 30% GT, 1% sodium carbonate, 1% sodium bicarbonate, 1% hydrochloric acid and 1% SDS solution for 24 h. Figure 6B shows the swelling degree of PMAA/PEI gel in various solvents. The gel in water showed a slight shrinkage, which was due to the tight hydrophobic network in the gel. However, in 30% GT solution, gel has almost no swelling. This is because PMAA/PEI gel is assembled by both ionic bonds and hydrogen bonds, and the ionic bonds are difficult to be destroyed by GT, so the swelling of gel is weak. In 1% sodium carbonate solution, the pH of the sodium carbonate solution can reach 10, which will seriously reduce the charge of PEI. The negative charge of PMAA network will also increase, leading to the destruction of the ionic bond assembly of gel, so the gel has a very obvious swelling. However, the pH of 1% sodium bicarbonate solution is only 8. At this pH value, the charge of PEI is less affected, so gel only shows weak swelling. In 1% hydrochloric acid, the pH has reached about 1. The negative charge of the PMAA network is basically neutralized, while only the PEI network remains positively charged. Therefore, the gel shows very serious swelling and has become transparent, indicating that the assembly structure of PEI/PMAA has been destroyed, and the phase separation and hydrophobic interaction have basically disappeared. The gel soaked in SDS solution did not appear to have obvious changes in appearance, but SDS was able to participate in the assembly of hydrophobic structure, showing a very obvious difference in the subsequent mechanical property test.

Mechanical properties

PMAA/PEI gel shows high mechanical strength and tolerance to various environments. As shown in Figure 7A, after the silicone oil dispersed in the gel up to 25% (compared with the mass ratio of the polymers in the gel), the tensile strength of the gel only decreased slightly. On the one hand, PEI and MAA are amphiphilic and can effectively disperse silicone oil that is not miscible with water; On the other hand, there are a large number of hydrophobic pore structures in gel, and these dispersed silicone oil can be directly filled in the hydrophobic pore structure of gel, without affecting the main force network structure of gel, and without defects due to the addition of these silicone oil. Figure 7B shows the force curve of these gel stretching to fracture, and the elongation at break of the gel added with silicone oil has increased significantly. This shows that some silicone oils participate in the hydrophobic interaction in the gel network structure. When stretching, these silicone oils act as lubricants, so the elongation of gel increases. In addition, there are very obvious necking points in these force curves. This means that near the necking point, the weak hydrophobic interaction force in the gel network is destroyed by external force, and the sliding between hydrophobic chains makes the stress drop.

PMAA/PEI gel can also show the same mechanical property changes as silicone oil after solvent replacement in several organic solvents. The strength after solvent replacement is shown in Figure 7C, and the force curve is shown in Figure 7D

. The tensile strength of PMAA/PEI gel soaked in ethyl acetate, n-hexane and silicone oil for 24 h decreased compared with that soaked in water, but the elongation at break of gel soaked in silicone oil and ethyl acetate increased significantly. This indicates that these solvents have partially replaced the water in the gel and entered the hydrophobic pores in the gel to play a certain role in lubrication. However, the strength of gel soaked in ethanol was significantly improved, and the elongation at break was significantly reduced, while the modulus was increased. This is because ethanol can be miscible with water, so ethanol can simultaneously enter the

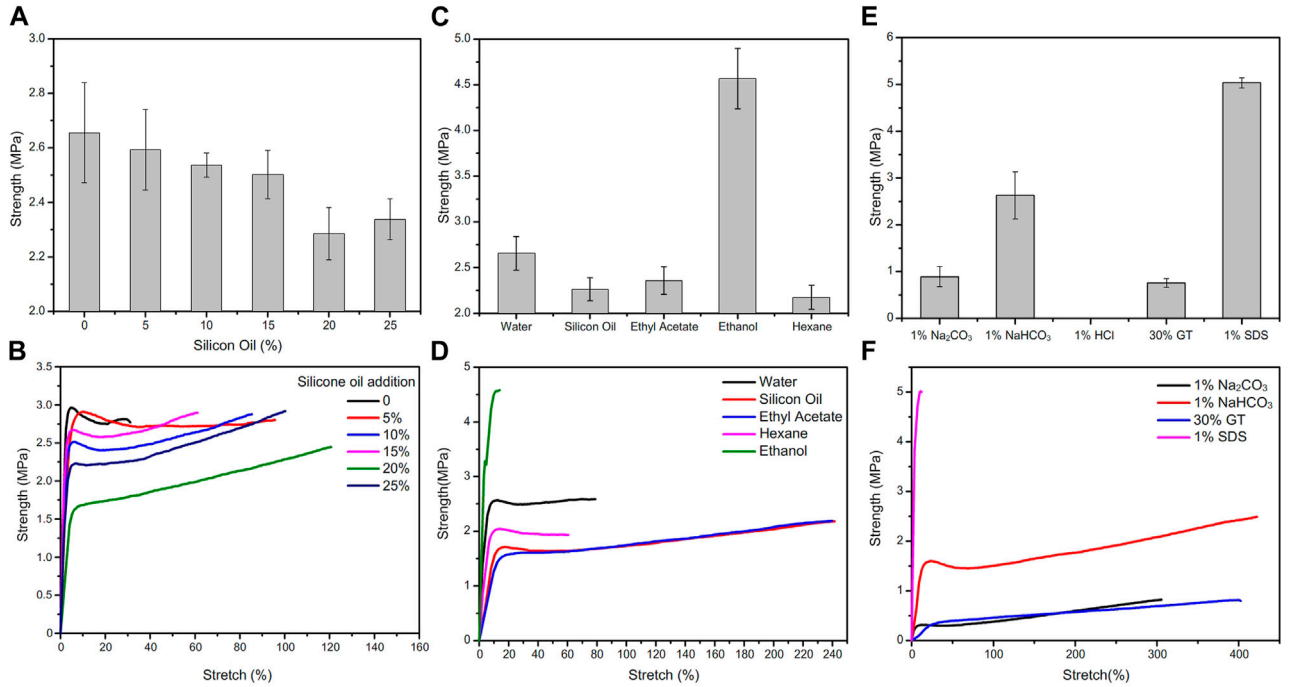

FIGURE 7
Change of tensile strength of PMAA/PEI gel under different conditions. **(A)** Adding silicone oil of different content to PMAA/PEI gel, the strength of gel slightly decreased with the increase of silicone oil content; **(B)** For the tensile force curve of gel with different silicone oil content, the breaking elongation of gel increases with the increase of silicone oil content; **(C)** The tensile strength of gel soaked in water and several organic solvents for 24 h; **(D)** Gel force curve after immersion in water and several organic solvents. The elongation at break of gel soaked in ethyl acetate and silicone oil increased a lot, while the modulus of gel soaked in ethanol increased a lot; **(E)** Tensile strength of PMAA/PEI gel soaked in several solutions; **(F)** The tensile force curve of gel soaked in several solutions.

hydrogen bond assembly structure and hydrophobic pores in the gel. However, the polarity of ethanol is lower than that of water, and the ability to form hydrogen bonds is also weaker than that of water. Therefore, after soaking in ethanol, the ionic bond assembly of gel is strengthened. Then, part of the bound water in the assembly structure is replaced, making the assembly structure more compact. Therefore, the mechanical properties of gel become stronger and the modulus increases.

After soaking in acid, alkali, SDS and guanidine thiocyanate solutions, the mechanical properties of PMAA/PEI gel also show obvious changes. The strength changes are shown in Figure 7E, and the force curve is shown in Figure 7F. The first is the PMAA/PEI gel soaked in hydrochloric acid. Due to the very serious swelling, its own strength is significantly reduced and even difficult to measure. The strength of PMAA/PEI gel soaked in 1% sodium carbonate solution also decreased significantly. The strength of gel samples soaked in sodium bicarbonate solution has no obvious change, because the alkalinity of sodium bicarbonate solution is weak, which has little effect on the electrification of gel. In addition, the gel soaked in 30% GT solution showed no obvious swelling and transparency changes, but its strength also decreased significantly. This is due to the destruction of hydrogen bond by GT, and the electrostatic interaction that is less affected plays a role in maintaining the structure and partial strength of gel. The strength of gel samples soaked in 1% SDS solution changes significantly, because SDS is not only charged, but also has hydrophilic and hydrophobic structures, so it can participate in both hydrophobic and electrostatic assembly in PMAA/PEI gel. In this process, part of the water in the gel structure will be replaced by SDS. Because the molecule of SDS is much larger than that of water, the entry of SDS will fill more gel pores, making PMAA/PEI gel more compact, resulting in a significant increase in the strength and modulus of gel.

Under water and organic solvents adhesive and applications

PMAA/PEI gel, as a bionic barnacle glue material, has a variety of complex interactions similar to barnacle glue, such as hydrogen bond, ionic bond, hydrophilic hydrophobic phase transition, hydrophobic interaction, and can also realize rapid thermal polymerization and curing at room temperature (about 180 s). Therefore, it has great potential as a bionic adhesive material. Figure 8A shows the underwater adhesion strength of PMAA/PEI gel to a variety of materials. It has very high underwater adhesion strength to polar materials such as titanium sheet, aluminum oxide, glass, and even far exceeds the underwater adhesion strength of barnacle glue, but it has almost no adhesion strength to non-polar materials such as PS and PP. This is because the components of PMAA/PEI gel are almost completely hydrophilic before polymerization, and hydrophobic interaction can be formed only after assembly after polymerization, which makes it difficult to

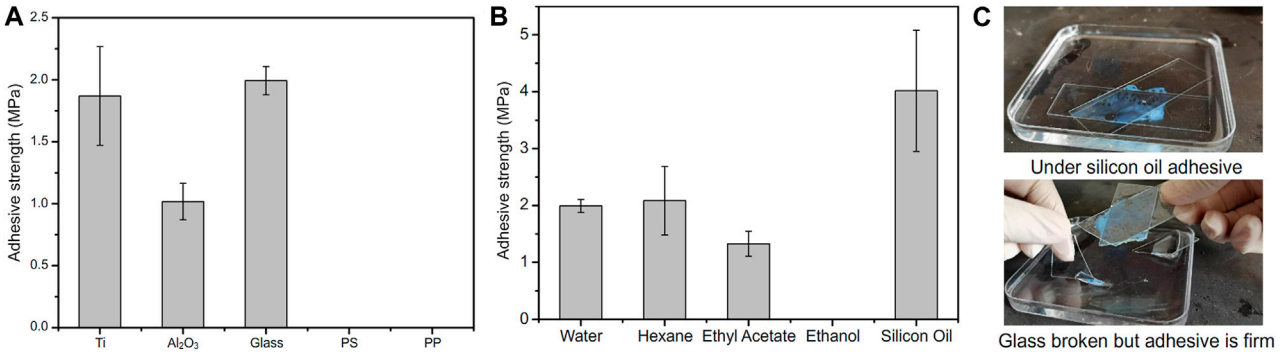

FIGURE 8
Adhesion performance of PMAA/PEI adhesive in water and organic solvent. **(A)** PMAA/PEI adhesive can firmly adhere titanium, aluminum oxide, glass and other polar materials under water, but shows almost no adhesion strength to non-polar materials such as PS and PP; **(B)** PMAA/PEI adhesive can achieve high strength adhesion to glass in a variety of organic solvents, such as n-hexane, ethyl acetate and silicone oil, but it cannot achieve adhesion in ethanol. The strength of adhesion glass under silicone oil is even higher than that under water; **(C)** The adhesion process of PMAA/PEI adhesive to glass under silicone oil. After the polymerization of PMAA/PEI adhesive, the PMAA/PEI adhesive cannot be damaged even when the glass is damaged under the action of tangential force.

generate strong interaction between the gel network and non-polar materials before polymerization, while after polymerization, the gel network has been assembled, movement is limited, and it is also difficult to generate sufficient interface interaction with non-polar surfaces. For the surface of polar materials, before gel polymerization, a large amount of electrostatic and hydrogen bonding interactions is enough to make the PEI chain that forms the gel network and MAA monomer adsorb and replace part of the bound water on the surface of polar materials, and the interaction of these interfaces is not affected after polymerization. The replaced interface water can be directly filled in the pores of gel without interfering with the interface interaction and the polymerization process of gel. PMAA/PEI gel has more electricity and more hydrogen bonds than barnacle glue. Therefore, the underwater adhesion strength of PMAA/PEI gel to polar material surface is better than barnacle glue.

For many adhesives, it is a considerable challenge to achieve adhesion in the presence of oil with low surface tension and high viscosity (such as silicone oil), because low surface tension means that these oils can easily wet various surfaces and are difficult to be rapidly replaced at the interface, resulting in the difficulty of achieving effective interface interaction. Previous experiments have confirmed that PMAA/PEI gel has a porous structure and can wrap water or a variety of organic solvents without affecting its strength. Therefore, we believe that even the silicone oil on the interface can be effectively replaced by PMAA/PEI gel adhesive and filled in the pores of gel without having an obvious impact on the adhesion process. Figure 8B shows the adhesion strength of PMAA/PEI gel to glass in water and various organic solvents. The hydrophobic self-assembly inside the gel is affected in ethanol, which makes it difficult for the gel to cure, the adhesion strength of PMAA/PEI gel in low polar solvents is almost no lower or even higher than that under water, especially under silicone oil, which even exceeds that under water, and even approaches the strength of gel itself. This shows that PMAA/PEI gel can quickly replace the oil layer at the interface and achieve effective interface interaction. Compared with underwater adhesion, PMAA/PEI pre-gel solution will not be diluted by water, so its bulk strength is higher. As shown in Figure 8C, the photo shows the process of glass sheet adhesion under silicone oil, and the corresponding Supplementary Video S3 is also included in the Supplementary Material. After curing (about 180 s), PMAA/PEI gel under silicone oil adhesive has firmly stuck two pieces of glass under silicone oil together, and even if external force is used to destroy the glass, it will preferentially destroy the glass rather than the adhesion position. This shows that PMAA/PEI, as a new adhesive of bio-inspired barnacle glue, has very good adaptability in underwater and oil environments.

Conclusion

In this work, we designed a gel composed of PMAA/PEI by imitating the adhesion principle of barnacle glue. The gel was assembled internally by hydrogen bonding, electrostatic force and hydrophobic interaction between PMAA/PEI assemblies, without chemical crosslinkers. The gel can achieve rapid curing in only 180 s at room temperature, and has very high mechanical properties. Its tensile strength reaches 2.66 ± 0.18 MPa. The gel has a porous phase separation structure, and the pores can be partially replaced by some organic solvents. Similar to barnacle glue, PMAA/PEI gel can achieve high strength underwater and organic solvents adhesion to a variety of polar materials, such as underwater adhesion strength of 1.99 ± 0.11 MPa to glass, the adhesion strength under silicone oil can even reach 2.70 ± 0.21 MPa. This is because PMAA/PEI assembly can form hydrogen bond, electrostatic force and other interactions at the interface, and can also transfer the water or organic solvent in the interface layer to the pores in the gel without affecting the strength of the gel itself. This new bio-inspired gel can not only rely on its own high mechanical properties and porous structure as a new bionic material, but also can be used as a new bionic adhesive for adhesion in a variety of organic solvents, and provides a new design idea for the new adhesive.

Data availability statement

The original contributions presented in the study are included in the article/Supplementary Material, further inquiries can be directed to the corresponding authors.

Author contributions

DH and YT contributed to the initiating idea. DH, XL, and EY performed the synthesize and mechanical test experiments. DH, YT, and LJ analysed all the data and wrote the manuscript. All authors commented on the manuscript.

Funding

This work was supported by the National Natural Science Foundation (21972154, 22090052, and 22002005), Frontier Science Key Projects of CAS (ZDBS-LY-SLH022), Key R&D Project of Shandong Province (2022CXGC010302).

Conflict of interest

The authors declare that the research was conducted in the absence of any commercial or financial relationships that could be construed as a potential conflict of interest.

Publisher's note

All claims expressed in this article are solely those of the authors and do not necessarily represent those of their affiliated organizations, or those of the publisher, the editors and the reviewers. Any product that may be evaluated in this article, or claim that may be made by its manufacturer, is not guaranteed or endorsed by the publisher.

Supplementary material

The Supplementary Material for this article can be found online at: https://www.frontiersin.org/articles/10.3389/fbioe.2023.1183799/full#supplementary-material

References

Abbott, A. (1990). Bioadhesives - potential for exploitation. *Sci. Prog.* 74 (293), 131–146.

Akdogan, Y., Wei, W., Huang, K. Y., Kageyama, Y., Danner, E. W., Miller, D. R., et al. (2014). Intrinsic surface-drying properties of bioadhesive proteins. *Angew. Chem. Inter Ed.* 53 (42), 11253–11256. doi:10.1002/anie.201406858

Aldred, N., and Clare, A. S. (2008). The adhesive strategies of cyprids and development of barnacle-resistant marine coatings. *Biofouling* 24 (5), 351–363. doi:10.1080/08927010802256117

Baik, S., Kim, D. W., Park, Y., Lee, T-J., Ho, S. B., and Pang, C. (2017). A wet-tolerant adhesive patch inspired by protuberances in suction cups of octopi. *Nature* 546, 396–400. doi:10.1038/nature22382

Barnes, H., and Blackstock, J. (1976). Further observations on the biochemical composition of the cement of Lepas fascicularis Ellis and Solander; electrophoretic examination of the protein moieties under various conditions. *J. Exp. Mar. Bio Ecol.* 25 (3), 263–271. doi:10.1016/0022-0981(76)90128-3

Cheung, P. J., Ruggieri, G. D., and Nigrelli, R. F. (1977). A new method for obtaining barnacle cement in the liquid state for polymerization studies. *Mar. Bio* 43 (2), 157–163. doi:10.1007/BF00391263

Cui, C., Fan, C., Wu, Y., Xiao, M., Wu, T., Zhang, D., et al. (2019). Water-triggered hyperbranched polymer universal adhesives: From strong underwater adhesion to rapid sealing hemostasis. *Adv. Mater* 0 (0), 1905761. doi:10.1002/adma.201905761

Kamino, K. (2013). Mini-review: Barnacle adhesives and adhesion. *Biofouling* 29 (6), 735–749. doi:10.1080/08927014.2013.800863

Kamino, K. (2001). Novel barnacle underwater adhesive protein is a charged amino acid-rich protein constituted by a Cys-rich repetitive sequence. *Biochem. J.* 356 (2), 503–507. doi:10.1042/bj3560503

Kamino, K., Inoue, K., Maruyama, T., Takamatsu, N., Harayama, S., and Shizuri, Y. (2000). Barnacle cement proteins. *J. Biol. Chem.* 275 (35), 27360–27365. doi:10.1016/s0021-9258(19)61519-x

Kord Forooshani, P., and Lee, B. P. (2017). Recent approaches in designing bioadhesive materials inspired by mussel adhesive protein. *J. Polym. Sci. A Polym. Chem.* 55 (1), 9–33. doi:10.1002/pola.28368

Li, X-C., De-Zhao, H., Hao, W-J., Guo, X-L., and Jiang, L. (2020). Bioinspired hydrogel–polymer hybrids with a tough and antifatigue interface via one-step polymerization. *ACS Appl. Mater Interf.* 12 (45), 51036–51043. doi:10.1021/acsami.0c14728

Maier, G. P., Rapp, M. V., Waite, J. H., Israelachvili, J. N., and Butler., A. (2015). Adaptive synergy between catechol and lysine promotes wet adhesion by surface salt displacement. *Science* 349 (6248), 628–632. doi:10.1126/science.aab0556

Murosaki, T., Ahmed, N., and Gong, J. P. (2011). Antifouling properties of hydrogels. *Sci. Technol. Adv. Mater* 12 (6), 064706. doi:10.1088/1468-6996/12/6/064706

Naldrett, M. J., and Kaplan, D. L. (1997). Characterization of barnacle (*Balanus eburneus* and B. cenatus) adhesive proteins. *Mar. Bio* 127 (4), 629–635. doi:10.1007/s002270050053

Naldrett, M. J. (1993). The importance of sulphur cross-links and hydrophobic interactions in the polymerization of barnacle cement. *J. Mar. Biol. Assoc. U. K.* 73 (3), 689–702. doi:10.1017/s0025315400033221

Narayanan, A., Ali, D., and Joy, A. (2021). Design principles for creating synthetic underwater adhesives. *Chem. Soc. Rev.* 50 (23), 13321–13345. doi:10.1039/D1CS00316J

Ping, R., SunLin, T., Liang, C., Takahashi, R., Gento, S., Guo, H., et al. (2018). Tough hydrogels with fast, strong, and reversible underwater adhesion based on a multiscale design. *Adv. Mater* 30 (32), 1801884. doi:10.1002/adma.201801884

Pugliese, M. C., and Fish, F. E.Stefanie Anne Böttger (2012). Barnacle bonding: Morphology of attachment of Xenobalanus globicipitis to its host *Tursiops truncatus*. *J. Morphol.* 273 (4), 453–459. doi:10.1002/jmor.20006

Ryu, J. H., Lee, Y., Kong, W. H., Kim, T. G., Park, T. G., and Lee, H. (2011). Catechol-functionalized chitosan/pluronic hydrogels for tissue adhesives and hemostatic materials. *Biomacromolecules* 12 (7), 2653–2659. doi:10.1021/bm200464x

Shao, H., and Stewart, R. J. (2010). Biomimetic underwater adhesives with environmentally triggered setting mechanisms. *Adv. Mater* 22 (6), 729–733. doi:10.1002/adma.200902380

Tian, Y., and Jiang, L. (2013). Intrinsically robust hydrophobicity. *Nat. Mater* 12 (4), 291–292. doi:10.1038/nmat3610

Vogler, E. A. (1998). Structure and reactivity of water at biomaterial surfaces. *Adv. Colloid Interfac.* 74 (1), 69–117. doi:10.1016/S0001-8686(97)00040-7

Waite, J. H. (1987). Nature's underwater adhesive specialist. *Inter J. Adhes. Adhes.* 7 (1), 9–14. doi:10.1016/0143-7496(87)90048-0

Walker, G. (1999). The cypris larvae of the rhizocephalan barnacle Heterosaccus lunatus with particular reference to antennular morphology. *Acta Zool.* 80 (3), 209–217. doi:10.1046/j.1463-6395.1999.00018.x

Wan, X., Gu, Z., Zhang, F., Hao, D., Liu, X., Dai, B., et al. (2019). Asymmetric Janus adhesive tape prepared by interfacial hydrosilylation for wet/dry amphibious adhesion. *NPG Asia Mater* 11 (1), 49. doi:10.1038/s41427-019-0150-x

Wan, X., Zhang, F., Zhang, K., Liu, X., Xu, X., Liu, M., et al. (2023). Interfacial instability-induced (3I) adhesives through "mediator" solvent diffusion for robust underoil adhesion. *Adv. Mater* 35 (6), 2208413. doi:10.1002/adma.202208413

Wang, W., Xu, Y., Li, A., Li, T., Liu, M., von Klitzing, R., et al. (2015). Zinc induced polyelectrolyte coacervate bioadhesive and its transition to a self-healing hydrogel. *Rsc Adv.* 5 (82), 66871–66878. doi:10.1039/c5ra11915d

Wiegemann, M., and Watermann, B. (2003). Peculiarities of barnacle adhesive cured on non-stick surfaces. *J. Adhes. Sci. Technol.* 17 (14), 1957–1977. doi:10.1163/156856103770572070

Wilker, J. J. (2011). Biomaterials: Redox and adhesion on the rocks. *Nat. Chem. Biol.* 7 (9), 579–580. doi:10.1038/nchembio.639

Xu, L., Gao, S., Guo, Q., Wang, C., Qiao, Y., and Dong, Q. (2020). A solvent-exchange strategy to regulate noncovalent interactions for strong and antiswelling hydrogels. *Adv. Mater* 32 (52), 2004579. doi:10.1002/adma.202004579

Yan, G., Sun, J., Wang, Z., Qian, P-Y., and He, L. (2020). Insights into the synthesis, secretion and curing of barnacle cyprid adhesive via transcriptomic and proteomic analyses of the cement gland. *Mar. Drugs* 18 (4), 186. doi:10.3390/md18040186

Zhao, H., Sun, C., Stewart, R. J., and Herbert Waite, J. (2005). Cement proteins of the tube-building polychaete phragmatopoma californica. *J. Biol. Chem.* 280 (52), 42938–42944. doi:10.1074/jbc.M508457200

Zhao, Q., Dong, W. L., Ahn, B. K., Seo, S., Kaufman, Y., Israelachvili, J. N., et al. (2016). Underwater contact adhesion and microarchitecture in polyelectrolyte complexes actuated by solvent exchange. *Nat. Mater* 15 (4), 407–412. doi:10.1038/nmat4539

Zhao, Y., Wu, Y., Wang, L., Zhang, M., Chen, X., Liu, M., et al. (2017). Bio-inspired reversible underwater adhesive. *Nat. Commun.* 8 (1), 2218. doi:10.1038/s41467-017-02387-2

frontiers | Frontiers in Bioengineering and Biotechnology

TYPE Brief Research Report
PUBLISHED 04 April 2023
DOI 10.3389/fbioe.2023.1188782

OPEN ACCESS

EDITED BY
Hongliang Liu,
Yantai University, China

REVIEWED BY
Zhongbing Huang,
Sichuan University, China
Pengbin Yin,
People's Liberation Army General Hospital, China

*CORRESPONDENCE
Lianxin Shi,
shilianxin@mail.ipc.ac.cn

SPECIALTY SECTION
This article was submitted to Biomaterials, a section of the journal Frontiers in Bioengineering and Biotechnology

RECEIVED 17 March 2023
ACCEPTED 23 March 2023
PUBLISHED 04 April 2023

CITATION
Lan J, Shi L, Xiao W, Zhang X, Wang Y and Wang S (2023), An enhanced fractal self-pumping dressing with continuous drainage for accelerated burn wound healing.
Front. Bioeng. Biotechnol. 11:1188782.
doi: 10.3389/fbioe.2023.1188782

An enhanced fractal self-pumping dressing with continuous drainage for accelerated burn wound healing

Jinze Lan[1,2], Lianxin Shi[1,3,4]*, Wuyi Xiao[1,2], Xiaobin Zhang[1,2], Yuzhe Wang[1,2] and Shutao Wang[1,2,4]

[1]CAS Key Laboratory of Bio-inspired Materials and Interfacial Science, Technical Institute of Physics and Chemistry, University of Chinese Academy of Sciences, Beijing, China, [2]University of Chinese Academy of Sciences, Beijing, China, [3]Binzhou Institute of Technology, Weiqiao-UCAS Science and Technology Park, Binzhou City, China, [4]Qingdao Casfuture Research Institute Co. Ltd., Qingdao, China

Massive exudates oversecreted from burn wounds always delay the healing process, accompanied by undesired adhesion, continuous inflammation, and high infection risk. Conventional dressings with limited draining ability cannot effectively remove the excessive exudates but constrain them in the wetted dressings immersing the wound bed. Herein, we fabricate an enhanced fractal self-pumping dressing by floating and accumulating hollow glass microspheres in the hydrogel precursor, that can continuously drain water at a non-declining high speed and effectively promote burn wound healing. Small hollow glass microspheres can split the fractal microchannels into smaller ones with higher fractal dimensions, resulting in higher absorption efficiency. In an *in vivo* burn wound model on the dorsum of murine, the enhanced fractal self-pumping dressing can significantly reduce the appearance of the wound area and alleviate tissue edema along the healing process. This study sheds light on designing high-efficiency and continuous-draining dressings for clinical applications.

KEYWORDS

hollow glass microsphere, ultra-fast water absorption, self-pumping dressing, burn wound, fractal hydrogel

1 Introduction

Burn injury is a typical trauma that is threatening people's health due to its high incidence of complications, multiple organ failure (Jeschke et al., 2011; Jeschke et al., 2020; Peck and Toppi, 2020) and mortality (Chauhan and Mir, 2018). Excessive exudates secreted from the burn wounds can probably cause tissue maceration (Cutting and White, 2002), which increases the risk of infection (Glik et al., 2018) and leads to prolonged wound healing (Cook et al., 2022). Lots of absorbent dressings have been developed for absorbing wound exudates to promote healing, such as polyacrylate fibers (Tyan et al., 2003; Desroche et al., 2016), chitosan foam (Loke et al., 2000), and bio-ceramic powder (Zhang Z. W. B. et al., 2021). However, the current dressings cannot effectively remove residual exudates remained at the tissue-dressing interface, usually resulting in secondary injuries (Li et al., 2019; Shi et al., 2019), prolonged healing process and infected wounds (Church et al., 2006).

Hydrogel dressings, due to their unique porous structure and swelling properties, can effectively absorb wound exudates and provide a moist environment for wound healing (Lee

and Mooney, 2012; Calo and Khutoryanskiy, 2015; Guo et al., 2021; Kharaziha et al., 2021; Montazerian et al., 2022). Various approaches have been developed for improving the water absorption capacity of hydrogels, such as grafting high water-absorbing polymer molecules and constructing oriented internal structures (Leonhardt et al., 2019; Wang et al., 2019; Li et al., 2020). Further, self-pumping dressings with asymmetric wettability were developed to directionally drain exudates. The air-side hydrophilic microfibers offer draining force, while the skin-side hydrophobic nanofiber array ensures its directional penetration (Shi et al., 2019). Based on this concept, some ingenuous self-pumping dressings have been developed with diverse functions for promoting wound healing, such as antibacterial and antioxidant properties (Zhang K. et al., 2021; Qi et al., 2021), bioactive ion releasing (Bao et al., 2020), and anti-adhesion (Luo et al., 2021). However, the above hydrogels or self-pumping dressings may not be adequate to remove the continuous exudates from burn wounds. It is an urgent need to develop novel dressings with high drainage efficiency that can promote healing and reduce the physical and psychological suffering of patients with burn wounds.

The design of fractal structure whose local structure is highly similar to the overall structure (Martin and Hurd, 1987) can increase the liquid transportation efficiency of draining model (Mauroy et al., 2004; Zhou et al., 2012; Poyet, 2021). In a given space, fractal structures can provide higher capillary pressure, shorter time of capillary flow (Shou et al., 2014) and faster liquid flow rate (Lee et al., 2020) in absorbing water compared to equivalent parallel capillary tube (Fan et al., 2015). Thus, further exploration is needed on how to design fractal structures in wound dressings that can meet clinical application requirements of removing continuous exudates from burn wounds.

In this study, we prepare an enhanced fractal self-pumping hydrogel (EFS hydrogel) dressing with ultra-fast water absorption and continuous drainage by a simple floating-accumulating process. Hollow glass microspheres (HGM) are introduced into the hydrogel precursor to form a fractal arrangement that diameter decreases along the gravity direction. Then a series of connected fractal hydrophilic microchannels with gradually decreased diameters are fabricated between HGM after crosslinking the hydrogel. The synthesized EFS hydrogel with fractal hydrophilic microchannels exhibits ultra-fast and continuous water absorbing performance. In the burn wound model on murine, the EFS hydrogel exhibits accelerated healing compared to the pure hydrogel, commercial Tegaderm™ dressing and gauze. The unique design of the enhanced fractal self-pumping dressing has great potential in developing biofluid management materials especially for those highly exudated wounds.

2 Materials and methods

2.1 Reagents and materials

Acrylamide (AAm), N,N-Methylene bisacrylamide (MBAA), 2,2-Diethoxyacetophenone (DEAP), Sodium alginate (SA) was purchased from Macklin reagent (China). All the regents were used directly without further purification. Rhodamine 123 (Rh123, J&K Scientific, China) were used for fluorescence staining. HGM was supported by Research and Development Center of Oil and Gas Development and New Materials for energy conservation and environmental protection, Institute of Physics and Chemistry, China. Commercial dressing Tegaderm™ film was obtained from 3M Healthcare (United States).

2.2 Preparation of the EFS hydrogel

The EFS hydrogel was prepared by adjusting the floating-accumulating process of HGM in hydrogel precursor solution. Hydrogel precursor solution: AAm (10 g) was dissolved in deionized water (100 mL), and then MBAA (0.1 g), and DEAP (0.1 g) were added to the hydrogel precursor solution respectively. To increase the viscosity, 2 g of SA was added to the hydrogel precursor solution. The hydrogel precursor and HGM were mixed at a volume ratio of 8:2 and dispersed by ultrasound at 150 W power through an ultrasonic cell breaker (JY92-IIN, Ningbo Kezhi Biotechnology Co., LTD., China). The precursor solution was allowed to stand for 30 min at room temperature to allow the HGM to float up and form a microspheres layer before the cross-linking step. They were then photocrosslinked under 365 nm UV for 20 min and freeze-dried to obtain the final sample. To investigate the effect of the enhanced fractal structure on the absorption performance, HGM with different diameter distributions, diameter 5–80 μm as enhanced fractal microchannels and 20–80 μm as normal fractal microchannels, were used for comparison.

2.3 Evaluation of continuous water absorption capability

The dynamic contact angles (CA) of water droplets on the samples (1 × 1 cm^2) were recorded by the OCA-20 machine (Dataphysics Germany). The volume of each water droplets was set as 2 μL.

2.4 Calculation of fractal dimension

The fractal dimension results are calculated by 'Fractal box count', a plug-in of software 'ImageJ 1.50i' (National Institutes of Health, United States).

2.5 *In vivo* burn wound model

8-week-old female Sprague Dawley (SD) rats were used for burn wound models (n = 5). After depilating the back of rats, four burn wounds were produced on the back of each rat under anesthesia. The desktop super temperature control scald device (YLS-5Q, Beijing, China) was employed to control the wound area (0.8 cm^2), burn time (5 s), temperature (100°C) and pressure (200 g). Then EFS hydrogel, pure hydrogel, Tegaderm™ (3M, United States), and gauze were immobilized on the wound sites with 3M Micropore™ tape and replaced every 2 days.

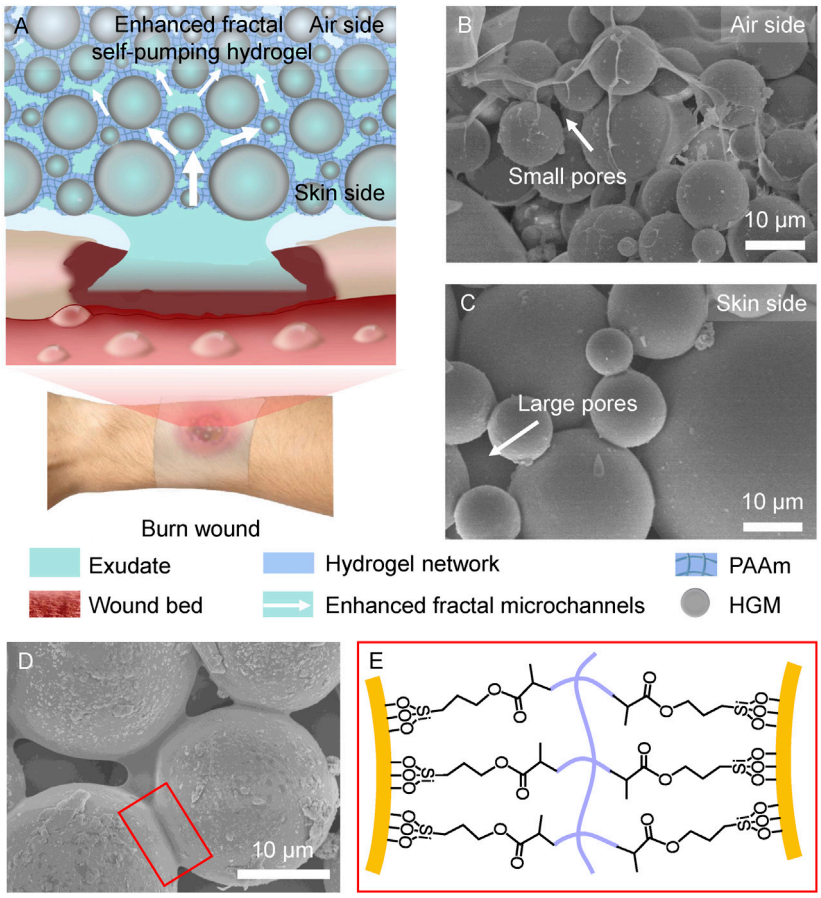

FIGURE 1
Design of the enhanced fractal self-pumping (EFS) hydrogel dressing. **(A)** Illustration of the EFS hydrogel with enhanced fractal microchannels for draining exudates from burn wounds. **(B, C)** SEM images of the gradient HGM with small pores at air side **(B)** and large pores at skin side **(C)** in the EFS hydrogel. **(D)** SEM image of the hydrogel network between the adjacent HGM. **(E)** Schematic graph of connection between HGM and hydrogel network by silane coupling agent.

3 Results and discussion

The design of enhanced fractal self-pumping hydrogel (EFS hydrogel) dressing is illustrated in Figure 1A that can remove excessive exudates from burn wounds through the enhanced fractal microchannels. In the EFS hydrogel, hollow glass microspheres (HGM) with diameter of 5–80 μm were embedded in polyacrylamide (PAAm) hydrogel network (blue frame) with a gradually decreased diameter from skin side to air side (as shown in Figures 1B, C). Different with the normal fractal structure, small HGM are inset into gaps between the adjacent large HGM in the EFS hydrogel (Figures 1B, C). By squeezing the hydrogel network, the enhanced fractal hydrophilic microchannels of hydrogel were formed between HGM (Figure 1D). The hydrogel network was anchored onto the surface of silane coupling agent modified HGM through C=C bond cross-linking (Figure 1E). The unique enhanced fractal self-pumping microchannels were successfully fabricated in EFS hydrogel.

The fractal structure was formed by the accumulation of floating HGM. When HGM whose density is lower than that of the hydrogel precursor solution is dispersed in the hydrogel precursor solution, it would float driven by the buoyancy. During this upward movement, it follows the Stokes law. The displacement velocity V_{Stokes} can be calculated using the Stokes settling formula (Goodarzi and Zendehboudi, 2019):

$$V_{Stokes} = \frac{(\rho_H - \rho_w) g d^2}{18 \mu_w} \quad (1)$$

Here ρ_H and ρ_w refer the densities of HGM and water phase, respectively. d refers to the HGM diameter. g refers to the acceleration of gravity. μ_w refers to the viscosity of the water phase.

According to Eq. 1, under the conditions of constant HGM density and water-related factors, larger diameter of HGM would increase its floating velocity (V_{Stokes}). High V_{Stokes} will drive large HGM to accumulate near the air-liquid interface, resulting in a fractal arrangement of HGM that diameter decreases along the gravity direction.

Further, we compared the dynamic contact angles of the continuous water dripping on HGM with the diameter distribution of 5–80 μm (enhanced fractal channels) and that of 20–80 μm (normal fractal channels). EFS hydrogels (Figure 2A) had a fast water absorption (initially 0.4 s) and no attenuation of water absorption performance during continuous absorption. In contrast, normal fractal self-pumping

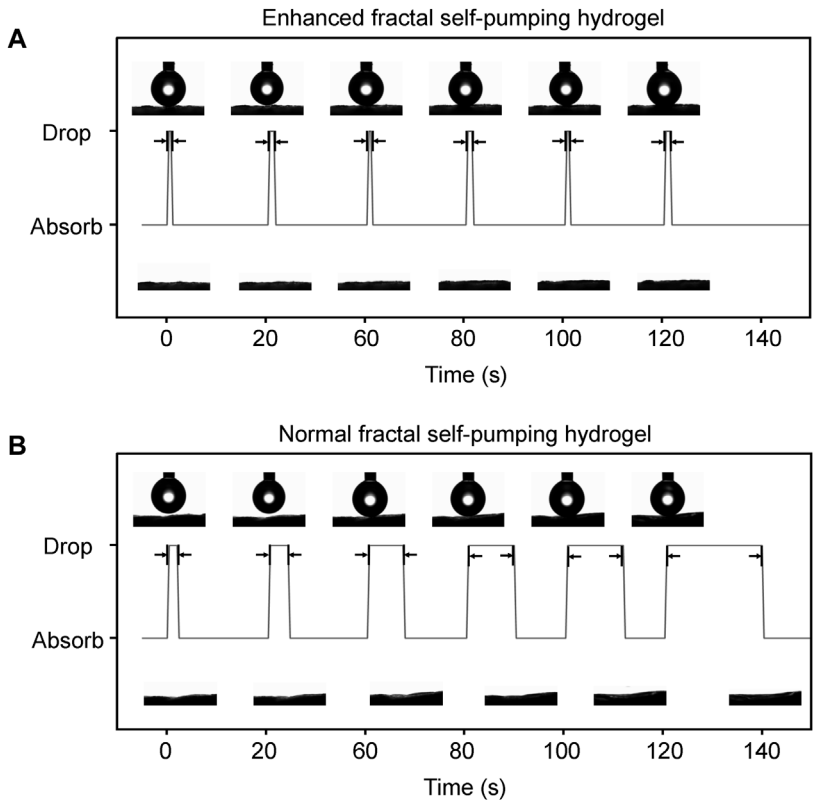

FIGURE 2
Comparison of the continuous absorption performance of the EFS hydrogel **(A)** with enhanced fractal microchannels and the normal fractal self-pumping hydrogel **(B)** without enhanced fractal microchannels.

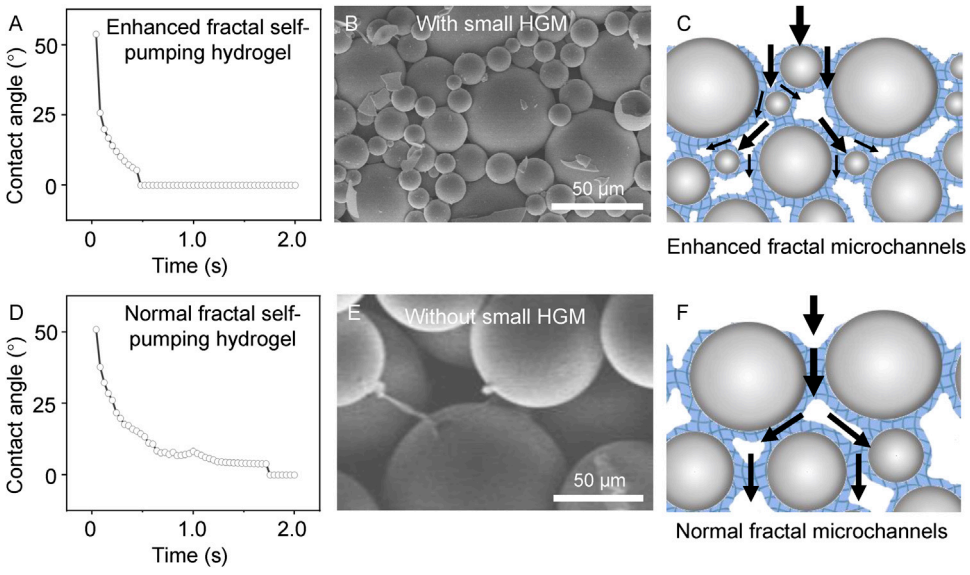

FIGURE 3
Comparison of the EFS hydrogel **(A–C)** and normal fractal self-pumping hydrogel **(D–F)** without enhanced fractal microchannels in absorption rate **(A, D)**, structure **(B, E)**, and draining model **(C, F)**.

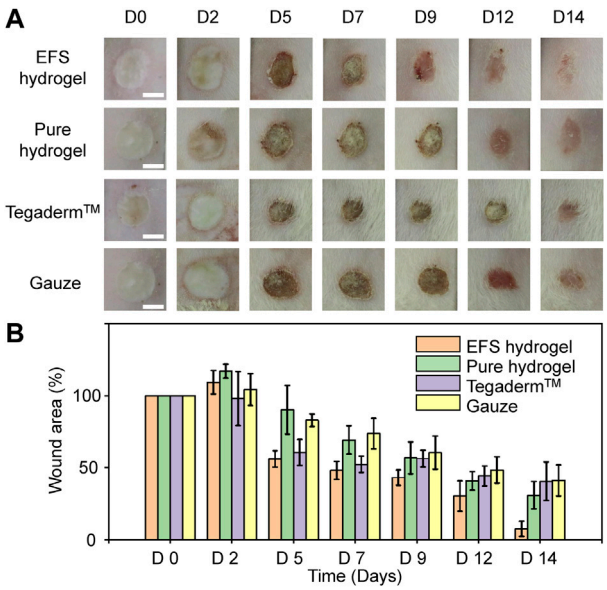

FIGURE 4
Burn healing performance treated by various dressings. **(A)** Digital photos of burn wound after 0, 2, 5, 7, 9, 12 and 14 days treatment by EFS hydrogel, pure hydrogel, commercial Tegaderm™ dressing, and gauze, respectively. **(B)** Statistical wound areas of the corresponding treatment during 14 days.

hydrogel (Figure 2B) had a slow water absorption (initially 1.6 s) and a significant increase in absorption time with continuous drip of water droplets (increasing to 19.2 s). The videos of the continuous water absorption performance of EFS hydrogel (Supplementary Video S1) and normal fractal self-pumping hydrogel (Supplementary Video S2) were included in the Supplementary Videos (The videos were played at 20x speed).

To explore the improvement in water absorption performance, we characterized the microstructures of two types of fractal self-pumping hydrogels (Figure 3). The EFS hydrogel can absorb water droplet (2 μL) within 0.4 s (Figure 3A), while normal fractal self-pumping hydrogel takes 1.6 s (Figure 3D). The reason of the ultra-fast absorption is that the enhanced fractal microchannels in EFS hydrogel are splitted into smaller ones by the small HGM, resulting in a larger fractal dimension. The large fractal dimension value indicates a more complex microchannel structure and higher conductivity efficiency (Xu et al., 2019). This theoretical deduction is consistent with the experimental result that EFS samples with a wider diameter distribution exhibit higher water absorption efficiency.

To verify the promoting effect of EFS hydrogel on wound healing, we explored the performance of EFS hydrogel dressings in the burn wound model on murine. We used the pure hydrogel, commercial dressing (Tegaderm™), and gauze as controls. According to the digital photos of the wound appearance in Figure 4, the edema of wounds treated with EFS hydrogel were alleviated compared to the other three groups on the second day, reflecting better draining of exudates. On the 5th day, the wound area of the EFS hydrogel group was significantly reduced. On the 9th day, the scab on the wound surface almost disappeared. It completed the decrustation process on the 14th day treated by the EFS hydrogel. Wound area quantification was conducted at days 2, 5, 7, 9, 12, and 14 after injury (Figure 4B). The reduction rate wound areas of EFS hydrogel treatment are significantly higher than those of other groups. Based on these results, EFS hydrogel can effectively promote burn wound healing compared to the other three treatments.

4 Conclusion

In conclusion, we have successfully fabricated an enhanced fractal self-pumping (EFS) hydrogel dressing with enhanced fractal microchannels constructed through a simple buoyancy-driven floating-accumulating process that can absorb water in a high absorption efficiency continuously and accelerate burn wound healing. The enhanced fractal microchannels are formed between the adjacent HGM by squeezing the hydrogel networks. The as synthesized EFS hydrogel possess enhanced draining ability that can absorb water within 0.4 s and continuously drain water without any decreasing efficiency. In the murine burn wound model, the EFS hydrogel exhibits accelerated wound healing. Enhanced fractal microchannels create a new construction model for fabricating functional materials with ultra-fast draining ability. This study will open a new avenue for managing continuous biofluids in clinical research and applications.

Data availability statement

The raw data supporting the conclusion of this article will be made available by the authors, without undue reservation.

Ethics statement

The animal study was reviewed and approved by The National Regulation of China for Care and Use of Laboratory Animals.

Author contributions

All authors were involved in drafting the article or revising it critically for important intellectual content, and all authors approved the final version to be published. Study conception and design. JL, LS, and SW. Acquisition of data. JL, WX, XZ, YW, and LS. Analysis and interpretation of data. JL and LS.

Funding

This study was supported by National Natural Science Foundation of China (Nos. 22002177, 21972155 and 22035008).

Conflict of interest

LS and SW were employed by Qingdao Casfuture Research Institute Co. Ltd.

The remaining authors declare that the research was conducted in the absence of any commercial or financial relationships that could be construed as a potential conflict of interest.

Publisher's note

All claims expressed in this article are solely those of the authors and do not necessarily represent those of their affiliated organizations, or those of the publisher, the editors and the reviewers. Any product that may be evaluated in this article, or claim that may be made by its manufacturer, is not guaranteed or endorsed by the publisher.

Supplementary material

The Supplementary Material for this article can be found online at: https://www.frontiersin.org/articles/10.3389/fbioe.2023.1188782/full#supplementary-material

References

Bao, F., Pei, G., Wu, Z., Zhuang, H., Zhang, Z., Huan, Z., et al. (2020). Bioactive self-pumping composite wound dressings with micropore array modified janus membrane for enhanced diabetic wound healing. *Adv. Funct. Mater.* 30 (49), 2005422. doi:10.1002/adfm.202005422

Calo, E., and Khutoryanskiy, V. V. (2015). Biomedical applications of hydrogels: A review of patents and commercial products. *Eur. Polym. J.* 65, 252–267. doi:10.1016/j.eurpolymj.2014.11.024

Chauhan, V. S., and Mir, M. A. (2018). Plaster burn: Challenge to plastic surgeon. *World J. plastic Surg.* 7 (2), 226–230.

Church, D., Elsayed, S., Reid, O., Winston, B., and Lindsay, R. (2006). Burn wound infections. *Clin. Microbiol. Rev.* 19 (2), 403–434. doi:10.1128/cmr.19.2.403-434.2006

Cook, K. A., Martinez-Lozano, E., Sheridan, R., Rodriguez, E. K., Nazarian, A., and Grinstaff, M. W. (2022). Hydrogels for the management of second-degree burns: Currently available options and future promise. *Burns trauma* 10, tkac047. doi:10.1093/burnst/tkac047

Cutting, K. F., and White, R. J. (2002). Maceration of the skin and wound bed. 1: Its nature and causes. *J. wound care* 11 (7), 275–278. doi:10.12968/jowc.2002.11.7.26414

Desroche, N., Dropet, C., Janod, P., and Guzzo, J. (2016). Antibacterial properties and reduction of MRSA biofilm with a dressing combining polyabsorbent fibres and a silver matrix. *J. Wound Care* 25 (10), 577–584. doi:10.12968/jowc.2016.25.10.577

Fan, J., Zhu, N., Liu, Z., Cheng, Q., and Liu, Y. (2015). A model for allometric permeation in fractal branching channel net driven by capillary pressure. *Int. J. Numer. Methods Heat Fluid Flow* 25 (8), 1886–1895. doi:10.1108/hff-01-2014-0011

Glik, J., Labus, W., Kitala, D., Mikus-Zagorska, K., Roberts, C. D., Nowak, M., et al. (2018). A 2000 patient retrospective assessment of a new strategy for burn wound management in view of infection prevention and treatment. *Int. Wound J.* 15 (3), 344–349. doi:10.1111/iwj.12871

Goodarzi, F., and Zendehboudi, S. (2019). A comprehensive review on emulsions and emulsion stability in chemical and energy industries. *Can. J. Chem. Eng.* 97 (1), 281–309. doi:10.1002/cjce.23336

Guo, B. L., Dong, R. N., Bang, Y. P., and Li, M. (2021). Haemostatic materials for wound healing applications. *Nat. Rev. Chem.* 5 (11), 773–791. doi:10.1038/s41570-021-00323-z

Jeschke, M. G., Gauglitz, G. G., Kulp, G. A., Finnerty, C. C., Williams, F. N., Kraft, R., et al. (2011). Long-term persistance of the pathophysiologic response to severe burn injury. *PLoS ONE* 6 (7), e21245. doi:10.1371/journal.pone.0021245

Jeschke, M. G., van Baar, M. E., Choudhry, M. A., Chung, K. K., Gibran, N. S., and Logsetty, S. (2020). Burn injury. *Nat. Rev. Dis. Prim.* 6 (1), 11. doi:10.1038/s41572-020-0145-5

Kharaziha, M., Baidya, A., and Annabi, N. (2021). Rational design of immunomodulatory hydrogels for chronic wound healing. *Adv. Mater.* 33 (39), 2100176. doi:10.1002/adma.202100176

Lee, J. J., Berthier, J., Kearney, K. E., Berthier, E., and Theberge, A. B. (2020). Open-Channel capillary trees and capillary pumping. *Langmuir* 36 (43), 12795–12803. doi:10.1021/acs.langmuir.0c01360

Lee, K. Y., and Mooney, D. J. (2012). Alginate: Properties and biomedical applications. *Prog. Polym. Sci.* 37 (1), 106–126. doi:10.1016/j.progpolymsci.2011.06.003

Leonhardt, E. E., Kang, N., Hamad, M. A., Wooley, K. L., and Elsabahy, M. (2019). Absorbable hemostatic hydrogels comprising composites of sacrificial templates and honeycomb-like nanofibrous mats of chitosan. *Nat. Commun.* 10, 2307. doi:10.1038/s41467-019-10290-1

Li, D. W., Bu, X. C., Xu, Z. P., Luo, Y. W., and Bai, H. (2020). Bioinspired multifunctional cellular plastics with a negative Poisson's ratio for high-energy dissipation. *Adv. Mater.* 32 (33), 2001222. doi:10.1002/adma.202001222

Li, Z., Milionis, A., Zheng, Y., Yee, M., Codispoti, L., Tan, F., et al. (2019). Superhydrophobic hemostatic nanofiber composites for fast clotting and minimal adhesion. *Nat. Commun.* 10, 5562. doi:10.1038/s41467-019-13512-8

Loke, W. K., Lau, S. K., Yong, L. L., Khor, E., and Sum, C. K. (2000). Wound dressing with sustained anti-microbial capability. *J. Biomed. Mater. Res.* 53 (1), 8–17. doi:10.1002/(sici)1097-4636(2000)53:1<8:aid-jbm2>3.0.co;2-3

Luo, Z., Jiang, L., Xu, C. F., Kai, D., Fan, X. S., You, M. L., et al. (2021). Engineered Janus amphipathic polymeric fiber films with unidirectional drainage and anti-adhesion abilities to accelerate wound healing. *Chem. Eng. J.* 421, 127725. doi:10.1016/j.cej.2020.127725

Martin, J. E., and Hurd, A. J. (1987). Scattering from fractals. *J. Appl. Crystallogr.* 20, 61–78. doi:10.1107/s0021889887087107

Mauroy, B., Filoche, M., Weibel, E. R., and Sapoval, B. (2004). An optimal bronchial tree may be dangerous. *Nature* 427 (6975), 633–636. doi:10.1038/nature02287

Montazerian, H., Davoodi, E., Baidya, A., Baghdasarian, S., Sarikhani, E., Meyer, C. E., et al. (2022). Engineered hemostatic biomaterials for sealing wounds. *Chem. Rev.* 122, 12864–12903. doi:10.1021/acs.chemrev.1c01015

Peck, M. D., and Toppi, J. T. (2020). *Handbook of burns volume 1 acute burn Care*. 2nd Edition. Switzerland: Springer.

Poyet, S. (2021). Water transport properties of virtual fractal porous media: Implications for the unsaturated transport properties of cement-based materials. *Cem. Concr. Res.* 150, 106613. doi:10.1016/j.cemconres.2021.106613

Qi, L. Y., Ou, K. K., Hou, Y. J., Yuan, P. P., Yu, W., Li, X., et al. (2021). Unidirectional water-transport antibacterial trilayered nano fi ber-based wound dressings induced by hydrophilic-hydrophobic gradient and self-pumping effects. *Mater. Des.* 201, 109461. doi:10.1016/j.matdes.2021.109461

Shi, L. X., Liu, X., Wang, W. S., Jiang, L., and Wang, S. T. (2019). A self-pumping dressing for draining excessive biofluid around wounds. *Adv. Mater.* 31 (5), 1804187. doi:10.1002/adma.201804187

Shou, D. H., Ye, L., and Fan, J. T. (2014). Treelike networks accelerating capillary flow. *Phys. Rev. E* 89 (5), 053007. doi:10.1103/PhysRevE.89.053007

Tyan, Y. C., Liao, J. D., and Lin, S. P. (2003). Surface properties and *in vitro* analyses of immobilized chitosan onto polypropylene nonwoven fabric surface using antenna-coupling microwave plasma. *J. Mater. Science-Materials Med.* 14 (9), 775–781. doi:10.1023/a:1025036421604

Wang, C. W., Niu, H. Y., Ma, X. Y., Hong, H., Yuan, Y., and Liu, C. S. (2019). Bioinspired, injectable, quaternized hydroxyethyl cellulose composite hydrogel coordinated by mesocellular silica foam for rapid, noncompressible hemostasis and wound healing. *ACS Appl. Mater. Interfaces* 11 (38), 34595–34608. doi:10.1021/acsami.9b08799

Xu, J., Wu, K., Li, R., Li, Z., Li, J., Xu, Q., et al. (2019). Nanoscale pore size distribution effects on gas production from fractal shale rocks. *Fractals* 27 (08), 1950142. doi:10.1142/s0218348x19501421

Zhang, K., Jiao, X., Zhou, L., Wang, J., Wang, C., Qin, Y., et al. (2021). Nanofibrous composite aerogel with multi-bioactive and fluid gating characteristics for promoting diabetic wound healing. *Biomaterials* 276, 121040. doi:10.1016/j.biomaterials.2021.121040

Zhang, Z. W. B., Li, W. B., Liu, Y., Yang, Z. G., Ma, L. L., Zhuang, H., et al. (2021). Design of a biofluid-absorbing bioactive sandwich-structured Zn-Si bioceramic composite wound dressing for hair follicle regeneration and skin burn wound healing. *Bioact. Mater.* 6 (7), 1910–1920. doi:10.1016/j.bioactmat.2020.12.006

Zhou, G. N., Simerly, T., Golovko, L., Tychinin, I., Trachevsky, V., Gomza, Y., et al. (2012). Highly functionalized bridged silsesquioxanes. *J. Sol-Gel Sci. Technol.* 62 (3), 470–482. doi:10.1007/s10971-012-2751-5

frontiers | Frontiers in Bioengineering and Biotechnology

TYPE Mini Review
PUBLISHED 09 May 2023
DOI 10.3389/fbioe.2023.1196174

OPEN ACCESS

EDITED BY
Pengchao Zhang,
Wuhan University of Technology, China

REVIEWED BY
Jie Jia,
Fudan University, China
Chunmei Ding,
Sichuan University, China

*CORRESPONDENCE
Xuejun Guo,
guojunkangfu@163.com
Ping Lu,
lupingdoctor@126.com

†These authors have contributed equally to this work

RECEIVED 29 March 2023
ACCEPTED 24 April 2023
PUBLISHED 09 May 2023

CITATION
Wang Z, Xiao C, Roy M, Yuan Z, Zhao L, Liu Y, Guo X and Lu P (2023), Bioinspired skin towards next-generation rehabilitation medicine.
Front. Bioeng. Biotechnol. 11:1196174.
doi: 10.3389/fbioe.2023.1196174

Bioinspired skin towards next-generation rehabilitation medicine

Zhenghui Wang[1†], Chen Xiao[1†], Mridul Roy[2†], Zhiyao Yuan[3], Lingyu Zhao[1], Yanting Liu[2], Xuejun Guo[1*] and Ping Lu[2*]

[1]Department of Rehabilitation, The First Affiliated Hospital of Xinxiang Medical University, Weihui, China, [2]Department of Oncology, The First Affiliated Hospital of Xinxiang Medical University, Weihui, China, [3]SanQuan College of Xinxiang Medical University, Xinxiang, China

The rapid progress of interdisciplinary researches from materials science, biotechnologies, biomedical engineering, and medicine, have resulted in the emerging of bioinspired skins for various fantasticating applications. Bioinspired skin is highly promising in the application of rehabilitation medicine owing to their advantages, including personalization, excellent biocompatibility, multi-functionality, easy maintainability and wearability, and mass production. Therefore, this review presents the recent progress of bioinspired skin towards next-generation rehabilitation medicine. The classification is first briefly introduced. Then, various applications of bioinspired skins in the field of rehabilitation medicine at home and abroad are discussed in detail. Last, we provide the challenges we are facing now, and propose the next research directions.

KEYWORDS

bioinspired skin, rehabilitation medicine, electronic skin, tissue-engineered artificial, prostheses and implant

1 Introduction

The skin is the body's first line of defense that provides protection against harmful foreign substances and plays a key role in maintaining the body's homeostasis (Li, 2017). As the largest organ in the body, it plays a wide range of functions, including respiratory, protective, secretory, thermoregulatory and sensory stimulation functions (Liang et al., 2022; Xie, 2022). Burns and ulcers cause about 9 million cases of skin lesions in China each year, of which 3.2 million require skin grafts. Additionally, more than 200,000 cases of burns require extensive skin replacement. Among them, some patients are unable to undergo autologous skin grafting due to having too many skin defects of their own. When allogeneic skin grafts, such as allografts and xenografts are chosen, the sources are extremely limited and there is a high probability of severe immune rejection of allogeneic skin (Zhao et al., 2017). For amputees, conventional prostheses only offer basic cosmetic and simple mobility functions, but they lack the tactile and sensory abilities that disabled patients really need. Therefore, the availability of high-quality skin remains a major factor limiting the development of rehabilitation medicine and affecting the health of patients. At this point, bioinspired skin with multiple functions is attracting significant interest as a novel area of research not only in human-machine interfaces, flexible wearable devices and soft robotics (Lei and Wu, 2018; Xing, 2021), but also has extraordinary significance for the development of rehabilitation medicine. Bioinspired skin technology has gained wider use in the field of rehabilitation medicine in recent years. For example, the development of skin tissue

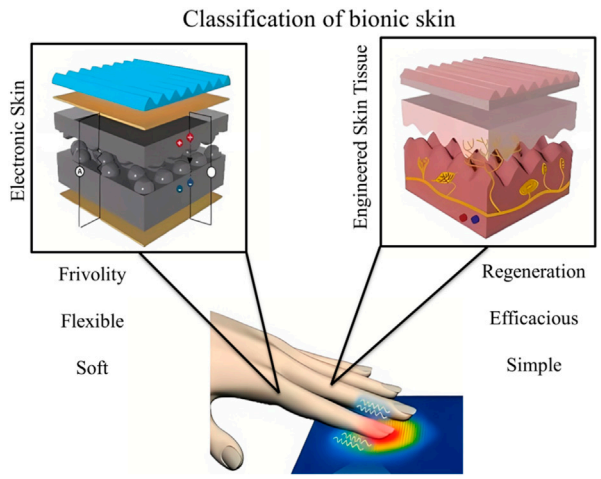

FIGURE 1
Classification of bionic skin: electronic skins and skin tissue engineering.

engineering has brought benefits to a large number of patients who need skin implants (Horch et al., 2005), while smart e-skin/bionic skin has made great progress in medical robotics and smart prosthetics (Wang et al., 2023). Bioinspired skin can improve the ability to transfer information between human-machine interfaces and increase the degree of human response to painful stimuli. Moreover, they are able to help patients regain self-care in daily life, regulate emotions and reconstruction to perform complex limb functions.

2 Classification of bioinspired skin

At this stage, research on bioinspired skin is mainly focused on two aspects: the first one is electronic skin (E-skin) and the second is tissue-engineered artificial skin (Figure 1). Early E-skin consists of rubber, conductive graphite and new transistors that can mimic the sensory functions of human skin (Lei, 2022). In recent years new materials such as polydimethylsiloxane, carbon nanotubes, graphene and hydrogels have been used to prepare E-skin sensors (Wan et al., 2020), making E-skin more convergent to human skin in terms of performance. Contrary, tissue-engineered artificial skin is being developed based on theories and methods from cell engineering and biology (Lin et al., 2022). And this skin substitute is artificially developed *in vitro* to repair and replace defective skin tissue (Naves et al., 2016).

2.1 Electronic skin

As the largest organ of the human body, the skin possesses a variety of interesting properties such as stretchability, self-healing ability, high malleability and haptic ability. Devices that mimic these properties of human skin, as well as additional functions, are referred to as electronic skins (Xiang, 2021). Advances in materials, mechanics, electronics and information technology have driven the development of smart electronic skins. For instance, due to the advancement of stretchable polymer materials, a wide variety of stretchable bioinspired sensors, such as pressure/strain sensors, thermal sensors, optical sensors and biochemical sensors, have been developed (Park et al., 2018). New organic semiconductors have extended the frontiers of smart electronic skin to integrate artificial nerves, including synapses and afferent nerves (Liu et al., 2022). Smart E-skins are exceedingly attractive in every respect. Although still under development, ionic skin, the next-generation of E-skin, is within reach of future development (Gong et al., 2022).

2.2 Tissue-engineered artificial skin

Skin tissue engineering is a modern approach to reconstruct structural and functional components of skin following chronic wound that generally occurs during the healing process and precludes skin regeneration. Currently, the scaffolding materials for tissue-engineered artificial skin are divided into two main categories: natural polymer materials and synthetic polymer materials (Wang et al., 2020). Tissue-engineered artificial skin can be broadly categorized into three types based on their structure and function: epidermal substitutes, dermal substitutes and skin substitutes containing a bilayer structure of epidermis and dermis (Yan et al., 2018). The development of 3D printing technology has significantly expanded the application of tissue-engineered skin in rehabilitation medicine owing to its excellent properties such as high resolution, flexibility, reproducibility and high throughput that paves the way for the preparation and medical application of tissue-engineered skin (Lian et al., 2021).

3 Distinctive features of electronic skin: stimuli-responsiveness and self-healing capacity

Wearable electronic skins can transform environmental stimulus variation into electronic signal change (Lee et al., 2020). To imitate this sensory ability of human skin, different sensitive conductive architectures are placed upon soft polymer substrates (Table 1). Guo et al. have provided a comprehensive review of the recent advances in the design strategy of material structures that imitate the multiple stimuli perception and self-healing functionalities of biological skins (Guo et al., 2022). The electronic sensors with the capacity to detect external stimulus include resistance-, capacity-, piezoelectric-, triboelectric, and potentiometric-type sensors (Yao et al., 2017). Through the unique coaxial structure and fibrous sensing architecture the sensor arrays could simultaneously map and quantify multiple mechanical stresses, including normal pressure, lateral strain and flexion. The capacitive sensor is one of the most traditional and popular sensors in tactile stimulation detection. Capacitance is a parameter to measure the charge storage capacity, and it is a function of the dielectric constant, area and the distance between the two electrodes of the parallel plate capacitor. The principle of the traditional capacitive sensor is that the pressure or shear force applied will lead to a change in the distance or area between the

TABLE 1 Materials and working principles used for Sense and self-healing characteristics of bioinspired skin.

Stimuli	Material	Working principle
Force	MXene nanosheets, MNOH, PDMS, Single Crystalline Silicon (Kim et al., 2014; Liao et al., 2019; Zhang L et al., 2021; Chen et al., 2022; Cheng et al., 2022)	These materials can make electronic skin have tensile properties. The sensor has a variety of functions because of its special materials, conduction methods (piezoresistive, piezoelectric, capacitance, *etc.*) and special arrangement structure (serpentine, paper-cut, *etc.*). (Xu et al., 2013; Nasreldin et al., 2020)
Temperature	$MoSe_2$, MoO_3, Graphene, ZnO, nanometer material, CNTs (Kang et al., 2018; Liu et al., 2019; Zeng et al., 2022; Zhang H et al., 2022)	
Humidity		
Healing	MoS_2、Silicon wafer、PDMS、3D porous graphene, Tattoo-base paper, Silicon/SU8, Single-walled carbon nanotube, PET film, Gold nanowires (García-Ávila et al., 2021; Wei et al., 2021; Cao and Cai, 2022; Li et al., 2022)	

two plates, which will change the capacitance (Chou and Lee, 2021). Based on this principle, super-stretchable capacitive strain sensors and high-sensitivity capacitive pressure sensors based on various nanomaterials can be developed.

Biological skins can recover their original appearance and critical functions after physical damage. Advanced e-skins are equipped with the self-healing ability to extend their service life and reduce maintenance costs (Keng et al., 2018). In order to achieve satisfying self-recovering properties, self-healable polymeric materials are specially designed and applied as the core functional component for self-healing electronics. According to different healing mechanisms, they could be generally categorized into extrinsic and intrinsic self-healing materials. Among them, single dynamic crosslinking networks are utilized to dynamically crosslink polymer materials and endow them with autonomous self-healing capabilities (Oh and Bao, 2019). Most of the organic polymer systems of flexible electronic skin materials are formed by the entanglement of long chains of polymer molecules, and when conditions such as temperature and humidity permit, the material itself can be reconstructed by the regeneration of dynamic covalent or non-covalent bonds and the re-entanglement of polymer chains at the damaged interface. Secondly, even if some polymers themselves cannot achieve self-healing, they can heal for a certain number of times after injury by adding a healing agent to the base material of the electronic skin in advance (Guo et al., 2022).

4 Application of bioinspired skin

4.1 Application of bioinspired skin in prostheses

The importance of a good pair of prostheses for disabled patients cannot be overstated, and the use of smart bioinspired skins with multiple functions in prostheses can make a world of difference to the lives of people with disabilities (Wang et al., 2022). Lei and Wu (2018) reported on a bioinspired smart skin based on supramolecular hydrogels. The transparent supramolecular hydrogel can polymerize into a series of skin-like or even skin-exceeding mechanical properties, combining compressive resilience, large stretching, self-healing, and can be shaped at will at room temperature by building multiple dynamic cross-linking networks with basic random copolymerization reactions (Figure 2A). When applied to the plastic fingers of a prosthesis, this supramolecular hydrogel-based bioinspired skin allows the prosthetic fingers to sense strain and temperature stimuli through capacitive and resistive signals, effectively mimicking the mechanical and temperature receptors of human skin. It can therefore record the bending and straightening movement of the finger based on the change in capacitance during the deformation process, and detects the rise in temperature of the prosthetic surface utilizing a real-time reduced resistance signal during manual contact with the prosthesis, allowing visual observation of the movement of the finger and the external temperature change (Figures 2B, C). However, as an exposed part of the prosthetic skin, it is susceptible to accidental mechanical damage caused by continuous wear and tear, resulting in interruption of function or reduced device life. Therefore, the ability to self-repair, similar to human skin, is an important inherent property necessary to restore damaged function to ensure stability and increase the longevity of the device. Boahen et al. (2022), designed and synthesized a novel thermoplastic polyurethane material containing dynamic disulfide bonding functional groups and chlorine substituents (Figure 2D). The material was based on the principle of mechanical stimulus-response of tactile cells, simulating the self-healing function of real human skin and biological ion signaling mechanisms. The dynamic disulfide bonding is always reversible and dynamic, enabling rapid self-healing of injuries at room temperature without additional energy. This reduces the frequency of prosthetic skin replacement, extends the life of the prosthesis, reduces the incidence of phantom limb pain and improves perception (Park et al., 2018). The new concept of ionic skin technology presented by this thermoplastic polyurethane material is of significant meaning as it simultaneously restores wound and haptic functions, making it an ideal candidate for future applications in human-computer interaction and wearable devices. Jie Zheng of the Zhejiang University of Technology (Jie, 2022) has developed a flexible electronic skin made of silk protein/graphene oxide (SP/GO) nanofibers (Figure 2E). This e-skin can be used to wirelessly monitor human joint movements and act as a pulse monitor to monitor human heart rate. The skin maintains stable sensing performance after 36,000 bend-release cycles, using a self-assembled wireless configuration to achieve SF/GO nanofiber composite flexible electronic skin. The SF/GO nanofiber composite flexible electronic skin can transmit data for real-time monitoring by connecting wirelessly to a smartphone. Park et al. have made great efforts in bioinspired skin electronic

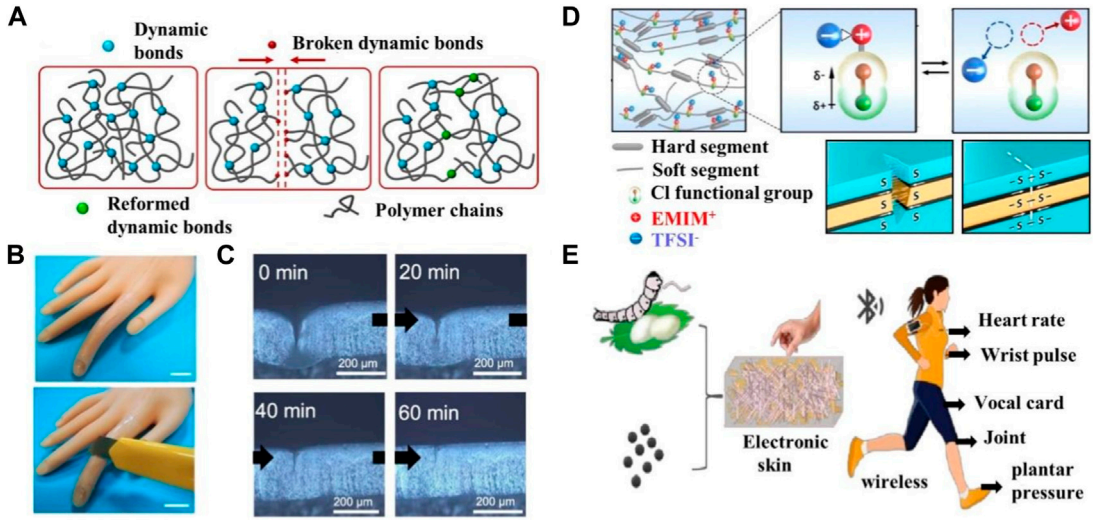

FIGURE 2
Application of bionic skin in prostheses. **(A)** The schematic illustration of the dynamic process of how dissociated groups tend to reform bridges to repair the networks for self-healing. Reproduced with permission from (Lei and Wu, 2018). **(B)** biomimetic skin has self-healability comparable to natural skin and can autonomously repair cracks. **(C)** Microscopic image observes the autonomous self-healing of a scar within 60 min at room temperature. **(D)** Representation of the conceptual design of the Cl-functionalized iontronic pressure-sensitive material (CLiPS) that uses dynamic disulfide bonds to construct the backbone for achieving autonomous self-healing properties to emulate the remarkable functionalities of human skin. Reproduced with permission from (Boahen et al., 2022). **(E)** Preparation process of SF/GO Nanofiber Composite flexible electronic skin. Reproduced with permission from (Jie, 2022).

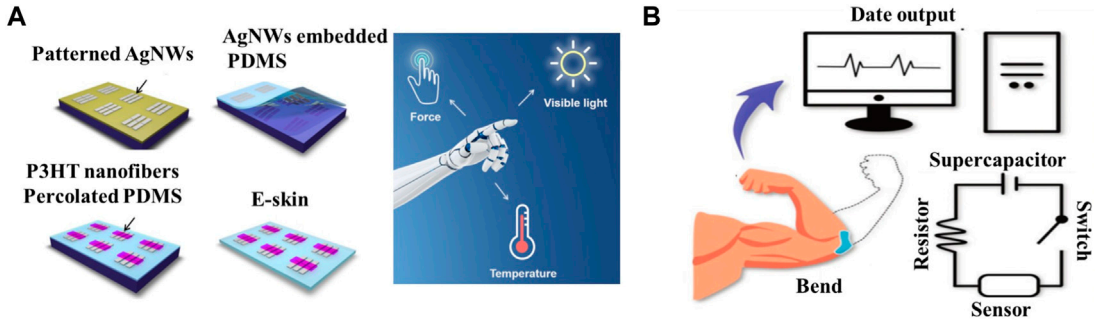

FIGURE 3
Application of bionic skin in rehabilitation equipment. **(A)** Schematic illustration of the process for fabricating the stretchable E-skin. Used with permission from (Liu et al., 2022). Sketch of the E-skin applied on an intelligent robot for multiple perceptions of force, temperature, and visible light. **(B)** Schematic illustration of the self-powered E-skin and corresponding sensing process. Reproduced with permission from (Liang et al., 2022).

sensors which allow people with disabilities to touch the world with the help of haptic sensors (Park et al., 2018). Researchers at RMIT University in Australia (Rahman et al., 2020) have developed a new electronic skin by combining three technologies previously pioneered and patented by the team: stretchable electronics, self-modifying coatings, and electronic memory cells. The resulting skin can be used to improve prosthetic interfaces, increase grip accuracy and enhance the ability to identify the source of injury, allowing the prostheses to act like human skin. Being able to perceive various pain sensations, it acts and responds as quickly as human skin, transmitting pain as a neural signal to the human brain, enabling the prosthetic limb to feel pain like a normal limb that can help people with disabilities to rediscover danger.

4.2 Application of bioinspired skin in rehabilitation equipment

Autonomous artificial intelligence rehabilitation robots with multi-sensory surfaces can perform rehabilitation diagnosis, while robots with sensory and sensing functions can perform highly interactive tasks such as rehabilitation therapy, and disease monitoring using bioinspired sensing skin applied on or in the

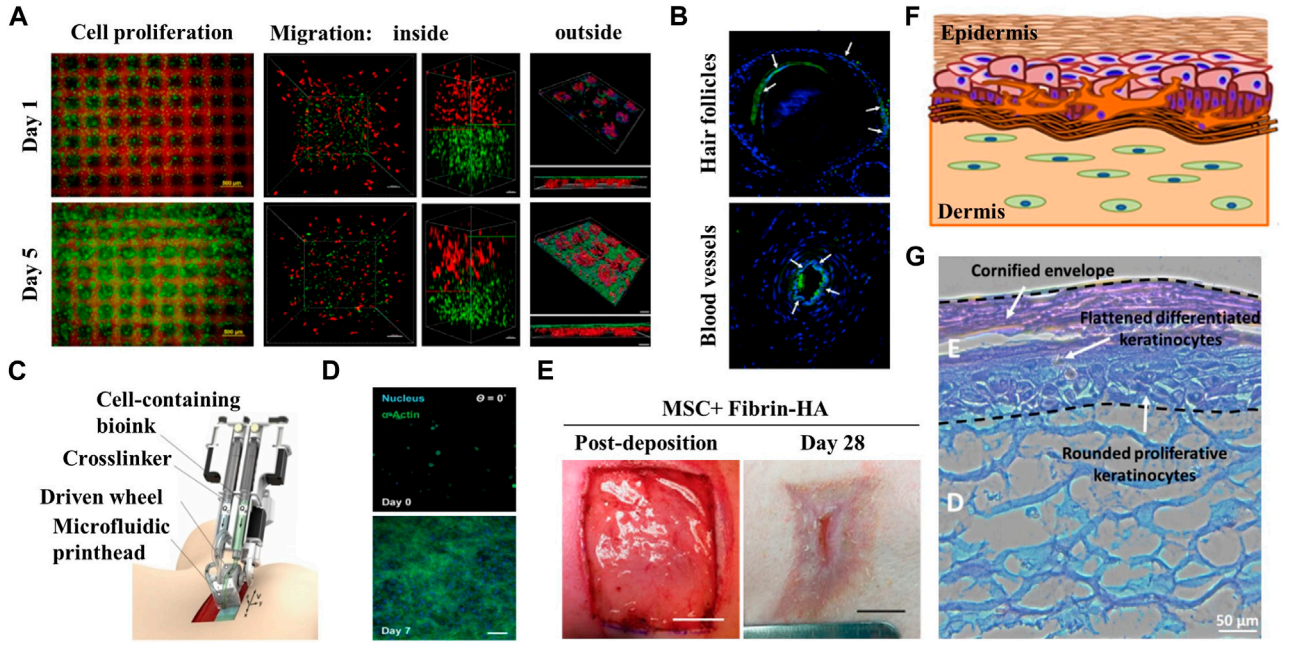

FIGURE 4
Application of bionic skin in burns/implants. **(A)** Microscope images of cell growth in the structure sustainable fabricated functional living skin (FLS) and analysis of cell migration and adhesion inside and outside of the bioprinting skin at day 1 and day 5. **(B)** Immunofluorescence staining showing the formation of hair follicles and blood vessels in FLS. Reproduced with permission from (Zhou et al., 2020). **(C)** Diagram of handheld instrument for controllable delivery of bionic. Reproduced with authorization from (Cheng et al., 2020). **(D)** 3D culture of MSC-fibrin-HA biomaterials at day 0 and day 7 after deposition showing the growth of MSC in biomaterial sheet. **(E)** *In-situ* deposition of MSC-containing fibrin-HA biomaterials into porcine full-thickness burn surface using the handheld device and recovery of the wound after 28 days. **(F)** Presentation of fabricated manual-cast 3D pigmented human skin constructs by bioprinting strategy. **(G)** H&E staining of pigmented human skin constructs obtained using the 3D bioprinting approach. Reproduced with permission from (Ng et al., 2018).

body (Hammock et al., 2013; Yang et al., 2019). Professor Mao and the team at Zhengzhou University (Liu et al., 2022) have developed an electronic skin using P3HT nanofiber permeable PDMS composites as intrinsically stretchable polymer semiconductors. The e-skin is capable of multiple senses such as force, temperature and visible light (Figure 3A). Using this electronic skin, an intelligent robotic sensing and control system was further developed, that can recognize robotic hand gestures, measure the temperature of the touching object and control the robotic hand with visible light beams. The strategy of using intrinsically stretchable polymer semiconductors to construct multi-sensory electronic skins with simple structures is expected to accelerate the development of artificial robotic skins. The bioinspired skin is also expected to replace hospital monitoring instruments, enabling the measurement of vital signs such as heart rate and other health physiological signals to parse out the wearer's health and physical condition and identify potential risk of disease onset promptly (Yao et al., 2020). A flexible electronics research team led by Professor Lan Wei (Liang et al., 2022) from Lanzhou University has proposed an all-in-one self-powered, fully transparent and flexible E-skin, which consists of a transparent supercapacitor, a stretchable transparent strain sensor and a serpentine resistor (Figure 3B). The flexible transparent supercapacitor was constituted using oxygen vacancy-rich molybdenum oxide nanowires as the active material and Nano-cellulose to modulate the refractive index of light to form a self-supporting paper electrode and it exhibited excellent flexibility, transparency and electrochemical performance. The "island bridge structure" strain sensor constructed from one-dimensional silver nanowires and two-dimensional MXene nanosheets has a very high sensitivity, with a GF factor of 220 at 1% strain, which was two orders of magnitude higher than that of similar devices. The supercapacitor is used as a 'stealth' power source to power the integrated E-skin system. Experimental results showed excellent sensing performance under dynamic and static deformation, regardless of the strain range. Once charged, the all-in-one E-skin can be applied to the human skin to detect real-time multi-scale human activities, including weak physiological signals such as pulse, swallowing, limb movements and a large range of limb motion as well. These bioinspired skins have a probable wide range of applications in rehabilitation equipment such as robotic rehabilitation training aids, artificial prosthesis-assisted functional rehabilitation and bioactive material-assisted functional rehabilitation to detect patient physiology at the same time they may assist healthcare professionals in various rehabilitation treatment activities (Yang et al., 2022). Professor Liu of Nanjing normal University (Shao et al., 2022) proposed a novel, conductive structure-colored composite hydrogel, which can be used to rehabilitate the skin of robot knuckles. The structure-colored composite hydrogel material has obvious color change and electromechanical properties in the bending process. Therefore, the film can be used as a multi-signal response of electronic skin to achieve real-time color sensing and electrical response, as well as for

human finger joint rehabilitation robot. It is very valuable for many practical biomedical rehabilitation exercises. Coincidentally, Professor Zhao of Southeast University (Zhang et al., 2020), proposed a multi-functional E-skin inspired by chameleon. The E-skin uses a composite conductive cellulose liquid crystal hydrogel which can provide quantitative feedback for multiple stimuli through electrical signals and report the location of the stimulation site directly through color changes. This kind of dual-signal sensor offers visible interaction with users and anti-interference capacities, making it a prospective candidate for multi-function E-skin application with potential research value in healthcare and variable equipment. These bioinspired skins have a probable wide range of applications in rehabilitation equipment, including robotic rehabilitation training aids, artificial prosthesis-assisted functional rehabilitation and bioactive material-assisted functional rehabilitation to detect patient physiology while assisting healthcare professionals in various rehabilitation treatment activities (Yang et al., 2022).

4.3 Application of bioinspired skin in skin implants

The primary application of bioinspired skin in skin implants is to repair damaged skin resulting from burns, wounds and scars to help to restore the function and appearance of the patients skin and improve their quality of life (Dearman et al., 2021; George et al., 2022). The group led by professor Zhang and professor Ouyang from Zhejiang University (Zhou et al., 2020) printed bioinspired skin with a unique structure by using a newly designed GelMA/HA-NB/LAP bio-ink and light-curing 3D printing technology. The interpenetrating pores within the bioinspired skin facilitate nutrient entry and oxygen exchange, which in turn promote cell adhesion, migration and proliferation leading to formation of new tissue (Figure 4A). *In vivo* studies have demonstrated the effectiveness of tissue-engineered artificial skin in promoting wound healing in both small and large animals, and superior regenerative performance for skin appendages such as hair follicles (Figure 4B). A team at the University of Toronto (Cheng et al., 2020) has developed a biological 3D printer which is a 3D printing device capable of generating large quantities of transplantable artificial skin in a relatively short time (Figure 4C). The printer allows for the extrusion of a hydrogel material known as a "living bandage", which is a mixture of biopolymers, human keratinocytes (a type of skin cell) and fibroblasts. These cellular structures play principal role in wound healing. During the extrusion process, the hydrogel material is printed as discrete and well-defined honeycomb structures that mimic human skin. The application of this artificial skin tissue is aimed to cover the skin wounds caused by burns to promote skin repair, which could potentially revolutionize the rehabilitation process for burn patients (Figures 4D, E). On the other hand, scientists from the Singapore Institute of Manufacturing Technology (SIMTech) and the Centre for 3D Printing at Nanyang Technological University (SC3DP) have developed a 3D-printed fabricated colored skin with uniform skin pigmentation by using bio-3D printing technology (Ng et al., 2018). This is a significant advancement for the technology used in artificial skin manufacturing, as this technology is able to create artificial skin with a matching skin tone to the human body, which will facilitate the use of artificial skin technology in rehabilitation medicine and aid to increase confidence and self-esteem of the implanted patients (Figures 4F, G). Artificial tissue-engineered skin can play a crucial role in case of emergency by preventing wound infection and excessive dehydration of patients. In addition, the use of highly transparent artificial skin in follow-up treatment can also facilitate observation of effusion and infection (Aoki et al., 2015). Scar healing inevitably occurs in the process of skin healing. However, excessive scar growth may lead to scar hyperplasia, contracture, and even deformity, which can severely affect the appearance and function, and at the same time cause serious heart trauma. This can result in several problems in various aspects such as life management, social communication and daily work, and the use of artificial skin also plays a certain role in reducing scar. It is particularly important for the comprehensive rehabilitation of patients (Finnerty et al., 2016).

5 Discussion

The current mainstream works on electronic skin focus on enhancing a single or a few stimulus perceptions attributes, such as pressure or temperature and investigating the combination of some physicochemical and perceptual attributes. However, this type of work usually covers only two or three properties of the skin, which is still far from achieving a skin-like richness of sensory and physicochemical properties of stimulus perception. Hence, the next milestone towards more complex multifunctional bioinspired applications and the next-generation of artificial skin is to cover all the physicochemical and sensory properties of human skin (Duan et al., 2023). Although 3D-printed skin structures that exactly replicate natural skin have not yet been achieved, the current state of skin bioprinting already showed promises for creating functional skin equivalents in several key aspects, from the pre-processing stage to the evaluation of the final product (Yan et al., 2018).

At the same time, however, there are still several problems associated with bioinspired skin that need to be addressed. These include:

(1) Bioinspired skin has poor compatibility with human tissue structures due to the rich and diverse microstructure and complex physical and mechanical properties of human skin (Dąbrowska et al., 2016).
(2) The limited number of sensors loaded in the bioinspired skin results in its inability to sense signals powerfully and accurately from the surrounding environment, and further improvement and refine the ability of bioinspired skin for sensing the signal is depend on the continuous development of new technologies and materials (Du et al., 2020).
(3) At present, the bioinspired skin can only control mechanical movements, and there are still many challenges in the neural interface and brain-machine interface, making it difficult to

achieve natural coordination between robots and the human body (Chortos et al., 2016).

(4) Current printed skin constructs are still distant from natural skin. In addition, addressing other ethical, regulatory and social barriers associated with bioprinting is essential (Tarassoli et al., 2018).

6 Conclusion and future perspective

Bioinspired skin has been used in a wide range of applications in the field of rehabilitation medicine, including prostheses, rehabilitation and burns/implants (Wang et al., 2021; Peng et al., 2023). The field of rehabilitation medicine has benefited most from the application of electronic skin particularly in two key aspects. Firstly, as an external control system, the electronic skin is precisely designed with high flexibility and low friction coefficient, so that it can be used as an external drive system for medical robots, through its control signal to achieve the precise operation of the robot (Yu et al., 2021). Secondly, sensors or micro control systems can be utilized to improve human-robot interaction (Zhang M et al., 2022). In the case of rehabilitation robots and prostheses, haptic sensors would allow rehabilitation robots or amputees to detect their physical surroundings, enabling the performer to handle and manipulate everyday objects and interact with other people among other tasks (Wang et al., 2023).

In the future, bioinspired artificial skin will have the ability to learn and perceive its environment, similar to human skin. It will be able to sense its surroundings and provide feedback to the brain through various sensing signals. For instance, when it comes into contact with other objects in the environment, it will sense the presence of that object and provide feedback to the brain accordingly, so that it can exist like natural skin, and even surpass its capabilities. To this end, the next step in the research should integrate computer intelligence technology for the design and production of artificial bioinspired skin, broaden the application of bioinspired skin, and bring new prospects in the field of rehabilitation medicine (Zhang et al., 2019; Zhang *p* et al., 2021). At the same time, researches should be extended with complex artificial skin having multifunctional physicochemical and sensory perceptions similar to human skin. The close collaboration of multidisciplinary and high-precision technologies will eventually make the extensive application of bioinspired skin in rehabilitation medicine a reality.

Author contributions

ZW, CX and MR contribute the same for manuscript preparation, ZY, YZ and YL prepared the Figures and Tables, XG and PL revised the manuscript, all authors approve the version of the manuscript to be published.

Funding

This work was financially supported by the Joint Fund Project of Xinxiang Medical University (No. LHGJ20200505 and LHGJ20220609), Henan Province Postdoctoral Research Grant (202102095), and the 2023 Henan Province's foreign professor introducing project (HNGD2023025).

Acknowledgments

We would like to thank Weiqing Liu from PICU, The First Affiliated Hospital of Xinxiang Medical University, for her kindly support of figures preparation.

Conflict of interest

The authors declare that the research was conducted in the absence of any commercial or financial relationships that could be construed as a potential conflict of interest.

Publisher's note

Supplementary material

The Supplementary Material for this article can be found online at: https://www.frontiersin.org/articles/10.3389/fbioe.2023.1196174/full#supplementary-material

References

Aoki, S., Takezawa, T., Ikeda, S., Narisawa, Y., Oshikata-Miyazaki, A., Miyauchi, S., et al. (2015). A new cell-free bandage-type artificial skin for cutaneous wounds. *Wound Repair Regen.* 23, 819–829. doi:10.1111/wrr.12321

Boahen, E. K., Pan, B., Kweon, H., Kim, J. S., Choi, H., Kong, Z., et al. (2022). Ultrafast, autonomous self-healable iontronic skin exhibiting piezo-ionic dynamics. *Nat. Commun.* 13, 7699. Epub 2022/12/13. doi:10.1038/s41467-022-35434-8

Cao, H-L., and Cai, S-Q. (2022). Recent advances in electronic skins: Material progress and applications. *Front. Bioeng. Biotechnol.* 2022, 1083579. doi:10.3389/fbioe.2022.1083579

Chen, B., Zhang, L., Li, H., Lai, X., and Zeng, X. (2022). Skin-inspired flexible and high-performance MXene@polydimethylsiloxane piezoresistive pressure sensor for human motion detection. *J. Colloid Interface Sci.* 617, 478–488. doi:10.1016/j.jcis.2022.03.013

Cheng, R. Y., Eylert, G., Gariepy, J. M., He, S., Ahmad, H., Gao, Y., et al. (2020). Handheld instrument for wound-conformal delivery of skin precursor sheets improves healing in full-thickness burns. *Biofabrication. Feb* 3, 025002. Epub 2020/02/06. doi:10.1088/1758-5090/ab6413

Cheng, S., Chen, W., and Zhang, P. (2022). Developing advanced polymer films based on microfluidic laminar flow. *Giant* 9, 100091. doi:10.1016/j.giant.2022.100091

Chortos, A., Liu, J., and Bao, Z. (2016). Pursuing prosthetic electronic skin. *Nat. Mat. Sep.* 15, 937–950. Epub 2016/07/05. doi:10.1038/nmat4671

Chou, H-H., and Lee, W-Y. (2021). "3 - tactile sensor based on capacitive structure," in *Functional tactile sensors* (Weihui, China: Woodhead Publishing), 31–52.

Dąbrowska, A. K., Rotaru, G-M., Derler, S., Spano, F., Camenzind, M., Annaheim, S., et al. (2016). Materials used to simulate physical properties of human skin. *Skin Res. Technol.* 22, 3–14. doi:10.1111/srt.12235

Dearman, B. L., Boyce, S. T., and Greenwood, J. E. (2021). Advances in skin tissue bioengineering and the challenges of clinical translation. *Front. Surg.* 8, 640879. doi:10.3389/fsurg.2021.640879

Du, Y., Yu, G., Dai, X., Wang, X., Yao, B., and Kong, J. (2020). Highly stretchable, self-healable, ultrasensitive strain and proximity sensors based on skin-inspired conductive film for human motion monitoring. *ACS Appl. Mater Interfaces* 12 (12), 51987–51998. Epub 2020/11/04. doi:10.1021/acsami.0c15578

Duan, S., Shi, Q., Hong, J., Zhu, D., Lin, Y., Li, Y., et al. (2023). Water-modulated biomimetic hyper-attribute-gel electronic skin for robotics and skin-attachable wearables. *ACS Nano* 2023, 2c09851. Jan 11. Epub 2023/01/12. doi:10.1021/acsnano.2c09851

Finnerty, C. C., Jeschke, M. G., Branski, L. K., Barret, J. P., Dziewulski, P., and Herndon, D. N. (2016). Hypertrophic scarring: The greatest unmet challenge after burn injury. *Lancet* 388, 1427–1436. Epub 2016/10/07. doi:10.1016/s0140-6736(16)31406-4

García-Ávila, J., Rodríguez, C. A., Vargas-Martínez, A., Ramírez-Cedillo, E., and Martínez-López, J. I. (2021). E-skin development and prototyping via soft tooling and composites with silicone rubber and carbon nanotubes. *Mater. (Basel)* 15. Epub 2022/01/12.

George, B., Bhatia, N., Kumar, A., and Vadakkadath Meethal, K. (2022). Bioinspired gelatin based sticky hydrogel for diverse surfaces in burn wound care. *Sci. Rep.* 12, 13735. doi:10.1038/s41598-022-17054-w

Gong, B., Yao, B., and Zhou, Z. (2022). Bionic skin for simulating human sweating[J]. *J. Sens. Technol.* 35 (01), 14–21.

Guo, Q., Qiu, X., and Zhang, X. (2022). Recent advances in electronic skins with multiple-stimuli-responsive and self-healing abilities. *Mater. (Basel)* 15. Epub 2022/03/11.

Hammock, M. L., Chortos, A., Tee, B. C-K., Tok, J. B-H., and Bao, Z. (2013). 25th anniversary article: The evolution of electronic skin (E-Skin): A brief history, design considerations, and recent progress. *Adv. Mater.* 25, 5997–6038. doi:10.1002/adma.201302240

Horch, R. E., Kopp, J., Kneser, U., Beier, J., and Bach, A. D. (2005). Tissue engineering of cultured skin substitutes. *J. Cell Mol. Med.* 9, 592–608. Epub 2005/10/06. doi:10.1111/j.1582-4934.2005.tb00491.x

Jie, Z. (2022). *Design of silk protein/graphene oxide nanofiber composite flexible electronic skin and its sensing performance[D]*. Zhejiang, China: Zhejiang University of Technology.

Kang, B., Lee, S. K., Jung, J., Joe, M., Lee, S. B., Kim, J., et al. (2018). Nanopatched graphene with molecular self-assembly toward graphene-organic hybrid soft electronics. *Adv. Mat. Jun* 30, e1706480. Epub 2018/05/01. doi:10.1002/adma.201706480

Keng, J., Son, D., Wang, G-J. N., Liu, Y., Lopez, J., Kim, Y., et al. (2018). Tough and water-insensitive self-healing elastomer for robust electronic skin. *Adv. Mater.* 30, 1706846. doi:10.1002/adma.201706846

Kim, J., Lee, M., Shim, H. J., Ghaffari, R., Cho, H. R., Son, D., et al. (2014). Stretchable silicon nanoribbon electronics for skin prosthesis. *Nat. Commun.* 5 (5), 5747. Epub 2014/12/10. doi:10.1038/ncomms6747

Lee, J., Llerena, Z. B., Woo, J., Yoon, K., and Lee, T. (2020). Recent advances in 1D stretchable electrodes and devices for textile and wearable electronics: Materials, fabrications, and applications. *Adv. Mater.Feb* 32 (5), e1902532. doi:10.1002/adma.201902532

Lei, Z., and Wu, P. (2018). A supramolecular biomimetic skin combining a wide spectrum of mechanical properties and multiple sensory capabilities. *Nat. Commun. Mar.* 19 (9), 1134. Epub 2018/03/21. doi:10.1038/s41467-018-03456-w

Lei, Z. (2022). *Preparation of flexible fitable composite proximity sensor and its application research[D]*. Changchun, Nanguan: Northeast Normal University.

Li, D. (2017). *Construction and application of skin tissue engineering composite scaffold based on bioactive glass/chitosan/silk fibroin*. South China: Doctor, South China University of Technology.

Li, Y., Liu, Y., Peng, B., Li, X., Fang, T., Liu, S., et al. (2022). Stretchable, conductive, breathable and moisture-sensitive e-skin based on CNTs/graphene/GelMA mat for wound monitoring. *Biomater. Adv. Dec* 143, 213172. Epub 2022/11/08. doi:10.1016/j.bioadv.2022.213172

Lian, W., Lian, Q., Jiao, T., He, X., Zhao, M., Hu, D., et al. (2021). The research progress and challenge of 3D bioprinting for skin repairing[J]. *Opto-Electron Eng.* 48 (8), 210105.

Liang, J., Sheng, H., Ma, H., Wang, P., Wang, Q., Yuan, J., et al. (2022). Transparent electronic skin from the integration of strain sensors and supercapacitors. *Adv. Mater. Technol.* 8, 2201234. doi:10.1002/admt.202201234

Liao, H., Guo, X., Wan, P., and Yu, G. (2019). Conductive MXene nanocomposite organohydrogel for flexible, healable, low-temperature tolerant strain sensors. *Adv. Funct. Mater.* 29, 1904507. doi:10.1002/adfm.201904507

Lin, M., Wang, J., Wang, S., and Huang, Y. (2022). Expression level of keratin 7 in epithelial ovarian cancer and malignant metastasis of benign epithelial ovarian tumors. *Cell Mol. Biol. (Noisy-le-grand)* 68 (2), 153–161. doi:10.14715/cmb/2022.68.2.22

Liu, D., Zhu, P., Zhang, F., Li, P., Huang, W., Li, C., et al. (2022). Intrinsically stretchable polymer semiconductor based electronic skin for multiple perceptions of force, temperature, and visible light. *Nano Res.* 16, 1196–1204. doi:10.1007/s12274-022-4622-x

Liu, Y-Q., Chen, Z-D., Mao, J-W., Han, D-D., and Sun, X. (2019). Laser fabrication of graphene-based electronic skin. *Front. Chem.* 2019, 461. doi:10.3389/fchem.2019.00461

Nasreldin, M., de Mulatier, S., Delattre, R., Ramuz, M., and Djenizian, T. (2020). Flexible and stretchable microbatteries for wearable technologies. *Adv. Mater. Technol.* 5, 2000412. doi:10.1002/admt.202000412

Naves, L. B., Dhand, C., Almeida, L., Rajamani, L., and Ramakrishna, S. (2016). *In vitro* skin models and tissue engineering protocols for skin graft applications. *Essays Biochem.* 60, 357–369. Epub 2016/12/03. doi:10.1042/ebc20160043

Ng, W. L., Qi, J. T. Z., Yeong, W. Y., and Naing, M. W. (2018). Proof-of-concept: 3D bioprinting of pigmented human skin constructs. *Biofabrication. Jan.* 23, 025005. Epub 2018/01/24. doi:10.1088/1758-5090/aa9e1e

Oh, J. Y., and Bao, Z. (2019). Second skin enabled by advanced electronics. *Adv. Sci.* 6, 1900186. doi:10.1002/advs.201900186

Park, M., Bok, B. G., Ahn, J. H., and Kim, M. S. (2018). Recent advances in tactile sensing technology. *Micromachines (Basel)* 9 (7), 321. Epub 2018/11/15. doi:10.3390/mi9070321

Peng, W., Pan, X., Liu, X., Gao, Y., Lu, T., Li, J., et al. (2023). A moisture self-regenerative, ultra-low temperature anti-freezing and self-adhesive polyvinyl alcohol/polyacrylamide/CaCl(2)/MXene ionotronics hydrogel for bionic skin strain sensor. *J. Colloid Interface Sci. Mar.* 15, 782–792. Epub 2022/12/25. doi:10.1016/j.jcis.2022.12.101

Rahman, M. A., Walia, S., Naznee, S., Taha, M., Nirantar, S., Rahman, F., et al. (2020). Artificial somatosensors: Feedback receptors for electronic skins. *Adv. Intell. Syst.* 2, 2070106. doi:10.1002/aisy.202070106

Shao, W., Zhang, L., Jiang, Z., Xu, M., Chen, Y., Li, S., et al. (2022). Bioinspired conductive structural color hydrogels as a robotic knuckle rehabilitation electrical skin. *Nanoscale Horizons* 7, 1411–1417. doi:10.1039/d2nh00322h

Tarassoli, S. P., Jessop, Z. M., Al-Sabah, A., Gao, N., Whitaker, S., Doak, S., et al. (2018). Skin tissue engineering using 3D bioprinting: An evolving research field. *J. Plast. Reconstr. Aesthet. Surg. May* 71, 615–623. Epub 2018/01/08. doi:10.1016/j.bjps.2017.12.006

Wan, S., JiaLin, C., ShiHong, L., and JunPeng, L. (2020). Research progress on novel materials and properties of electronic skin[J]. *J. Eng. Sci.* 42 (06), 704–714.

Wang, C., Liu, C., Shang, F., Niu, S., Ke, L., Zhang, N., et al. (2023). Tactile sensing technology in bionic skin: A review. *Biosens. Bioelectron.* 220, 114882. Epub 2022/11/19.

Wang, M., Luo, Y., Wang, T., Wan, C., Pan, L., Pan, S., et al. (2021). Artificial skin perception. *Adv. Mater.* 33, 2003014. doi:10.1002/adma.202003014

Wang, M., Tu, J., Huang, Z., Wang, T., Liu, Z., Zhang, F., et al. (2022). Tactile near-sensor analogue computing for ultrafast responsive artificial skin. *Adv. Mater.* 34, 2201962. doi:10.1002/adma.202201962

Wang, X., Wu, Y., and Mei, C. (2020). Biomedical materials: A review of artificial skin research. *Knowledge-Power.* 2020.

Wei, J., Xie, J., Zhang, P., Zou, Z., Ping, H., Wang, W., et al. (2021). Bioinspired 3D printable, self-healable, and stretchable hydrogels with multiple conductivities for skin-like wearable strain sensors. *ACS Appl. Mater. Interfaces* 13, 2952–2960. doi:10.1021/acsami.0c19512

Xiang, S. (2021). *Dynamic thermal management based on liquid metal with self-driven electronic skin[D]*. Zhengzhou: Zhengzhou University.

Xie, W. (2022). Transparent electronic skin from substitutes. *Chin. Med. J.* 57 (12), 1282–1286.

Xing, H. (2021). *Ion skin development based on printable double network hydrogel material*. Dalian, Ganjingzi: Dalian University of Technology.

Xu, S., Zhang, Y., Cho, J., Lee, J., Huang, X., Jia, L., et al. (2013). Stretchable batteries with self-similar serpentine interconnects and integrated wireless recharging systems. *Nat. Commun.* 4, 1543. doi:10.1038/ncomms2553

Yan, W. C., Davoodi, P., Vijayavenkataraman, S., Tian, Y., Ng, W. C., Fuh, J. Y. H., et al. (2018). 3D bioprinting of skin tissue: From pre-processing to final product evaluation. *Adv. Drug Deliv. Rev. Jul* 132, 270–295. Epub 2018/07/29. doi:10.1016/j.addr.2018.07.016

Yang, J. C., Mun, J., Kwon, S. Y., Park, S., Bao, Z., and Park, S. (2019). Electronic skin: Recent progress and future prospects for skin-attachable devices for health monitoring, robotics, and prosthetics. *Adv. Mater.* 31, 1904765. doi:10.1002/adma.201904765

Yang, X., Yi, J., Wang, T., Feng, Y., Wang, J., Yu, J., et al. (2022). Wet-Adhesive on-skin sensors based on metal-organic frameworks for wireless monitoring of metabolites in sweat. *Adv. Mat. Nov.* 34, e2201768. Epub 2022/09/23. doi:10.1002/adma.202201768

Yao, K.-M., Jing-Yi, Y., Zhao, H., Deng-Feng, L., Zhao-Qian, X., and Xin-Ge, Y. (2020). Stretchable self-powered epidermal electronics from piezoelectric rubber for tactile sensing. *Acta Phys. Sin.* 69 (17), 178701. doi:10.7498/aps.69.20200664

Yao, S., Swetha, P., and Zhu, Y. (2017). Nanomaterial-enabled wearable sensors for healthcare. *Adv. Healthc. Mater* 7 (1), 1700889. doi:10.1002/adhm.201700889

Yu, Z., Yanan, D., Shengyun, L., Chaoxiang, Y., Yanxia, Z., and Guoru, Z. (2021). *Application design of cognitive-motor rehabilitation medical robot.* (Weihui, China. Information and Control.

Zeng, X., Liu, Y., Liu, F., Wang, W., Liu, X., Wei, X., et al. (2022). A bioinspired three-dimensional integrated e-skin for multiple mechanical stimuli recognition. *Nano Energy* 92, 106777. doi:10.1016/j.nanoen.2021.106777

Zhang, H., Chen, H., Lee, J-H., Kim, E., Chan, K-Y., Venkatesan, H., et al. (2022). Bioinspired chromotropic ionic skin with in-plane strain/temperature/pressure multimodal sensing and ultrahigh stimuli discriminability. *Adv. Funct. Mater.* 32, 2208362. doi:10.1002/adfm.202208362

Zhang, L., Zhang, S., Wang, C., Zhou, Q., Zhang, H., and Ge-Bo, P. (2021). Highly sensitive capacitive flexible pressure sensor based on a high-permittivity MXene nanocomposite and 3D network electrode for wearable electronics. *ACS Sens.* 6, 2630–2641. doi:10.1021/acssensors.1c00484

Zhang, M., Jing, Y., and Zhang, J. (2022). Performance prediction ofmagnetorheologicalfluid-baseoliquid gating membrane byKriging machine learningmethod. *Mater* 1, 157–169. Interdiscip.

Zhang, P., Han, X., Yao, J., Shao, N., Zhang, K., Zhou, Y., et al. (2019). High-throughput isolation of cell protrusions with single-cell precision for profiling subcellular gene expression. *Angew. Chem. Int. Ed.* 58, 13838–13843. doi:10.1002/ange.201903694

Zhang, P., Shao, N., and Qin, L. (2021). Recent advances in microfluidic platforms for programming cell-based living materials. *Adv. Mater.* 33, 2005944. doi:10.1002/adma.202005944

Zhang, Z., Chen, Z., Wang, Y., and Zhao, Y. (2020). Bioinspired conductive cellulose liquid-crystal hydrogels as multifunctional electrical skins. *Proc. Natl. Acad. Sci.* 117, 18310–18316. doi:10.1073/pnas.2007032117

Zhao, L., Bowen, B., and Zhenglu, W. (2017). Current status of development of skin grafts and skin tissue banks. *Electron. J. Pract. Organ Transplant.* 5 (06), 473–475.

Zhou, F., Hong, Y., Liang, R., Zhang, X., Liao, Y., Jiang, D., et al. (2020). Rapid printing of bio-inspired 3D tissue constructs for skin regeneration. *Biomaterials* 258, 120287. Epub 2020/08/28. doi:10.1016/j.biomaterials.2020.120287

Frontiers in
Bioengineering and Biotechnology

Accelerates the development of therapies, devices, and technologies to improve our lives

A multidisciplinary journal that accelerates the development of biological therapies, devices, processes and technologies to improve our lives by bridging the gap between discoveries and their application.

Discover the latest Research Topics

See more →

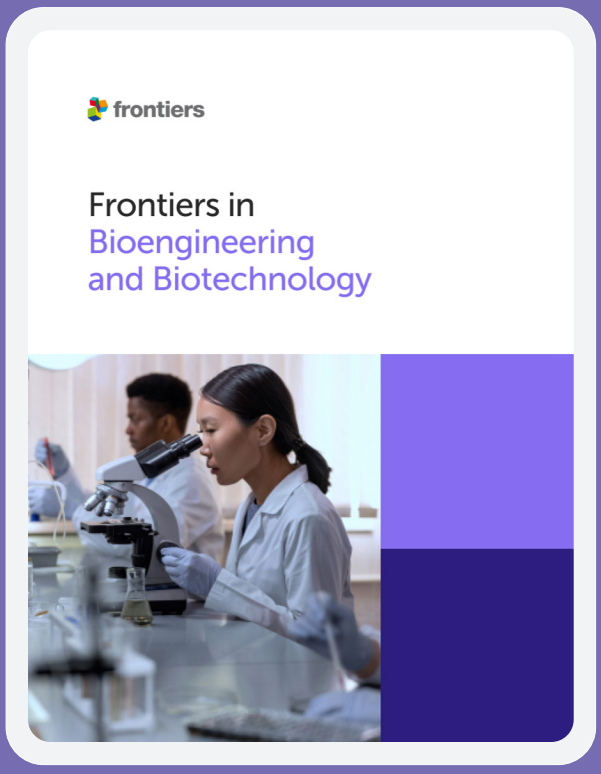

Frontiers

Avenue du Tribunal-Fédéral 34
1005 Lausanne, Switzerland
frontiersin.org

Contact us

+41 (0)21 510 17 00
frontiersin.org/about/contact